Scholar Commons
USF University of South Florida

University of South Florida
Scholar Commons

Graduate Theses and Dissertations | Graduate School

2007

Development of micro/nanosensor elements and packaging techniques for oceanography

Shyam Aravamudhan
University of South Florida

Follow this and additional works at: http://scholarcommons.usf.edu/etd

 Part of the American Studies Commons

Scholar Commons Citation
Aravamudhan, Shyam, "Development of micro/nanosensor elements and packaging techniques for oceanography" (2007). *Graduate Theses and Dissertations.*
http://scholarcommons.usf.edu/etd/607

This Dissertation is brought to you for free and open access by the Graduate School at Scholar Commons. It has been accepted for inclusion in Graduate Theses and Dissertations by an authorized administrator of Scholar Commons. For more information, please contact scholarcommons@usf.edu.

Development of Micro/Nanosensor Elements and Packaging Techniques for Oceanography

by

Shyam Aravamudhan

A dissertation submitted in partial fulfillment
of the requirements for the degree of
Doctor of Philosophy
Department of Electrical Engineering
College of Engineering
University of South Florida

Major Professor: Shekhar Bhansali, Ph.D.
Thomas M. Weller, Ph.D.
Jing Wang, Ph.D.
Ashok Kumar, Ph.D.
Larry Langebrake, M.S.E.E.

Date of Approval:
October 25, 2007

Keywords: mems, pressure sensor, electrochemical, nitrate sensor, nanowires

© Copyright 2007 , Shyam Aravamudhan

DEDICATION

This dissertation is dedicated to Matha, Pitha, Guru, and Deivam.

ACKNOWLEDGEMENTS

First and foremost, I would like to express my sincere gratitude and appreciation to Dr. Shekhar Bhansali for providing me this wonderful opportunity to work in the BioMEMS and Microsystems laboratory. His encouragement, guidance, and direction during this work have been invaluable. Dr. Bhansali's support, while I worked on quite complimentary projects and his technical and non-technical insights, will remain forever in me.

Next, I would like to thank to Mr. Larry Langebrake, SRI/COT for his technical assistance and facilities support at the Center for Ocean Technology. Many thanks to Dr. Thomas Weller and Dr. Ashok Kumar for their suggestions and support in the form of fabrication and measurement instruments. I would also like to thank Dr. Jing Wang for his participation in my committee. My sincere appreciation and thanks to Dr. Rajiv Dubey (Chair of Mechanical Engineering) for agreeing to chair this defense. Special thanks for Dr. Andrew Hoff for introducing me to the world of semiconductor fabrication.

I would like to thank funding support from USF Graduate School Predoctoral fellowship, USF MEMS Fellowship, National Science Foundation (NSF) NER award 0403800 and Center for Ocean Technology. This work would not have been possible without the support of our collaborators – Drs Shyam Mohapatra and Arun Kumar (Internal Medicine, USF); Dr. John Singleton (NHMFL, Los Alamos), Dr. Paul Goddard (Physics, Oxford), Dr. James Brooks (NHMFL, FSU) and Dr. Srikanth Hariharan (Physics, USF).

I would also like to gratefully acknowledge the time and effort put in by members of the COT/SRI staff (Dr. Weidong Wang, Dr. Scott Samson and Mr. Gino Gonzales), members of the NNRC staff (Mr. Robert Tufts, Mr. Rich Everly and Mr. Jay Bieber), members of EE staff (Mike, Trung, Harris, Maria, Becky, Gayla and Norma). Special thanks to Mr. Bernard Batson (Coordinator, IGERT/SKINS program) for all his support. I would also like to thank present and former members of the BioMEMS group (Praveen, Dr. Niranjan Ramgir, Rahul, Kevin, Subbu, Supriya, Puneet, Sun Ke, Carl and Johnny) and RF Microsystems group (Dr. Balaji Lakshminarayanan, Saravana and Srinath) for their unyielding support. Finally, I can't thank enough the support and encouragement of my family and all my friends.

NOTE TO READER

The original of this document contains color that is necessary for understanding the data. The original dissertation is on file with the USF library in Tampa, Florida.

TABLE OF CONTENTS

LIST OF TABLES vi

LIST OF FIGURES vii

ABSTRACT xiv

CHAPTER 1 INTRODUCTION 1

1.1 Overview 1

1.2 Significance of this research 3

1.3 Contributions 6

1.4 Dissertation organization 7

CHAPTER 2 DYNAMICS OF OCEAN SENSING 9

2.1 Overview 9

2.2 Motivation for ocean sensing 12

2.2.1 Chemical and biological ocean processes 13

2.2.2 Physical measurement needs 16

2.3 Ocean sensing mechanisms 17

2.4 Current state of the art in chemical and biological measurements 18

2.4.1 Classification based on technology 18

2.4.2 Classification based on measurands 22

2.5 Technology for detecting pressure/depth variations 24

2.5.1 Introduction 24

2.5.2 Classification based on transduction mechanisms 27

2.6 Summary 29

CHAPTER 3 DESIGN AND ANALYSIS OF REINFORCED PRESSURE SENSORS 30
3.1 Introduction 30
3.2 Theory of piezoresistivity 31
3.2.1 Overview 31
3.2.2 Mathematical description 35
3.2.3 Average over stress and doping variations 40
3.3 Theory of piezoresistive pressure sensors 40
3.3.1 Overview 40
3.3.2 Placement of piezoresistors 42
3.3.3 Theory of reinforced diaphragm pressure sensor 44
3.3.4 Stress analysis of reinforced diaphragm design 46
3.4 Design of reinforced diaphragm pressure sensors 54
3.4.1 Overview 54
3.4.2 Generation I: design 55
3.4.3 Effect of residual stress 58
3.4.4 Temperature compensation bridge 60
3.5 Design of Generation II reinforced diaphragm pressure sensors 61
3.5.1 Overview 61
3.5.2 Description of masked-maskless etching process 62
3.5.3 Design of Generation II sensors 64
3.6 Design of Generation III reinforced diaphragm pressure sensors 65
3.7 Summary 66

CHAPTER 4 REINFORCED PRESSURE SENSOR FABRICATION AND PACKAGING 67
4.1 Overview 67
4.2 Generation I: fabrication process 68
4.3 Generation II: fabrication using masked-maskless process 72
4.3.1 Introduction 72
4.3.2 Characterization of masked-maskless etching process 73
4.3.3 Etch3D™ simulation analysis 75
4.4 Packaging approach I 81
4.5 Packaging approach II 85
4.6 Description of packaging elements 87

4.6.1 Protective coatings 87
4.6.2 Flip chip technology with anisotropic conductive films (ACF) 87
4.7 Summary 90

CHAPTER 5 PERFORMANCE OF REINFORCED DIAPHRAGM PRESSURE SENSORS 91
5.1 Overview 91
5.2 Generation I: results and discussion 91
5.2.1 Maximum burst pressure and sensor calibration testing 91
5.2.2 Sensitivity analysis of single diaphragm configuration 93
5.2.3 Sensitivity analysis of reinforced diaphragm configuration 93
5.2.4 Comparison of experimental and simulation results 97
5.2.5 Mechanical and output sensitivity 99
5.3 Effect of temperature sensitive bridge 99
5.4 Package and protective coatings analysis 100
5.5 Generation II: results and discussion 102
5.5.1 Overview 102
5.5.2 Sensitivity analysis of Generation II sensors 102
5.5.3 Comparison of Generation I and Generation II sensors 107
5.6 Generation III: results and discussion 108
5.6.1 Overview 108
5.6.2 Sensitivity analysis of Generation III sensors 109
5.7 Summary 110

CHAPTER 6 NANOWIRE-BASED ELECTROCHEMICAL DETECTION-ON-CHIP 111
6.1 Introduction 111
6.2 Electrochemical sensors 112
6.2.1 Controlled-potential techniques 113
6.2.2 Working electrodes 115
6.3 One-dimensional (1-D) nanostructures (nanowires) 116
6.3.1 Properties at nanoscale 116
6.3.2 Synthesis techniques for nanowires 117
6.4 Template-directed synthesis of nanowires 119
6.4.1 Overview 119

6.4.2 Template fabrication 120
6.4.3 Nanowire synthesis via electrodeposition 121
6.5 Sensing modalities 123
6.5.1 Fabrication of nanosensor elements 123
6.5.2 Assembly of nanowires on silicon substrate 127
6.6 Microfluidic electrochemical biosensor for targeted detection using Au nanowires 130
6.6.1 Introduction 130
6.6.2 Importance of cholesterol detection in blood 131
6.6.3 Materials and instruments 132
6.6.4 Electrochemical cell fabrication 133
6.6.5 Enzyme immobilization on Au-NWs 133
6.6.6 Electrochemical measurements 134
6.6.7 Structural and morphological results 134
6.6.8 Calibration results 136
6.6.9 Selectivity and storage stability 140
6.7 Summary 142

CHAPTER 7 ELECTROCHEMICAL NITRATE SENSOR WITH INTEGRATED MICROFLUIDICS 143
7.1 Introduction 143
7.2 Current methods of nitrate detection 145
7.3 Sensing modality 147
7.3.1 Nanosensor elements: polypyrrole nanowires 147
7.3.2 Synthesis of polypyrrole nanowires 149
7.3.3 Incorporation of chemical recognition sites 151
7.4 Development of electrochemical sensor with integrated microfluidics 152
7.4.1 Overview 152
7.4.2 Materials 154
7.4.3 Fabrication of electrochemical sensor chip and microfluidic platform 154
7.4.4 Electroactivity of doped PPy nanowires 156
7.4.5 Generation I: electrochemical measurements under static conditions 157
7.4.6 Generation II: flow cell analysis under dynamic conditions 160
7.4.7 Effect of interfering ions and storage stability 164

7.4.8 Generation III: all micromachined flow cell 165
7.5 Summary 167

CHAPTER 8 CONCLUSIONS AND FUTURE OUTLOOK 168
8.1 Conclusions 168
8.2 Future outlook 169

REFERENCES 175

APPENDICES 184
APPENDIX A CONVERSION OF PRESSURE TO DEPTH 185
APPENDIX B ETCH3D™ SIMULATION CODE FOR DOUBLE DIAPHRAGM ETCHING 186
APPENDIX C PHOTOLITHOGRAPHY PROCESSES 193
APPENDIX D THROUGH WAFER NANOSTRUCTURES (INTERCONNECTS) IN POROUS SILICON 195
APPENDIX E MAGNETIC PROPERTIES OF NI-FE NANOWIRES: EFFECT OF TEMPLATE MATERIAL AND DEPOSITION CONDITIONS 202
APPENDIX F POROUS SILICON BASED MICRO DIRECT ETHANOL FUEL CELL 214

ABOUT THE AUTHOR End page

LIST OF TABLES

Table 1.1	Core ocean variables monitored by IOOS infrastructure.	3
Table 2.1	Commercially available chemical sensor modules for ocean measurements.	23
Table 2.2	Commercially available ocean pressure/depth sensors.	26
Table 3.1	Typical piezoresistive coefficients at room temperature.	38
Table 3.2	Longitudinal and transverse coefficients for various combinations of directions in cubic crystal.	39
Table 3.3	List of Generation I sensor design parameters.	56
Table 3.4	List of diaphragm dimensions for Generation I sensors.	57
Table 3.5	Design parameters for Generation II sensors.	64
Table 3.6	Design parameters for Generation III diaphragm structures.	66
Table 5.1	Summary of maximum burst pressure for different sensor designs.	92
Table 5.2	Summary of Generation II device dimensions (measured).	102
Table 5.3	Summary of experimental results for Generation II devices.	107
Table 5.4	Summary of Generation III sensors.	109
Table 7.1	Methods for nitrate determination.	145
Table A.1	List of values for constants in pressure and gravity calculations.	185
Table A.2	Typical depth-pressure conversion at different latitudes.	185
Table E.1	Template parameters and characteristics.	205
Table E.2	Magnetic characterization parameters for Ni-Fe nanowires in different template and magnetic field during deposition.	213

LIST OF FIGURES

Figure 2.1	Physical and biogeochemical processes in ocean.	9
Figure 2.2	Time and space scales for ocean processes and phenomenon relevant to biogeochemical cycling.	10
Figure 2.3	Example of under sampling problem.	11
Figure 2.4	Data from MBARI pier in Moss Landing harbor.	12
Figure 2.5	Variability of different parameters in time and space scales.	14
Figure 2.6	Images of ocean sensing modules.	16
Figure 2.7	Illustration of different ocean measurement approaches.	17
Figure 2.8	SEM image of diatom slime growth on copper screens.	18
Figure 2.9	Illustration of nitrate concentration spread across the globe.	23
Figure 2.10	Macroscopic pressure sensors a) simple diaphragm, b) corrugated diaphragm, c) capsule, d) capacitive sensor, e) bellows, f) bourdon tube, g) straight tube.	25
Figure 2.11	Illustration of quartz-beam resonators as pressure sensor.	26
Figure 2.12	Illustration of piezoresistive pressure sensor.	27
Figure 2.13	Illustration of capacitive pressure sensing principle.	27
Figure 3.1	Illustration of isotropic stress applied on silicon crystal.	32
Figure 3.2	Piezoresistance factor P(n, T) as a function of impurity concentration and temperature a) n-Si, b) p-Si.	34
Figure 3.3	Effect on piezoresistive coefficient on a) Si, b) heavily doped, c) lightly doped.	35
Figure 3.4	Definition of normal stresses (σ) and shear stresses (τ).	36
Figure 3.5	Schematic for piezoresistive coefficients: longitudinal and transverse.	37
Figure 3.6	π_l and π_t for p-type Si on different planes at room temperature.	39
Figure 3.7	Typical bulk etching of (100) silicon.	41
Figure 3.8	Proposed diaphragm architectures a) reinforced diaphragm, b) with bossed structure.	42
Figure 3.9	Illustration of piezoresistor placement in a square diaphragm with wheatstone bridge network.	43
Figure 3.10	Schematic of the double diaphragm/wheatstone bridge piezoresistive sensor.	44

Figure 3.11	Illustration of diaphragm deflection in reinforced and bossed configurations.	46
Figure 3.12	Example of stress distribution for single (a) and inner (b) diaphragm designs (1500.x 1500 μm) for an applied load of 1 MPa or 145 psi.	55
Figure 3.13	Plot of diaphragm center deflection versus applied pressure.	56
Figure 3.14	Plot of diaphragm deflection at x, y=0 versus position on diaphragm (x/L).	57
Figure 3.15	Plot of center deflection as function of applied pressure for sensors D1, D2 and S2.	58
Figure 3.16	Plot of stress at the piezoresistor versus pressure for sensors D1, D2, S2 and S3.	58
Figure 3.17	Illustration of multi-level structure etching.	61
Figure 3.18	Cross-sectional evolution of (311) plane during maskless etching.	63
Figure 3.19	Conventorware stress map of a) low pressure (100 psi) peak stress at inner diaphragm, b) high pressure (300 psi) peak stress at outer diaphragm.	65
Figure 3.20	Illustration of Generation III sensor with central boss.	65
Figure 4.1	Schematic of system-level packaging of pressure sensors following packaging approach I.	68
Figure 4.2	Schematic of system-level packaging of pressure sensors following packaging approach II.	68
Figure 4.3	Illustration showing process flow for Generation I sensors.	70
Figure 4.4	Image of a) piezoresistors (boron), b) after first etch (inner diaphragm), c) inner and outer diaphragm.	72
Figure 4.5	Illustration of the maskless etching edge.	73
Figure 4.6	Experimentally determined critical depths for a range of initial masked depth.	73
Figure 4.7	Experimentally determined recession distance for a range of maskless etching depth.	74
Figure 4.8	Image showing the evolved (311) plane during maskless etching.	74
Figure 4.9	Etch3D™ image of conventional single etched trench.	75
Figure 4.10	a) Top view of double diaphragm etching, b) and c) cross-sectional view of double etched diaphragm.	76
Figure 4.11	Illustration of a) exposed concave corner during maskless etching, b) exposed convex and concave corner during maskless etching.	77
Figure 4.12	Relationship of masked undercutting versus time (simulated).	78
Figure 4.13	Relationship of maskless undercutting versus time (simulated).	78
Figure 4.14	a) AFM surface map.	79
Figure 4.15	Image showing convex corner undercutting in Generation III devices.	80
Figure 4.16	Corner compensation structure in Generation III sensors.	81

Figure 4.17	Illustration of anodic bonding process.	82
Figure 4.18	Illustration of the packaging I process flow.	83
Figure 4.19	Image of a) zeroth-level package on pressure sensors, b) contacts through conductive epoxy.	84
Figure 4.20	Image of system-level package (array of pressure sensors).	84
Figure 4.21	Illustration of packaging approach II process flow.	86
Figure 4.22	Images of pressure sensors packaged using approach II.	87
Figure 4.23	Typical system-level package with ACF and flexible circuit board.	89
Figure 4.24	Process flow for bonding sensing chip with flexible electronics using ACF.	90
Figure 5.1	Custom-built pressure chamber to simulate ocean conditions (left), sensor testing setup: pressure pump, water chamber and test rig (right).	92
Figure 5.2	Variation of output voltage to input pressure for single diaphragms (S1, S2).	93
Figure 5.3	Variation of output response to input pressure variations for sensor D1.	94
Figure 5.4	Variation of output response to input pressure variations for sensor D2.	94
Figure 5.5	Comparison of output response to input pressure variations for single and reinforced sensors (ratio of outer/inner less than 3).	95
Figure 5.6	Comparison of output response to input pressure variations for single and reinforced sensors (ratio of outer/inner greater than 3).	96
Figure 5.7	Comparison of design and experimental (same dimensions) output response a) sensor D3, b) sensor D4.	96
Figure 5.8	Comparison of experimental results with re-simulated (model) data accounting for process variations.	97
Figure 5.9	Comparison of experimental results with re-simulated (model) data accounting for process variations and residual stress on diaphragm.	98
Figure 5.10	Mechanical and output sensitivity for Generation I sensors.	98
Figure 5.11	Variation of piezoresistance values for a temperature range.	99
Figure 5.12	Images of sensor surface after exposure for one week in winter a) CYTOP®, b) BCB, c) oxide, d) SU-8 50, e) lumiflon®, f) nitride.	100
Figure 5.13	Images of sensor surface after exposure for one week in summer a) parylene, b) CYTOP®, c) lumiflon®, d) oxide, e) SU-8 50, f) nitride.	101
Figure 5.14	Effect of package and protective coatings on output voltage.	101
Figure 5.15	Variation of output response to input pressure variations for sensor II-D5.	103
Figure 5.16	Variation of output response to input pressure variations for sensor II-D6.	104
Figure 5.17	Variation of output response to input pressure variations for sensor II-D7.	105
Figure 5.18	3D plot of variation of outer bridge sensitivity to outer diaphragm dimensions for constant inner dimensions.	105

Figure 5.19 3D plot of variation of inner bridge sensitivity and transition point to outer diaphragm length. 106
Figure 5.20 Comparison of experimental results of Generation I-D2 and II-D6 sensors. 107
Figure 5.21 Re-simulated output response for input pressure variation for single, Generation I and Generation II sensors. 108
Figure 5.22 Variation of output response to input pressure variations for Generation III sensors (inner diaphragm). 109
Figure 5.23 Comparison of output response of Generation I-D2, II-D6 and III-B2 sensors. 110
Figure 6.1 Aspects of an electrochemical sensor for environmental monitoring. 112
Figure 6.2 Illustration of the six different techniques for obtaining nanowire growth. 118
Figure 6.3 Illustration of template synthesis method of creating metallic nanowires. 120
Figure 6.4 Illustration of the electroplating setup and the different regimes in the electroplating process. 122
Figure 6.5 a) SEM image of alumina template with 200 nm diameter pores. 123
Figure 6.6 a) SEM image of cluster of 275±25 nm Ni-Fe nanowires partially released by 10 μm. 125
Figure 6.7 SEM image of two-segmented Ni-Fe/Au nanowires. 126
Figure 6.8 Illustration of magnetic alignment process showing NiFe-Au-NiFe nanowires assembled using magnetic field. 128
Figure 6.9 Illustration of the through wafer interconnection scheme for assembly on nanowires deposited in porous silicon. 129
Figure 6.10 Schematic top view of the interdigitated Pt lines for dielectrophoresis. 130
Figure 6.11 Cross-sectional schematic of the electrochemical test cell. 133
Figure 6.12 SEM images showing the top view and cross-sectional view (inset) of the 175±25 nm Au nanowires released from alumina template. 135
Figure 6.13 SEM image of Au nanowires specifically modified with biotin/avidin linkage. 136
Figure 6.14 AFM images of Au nanowires a) before modification (left), b) after enzyme immobilization (right), showing the modified working electrode. 137
Figure 6.15 FTIR spectra of the Au nanowires after immobilization with enzymes COX and CE. 137
Figure 6.16 Square wave voltammograms (0.01 to 0.10 V) recorded at different concentration of cholesterol, from 10 to 60 μM with step of 10 μM. 138
Figure 6.17 Calibration plot for cholesterol levels (10 to 60 μM with step of 10 μM). 138
Figure 6.18 Comparison of current response between Au nanowires electrode and Au microelectrode. 139
Figure 6.19 Lineweaver-Burk Plot of I_r^{-1} versus C_s^{-1} for the results shown in calibration

	plot of cholesterol biosensor.	140
Figure 6.20	Interference study for cholesterol levels (30 and 50 μM) and higher level of interfering species (20 μM of urea, 50 μM of glucose and 4 M of ascorbic acid).	141
Figure 6.21	Storage stability study of current response as a function of time in days for three different concentrations (1, 3, 5 mM).	141
Figure 7.1	Two compartment cell for synthesis of polypyrrole nanowires.	149
Figure 7.2	a) SEM image of alumina template (front side) with 200-250 nm PPy nanowires polymerized in the nanopores, b) SEM backside view of alumina with pores partially filled with PPy nanowires.	150
Figure 7.3	SEM view of bunch of 200±25 nm PPy nanowires after released from alumina template.	151
Figure 7.4	FTIR spectra of polypyrrole nanowires in alumina template.	152
Figure 7.5	Electrochemical nitrate sensor chip.	154
Figure 7.6	Test cell with Pt assembly lines and counter electrode.	156
Figure 7.7	Picture of the flow through analysis setup with assembled microfluidic components, connectors and tubing.	156
Figure 7.8	Cyclic voltammogram of PPy-NWs electrodes.	157
Figure 7.9	Complete experimental set up for measuring nitrate concentration in flow through conditions.	158
Figure 7.10	Calibration plot for *DI-cal* baseline solution; peak current response versus nitrate concentration (10-200 μM).	160
Figure 7.11	Calibration plot for *Ocean-cal* baseline solution; peak current response versus nitrate concentration (20-1000 μM).	160
Figure 7.12	Illustration of the flow through set up for measuring nitrate concentration under realistic and controlled environment.	161
Figure 7.13	Flow through analysis plot of peak current response at regular time intervals for successive nitrate increments (50-300 μM).	163
Figure 7.14	Flow through analysis plot of peak current response for intermittent nitrate spikes.	163
Figure 7.15	Lifetime study of nitrate doped PPy-NWs electrodes at different nitrate concentrations (50, 100, and 200 μM).	165
Figure 7.16	Schematic of the all micromachined electrochemical flow cell.	166
Figure 7.17	Image of all micromachined electrochemical sensor with integrated microfluidics.	167
Figure 8.1	Cable deployment strategy for pressure/depth sensors.	170
Figure 8.2	Illustration of signal conditioner ZMD31050 and bridge network mode of operation.	172
Figure 8.3	Schematic diagram of Lab-on-a-cable concept.	173

Figure 8.4	Single pair of electrodes for nanowire assembly.	173
Figure 8.5	Pressure-driven fluid flow through a) straight micro-channel, b) T-channel at time t_1, c) time t_2, d) time t_3 and e) time t_4.	174
Figure 8.6	Integrated sensors in a single package (patent pending).	174
Figure D.1	Process flow for fabrication of nanowires.	197
Figure D.2	SEM image of 290 nm diameter and 145 μm deep nanopores in n-type Si substrate.	198
Figure D.3	SEM image of 40 nm diameter nanopores in p-type Si substrate.	199
Figure D.4	SEM image of nanopores, 235 μm deep after 160 minutes of etching in 25% (v/v) HF/ethanol at a constant current density of 35 mA/cm^2.	200
Figure D.5	SEM image showing cluster of 275±25 nm Au nanowires.	201
Figure E.1	a) SEM image of 280-300 nm diameter and 145 μm deep nanopores in n-type Si substrate b) SEM view of the starting alumina template c) SEM view of the polycarbonate template.	204
Figure E.2	a) SEM image of a cluster of 250-300 nm Ni-Fe nanowires (left), b) SEM view of nanowires released from alumina template (right).	205
Figure E.3	X-ray diffraction pattern of Ni-Fe nanowires deposited in a) without magnetic field in porous silicon, b) with perpendicular magnetic field in polycarbonate template.	207
Figure E.4	Typical magnetic hysteresis curves of Ni-Fe nanowire arrays measured parallel and perpendicular to the template plane in a) porous silicon, b) alumina, c) polycarbonate in absence of magnetic field.	208
Figure E.5	Typical magnetic hysteresis curves of Ni-Fe nanowire arrays measured parallel and perpendicular to the template plane in a) porous silicon, b) alumina, c) polycarbonate in presence of perpendicular magnetic field.	209
Figure E.6	Dependence of coercivity and squareness ratio on applied perpendicular magnetic field during Ni-Fe electrodeposition in polycarbonate template.	211
Figure E.7	Dependence of coercivity and squareness ratio on Ni-Fe wire length, deposited in polycarbonate template.	212
Figure F.1	Schematic illustration of a bipolar direct ethanol fuel cell (DEFC).	215
Figure F.2	a) Cross-sectional view of the porous silicon based micro DEFC stack, b) alternative design for the porous silicon based micro DEFC stack.	217
Figure F.3	Schematic of the setup for porous silicon etching.	219
Figure F.4	Illustration of the fabrication process flow for making porous silicon.	220
Figure F.5	SEM of the silicon substrate after the pore initiation lithography and etching (left), SEM cross-sectional view of the final through porous silicon substrate (right).	221
Figure F.6	SEM cross-sectional view of the membrane electrode assembly (MEA) in the fuel cell stack.	222

Figure F.7	Picture of the micro DEFC in a custom-built package.	222
Figure F.8	Variation of cell voltage as a function of time for the micro DEFC.	223
Figure F.9	Polarization curves at different cell orientations for the micro DEFC.	224
Figure F.10	Statistical analysis of voltage versus current density using voltage error bars.	225

DEVELOPMENT OF MICRO/NANOSENSOR ELEMENTS AND PACKAGING TECHNIQUES FOR OCEANOGRAPHY

Shyam Aravamudhan

ABSTRACT

In this research, novel high resolution reinforced diaphragm MEMS piezoresistive pressure sensors were designed, fabricated and tested to measure physical phenomena (such as depth/pressure variations) in the ocean. To complement the physical sensing elements, a microfluidic electrochemical nitrate sensor, was also developed to detect chemical fluxes. The electrochemical sensor was designed and packaged to conform to a flow through system. The multisensor approach will enable better measurement quality compared to the current ocean sensors. This, in turn, will potentially improve the current understanding of physical and biogeochemical processes from coastal to deep-sea environment.

The pressure sensor element utilized a reinforced bulk micromachined diaphragm to achieve both higher sensitivity (27% higher, model data) and wider linear pressure operating range (> 400 psi, from combination of inner and outer bridge) compared to the conventional single diaphragm design. A temperature compensation bridge was incorporated on the sensor die to account for temperature drifts. A two-level packaging (wafer and system-level) scheme with protective coatings were developed to test the sensor in “simulated” ocean conditions. Finally, the reinforced diaphragm edge and the bossed structures were designed and fabricated using the masked-maskless etching process and their sensor performance were evaluated against the single diaphragm design.

A nanowire-based Electrochemical detection-on-Chip (EoC) system was also developed to detect chemical/biological markers, especially nitrate fluxes. Different sensing modalities,

involving a variety of nanosensor electrodes and different assembly techniques were investigated for suitability as electrochemical nitrate sensor. These architectures were also evaluated for robustness as a sensing platform. Enzyme-modified Au nanowires based electrochemical sensor showed excellent sensitivity (μM level) to biomarkers (cholesterol) in biological fluids (blood). These sensors, however, exhibited poor detection limits towards nitrate ions. Doped polypyrrole nanowire electrodes proved to be effective as nitrate sensors. A detection limit of 4.5±1 μM, sensitivity of 1.65 nA/μM and stability of <15% variation from interfering ions were achieved on testing in a flow through environment. The nitrate sensor performance was at par with the current state of the art. Additionally, these sensors are batch fabricated (as arrays) reducing cost, require smaller sample volume, lesser space, power and are less prone to contamination problems.

CHAPTER 1

INTRODUCTION

1.1 Overview

The United States commission on Ocean Policy report, "*An ocean blueprint for the 21st century*," states an urgent need to enact major changes in the ocean resources monitoring and management (Watkins et al., 2004). According to the report tabled to the President and the Congress, "*Human ingenuity and ever-improving technologies have exploited and significantly altered – the ocean's bounty to meet the society's escalating needs. Pollution runs off the land, degrading coastal waters and harming marine life. The introduction of non-native species and increase in nonpoint source pollution were found as the primary causes of nutrient enrichment, hypoxia, harmful algae blooms, toxic contamination and other problems that plague coastal waters.*" In these situations, an unprecedented need for ocean monitoring systems is recognized. One such initiative to monitor ocean processes forms the basis for this dissertation research.

The central objective of this research was to develop ocean sensing elements and packaging techniques to measure ocean processes. Specifically, in this research, MicroElectroMechanical Systems (MEMS) and nanotechnology enabled sensors were developed to measure physical phenomenon such as pressure/depth variations and chemical markers such as nitrate (nutrient) fluxes.

Despite the fact that oceans cover 70% of the earth's surface and have profound impact on the assessment of ocean cycles (nitrogen, carbon), strength of ocean currents, coral growth, agriculture, economy, human health and even global climate and weather patterns, our ability to make long-term sustained and simultaneous measurements of the ocean processes (physical, chemical or biological) is limited and much of the ocean interactions remains largely unexplored. What is required is a new approach with extensive sensing systems (such as an integrated micro/nanosensor network) on both permanent and mobile platforms to enable real-

time, in-situ measurements of the dynamic physical, chemical and biological processes that occur over varying temporal and spatial scales. The National Science Foundation's ocean observatories initiative through Ocean Research Interactive Observatory Networks (ORION) program, will establish a network of seafloor observatories linked by fiber-optic or power cables, as well as permanent and mobile moorings in coastal and deep-sea zones (www.orionprogram.org). Along the continental US, the ORION infrastructure will be coupled with the National Ocean Partnership Program's Integrated Ocean Observing System (IOOS) (Malone et al., 2006). These combined systems will potentially address the seven societal goals of US ocean policy in the 21st century: (1) improve climate predictions, (2) improve safety and efficiency of maritime operations, (3) improve prediction and mitigation of natural hazards, (4) improve homeland security, (5) reduce the public health risks, (6) sustain and restore healthy marine and estuarine ecosystems, and (7) sustain and restore living marine resources.

The *specific* objectives of this research were:

(1) Develop MEMS based piezoresistive pressure/depth sensor element, using a novel reinforced diaphragm configuration.
   (a) To improve both sensitivity and linear pressure operating range of conventional single diaphragm piezoresistive pressure sensors.
   (b) To achieve sensitivity of better than 0.1 m (0.14 psi) of water at linear operating range of 300 meters (about 430 psi).
   (c) To study the effect of reinforcement edge and bossed structure to sensor performance.

(2) Develop ocean specific packaging schemes and protective coatings for pressure/depth sensors.
   (a) To investigate package behavior in the harsh ocean ambient.
   (b) To study the effect of package and protective coating on sensor performance.

(3) Integrate nano-enabled structures (nanowires) and electrochemical techniques on a MEMS/microfluidic platform to detect chemical and biological markers, especially, nitrate fluxes.
   (a) Investigate the suitability of different sensing modalities such as Au, Ni-Fe and polypyrrole nanoelectrodes for electrochemical nitrate sensing.
   (b) Establish a reliable assembly technique (magnetic, through wafer interconnection, dielectropherosis) for nanowires on electrochemical sensor surfaces.

(c) Finally, develop a proof-of-concept electrochemical sensor to validate nanowire-based Electrochemical detection-on-Chip (EoC).

(4) Develop a nanowire-based nitrate-selective electrochemical sensor with integrated microfluidics.

(a) To detect nitrate fluxes at micro-molar levels with high selectivity.

(b) To monitor nitrate levels in a real-time flow through system.

(c) To assemble an all-micromachined flow through sensor with package.

This dissertation forms the foundation for the miniature integrated physical, chemical and biological sensor based system, thus making them ubiquitous for in-situ ocean measurements. Such miniature integrated systems would also house electronics, control systems, data storage and communications modules into one package. An example of such a system is the chemical microlaboratory (Lab-on-Cable) proposed by Wang et al., 2004. Such systems can be readily deployed as distributed sensors to enable data collection spread over large area (sq. nautical miles). These systems can acquire water column data and store them in the on-board memory. Later, the data can be transmitted via low-power radio frequency (RF) link using commercial off the shelf technology. This system integration approach will enable affordable, unmanned and efficient measurement of ocean parameters, even in hostile territory.

1.2 Significance of this research

In spite of the limited understanding of physical and biogeochemical processes from coastal to deep-sea environment, technological advances in developing sensor technology, in data management, power and telemetry are improving our current standards in ocean measurements. According to the IOOS observing subsystem, core variables that need to be monitored by the National Backbone infrastructure are listed in Table 1.1.

Table 1.1 Core ocean variables monitored by IOOS infrastructure.

Physical	Chemical	Biological
Salinity	Dissolved nutrients (N, P, Si)	Fish species and abundance
Temperature	Dissolved oxygen	Zooplankton species and abundance
Sea/Depth level	Chemical contaminants	
Surface waves and currents	Optical properties	Phytoplankton species and abundances
Heat flux		
Bathymetry		Water borne pathogens

In this chapter, the ocean parameters measured and their ecosystem significance are briefly presented. A more elaborate motivation, current sensing mechanisms and ecosystem dynamics will be presented in Chapter 2.

Among the physical variables, Conductivity, Temperature and Depth (CTD) are increasingly being monitored by oceanographers studying fish behavior and migration, climate changes and weather patterns. An accurate measurement of depth is a key requirement in any underwater observatory and construction activities. It is worth mentioning here that the linear depth in ocean can be determined from hydrostatic pressure measurements.

The standard ocean depth formula, UNESCO International Equation of State (IES 80):

$$z = D \big/ < g > \tag{1.1}$$

z is the depth in meter, D is the geopotential distance fitted to the fourth order polynomial in pressure and <g> is the average gravity.

$$D = C_1 + C_2 P^2 + C_3 P^3 + C_4 P^4 \tag{1.2}$$

$$< g >= g(\theta) + 1/2\,\gamma P \tag{1.3}$$

P is in decibar, g(θ) is the local gravity at latitude θ, and C1, C2, C3, C4, γ are constants (Appendix A). For example, 1 decibar (1.45 psi) of pressure is approximately equivalent to 1 meter of depth in a water column. The other significant factors for pressure/depth measurements are as the primary observation data in tsunami detection, wave and tide gauges, platform leveling applications, or in ROV's, profiling instruments, and towed arrays measuring other chemical/biological parameters. To better illustrate the significance of depth measurement, for example, 1% variation in 1000 m of water depth is equivalent to 10 m of water column. Such variations are huge and unaffordable for instrument leveling and ROV's (submarine). In this research, no attempt has been made to convert pressure into linear depth.

In this research, a high resolution novel reinforced diaphragm MEMS pressure (depth) sensor elements using piezoresistive technology was designed (Chapter 3), fabricated (Chapter 4) and tested (Chapter 5) up to pressure of 430 psi (approximately 300 m of water). This work introduces a reinforced or double diaphragm configuration with wafer and system-level packaging along with protective coatings for the harsh ocean environment. The re-simulation (from actual fabricated dimensions) and experimental data show that both higher sensitivity

(about 27% greater than conventional) and operating pressure range (100% greater) were achieved compared to conventional single diaphragm sensors. This was achieved by eliminating large deflections (deflection more than 0.2 times of diaphragm thickness) and non-linearities, which are often encountered in single diaphragm design. As the diaphragm approaches the large deflection regime, peak stresses are effectively transferred from inner to outer diaphragm. At this point the piezos of the outer diaphragm are measured, thus enhancing the operating range, without compromising on sensitivity.

The next part of this research focused on the development of chemical and biological sensors for in-situ measurement of chemical or biological variables of interest, especially nitrate in ocean. Dissolved nutrients such as nitrate, phosphate and ammonia play a key role in controlling the ecosystems balance. These nutrients are essential for phytoplankton and benthic plant growth. However, increase flux of nutrients has led to a number of negative impacts on coastal and deep-sea environment such as eutrophication and "red tides." The increase in nutrient concentrations may also lead to shift in ecosystems structure. Some plants, which are more tolerant of low nutrient concentrations, are replaced as nutrient input increases. In other cases, the ecosystem structure shifts because of change in relative abundance of nutrient elements. For example, enrichment of coastal waters with nitrate and phosphate is often accompanied by loss of diatoms, a major phytoplankton group in unperturbed waters. The challenges involved in ocean chemical sensing are formidable. Only seven ions are present in seawater at concentrations, >1 mM. A typical milliliter of surface seawater may contain on the order of 10 million viruses, 1 million bacteria and 100,000 phytoplankton. All these living and nonliving particles will affect the cycling of chemicals in the ocean (Johnson et al., 1992).

In this research, nanotechnology-enabled electrochemical sensors on a MEMS/microfluidic platform were developed to measure nitrate fluxes. Different sensing modalities and assembly techniques were investigated to integrate nanowires on to electrochemical sensor surfaces. First, a prototype MEMS based electrochemical biosensor using enzyme modified Au nanowire electrodes (Chapter 6) was developed for selective detection of biotargets (cholesterol) in biological fluids (blood). However, these sensors exhibited poor detection limits towards nitrate ions, hence polypyrrole nanowires were investigated. The development of polypyrrole nanowire-based Electrochemical detection-on-Chip (EoC) module to detect nitrate in a real-time flow through system (Chapter 7) is significant. Nitrate, as stated

earlier is an important constituent both to the local biogeochemistry cycles and to the global N-cycle (ACT, 2003). The primary advantages of electrochemical devices are their simplicity, high sensitivity, selectivity and inherent miniaturization into MEMS platforms. Such miniaturization allows for packing of numerous electrodes onto a small footprint of a chemical/biological device, and hence the design of high-density arrays. In addition, the use of nanoelectrodes in electrochemical detection has a variety of advantages: (1) efficient transporter of electrons, (2) high surface-to-volume ratio and small diffusion length, (3) charge accumulation or depletion takes place in the "bulk" of the structure, instead of on surface 2D films, (4) enables label-free and direct electrical readout as there is no reduction in signal intensities, (5) size similarity between the target macromolecules and the nanoscale electrode leads to significant changes in electrical properties of nanowires, when they interact with the molecules. (6) provides enhanced mass transport or flux of species as the diffusion is essentially spherical (three-dimensional), (7) ratio of faradaic to charging current is high, (8) less distortion from IR drop, and (9) use of nanoelectrode ensembles (arrays) enables current amplification.

1.3 Contributions

This section summarizes the significant contributions of this research:

(1) This research provided a new direction to the in-situ miniaturized ocean sensing requirements (such as integrated micro/nanosensors) by integration of micro and nanosensor elements and their associated packaging techniques in a MEMS/microfluidic format.

(2) Development of reinforced diaphragm pressure/depth sensor: This research facilitated marked improvement in inexpensive, batch fabricated high resolution pressure/depth ocean sensors in terms of both sensitivity (27% higher, from re-simulated/model data) and operating pressure range (430 psi), from a combination of inner and outer bridge response over the conventional single diaphragm piezoresistive pressure sensors. The temperature compensation scheme incorporated on the same process die will significantly reduce erroneous temperature effects.

(3) Characterization of the reinforcement edge structure and reinforced boss structure against sensor performance provided the ability to control the operating pressure range and sensitivity. Furthermore, a new wafer and system-level packaging scheme was proposed for ocean physical sensors.

(4) Nanowire-based Electrochemical detection-on-Chip (EoC): In this work, a complete life cycle of nanowire-based electrochemical sensors from synthesis and assembly to integration and testing was proposed and implemented. A prototype MEMS based electrochemical biosensor was demonstrated to detect micro-molar cholesterol levels with better sensitivity (0.85 nA/μM) and apparent Michaelis-Menton constant (17.1 mM) compared to the current state of the art enzymatic nanoelectrode systems.

(5) Nitrate-selective electrochemical sensor with integrated microfluidics: The integration of polypyrrole nanowires on electrochemical sensor surface yielded a flow through microfluidic system to detect nitrate fluxes in seawater samples. A detection limit of 4.5±1 μM, sensitivity of 1.65 nA/μM and good stability (<15% variation to interfering ions) were achieved in this system.

1.4 Dissertation organization

Chapter 2 presents the motivation to ocean sensing, in particular the physical, chemical and biological ocean processes. Then, the current sensing platforms, and state of the art in chemical, biological and physical ocean sensors are discussed.

Chapter 3 starts with introducing the theory of piezoresistivity and piezoresistive pressure sensors, with emphasis on stress analysis using Conventorware® simulation tool and analytical equations. Then, the significance of the reinforced diaphragm pressure sensors over conventional single diaphragm designs is presented, followed by the design specifications for the three generations of reinforced diaphragm pressures sensors.

Chapter 4 discusses the fabrication process and packaging schemes used in the three generations of reinforced pressure sensors. The mathematical description and characterization of the masked-maskless process is then presented. Finally, the two packaging approaches along with system-level integration using anisotropic conductive films and signal conditioning circuit are presented.

Chapter 5 discusses the performance and measurement analysis of the three generations of reinforced diaphragm pressure sensors. Then, the temperature compensation bridge response, package-induced stress and protective coatings are discussed. Finally, output sensitivity

comparison between the different generations of reinforced diaphragm pressure sensors is presented.

Chapter 6 starts with reviewing the electrochemical sensing techniques, properties of nanostructures and nanowire synthesis techniques. Then, template-directed growth process and synthesis of different nanosensor elements were discussed. Next, the different sensing modalities in terms of materials and assembly techniques were presented. Finally, the development and testing of a prototype MEMS based electrochemical biosensor using nanoelectrodes is discussed.

Chapter 7 starts with review of current state of art in nitrate detection, followed by discussion on the proposed sensing modality using polypyrrole nanowires, chemical recognition sites and microfluidic electrochemical platform. Then, the development, calibration and flow through testing of the nitrate-selective electrochemical sensor was presented.

Chapter 8 concludes the dissertation with a brief summary and a discussion on the future outlook for MEMS-microfluidics-nanotechnology-electrochemical techniques in ocean based sensors/systems and their deployment strategies. Several appendices are included for the sake of completeness.

CHAPTER 2

DYNAMICS OF OCEAN SENSING

2.1 Overview

The major objective of oceanographic research is to develop sensors and systems that will allow measurement of significant and complementary ocean processes (physical, chemical and biological) throughout large volumes and over large time spans. Figure 2.1 illustrates an example of physical and biological ocean processes and the variables (such as biotargets, tides, surface waves and chemical concentration) that need to be monitored. The high priority ocean sensors include physical (such as salinity, conductivity, depth and density sensors), chemical (such as nitrate, ammonium, urea, silica, phosphate, total inorganic and organic carbon, oxygen, pH, pCO_2, alkalinity, nitrogen, methane, trace metals, explosives), biological (such as micro-organisms, algae, bacteria, viruses), and magnetic sensors (Daly et al., 2001). Figure 2.2, further elucidates the fact that these ocean processes span a vast range of scales, both temporal and spatial, from the sub-second and sub-millimeter scale of molecular processes to climate change; spanning decades and ocean basins (Dickey, 2001). To investigate such wide of processes, a large volume of data through a variety of sensors has to be collected.

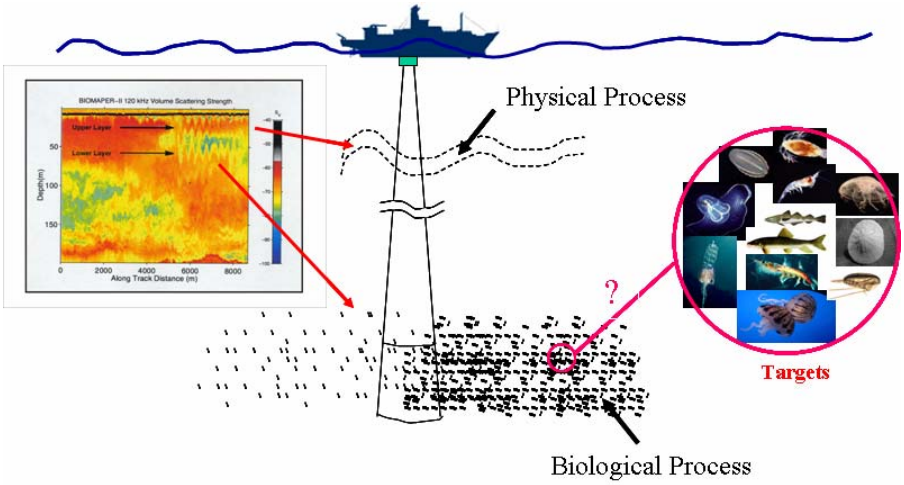

Figure 2.1 Physical and biogeochemical processes in ocean. Adapted from Woods Hole Oceanographic Institution, MA.

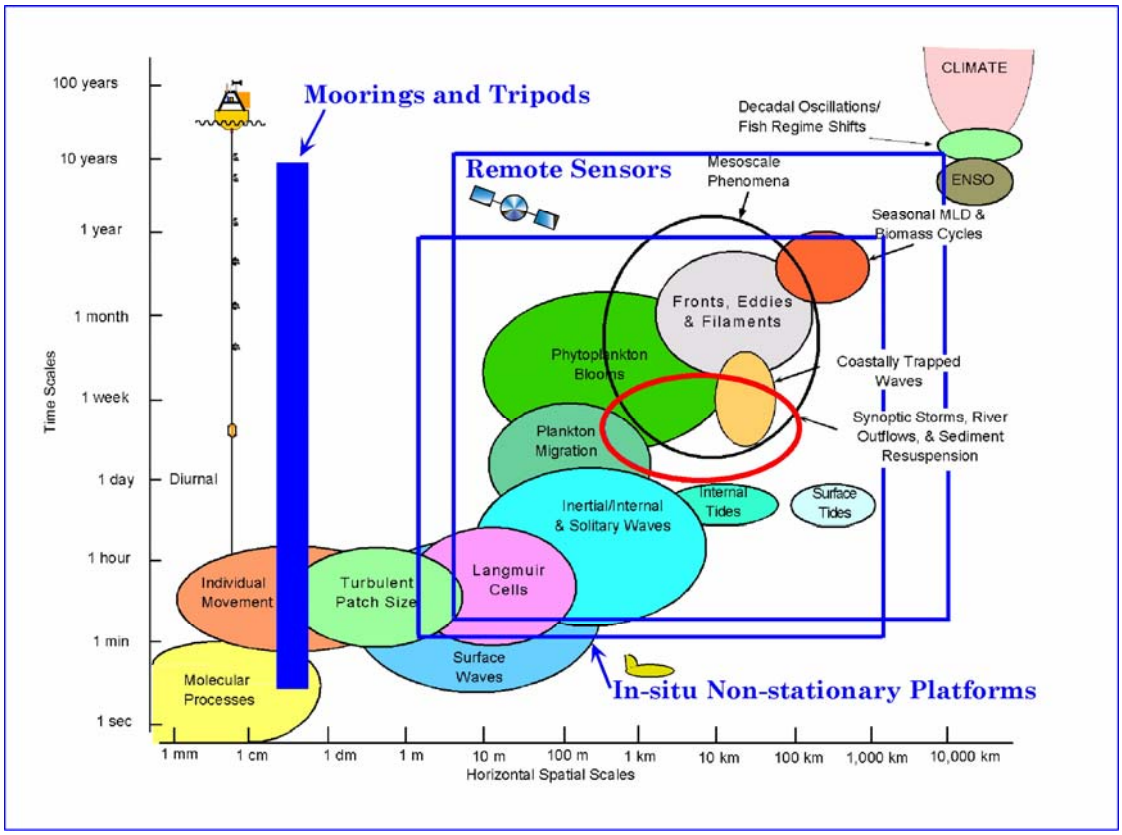

Figure 2.2 Time and space scales for ocean processes and phenomenon relevant to biogeochemical cycling. Adapted from Dickey, 2001.

Of particular importance are the chemical and biological sensors that need to be routinely deployed on autonomous platforms for a variety of studies. These studies range from assessments of natural biogeochemical cycles, to marine pollution monitoring, and even national security applications. In chemical and biological oceanography, the measurement task is exacerbated by the low concentrations of many measurands, often in the presence of relatively high concentrations of interferences, necessitating high specificity coupled with low level of detection, high precision and accuracy in measurements. Traditionally, these requirements were (and to a large extent are still) only met by manual sampling procedures for analysis either on board of research vessels or in research laboratory. The other measurement technologies include remote sensing, AUVs, ROVs and buoys for automated in-situ measurements. However, these technologies can sense only local environmental variables at a single point in space-time. For widely varying parameters in time and space, such infrequent fixed interval sampling may not be enough (Daly, 2000; Gallager et al., 2004; Seyfried at al., 2000; Weisberg et al., 2004). The use of multiple vehicles improves the measurement quality. The gain from higher spatial sampling

frequency is directly related to the number of additional vessels used. Using more support vessels, whether AUVs or ships, will add to the cost. While remote sensing and in-situ buoy systems have provided part of the solution, both have limitations in terms of energy consumption and non-steady responses. In case of manual sampling, episodic and transient events often are completely missed because sampling does not take place at the time of the event occurrence. An example is shown in Figure 2.3; the dynamics in the nutrient concentrations that show in the hourly data is not captured by sampling weekly or even every three days (Prien et al., 2007). To increase spatial and temporal resolution in-situ instruments that continuously measure large volumes of sea-space over large time spans (weeks or months) are required.

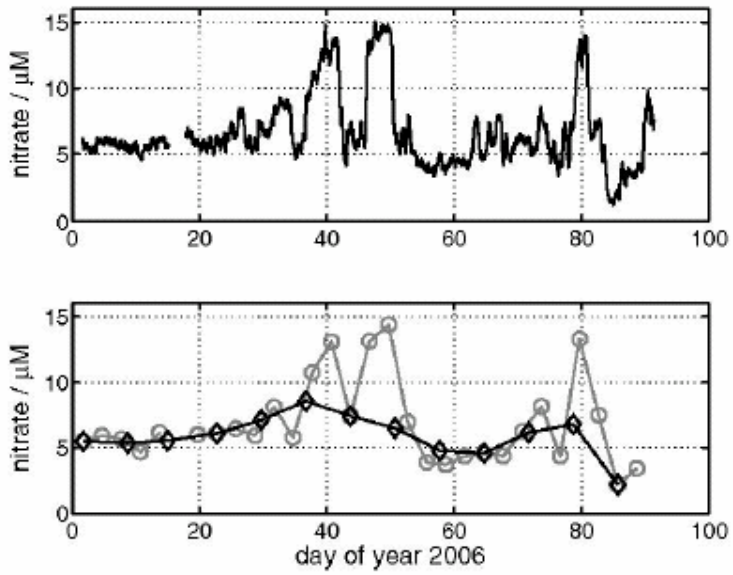

Figure 2.3 Example of under sampling problem. Upper panel shows hourly nitrate data from MBARI mooring M1. Lower panel shows the same data sampled at 7 day interval (black diamonds) and 3 day interval (grey circles). Adapted from Prien et al., 2007.

Figure 2.4 illustrates an example of coastal monitoring, which may be the region of the ocean that is best monitored due to its relative accessibility to most shipboard programs. Figure 2.4 shows the salinity, tide height, phosphate and nitrate concentrations monitored in the Moss Landing harbor during November 2002 with two different sensor systems (Johnson, 2003). The researchers established that with the first rain event, a pulse of fresh water with nitrate concentrations up to nearly 500 µM (typically in unperturbed ocean, < 45 µM) passes through the harbor and into the coastal waters. This nitrate pulse may have happened from the extensively cultivated agricultural fields and would be difficult to observe in most conventional monitoring

systems. Such processes may impact the coastal ecosystem in an unpredictable manner. Such coastal processes are often believed to contribute to the occurrence of Harmful Algal Blooms (HAB). In the following section, the motivation for the development of chemical/biological and physical ocean sensors will be discussed.

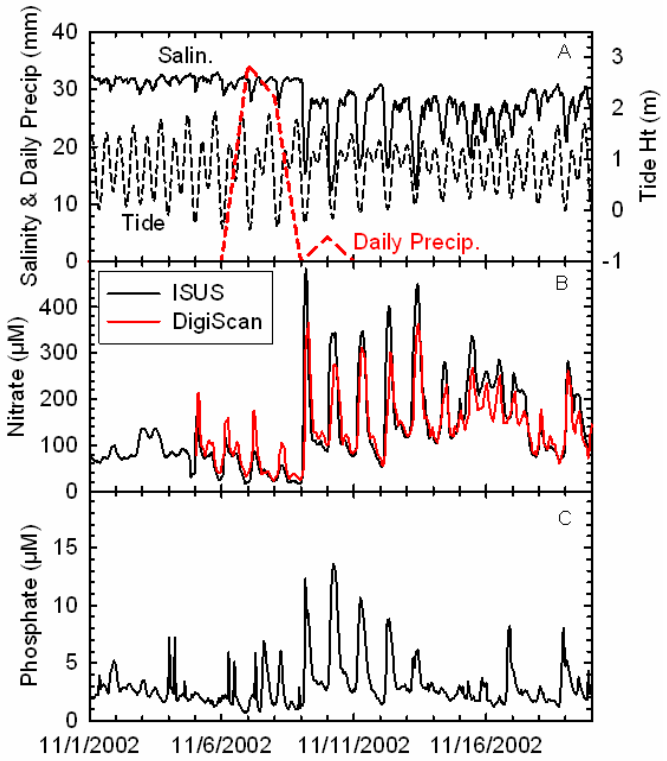

Figure 2.4 Data from MBARI pier in Moss Landing harbor. a) Salinity and tidal height, b) Nitrate measured with ISUS optical sensor and DigiSCAN submersible chemical analyzer, c) Phosphate measured using DigiSCAN. Adapted from Johnson et al., 2003.

2.2 Motivation for ocean sensing

Sustained, long-term, high-resolution measurements are necessary to improve our understanding of biogeochemical processes from coastal to deep-sea environments. Further, the importance of the ocean in terms of food supply, raw material extraction, waste product disposal, transport and recreational use is unquestionable (Gallager et al., 2004). In addition to the scientific interest in ecosystem function and interactions, a range of initiatives and legislative requirements forced governments worldwide to investigate marine processes and monitor inputs and temporal trends as well as subsequent fate and impact of chemical release (Kroger et al., 2005). Nutrient chemicals such as nitrate, phosphate, silicate and iron regulate production of

phytoplankton biomass and hence the structure of the ecosystems throughout the ocean. However, there are only few environments where anything beyond a very basic understanding of the annual nutrient cycle is known. Most of these areas are coastal locations where a small vessel can readily access sampling sites. In open ocean, very little is known about the process of nutrient uptake either in annual cycle or during an episodic event or spring bloom.

Apart from chemical and biological sensors, certain physical sensors (such as pressure/depth, temperature, and conductivity/salinity) are also important in ocean monitoring. Depth or pressure measurements are primary observation data for tsunami detection, wave and tide gauges, platform leveling applications, in depth sensors for ROV's, profiling instruments and towed arrays. Apart from the monitoring the important ocean processes, pressure sensors also find use in maritime or homeland port security. Detecting the movement of surface vessels such as ships, boats, or buoys and subsurface systems such as submarines, unmanned submerged vehicles, mining systems or surveillance systems have become important in current times (Wren et al., 1997).

The primary reason for lack of marine-specific sensors is that a very demanding working environment. Long-term reliability challenges often render even reliable and fully developed sensors (working well in other fields) unsuitable for ocean applications. The ocean environment brings a new set of ocean specific challenges, which include bio-fouling, electrolysis, corrosion, calibration errors, sensor drift, need for miniaturization, power requirements, deployment issues etc. In this section is to further elucidate the motivation scenarios for the various ocean processes.

2.2.1 Chemical and biological ocean processes

In recent years, increasing attention has been focused on ocean chemistry because of civilization's impact on the flow of chemicals through the ocean (Johnson et al., 1992). The motivation to perform chemical sensing can be two-fold: local and global scale. On a local scale, nutrient loading from sources such as sewage plants or runoff from farmland (ammonia, nitrates, and phosphates) can lead to increased rates of plant production, or eutrophication, in surface waters.

Eutrophication refers to the enrichment of waters by nutrients causing an accelerated growth of algae and higher forms of plant life to produce an undesirable disturbance to the

balance of organisms present in the water and to the quality of the water concerned, and therefore refers to the undesirable effects resulting from anthropogenic enrichment by nutrients (Kroger et al., 2005). A large number of variables to be determined arise: nutrient concentrations (nitrate, nitrite, ammonium, phosphate and silicate), algal biomass, species composition and "water quality" (oxygen concentration, presence of toxins etc.). Eutrophication is also linked to toxic phytoplankton blooms (red tides) and greater oxygen demand in the subsurface waters. Increasing anoxia in the water attributable to eutrophication has had a negative impact on marine resources.

On a global scale, the flow of chemicals through the ocean system is closely linked to the Earth's climate. Figure 2.5 illustrates the variability of different ocean chemical parameters to vertical depth. The ocean holds 60 times more inorganic carbon than does the atmosphere, and perturbations in the flow of CO_2 through the ocean are related to changes in atmospheric CO_2 and global temperature (Broecker et al., 1985). Much of this CO_2 will enter the ocean, but the rates of CO_2, absorption in seawater are not yet well known (Sarmiento et al., 1992; Martin et al., 1990).

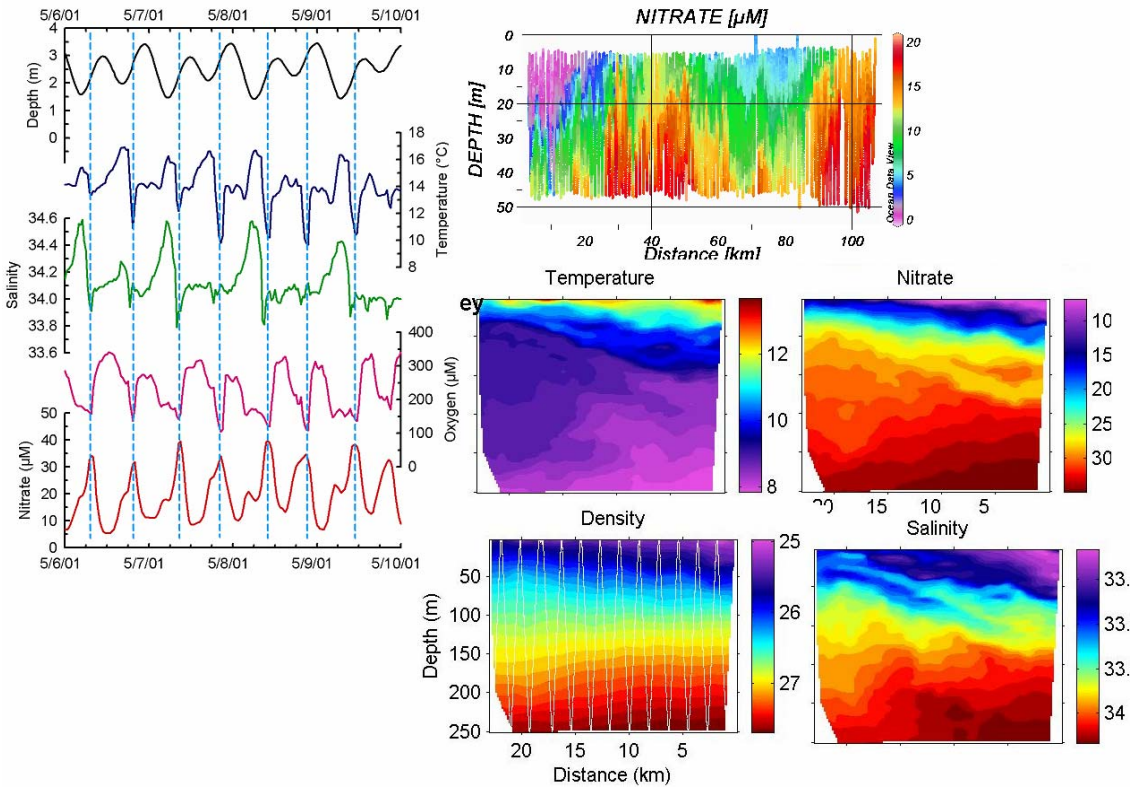

Figure 2.5 Variability of different parameters in time and space scales. Adapted from Johnson et al., 2003.

Despite an understanding on the importance of ocean cycles, there are large gaps in our most fundamental understanding of the ocean processes that drive the flow of chemicals through the ocean. Firstly, the current understanding on what combination of processes controls the rates at which phytoplankton will fix dissolved CO_2 into organic carbon in large areas of the ocean is very limited (Martin et al., 1989). Secondly, one of the major results of the JGOFS North Atlantic Bloom Experiment was the discovery that dissolved silica was exhausted before nitrate during a spring bloom period (Sieracki et al., 1993). Diatoms require silicon, while other phytoplanktons such as dinoflagellates do not. As a result, depletion of silica has a profound implication for the succession of the phytoplankton community and carbon export processes.

Chemical sensors on autonomous platforms are also essential to study the impact of changing physical conditions on carbon cycling in the ocean. One typical example is the air-sea carbon dioxide flux in the equatorial Pacific, where the physics are dominated by enhanced vertical transport (Takahashi et al., 2002) and processes such as El Niño impact the composition of the upwelled water and the air-sea carbon dioxide flux. The effect is large enough that the carbon dioxide concentration of the atmosphere may be temporarily altered during El Niño events (Feely et al., 1997). It is essential to have chemical sensors for carbon dioxide species that are deployed on autonomous platforms in these areas to fully understand the impacts of ocean physics on these processes (Chavez et al., 1999). Such monitoring is particularly crucial to identify climate driven processes that may alter the uptake of anthropogenic carbon dioxide by the ocean.

The other significant chemical factors (Kroger et al., 2005) involve: a) Biodiversity issues and Habitat protection, which are clearly not only connected with nutrient inputs but also with other forms of discharges and anthropogenic impacts, b) Discharge monitoring from coastal industrial sites and offshore installations. Processes such as the dredging of marinas generate waste products, c) Pollution research is to identify the contaminant nature, concentration, sources, distribution, persistence and uptake into biota, d) Ecotoxicology, which looks at the consequences of exposure of biota to a range of chemicals, e) Fisheries management and the associated fish stock assessment is an another factor from which a multitude of measurement needs arise and finally, f) Food safety, which is an important driver in the analysis of marine products such as shellfish. The occurrence of toxic algae and their subsequent accumulation in filter feeders can also have severe impacts on human health.

2.2.2 Physical measurement needs

In addition to chemical and biological parameters monitoring, physical parameters such as pressure, mixed layer depth, salinity, temperature are also known to be critically influence the ocean processes. These processes range from changing strengths of ocean currents to coral growth to global warming. Apart from monitoring the important ocean processes, pressure/depth sensors also find use in maritime or homeland port security. Detecting the movement of surface vessels such as ships, boats, or buoys and subsurface systems such as submarines, unmanned submerged vehicles, mining systems or surveillance systems have become important in current times (Wren et al., 1997). A continuous pressure measurement in the ocean contributes to fundamental understanding of oceanographic processes over a wide range of time scales. These vary from long-period fluctuations induced by planetary waves, oceanic tides and meteorological forcing events, to relatively shorter-period phenomena such as long surface gravity waves, microseisms, and tsunamis. In addition, any oceanographic instrument used to detect ocean processes will need an accurate depth measurement tool to capture the event on a vertical scale (Eble et al., 1991). In many other applications, measurements of relative depths difference in nearby locations such as in platform leveling, sea floor subsidence, and vertical changes in the sea floor during magma flow and plate movements will be required (Houston et al., 1998). The pressure measurement (P) of the vertical water column (h) is given by:

$$P = \rho g h \tag{2.1}$$

ρ is the density of water and g is the local gravity.

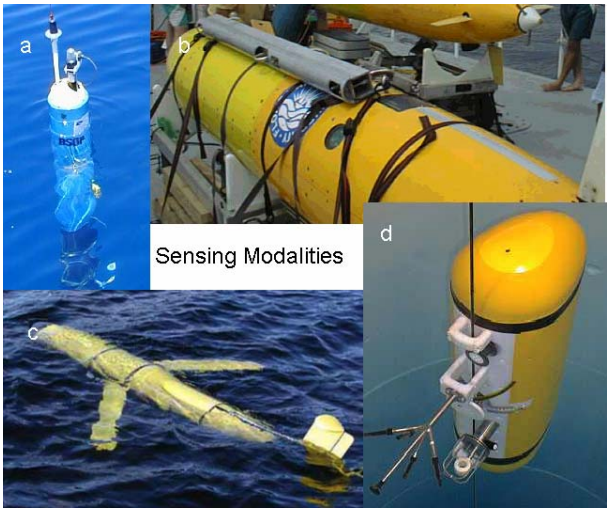

Figure 2.6 Images of ocean sensing modules. a) Bottom stationed profiler (MBARI), b) submersible buoy (COT), c) gliders (Webb research) d) moored profilers (Melean research lab).

2.3 Ocean sensing mechanisms

Traditionally, the samples were mostly collected from coastal regions or by research vessels (ships) and analyzed either on board or in the laboratory. In recent times, more autonomous and mobile platforms are being deployed for automated measurements in field. Figure 2.6 and figure 2.7 illustrate the different measurement approaches used for field analysis. An important aspect of any measurement strategy is to get appropriate spatial and temporal resolution of data. Ships, ROVs and submersibles are useful tools for spatial surveys or specific point measurements for short period of time. Moorings and bottom landers can provide excellent time series in fixed location (temporal resolution, resolution of trends or episodic events). Profilers can add a vertical dimension to either ship-based or mooring-based measurements or drifters can follow currents and help in elucidating transport and pathways. A recent addition to this measurements spectrum is tagging of fishes/mammals with sensors, both to study their behavior and for information gathering (Hyldgaard et al., 2005). Historically, most of the measurements collected were individual parameters such as nitrate concentration, depth or conductivity. However, with current needs, it is apparent a host of parameters are required in an integrated sensing system. For example, varying nitrate or silicate concentration resolved at specified time intervals at different depths and scale spans (refer to figure 2.5).

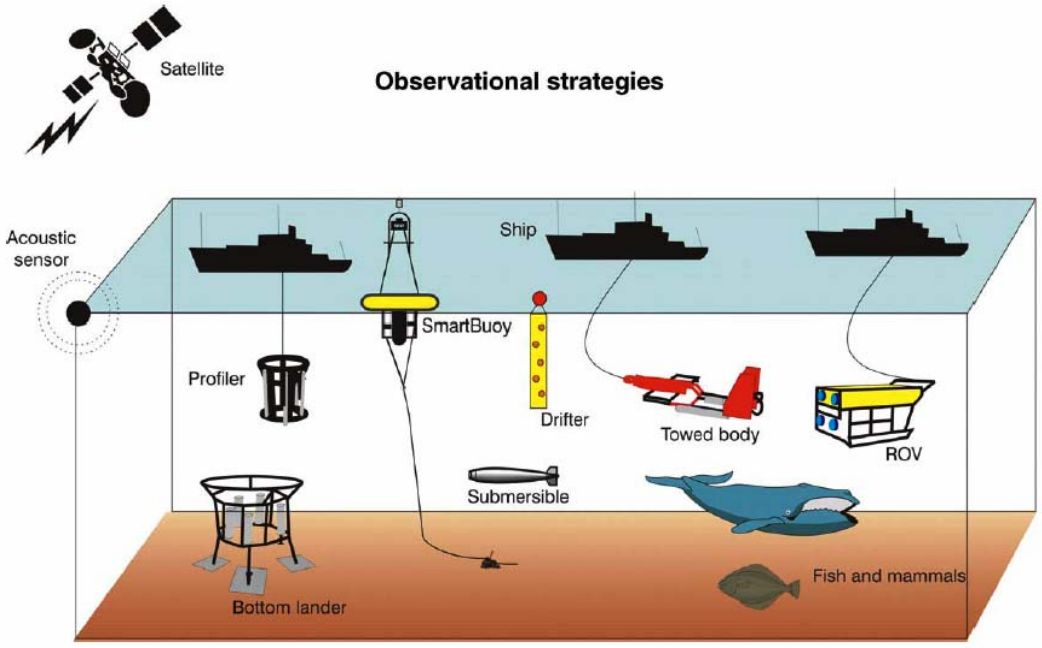

Figure 2.7 Illustration of different ocean measurement approaches. Adapted from Kroger et al., 2005.

2.4 Current state of the art in chemical and biological measurements

A selection of technologies and sensors are described that have the potential, or already have proven the ability, to measure chemical parameters in-situ with high temporal and/or spatial resolution. Before, discussing the current sensing methods, the challenges and requirements for chemical sensing are presented. Specificity, accuracy, precision, resolution and level of detection are the main specifications for any chemical sensor. For extended deployments in a dynamic environment in-situ sensors will need an in-situ calibration, an integrated performance monitor, should be able to detect sensor drift, and effects due to bio-fouling (figure 2.8). Operating a number of sensors in parallel increases reliability of measurements and allows the detection of sensor failures. This is a viable way to avoid missing data sets time series analysis caused by limitations in operation reliability of individual sensors, To determine the effects due to cross sensitivities, multiple sensors working on different detection principles (and therefore exhibiting different specificities) can be used. With multivariate analysis of the sensor data this approach can increase the specificity of the combined measurements. Also, chemical instruments yielding spatial surveys must also provide data that is integrated with other sensors such CTD (depth profilers). In summary, the challenges to ocean chemical sensing include: a) Bio-fouling, b) Electrolysis, c) Calibration, d) Miniaturization, e) Power requirements, and f) Telemetry.

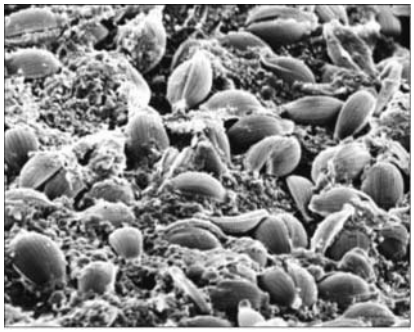

Figure 2.8 SEM image of diatom slime growth on copper screens. Adapted from Callow et al., 2002.

2.4.1 Classification based on technology

Optical absorption spectroscopy**:** Optical absorption measurements are a well established tool in the research laboratory. The absorption of light in a molecule is very selective as the energy of an absorbed photon has to match the difference in energy between the molecules relaxed and in the excited state. The spectra of target molecules, however, are modified within water and this makes absorption spectroscopy in seawater more difficult.

Johnson et al., 2002 introduced an in-situ ultraviolet spectrophotometer (ISUS) for the measurement of nitrate, bromide and bisulfite, which was capable of making measurements at a sample rate of 1 Hz. An advantage of the ISUS and similar instruments was that the compounds exhibiting absorption in the UV portion of the spectrum were measured at the same time and in the same water volume. For nitrate measurements, an accuracy of ±2 μM and a precision of ±0.15 μM for a 2.5 year deployment were reported (Johnson et al., 2006). The detection limits of commercial wet chemical analyzers are in the region of 40 nM for nitrate (e.g. sensors from Systea Srl, SubChem Systems Inc.) but the deployment times are limited by reagent consumption and degradation to less than ten weeks. The deployment time of the ISUS is mainly limited by bio-fouling and continuous deployments of greater than 3 months without any apparent degradation of performance have been reported. With LEDs reaching down to wavelengths of 210 nm, it can be expected that more compact and lower power UV absorption spectrometers of this type will be developed (Taniyasu et al., 2006).

Raman spectroscopy**:** Another optical spectroscopic method is Raman spectroscopy. When a molecule does exhibit rotation or vibration (and its polarisability is changing with change of position) a part of light that is scattered by this molecule (about 1 in 10^7) encounters a frequency shift. The Raman shift is characteristic for the molecules in rotational and/or vibrational state. This makes Raman spectroscopy, an analysis method with high specificity, as it detects the fundamental vibrations of target analyte molecules.

Raman spectroscopy is also suitable for use in water as the excitation wavelength can be in the visible part of the spectrum where absorption in water, and therefore interference by the water, is relatively low. Raman spectra can be taken fairly rapidly (on the order of seconds) which makes the method suitable for profiling measurements. Brewer et al. 2004 reported the development of a Raman spectrometer for deep ocean science and demonstrated the prototype in-situ on gaseous, liquid and solid samples. Murphy et al. 2000 designed an in-situ surface enhanced Raman scattering (SERS) instrument and tested it in the laboratory. SERS uses the effect that if a target molecule is adsorbed onto some metals (such as silver or gold) and the excitation light excites electrons in the conduction band of the metal, the Raman signal is enhanced greatly, usually by 6 to 8 orders of magnitude.

Electrode Sensors**:** Electrode based sensors have been used in oceanography for a very long time, most prominently in the form of the Clark cell for oxygen measurements with or without a membrane (Clark et al., 1953). Even with membranes attached to the microelectrodes, to either enhance specificity or to enrich the analyte concentration, the response times can be on the order of seconds. However, a disadvantage of microelectrodes is that the reduction current is very small (in the order of pA) and therefore the precision of measurements carried out with a microelectrode often is limited by electronic noise (Prien et al., 2007. This limitation, however, can be counteracted by using arrays of microelectrodes; they still exhibit the advantage of hemispherical diffusion regions while at the same time the total electrode area, and therefore the signal, is increased.

A voltammetric in-situ profiling system has been introduced by Tercier et al., 1998 using an agarose membrane covered mercury-plated Ir-based microelectrode. This instrument performs in-situ measurements of the mobile metal fractions using either square wave anodic stripping voltammetry (where the metal ions are enriched in an amalgam in the reduction step and then reoxidised to generate the signal), or square wave cathodic sweep voltammetry (without the enrichment in the amalgam). It is expected that more in-situ sensors based on microelectrodes will be developed for oceanographic applications. The technology has the potential for enabling small, low power instruments that can assess a variety of chemical parameters rapidly.

Optodes**:** Optodes use indicator chemistries (such as ruthenium complexes) immobilized in sol-gel matrices or embedded in a polymer layer. The presence of the analyte modifies a property of the indicator (fluorescence) and thus forms the sensor. The modification of the indicator property is a measure for either presence or concentration of the target analyte. Oxygen sensors are based on the optode principle and have proven to have excellent long term stability on profiling floats (Aanderaa Inc). They use a platinum porphyrine complex as the indicator fluorophore. The fluorescence is excited by a LED light and measured by a photodiode with an optical filter to exclude excitation light. A high accuracy (±2 μM) and long-term stability over a period of 20 months has been reported (Tengberg et al., 2006).

Mass spectroscopy**:** Another prominent laboratory method that has been used successfully in-situ is mass spectrometry. Short et al. 1999 described a system consisting of a membrane introduction interface coupled with a linear quadruple mass filter for in-situ detection

and quantification of dissolved gases and volatile organic compounds (VOCs) with detection limits of 1 to 5 ppb. One of the advantages of mass spectrometers is that a number of analytes can be measured in parallel and from the same water volume.

MicroElectroMechanical Systems (MEMS) and Nanotechnology based analyzers**:** Wet chemical analyzers have shown to have necessary accuracy and detection limits for long term use. However, the disadvantages they pose can be minimized with the potential technology called MicroElectroMechanical Systems (MEMS) or more specifically using microfluidics. To satisfy the demands of low power consumption and to minimize reagent consumption in in-situ analyzers, MEMS and nanotechnology are considered as the technologies of the future. MEMS consist of mechanical systems fabricated by silicon or non-silicon fabrication techniques such as deposition and etching to produce miniature mechanical features. Microfluidic devices already have had great impact on the biomedical field as lab-on-a-chip and micro-total-analysis-systems (μTAS).

One of the advantages of these analyzers is the low production cost when batch fabricated. This allows for MEMS analyzers to be used as disposable devices, avoiding the need to clean after use and thus minimizing the risk of contamination. Another advantage of microfluidic analyzers is that it is comparatively easy to add an in-situ calibration; by adding two valves and reservoirs, for example with blank and standard solution, analyzers can perform control runs to check for detector drift at predetermined intervals. There are a multitude of wet chemical analysis methods for a vast range of analytes such as nitrate, nitrite, phosphate, ammonia, silicate, iron, manganese that have been employed by in-situ wet chemical analyzers, which could be adapted in MEMS analyzers (Grasshoff et al. 1997).

However, some challenges needs to be overcome such as packaging for operation in ocean and bio-fouling. Bio-fouling is a major issue for all in-situ sensors, including MEMS analyzers with small fluidic channels that are blocked easily even by small particles the risk of malfunction due to bio-fouling seems to be exacerbated. With suitable filters this risk can be minimized and by deploying analyzers in parallel, a bad analyzer can be easily eliminated.

The Woods Hole Oceanographic report on “The next generation of in-situ biological and chemical sensors in the ocean,” elucidates the use of technologies such as MEMS and nanotechnology to enable improved sensor integration; reduced power consumption, size and cost.

(WHOI, 2003). Some promising examples of MEMS ocean sensors include multi-parameter systems measuring conductivity, temperature, oxygen and chemical compounds using ion-selective electrodes, lab-on-chip microfluidic chemical detection systems, in-situ spectrometers and Polymerase Chain Reaction in microfluidic systems.

2.4.2 Classification based on measurands

Chemical sensors can be classified according to the measured species as dissolved gas, macronutrients, inorganic carbon, dissolved metals and biological sensors. Even though, in this research, only nitrate (nutrient) is measured, for a sake of completeness, a brief introduction to other relevant sensors is presented.

Dissolved gas sensors**:** Oxygen sensors based on a membrane covered, amperometric electrode (or Clark electrode) are probably the most common chemical sensor used in ocean research. They are routinely used on CTD/Rosette packages. One of the major applications of the Clark electrode has been to measure fine scale oxygen gradients across the sea floor with microelectrodes deployed from autonomous benthic landers (Cai et al., 1995). Fouling of oxygen electrodes typically limits the time frame for reliable measurements to one month or less in the upper ocean without sensor recalibration (Emerson et al., 2002).

Macronutrients (nitrate, phosphate, and silicate): The profiles of nutrients elements: nitrogen, phosphorus and silicon exhibit an extraordinary dynamic range (figure 2.9). Nutrients characteristically have high concentration in the deep ocean, while concentrations near the surface are often below detection limits. The gradient of nutrient concentrations in the transition zone, between high and low concentrations, generally encompasses the euphotic zone and can be very dynamic in response to both physical and biological processes. Thus, in-situ nutrient measurements are extremely challenging.

Table 2.1 describes the some of commercially available nutrient sensors, in particular nitrate sensors. Potentiometric measurements of nitrate (YSI Inc.) are suitable only for freshwater systems. The UV sensors for nitrate absorbance measurements (MBARI-ISUS and SUV-6) have fast response times. These are suitable for profiling operations. The sensitivity of direct measurements is poorer than colorimetric sensors. The detection limit of ISUS sensor is on order of 1.5 μM. The resolution limit of the SUV-6 is 0.2 μM.

Table 2.1 Commercially available chemical sensor modules for ocean measurements.

Technique/Company	Detection limit	Sampling Time	comments
Wet chemical analyzer/EnviroTech	50 nM	minutes	3.4W
Optical sensor/Satlantic	0.2 µM	seconds	MBARI-ISUS, 12W
Wet chemical analyzer/ SubChem Systems	nM	seconds	50-150W
Ion Selective Electrodes/ YSI Environmental	0.16 µM	seconds	freshwater only
Absorbance/Fluorescence SEAS-II, COT	2 nM	seconds	15W

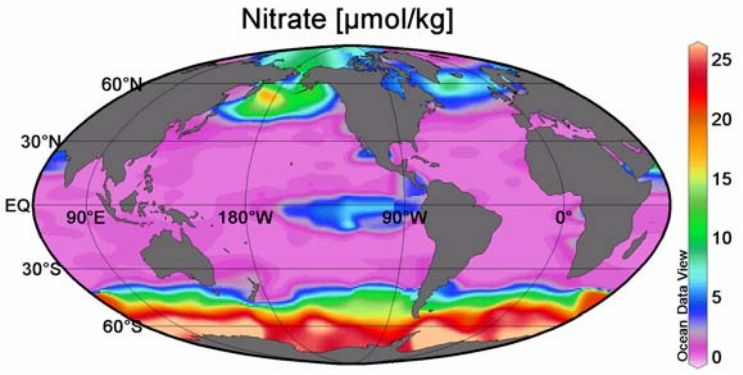

Figure 2.9 Illustration of nitrate concentration spread across the globe. Adapted from Johnson et al., 2003.

Inorganic carbon (pH, TCO_2, PCO_2): Characterization of the carbon system requires measurement of two independent carbon dioxide parameters, such as pCO_2 or pH and Total Inorganic Carbon. The partial pressure of CO_2 (pCO_2) are currently measured by in-situ variety of optical or IR methods (DeGrandpre et al., 1997). These methods are generally based on equilibrating seawater carbon dioxide across a gas-permeable membrane with a solution containing an acid-base indicator dye.

Dissolved metals: Continuous flow analysis and several analytical systems based on electrochemical analyses using amperometric have been developed (Coale et al., 1999). These

systems generally have not been widely adapted to autonomous platforms due to high power requirements, complexity, and lack of stability.

2.5 Technology for detecting pressure/depth variations

2.5.1 Introduction

The depth of any device lowered in the water column can be determined by the length of the hydrographic cable paid out, if the cable angle is considered. Depth determined in this manner is only approximate, since the cable does not extend in a straight line but, curves somewhat. However, for most of the oceanographic sensors accurate and high resolution depth determination is required. One of popular mechanism for depth measurement is by using pressure sensors. Pressure sensors are perhaps, the most mature MEMS technology and have been used in a wide range of applications, including as ocean depth sensor (Hyldgaard et al., 2005; Wren et al., 1997; Brown et al., 1987; Kroebl et al., 1987; Aravamudhan et al., 2005). Particularly, piezoresistive pressure sensors, which are made using a silicon diaphragm containing four piezoresistors near the edges in a Wheatstone bridge configuration (Lin et al., 1999; Clark et al., 1979; Kanda et al., 1982; Smith et al., 1954; Tufts et al., 1962). One side of the diaphragm is in a sealed cavity at a reference pressure. The changes in pressure on the other side of the diaphragm cause it to flex, which increases the resistance in two of the resistors and decreases it in the other two. By calibrating the device, changes in resistance can be converted to pressure measurements.

Apart from piezoresistive pressure sensor, various sensing mechanisms have been incorporated in pressure sensors such as batch-sealed capacitive sensors, force-balanced sensors, ceramic sensors, silicon-fiber optic sensor array, piezoelectric sensors and quartz beam resonating sensors. Even though our focus in this research is micromachined pressure sensors, it is instructive to first examine macroscopic devices, since many MEMS sensors are miniaturized versions of the larger counterparts.

Figure 2.10 shows the several macroscopic pressure sensors. The common feature all of these sensors was that they converted pressure to motion of a mechanical element. Most of the devices were based on diaphragm structures (a, b, d). Other devices improved upon the amount of deflection of a simple diaphragm by using the capsule (c) and bellows (e). On these diaphragm based devices, strain gauges were commonly used. A Pirani gauge measures the thermal conductivity of the ambient gas, which is directly proportional to the pressure.

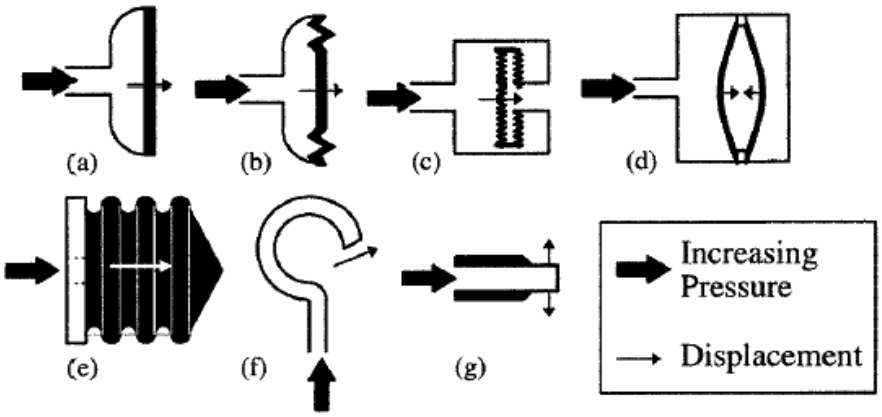

Figure 2.10 Macroscopic pressure sensors a) simple diaphragm, b) corrugated diaphragm, c) capsule, d) capacitive sensor, e) bellows, f) bourdon tube, g) straight tube. Adapted from Oliver et al., 1971.

To capture ocean events, several types of transducers have been incorporated into pressure sensor units designed for oceanic applications. The most common types include the vibrating wire, strain gauge, quartz-resonator, Bourdon tube, and various capacitance devices. Vibrating wire designs typically correlate vibrational frequency with pressure-induced mechanical motion (Lefcort et al., 1968; Vitousek et al., 1970). Capacitance plate transducers incorporated using parallel capacitance plates in which the distance between plates varies as a function of applied pressure (Harris et al., 1963). Capacitance is inversely proportional to the plate gap and acts to tune an LC oscillator. Although an improvement over vibrating wire designs with respect to accuracy, flexibility, and cost, instability were inherent in the mechanical design of the capacitance plate transducer.

As an improved alternative, the strain gauge was developed and extensively used by researchers. Strain gauge pressure sensors utilize the variation in the resistance of a conductor with mechanical deformation caused by pressure acting on a flexible element. Many designs have been used, most incorporating a Wheatstone bridge to increase the sensitivity and minimize temperature effects. Gwilliam et al., 1974 and Collar et al., 1972 report on successful uses of strain gauge sensors to measure tides. They are not, however, well suited for long-term deep deployments where a large dynamic range, high sensitivity, and low drift are required. In contrast to the strain gauge, quartz-resonator transducers measure the changes in vibrational frequency of a quartz beam. An early HP sensor utilized a piezoelectric resonator characterized by increased

pressure sensitivity and decreased temperature dependency. This design represented an improvement over previous designs incorporating the vibrating wire, capacitance plate, and strain gauges (Collar et al., 1972). More recent quartz-crystal transducers, such as those currently manufactured by Paroscientific, Inc., show improved long-term stability and significantly greater accuracy than their predecessors (Wearn et al., 1985).

Table 2.2 Commercially available ocean pressure/depth sensors.

Technique(Company)	Range	Accuracy/Resolution	Comments
Silicon Piezoresistive (SenCorr)	15,000 psi	0.067 % of FS	Conventional wheatstone bridge. Array of sensors
Quartz resonant (Paroscientific)	10,000 psi	0.01% of FS	DigiQuarts transducer, expensive.
Strain gauge (Aanderaa)	160 psi	0.2% of FS/0.15	Low-end, cost-effective. Cable approach. Array
Semiconductor bridge strain gauge (Applied Microsystems)	700 psi	0.05% of FS	Stainless steel housing, 25 Hz sampling.
Quartz transducer (SeaBird)	10,000 psi	0.01% of Fs/0.045 ppm	Temperature compensation, data storage, array based
Piezoresistive (Druck)	5,000 psi	0.025% of FS	Not suited for harsh marine environment. Array
Piezoresistive silicon (advanced custom sensors)	300 psi	0.25% of FS	SST316T housing, stainless steel diaphragm

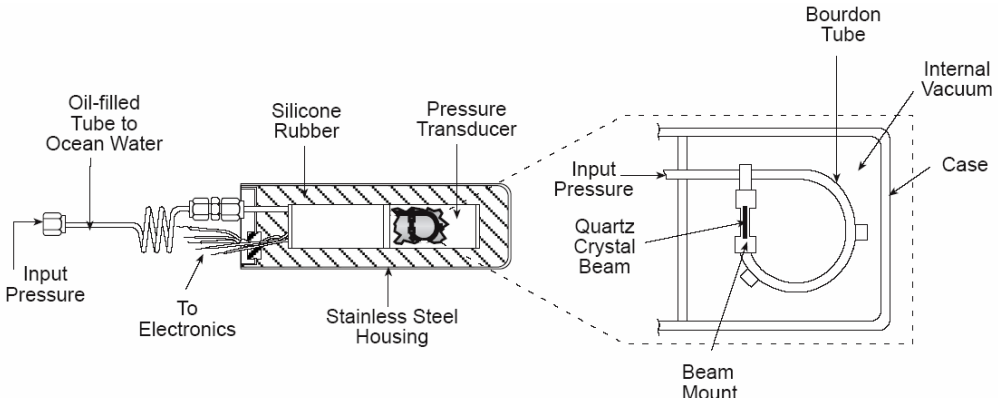

Figure 2.11 Illustration of quartz-beam resonators as pressure sensor. Adapted from Wearn et al., 1985.

Next, these sensors were incorporated in self-contained bottom recording pressure units Snodgrass et al., 1968; Filloux et al., 1969). More recently, Gonzalez et al. 1987 successfully

detected small tsunamis in the northeast Pacific Ocean using quartz-beam resonators, as shown in figure 2.11. The requirements and challenges in harsh marine environment has forced only one of the sensing mechanisms namely quartz crystal resonators to be successfully applied in ocean application, apart from the conventional piezoresistive pressure sensors.

2.5.2 Classification based on transduction mechanisms

In this section a general overview of the different MEMS based transduction mechanisms is presented (Eaton et al., 1997). The advantages of MEMS based pressure sensors include batch fabrication, lower cost, smaller form factor and monolithic integration.

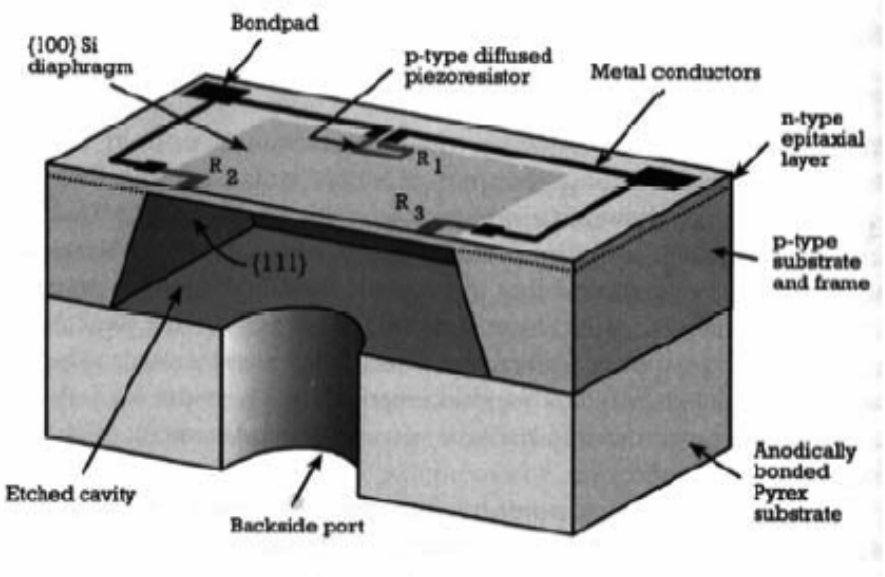

Figure 2.12 Illustration of piezoresistive pressure sensor. Adapted from Motorola Inc.

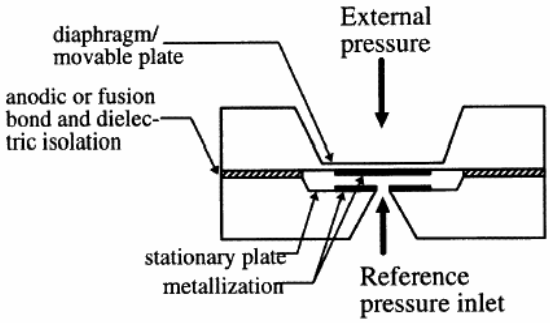

Figure 2.13 Illustration of capacitive pressure sensing principle. Adpated from Clark et al., 1979.

Piezoresistive sensors: Here piezoresistors mounted on or in a diaphragm. For thin diaphragms and small deflections, the resistance change is linear with applied pressure (figure 2.12). A detailed review of the theory and mathematical description of piezoresistive theory is presented in the next chapter. Silicon strain gauge, metal-diaphragm sensors were first introduced in 1958 (Bryzek et al., 1990).. The evolution of piezoresistive pressure sensor technology started with metal diaphragm sensors with bonded silicon strain gauges Metal diaphragms were quickly superseded by single crystal diaphragms with diffused piezoresistors. These new types of sensor had many advantages related to the properties of silicon. Hysteresis and creep associated with metal diaphragms were eliminated.

At temperatures (<500 ˚C), silicon is perfectly elastic and will not plastically deform, but is however brittle in nature (Gieles et al., 1973). Silicon obeys Hooke's law up to 1% strain, a ten-fold increase over common metal alloys. Also, the ultimate tensile strength of silicon can be three times higher than that of stainless steel. As a piezoresistive material, silicon has gauge factors that are over an order of magnitude higher than those of metal alloys (Gieles et al., 1973). In this research, all the pressure sensors developed were based on this technology.

Capacitive sensors**:** Capacitive sensors are based upon parallel plate capacitors. A typical capacitive pressure sensor is shown in figure 2.13 (Clark et al., 1979). The principal advantages of capacitive pressure sensors over piezoresistive sensors are increased pressure sensitivity and decreased temperature sensitivity (Sander et al., 1990). However, excessive signal loss from parasitic capacitance is a major disadvantage.

Optical sensors**:** Diaphragm-based optical sensors measure pressure induced deflections by Mach-Zehnder interferometry (Wagner et al., 1994) or Fabry-Perot interferometry (Chan et al., 1994). Optical sensors are quite accurate, however, they often offer from temperature problems. Furthermore, aligning the optics and calibrating the sensors is challenging and expensive.

Resonant sensors: A new class of pressure sensor called resonant beam pressure sensor have been developed. These sensors operate by monitoring the resonant frequency of an embedded doubly clamped bridge or comb drive (Petersen et al., 1991). The resonant beam acts as a sensitive strain gauge. As the stress state of the diaphragm changes, the tension in the embedded structures also changes and hence the change resonant frequency can be detected.

These sensors have exhibited better pressure sensitivity and lower temperature sensitivity than piezoresistive sensors. However, their cost of production, electronic circuitry and deployment as distributed sensors are more expensive compared to piezoresistive sensors.

2.6 Summary

In summary, this chapter presented the motivation and significance towards ocean sensors to measure physical, chemical and biological processes on a time and space scale. In addition, the dynamics of ocean processes is so challenging that in-situ sensors will be required to monitor the ocean parameters of interest. Of specific interest was the development of integrated chemical and physical ocean sensors to measure episodic events on vertical and horizontal scales. Therefore, in this chapter, the current of the art in chemical and physical sensing mechanisms were reviewed. In particular, nitrate (nutrient) sensor based on electrochemical technique, together with MEMS based pressure/depth sensor will be the focus of this current research. Later, in the chapter, current sensing methodologies used for nitrate and pressure/depth sensors were reviewed.

CHAPTER 3

DESIGN AND ANALYSIS OF REINFORCED PRESURE SENSORS

3.1 Introduction

One of the objectives of this research is to develop a reinforced diaphragm micromachined pressure sensor based on piezoresistive technology for marine applications. Therefore, the focus of this chapter will be to present a detailed design, analytical and Finite-Element-Method (FEM) performance analysis of such reinforced diaphragm pressures sensors. In addition, this chapter will also elucidate the significance of reinforced diaphragm pressure sensor compared to a conventional single diaphragm design. As discussed earlier, the motivation to develop ocean pressure sensors stems from the importance to measure physical, chemical and biological ocean processes. In particular, high resolution pressure measurements are important for accurate leveling of oceanographic instruments and for applications ranging from wave/tide detection to weather patterns to maritime security. In this research, the focus has been to develop an inexpensive, yet highly sensitive prototype reinforced piezoresistive pressure sensor to potentially accomplish distributed (wide-area sensing) and continuous depth measurements over large volumes of sea-space over large time spans (weeks or months). In general, piezoresistive pressure sensors have been used in a wide range of applications, including as ocean depth sensor (Hyldgaard et al., 2005; Wren et al., 1997; Brown et al., 1987; Kroebl et al., 1987; Aravamudhan et al., 2005). The piezoresistive pressure sensor array fabricated for validation consisted of a double diaphragm (instead of a conventional single diaphragm), with the outer diaphragm acting both as reinforcement and sensing structure along with the inner sensing diaphragm and temperature compensation bridge.

When a conventional thin diaphragm, in case of a bulk micromachined piezoresistive sensor is subjected to high pressure, it may result in large deflections and will induce non-linearities, transfer from small deflection regime to membrane regime (Lin et al., 1999). To overcome this limitation, in this research, a double or reinforced diaphragm is used. A thinner

inner diaphragm (5-25 μm) and thicker outer diaphragm (25-40 μm), with piezoresistors embedded in both of them are used to transfer the peak stresses from inner to outer diaphragm. Even though, large deflections and non-linearities are avoided in this current design, sensitivity and operating range are not compromised. In fact, the sensitivity is improved by up to 27% (modeled data of Generation II sensors) and operating pressure range is doubled compared to conventional single diaphragm pressure sensors. Before, we discuss the significance and analytical concepts involved in the design of reinforced diaphragm pressure sensors; an introduction to theory of piezoresistivity in semiconductors is presented.

3.2 Theory of piezoresistivity

3.2.1 Overview

Piezoresistivity is a material property where the resistivity of the material is influenced by the mechanical stress applied to the material. In case of piezoresistive pressure sensors, they can detect applied pressure due to deformation. The change in dimensions of piezoresistors causes change in resistance, which can be detected by connecting the resistors in a wheatstone bridge configuration. Metals were initially used as they exhibit piezoresistive effect. Smith et al., 1954 discovered the piezoresistive effect in silicon and found that pressure sensitivity in silicon piezoresistors to be many times larger than that of thin-metal film resistors. Unlike metals, whose piezoresistivity are based on geometric changes, the piezoresistive effect of silicon are based on mobility changes of carriers. Volume changes affect the energy gap between the valence and conduction and, the number of carriers and thus the resistivity changes. The solid state physics theory postulates that the energy of electrons in the crystal lattices is not continuous but is separated as energy bands due to interaction between electrons and lattice atoms, namely conduction and valence bands. Between these energy bands, there is a forbidden band, called band gap. For semiconductors, this band gap is small and therefore, some electrons would be thermally excited to overcome this band gap.

In the conduction band, there is a minimum energy necessary for electrons to exist. This minimum energy is called band edge point (BEP), as shown in figure 3.1. In the case of silicon, the peak of valence band and valley of conduction band are not aligned at the same wave-number k. This refers to indirect band gap semiconductor. Instead the valleys of conduction band sit on the six <100> equivalent axes, [100], [100], [010], [01-0], [001], [001-]. This is called the one band many valley model. At room temperature, there will be electrons getting enough thermal

energy to partially fill these valleys. In the absence of stress, these six valleys have the BEP at the same energy level, and electrons fill these valleys equally. But when the stress is introduced into crystal, the lattice structure and the distance between lattice points will also be distorted by stress. As a result, the interaction between the electrons and lattice atoms will also be changed accordingly. This causes the BEP for some valleys to decrease and for some other valleys to increase. Therefore, more electrons would get enough energy to get into some valleys and fewer electrons would get into other valleys.

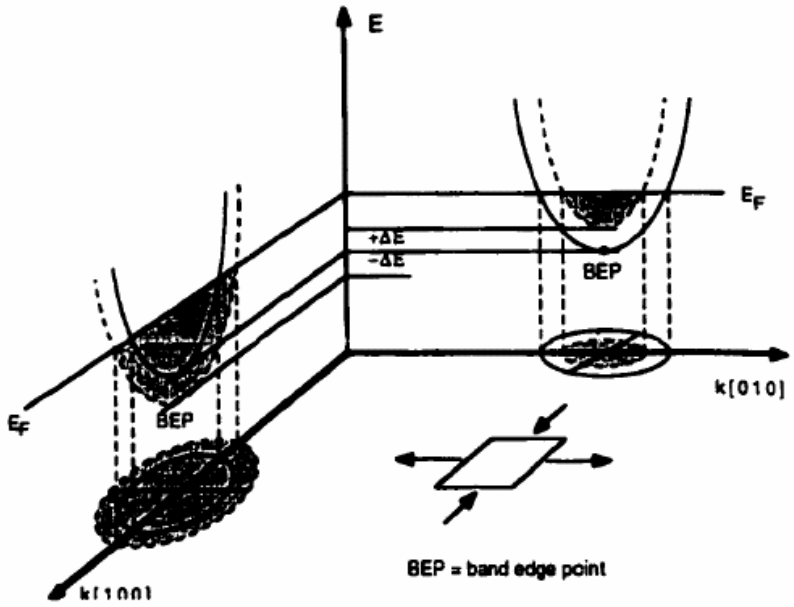

Figure 3.1 Illustration of isotropic stress applied on silicon crystal. Band edge point (BEP) refers to the minimum energy for electrons to exist in conduction band. Adapted from Smith et al., 1954.

Figure 3.1 illustrates that as an isotropic stress is applied in [100] direction, it causes lattice compression in the same direction (Smith et al., 1954). Usually this compressive stress would reduce lattice traction in other principal axes and under this situation, the minimum energy of conductive band valley in [100] direction will be lowered while the minima on the other axes will be raised. The Fermi levels doesn't change according to crystal lattice distortion, hence when there is a compressive stress in [100] and results in its BEP to be lower, it causes the redistribution of electrons between the band valleys and more electrons will move in [100] valley from [010] and [001] valleys, which experience traction stress. Consequently, the average mobility of electrons in [100] direction, the direction of compressive will decrease. While, the mobility of electrons in the direction of traction will increase. This phenomenon can be better

explained using quantum mechanics. In quantum mechanics, the mass of electrons varies due to the interaction with lattice atoms (Toriyama et al., 2002).. When the energy band structure is distorted due to application of stress, the curvature of energy band in k space, d^2E/d^2k, will also be changed. This change therefore, alters the effective mass of carriers and further changes the mobility of carriers.

$$\mu = q\tau / m^* \tag{3.1}$$

τ is the mean time between collisions of carriers with lattice atoms, q is the charge of carriers and m* is the effective mass. It can be calculated that the electrons moving from [010] and [001] into [100] carry smaller effective mass. That is the conduction process is based on the superposition of two kinds of electrons and the average mobility, μ is then given by:

$$\mu = (2\mu_{per} + \mu_{par}) / 3 \tag{3.2}$$

The two factors that influence the piezoresistive coefficient are temperature and impurity doping level (Kanda et al., 1982). Figure 3.2a and 3.2b show the piezoresistive coefficient as a function of temperature and doping level for p and n-type silicon. Figure 3.3a depicts how this phenomenon affects the piezoresistive coefficient. The [100] valley gains more electrons as the [010] and [001] valleys lose electrons upon compression in the [100] direction. Figure 3.3b shows the electrons distribution in the valleys of heavily doped silicon. The relative change of electrons redistribution is insignificant compared to total quantity of electrons. Therefore, its piezoresistive coefficient is smaller. The same phenomenon for lightly doped silicon is depicts in figure 3.3c. In this case, the relative change of electron redistribution is greater and therefore results in higher piezoresistive coefficient.

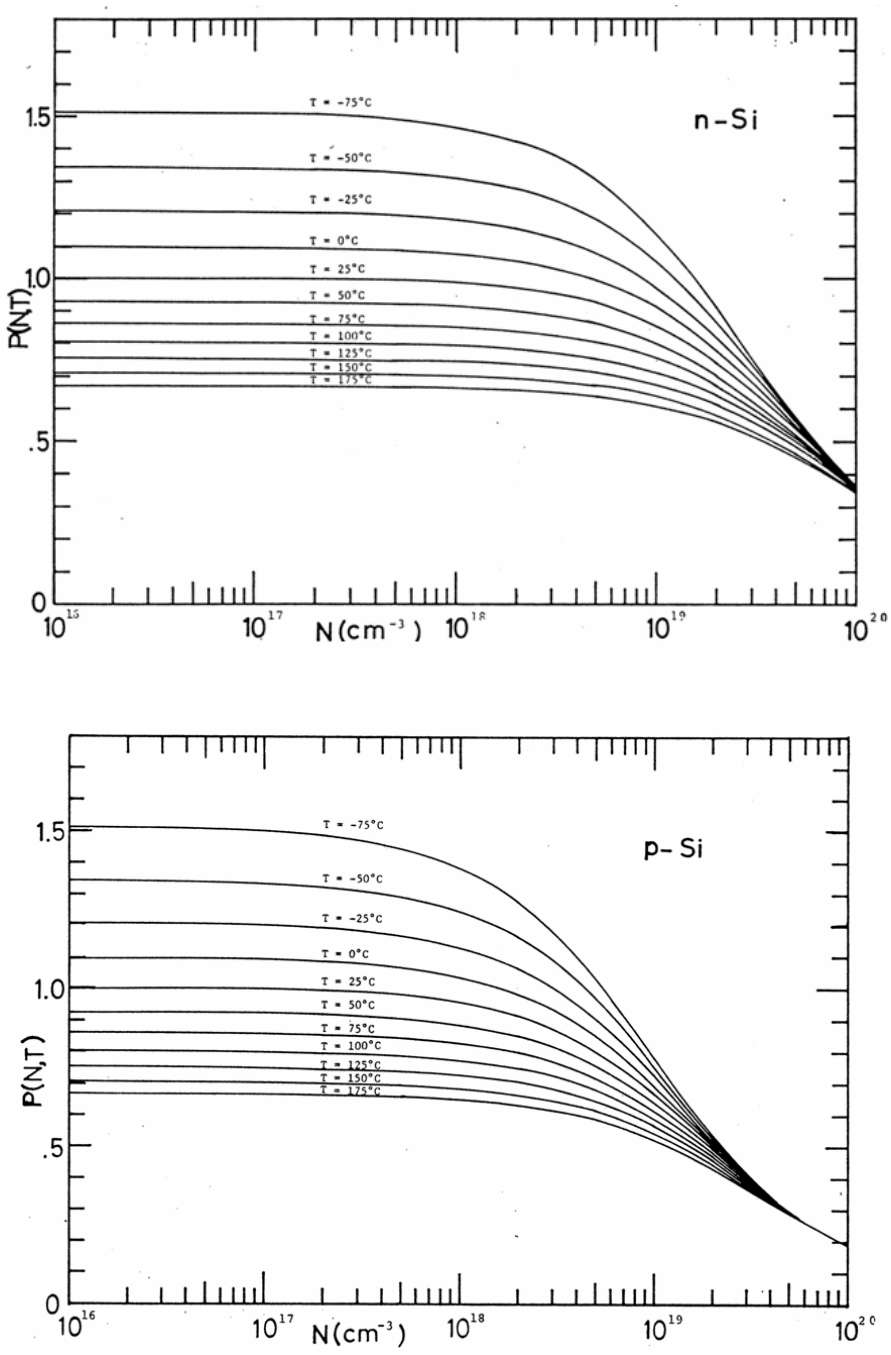

Figure 3.2 Piezoresistance factor P(n, T) as a function of impurity concentration and temperature a) n-Si, b) p-Si. Adapted from Kanda et al., 1982.

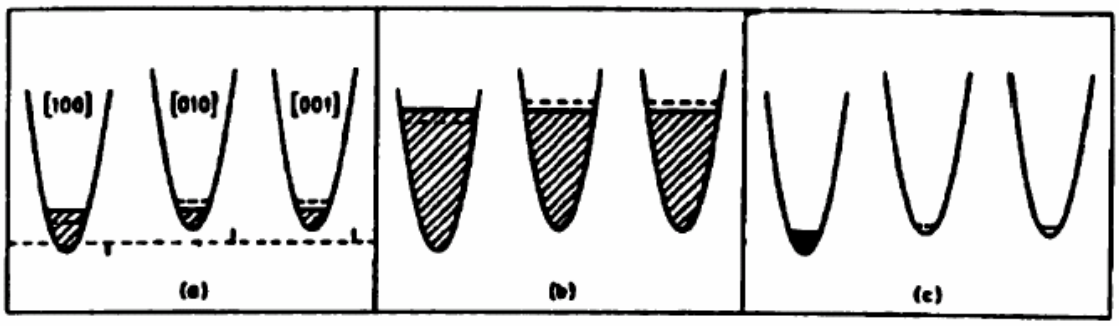

Figure 3.3 Effect on piezoresistive coefficient on a) Si, b) heavily doped, c) lightly doped. Adapted from Kanda et al., 1982.

3.2.2 Mathematical description

In this section, a detailed mathematical description of piezoresistive theory is presented. A piezoresistor can be viewed as a simple resistor following Ohm's law (V=IR). In a conservative field theory, E = jρ, where E is the electrical field and j is current density and ρ is resistivity. This equation is true for metals and other materials without piezoresistive effect. However, for a piezoresistive material, an additional disturbance term, Δρ/ρ needs to be added, and is expressed as

$$E = j\rho(1 + \Delta\rho/\rho) \tag{3.3}$$

Δρ/ρ is the relative change of resistivity and is defined as

$$\Delta\rho/\rho = \pi\sigma \tag{3.4}$$

π is the piezoresistive coefficient and σ is the stress applied on the material. In terms of three-dimensional tensors for a cubic crystal system because of symmetry

$$\begin{bmatrix} E_1 \\ E_2 \\ E_3 \end{bmatrix} = \begin{bmatrix} \rho_1 & \rho_6 & \rho_5 \\ \rho_6 & \rho_2 & \rho_4 \\ \rho_5 & \rho_4 & \rho_3 \end{bmatrix} \times \begin{bmatrix} J_1 \\ J_2 \\ J_3 \end{bmatrix} \tag{3.5}$$

For an isotropic material (where the characteristics of a material are the same in all directions), $\rho_1 = \rho_2 = \rho_3 = \rho$ and $\rho_4 = \rho_5 = \rho_6 = \rho = 0$. Thus, a more general form for the resistivity in an isotropic material is

$$\begin{bmatrix}\rho_1\\ \rho_2\\ \rho_3\\ \rho_4\\ \rho_5\\ \rho_6\end{bmatrix} = \begin{bmatrix}\rho\\ \rho\\ \rho\\ 0\\ 0\\ 0\end{bmatrix} + \begin{bmatrix}\Delta\rho_1\\ \Delta\rho_2\\ \Delta\rho_3\\ \Delta\rho_4\\ \Delta\rho_5\\ \Delta\rho_6\end{bmatrix} \tag{3.6}$$

When a stress is applied on the piezoresistive elements, the crystal lattice is compressed in one direction and experiences tensile stress in other directions. Therefore, the stress on a crystal lattice can be mapped as 3 normal stresses and 3 shear stresses. Figure 3.4 shows the definition of these six stresses on a crystal lattice. .

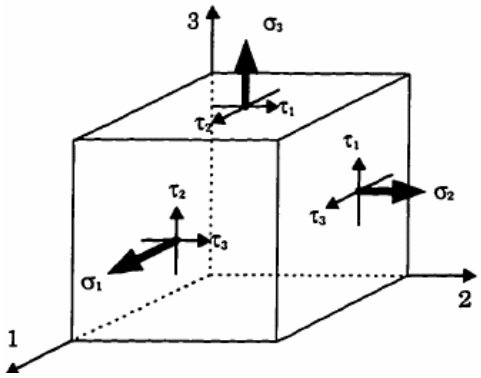

Figure 3.4 Definition of normal stresses (σ) and shear stresses (τ). Adapted from Yamada et al., 1982.

Generalizing, the resistivity components in a stressed crystal by associating gauge factor π with every stress components. It would yield a 6x6 tensor as:

$$\frac{1}{\rho}[\Delta\rho_1] = [\pi_{11}][\sigma_1] \tag{3.7}$$

However, due to symmetry of a cubic material, the π tensor is greatly simplified because only three coefficients remain π_{11}, π_{12}, π_{44} (Smith et al., 1954).

$$\frac{1}{\rho}\begin{bmatrix}\Delta\rho_1\\ \Delta\rho_2\\ \Delta\rho_3\\ \Delta\rho_4\\ \Delta\rho_5\\ \Delta\rho_6\end{bmatrix}=\begin{bmatrix}\pi_{11} & \pi_{12} & \pi_{12} & 0 & 0 & 0\\ \pi_{12} & \pi_{11} & \pi_{12} & 0 & 0 & 0\\ \pi_{11} & \pi_{11} & \pi_{12} & 0 & 0 & 0\\ 0 & 0 & 0 & \pi_{44} & 0 & 0\\ 0 & 0 & 0 & 0 & \pi_{44} & 0\\ 0 & 0 & 0 & 0 & 0 & \pi_{44}\end{bmatrix}=\begin{bmatrix}\sigma_1\\ \sigma_2\\ \sigma_3\\ \tau_1\\ \tau_2\\ \tau_3\end{bmatrix} \tag{3.8}$$

The shear stresses replace the logical stresses σ_4, σ_5, σ_6 by the following mapping:

$$[\sigma_4,\sigma_5,\sigma_6]\Leftrightarrow[\tau_1,\tau_2,\tau_3] \tag{3.9}$$

$$\begin{aligned}E_1&=\rho J_1+\rho\pi_{11}\sigma_1 J_1+\rho\pi_{12}(\sigma_2+\sigma_3)J_1+\rho\pi_{44}(J_2\tau_3+J_3\tau_2)\\ E_2&=\rho J_2+\rho\pi_{11}\sigma_2 J_2+\rho\pi_{12}(\sigma_1+\sigma_3)J_2+\rho\pi_{44}(J_1\tau_3+J_3\tau_1)\\ E_3&=\rho J_3+\rho\pi_{11}\sigma_3 J_3+\rho\pi_{12}(\sigma_2+\sigma_1)J_3+\rho\pi_{44}(J_1\tau_2+J_3\tau_1)\end{aligned} \tag{3.10}$$

The first term represents the unstressed crystal and ohm's law. The second term is the first order piezoresistive effect. The addition last two terms completes the full description of the behavior of a bulk stressed crystal (Toriyama et al., 2002). The above equations with coordinate axes are corresponding to the <100> direction of a crystal in the cubic family. It would be more general and useful to express the π coefficients for arbitrary directions. This is typically done by defining longitudinal and transverse coefficients, π_l, and π_t respectively (figure 3.7). The longitudinal coefficient refers to the case where the applied stress is in the same direction as the electric field, whereas the transverse coefficient refers to the case where the applied stress is perpendicular to the electric field.

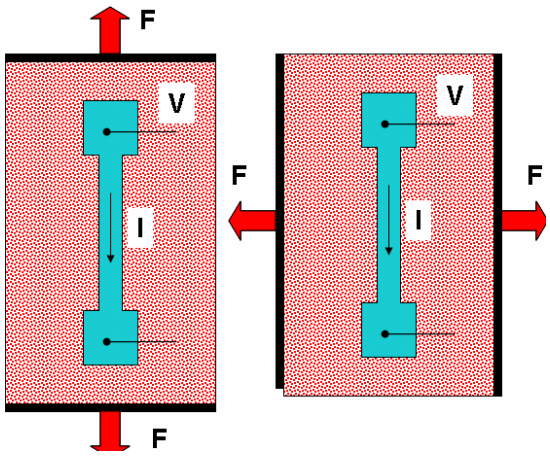

Figure 3.5 Schematic for piezoresistive coefficients: longitudinal and transverse. Adapted from Yamada et al., 1982; Kanda et al., 1982.

$$\frac{\Delta R}{R_0} = \pi_l \sigma_l + \pi_t \sigma_t \tag{3.11}$$

R is the resistance of the piezoresistor, and subscripts l and t refer to the longitudinal and transverse stresses with respect tot the resistor axis. Now the general expression for π_l, and π_t are obtained by applying coordinate transforms to the original full tensors.

$$\pi_l = \pi_{11} - 2(\pi_{11} - \pi_{12} - \pi_{44})(l_1^2 m_1^2 + l_1^2 n_1^2 + m_1^2 n_1^2 \tag{3.12}$$

$$\pi_t = \pi_{12} - 2(\pi_{11} - \pi_{12} - \pi_{44})(l_1^2 l_2^2 + m_1^2 m_2^2 + n_1^2 n_2^2 \tag{3.13}$$

(l_1, m_1, n_1) and (l_2, m_2, n_2) are the sets of direction cosines between the longitudinal resistor direction (subscript 1) and the crystal axis, and between the transverse resistor direction (subscript 2) and the crystal axis. Table 3.1 below lists the piezoresistive coefficients at room temperature for n-type and p-type silicon.

Table 3.1 Typical piezoresistive coefficients at room temperature. Adapted from Smith et al., 1954.

Si type	Resistivity Ω-cm	π_{11} 10^{-11} Pa^{-1}	π_{12} 10^{-11} Pa^{-1}	π_{44} 10^{-11} Pa^{-1}
n-type	11.7	-102.2	53.4	-13.6
p-type	7.8	6.6	-1.1	138.1

Figure 3.6 shows the longitudinal and transverse piezoresistive coefficients for p-type silicon on a) (100), b) (110) and c) (111) planes at room temperature. We can see that longitudinal coefficients are maximized in [011] direction, which is equivalent to [110] in (100) wafers, and [110] is the direction of primary flat of wafers is aligned with. Therefore in fabrication of piezoresistive sensors, the piezoresistors should be perpendicular or parallel to the primary flat of wafers. Table 3.2 lists the longitudinal and transverse coefficients for various combinations of directions in a cubic crystal.

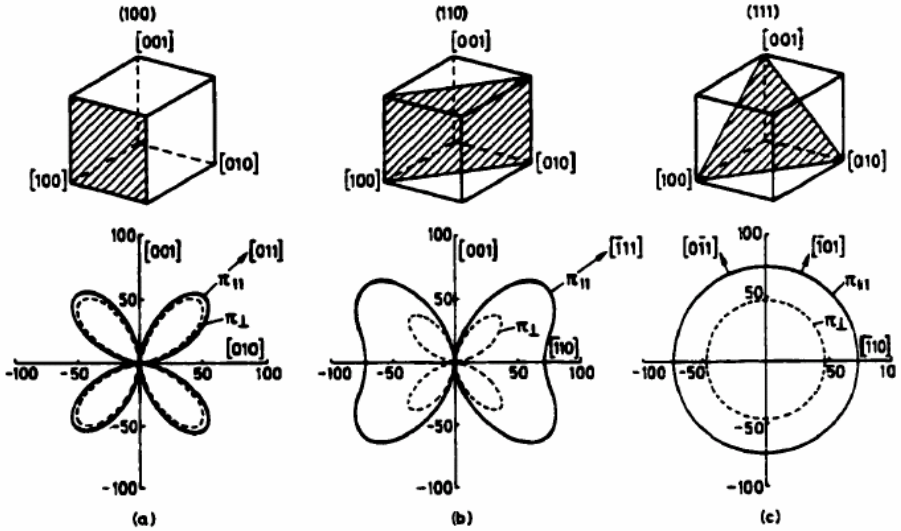

Figure 3.6 π_l and π_t for p-type Si on different planes at room temperature. Adapted from Kanda et al., 1982.

Table 3.2 Longitudinal and transverse coefficients for various combinations of directions in cubic crystal. Adapted from Kanda et al., 1982.

Longitudinal Direction	π_l	Transverse Direction	π_t
(1 0 0)	π_{11}	(0 1 0)	π_{12}
(0 0 1)	π_{11}	(1 1 0)	π_{12}
(1 1 1)	$\frac{1}{3}(\pi_{11}+2\pi_{12}+2\pi_{44})$	(1 $\bar{1}$ 0)	$\frac{1}{3}(\pi_{11}+2\pi_{12}-\pi_{44})$
(1 1 $\bar{0}$)	$\frac{1}{2}(\pi_{11}+\pi_{12}+\pi_{44})$	(1 1 1)	$\frac{1}{3}(\pi_{11}+2\pi_{12}-\pi_{44})$
(1 1 $\bar{0}$)	$\frac{1}{2}(\pi_{11}+\pi_{12}+\pi_{44})$	(0 0 1)	π_{12}
(1 1 0)	$\frac{1}{2}(\pi_{11}+\pi_{12}+\pi_{44})$	(1 $\bar{1}$ 0)	$\frac{1}{2}(\pi_{11}+\pi_{12}-\pi_{44})$

In case of silicon micromachined devices, the resistors are oriented along the [110] directions in the (100) wafers. The longitudinal cosines (1/√2, 1/√2, 0) and the transverse direction cosines are (-1/√2, 1/√2, 0). This results in

$$\pi_{i,110} = \frac{1}{2}(\pi_{11} + \pi_{12} + \pi_{44}) \tag{3.14}$$

$$\pi_{t,110} = \frac{1}{2}(\pi_{11} + \pi_{12} - \pi_{44}) \tag{3.15}$$

3.2.3 Average over stress and doping variations

The piezoresistors are typically formed by ion-implantation or diffusion, and hence have non-uniform doping. They also span a finite area on the device, hence have non-uniform stress. For complete representation of these effects, Poisson equation for the electrostatic potential throughout the piezoresistor must be solved. Taking into account boundary conditions of applied potentials ay its contacts and subject to stress variations created by deformation of the structural elements (Senturia, 2001). A good approximation is to begin with the doping variation which occurs in a direction normal to the surface. Thus to calculate the unstrained resistance R_0, conductance of resistance slices are summed.

$$\frac{1}{R_o} = \int_0^z \frac{W}{L\rho(z)} dz \tag{3.16}$$

ρ is the unstrained doping-dependent resistivity. W and L are the width and length of the resistor and z is the depth of the resistor, equal to the edge of the space-charge layer at the isolating junction. The value of z relative diaphragm thickness is important and stress averaging is necessary. This will be solved by considering the diaphragm thickness into multiple slices. The conductance, g of a single differential of thickness dz is

$$g(z) = \frac{W.dz}{L\rho(z)} \tag{3.17}$$

ρ(z) is the strained resistivity which varies with depth due tooth doping and stress. Combining doping and averaging stress piezoresistance can be expressed as:

$$R = R_0[1 + R_0 \int_0^z \frac{W}{L\rho(z)} \pi_l \sigma_l(z) dz \tag{3.18}$$

3.3 Theory of piezoresistive pressure sensors

3.3.1 Overview

The first part of this chapter, we discussed about the one of the key elements in silicon based piezoresistive pressure sensor, which is piezoresisivity. In this section, attention will be devoted to the design and analysis of the deformable element in pressure sensors. Since pressure is a normal stress (force per unit area), one could apply the pressure to one side of a deformable diaphragm, a reference pressure to the other side, and determine how much the diaphragm deforms. This approach is by far the most dominant method of measuring pressure in micromachined pressure sensors. The key element in pressure sensors is the sensing diaphragm. The diaphragm is normally made of doped single crystal silicon or polysilicon. Bulk and surface

micromachining are the two major micromachining techniques use for fabricating the sensing diaphragm. Silicon diaphragms are fabricated using (1) timed-etched bulk micromachining, (2) using a boron etch-stop or (3) electrochemical etch-stop method. Usually, the backside of the silicon wafer is patterned with a square or circular opening and then anisotropically etched using EDP, KOH or TMAH until the required thickness (few microns to tens of microns) is obtained. Figure 3.7 shows the cross-section of a bulk micromachined structure, the device size is determined by the enlargement due to the propagation of <111> crystal planes during the anisotropic etch process. The enlarged size is (2 x cot(54.74˚) x thickness of wafer).

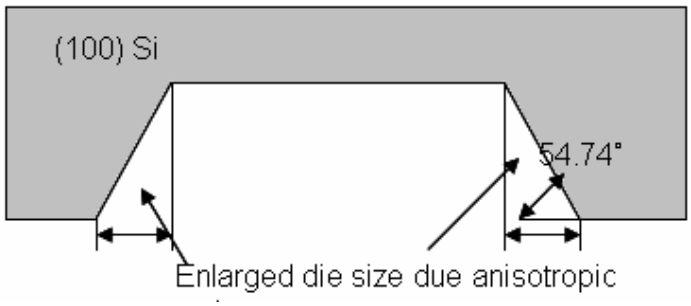

Figure 3.7 Typical bulk etching of (100) silicon.

The silicon crystal diaphragm fabricated by bulk micromachining process yields well-defined mechanical properties and has reproducible characteristics with negligible creep and hysteresis. This is one of major reasons that silicon bulk micromachined piezoresistive pressure sensors are still popular for pressures sensors. Conventional bulk micromachined piezoresistive sensors use a single diaphragm as the deformable element. However, this single deformable element becomes non-linear for large deflections of the diaphragm. This has necessitated the use of multiple diaphragms to cover specified range of pressures. To overcome this limitation, in this research, two architectures have been proposed and implemented. In the first architecture, a double or reinforced diaphragm is proposed (as shown in figure 3.8a), wherein two diaphragms, namely, inner and outer diaphragm are used. When operating under lower pressures, the inner diaphragm deflects and the outer remains insensitive. At higher pressures, inner diaphragm is in state of tension and outer diaphragm deflects and thus avoids the non-linearity of the single diaphragm. A detailed stress analysis of such deformation is discussed later in this chapter. In the second architecture, a bossed structure is included in the inner diaphragm part of the reinforced design (Figure 3.8b). This bossed structure helps in further linearizing the response and increases the sensitivity.

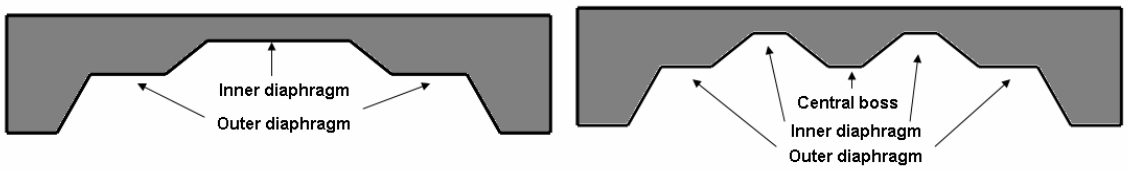

Figure 3.8 Proposed diaphragm architectures a) reinforced diaphragm, b) with bossed structure.

3.3.2 Placement of piezoresistors

The maximum stress in a diaphragm occurs at the center of the edge of a square diaphragm. One possible placement is to construct a wheatstone bridge of piezoresistors that is by connecting four piezoresistors placed (at each edge center of the square diaphragm) perpendicular and parallel to the diaphragm edge. In a simple bulk micromachined structure, these piezoresistors are placed along one of <110> directions, and are aligned along an axis of principal stress at the edge of the diaphragm (figure 3.9). However, resistors R1 and R3 experiences stresses that are rotated 90˚ compared to the stresses experienced by R2 and R4. That is, the longitudinal stress on R1 and R3 is the transverse stress at R2 and R4, and vice versa (Senturia, 2001). Further, each resistor will experience both a longitudinal and transverse stress. For example, if resistor R1 experiences a longitudinal stress σt, then it must also experience a transverse stress υσt, where υ is the poisson's ratio. As a result, the total change in resistance for R1, assuming uniform stress would be:

$$\frac{\Delta R_1}{R_1} = (\pi_l + \upsilon\pi_t)\sigma_l \tag{3.19}$$

Similarly, for R2, by reversing the roles of longitudinal and transverse stresses:

$$\frac{\Delta R_2}{R_2} = (\upsilon\pi_l + \pi_t)\sigma_l \tag{3.20}$$

If all the four resistors are connected in form of a wheatstone bridge, and assuming R1=R2=R3=R4=R, then fact the resistors in the same leg of the bridge move in opposite direction makes the bridge output larger.

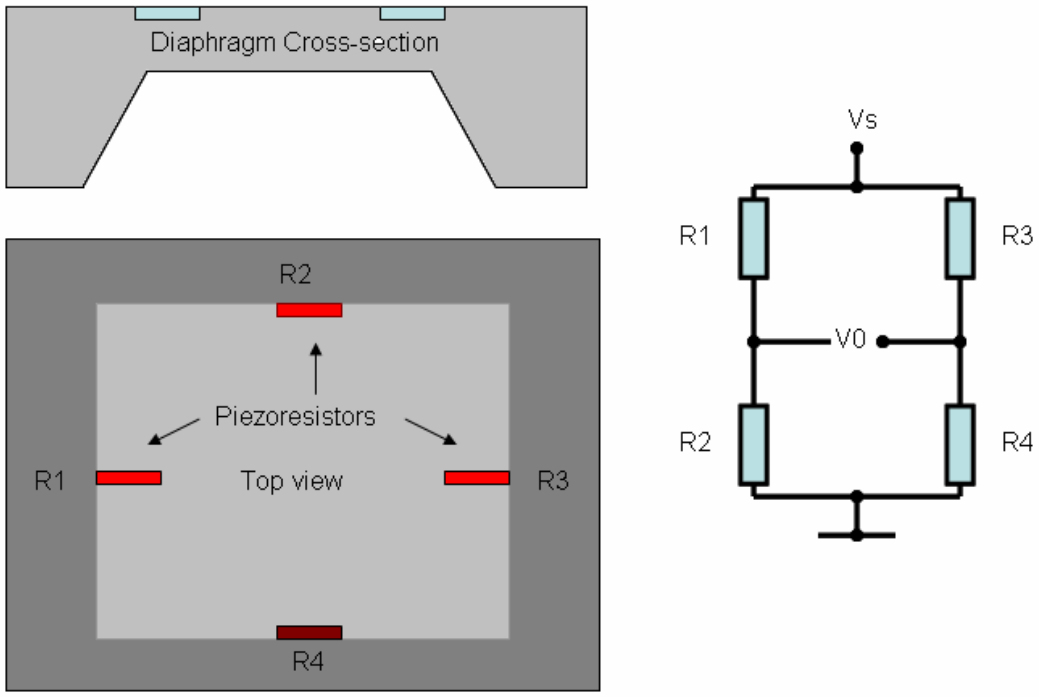

Figure 3.9 Illustration of piezoresistor placement in a square diaphragm with wheatstone bridge network.

The important advantage of connecting the piezoresistors in the form of Wheatstone bridge (figure 3.9) is to promote constant current flow through each of the elements even as the resistance of the individual elements changes under stress. Ideally, a full bridge design permits a constant voltage source to supply constant current to the sensor. The constant current supply reduces error caused by temperature fluctuations within the elements, and the full bridge sensor provides greater sensitivity to pressure. Initially, in a unstressed condition, all four piezoresistors have a resistance R and resistance changes due to applied stress by ΔR (assumed to be of same magnitude). The two piezoresistors sitting in opposite branches in the bridge sense longitudinal stress and the other two are aligned to sense transverse stress. Hence when a stress is applied, the resistance for the piezoresistors sensing longitudinal stress either increase or decrease depending on whether it is compressive or tensile, and the other two piezoresistors sensing transverse stress would decrease or increase respectively (they carry opposite signs),. Hence, the total output voltage of wheatstone bridge is expressed as:

$$V_o = \frac{V_s}{2R}(R+\Delta R) - \frac{V_s}{2R}(R-\Delta R) = \frac{\Delta R}{R}V_s \tag{3.21}$$

To further relate the output of the Wheatstone bridge to relative change in resistivity.

$$R = \frac{\rho l}{A} \; or \; \frac{\Delta R}{R} = \frac{\Delta l}{l} - \frac{\Delta A}{A} + \frac{\Delta \rho}{\rho} \tag{3.22}$$

The geometric change in negligible compared to piezoresistive effect.

$$\frac{\Delta R}{R} = \frac{\Delta \rho}{\rho} = \sigma_i \pi_i + \sigma_t \pi_t \tag{3.23}$$

Further, we know that π_{44} dominates, so other coefficients can be disregarded, or

$$\frac{\Delta R}{R} = \frac{\pi_{44}}{2}(\sigma_i - \sigma_t) \tag{3.24}$$

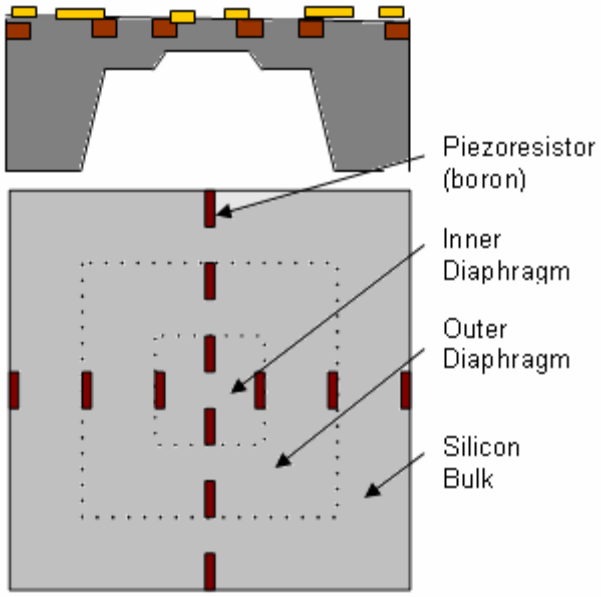

.Figure 3.10 Schematic of the double diaphragm/wheatstone bridge piezoresistive sensor.

3.3.3 Theory of reinforced diaphragm pressure sensor

In the case of the reinforced diaphragm configuration, two sets of four piezoresistors each are placed in a double wheatstone bridge network. Figure 3.10 illustrates the schematic of the proposed double diaphragm/wheatstone bridge piezoresistive sensor. The resistance change in piezoresistors is measured using a Wheatstone bridge network to reduce cross-sensitivity to temperature. However, even if all the piezoresistors are evenly matched and variations with temperature are linear, it will still create pressure offsets. Therefore, in this design, along with double piezoresistive network, a third wheatstone bridge is used to compensate for temperature variations. Even though, in this work, a Wheatstone bridge configuration is used, zero temperature coefficient of offset is possible. The temperature dependence of Vo/Vs is given as:

$$\frac{d(V_o/V_s)}{(V_o/V_s)dT} = \frac{2(d\Delta R/dR\, xR - \Delta R\, dR/dT}{\Delta R(2R+\Delta R)} \tag{3.25}$$

Hence, if all the resistors have the same temperature coefficient, $\frac{d\Delta R/dT}{\Delta R} = \frac{dR/dT}{R}$. Secondly, the bridge output has negligible temperature coefficient of sensitivity for constant applied current. The temperature coefficient of sensitivity is given as:

$$\frac{dS}{SdT} = \frac{d\pi_{44}}{\pi_{44}dT} + \frac{dR}{RdT} + \frac{\sigma_l - \sigma_t}{(\sigma_l - \sigma_t)dT} \tag{3.26}$$

The first two terms carry opposite signs and compensate each other. Therefore, the temperature coefficient of sensitivity in the wheatstone bridge configuration is very low. In spite of these compensations, piezoresistors in form of a bridge are also implanted in the silicon bulk away from the diaphragm area to help better compensate for temperature variations. These piezos only experience temperature variations and not stress dependent variations. Hence, by making differential measurements, that is by subtracting the output of the temperature compensation bridge from the pressure sensing inner and outer piezoresistive bridge, better temperature compensation can be achieved.

The double diaphragm design uses a thin inner diaphragm and thicker outer diaphragm. As described by Gotz et al 1998 by using a thicker outer diaphragm as reinforcement structure, or by edge smoothing, the sharp peak stresses at the inner diaphragm edges can be avoided. This in turn improves the maximum operating pressure capability. Also, since reinforcements have much higher stiffness than the inner diaphragm, they provide increased mechanical support. This opens the possibility for designing inner diaphragms much thinner than that possible with single diaphragm design, thus increasing the sensitivity. In this work, each individual die is designed as a square diaphragm with a piezoresistive bridge supported by a thicker square diaphragm, also with a piezoresistive bridge (Figure 3.11). Thereby, transferring larger stresses to the outer thicker rim, upon transition from small deflection to membrane regime (next section). When operating under lower pressure, the inner diaphragm deflects and outer remains relatively insensitive. At higher pressures, the inner diaphragm is in tension and changes in resistance of piezos in the outer diaphragm (under stress) are significant and measured. In summary, by using the reinforced design both the operating range capability and sensitivity are increased at the same time. In this

research, reinforced/double diaphragm pressure sensors are designed to achieve at the same time both higher sensitivity and wider full scale span (up to 1000 psi)

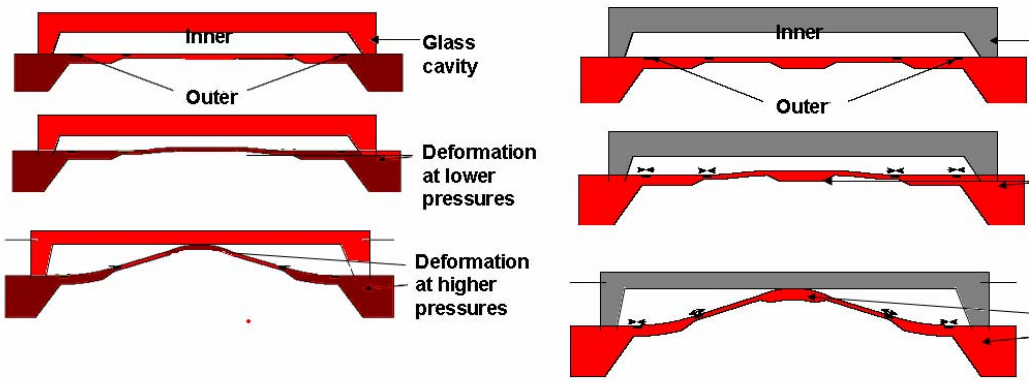

Figure 3.11 Illustration of diaphragm deflection in reinforced and bossed configurations. Adapted from Gotz et al., 1998.

3.3.4 Stress analysis of reinforced diaphragm design

This section explains the mechanical behavior of a diaphragm under applied stress. Understanding the behavior of a micromachined diaphragm is important before designing mechanical sensors or actuators such as pressure sensors, accelerometers, or gyroscopes. Behavior of diaphragm and plate are probably the most widely published topics in mechanics (Timoshenko et al., 1959). It is generally, assumed that the applied load is constant over the entire diaphragm surface. Optical and capacitive based devices measure diaphragm deflection directly. While piezoresistive sensor, which is the focus of this research, will measure deflection indirectly through piezoresistors. In spite of this indirect measurements, the diaphragm stress analysis of importance. Later, in this section numerical analysis techniques such as FEM based simulation tool – Coventorware will be used to more accurately predict the diaphragm behavior. However, these techniques don't provide the same insight as analytical or exact variational solutions. The analysis of the reinforced diaphragm can broken down into three components: a) stress analysis of inner diaphragm under lower pressures (small deflection theory), b) state of inner diaphragm under large deflections (large deflection or membrane theory), c) analysis of reinforced stare or bossed structure analysis.

(1) Small deflection plate theory: Under lower pressures, the reinforced diaphragm design behaves as a conventional single diaphragm design, wherein the small deflection plate theory can

be applied. The use of plate theory for the analysis of thin micromachined diaphragm is appropriate (Timoshenko et al., 1959). For small deflection, the thin plate or small deflection theory is used and for large deflections of diaphragm, the thick plate or large deflection theory will be used. The conditions for using either plate theory

Small plate deflection: ≤ 0.2 (plate thickness) and/or (plate deflection) ≤ 0.04 (plate diameter)
Large plate deflection: ≤ 3 (plate thickness)

In the classical plate theory established by Timoshenko, the mechanical behavior of a plate is said to be dominated by the resistance of the diaphragm to bending, measured by the flexural rigidity, D. The total stress only includes bending stress and tensile stress derived from the mid-plane of diaphragm strain is small enough to be neglected.

$$D = \frac{EH^3}{12(1-\upsilon^2)} \tag{3.27}$$

E, H and υ are the Young's modulus, plate thickness and Poisson's ratio, respectively. For diaphragms of small thickness, or for large deflections of plates, the mechanical behavior becomes dominant by the internal stresses of the diaphragm, which is said to be behaving like a membrane. Analytical equations for bending dominated structures (small deflections of thin plates) and stress dominated structures (pure membranes) are presented here. For more complicated structures involving both of them, FEA tools will be used to avoid solving non-linear equations manually. In the rest of the section, governing differential equations and analytical solutions for diaphragm under applied stress will be presented.

Small deflection theory is based on Kirchoff-Love hypotheses.

1) Plate material is inelastic, homogenous, continuous and isotropic
2) Bending deflections are small compared to the thickness of the plate
3) Plate sections originally normal to the surface are presumed to be normal after bending. Hence shearing strain is negligible.
4) Deflections of the plate are due to displacements of points in the middle surface of the plate in a direction normal to the non-deflected middle surface.

This thin plate theory can be applied to the thin silicon diaphragm using governing differential equation introduced by von Karmen, which relate the deflection with residual stress.

W is the center deflection, F is the location dependent stress functions, H is thickness and M_T is the thermal moment per unit length of diaphragm thickness, due to the thermal mismatch between silicon and dielectric layer. Using closed-form expressions from Elgamel et al., 1995 is given as:

$$\frac{\delta^4 F}{\delta x^4} + \frac{\delta^4 F}{\delta x^4 \delta y^4} + \frac{\delta^4 F}{\delta y^4} = E[(\frac{\delta^2 W}{\delta x \delta y})^2 - \frac{\delta^2 W}{\delta x^2}\frac{\delta^2 W}{\delta y^2} \tag{3.28}$$

$$\frac{\delta^4 W}{\delta x^4} - 2\frac{\delta^4 W}{\delta x^4 \delta y^4} + \frac{\delta^4 W}{\delta y^4} = \frac{1}{D} \times [P_a + H(\frac{\delta^2 F}{\delta x^2}\frac{\delta^2 W}{\delta y^2} - 2\frac{\delta^2 F}{\delta x \delta y}\frac{\delta^2 W}{\delta x \delta y} + \frac{\delta^2 W}{\delta x^2}\frac{\delta^2 F}{\delta y^2})]$$

$$+ \frac{2}{1-\upsilon}(\frac{\delta^2 M_T}{\delta x^2} + \frac{\delta^2 M_T}{\delta y^2}) \tag{3.29}$$

Substituting for flexural rigidity, D, we get

$$\frac{\delta^4 W}{\delta x^4} - 2\frac{\delta^4 W}{\delta x^4 \delta y^4} + \frac{\delta^4 W}{\delta y^4} = 12\frac{(1-\upsilon^2)}{EH^3} \times [P_a + H(\frac{\delta^2 F}{\delta x^2}\frac{\delta^2 W}{\delta y^2} - 2\frac{\delta^2 F}{\delta x \delta y}\frac{\delta^2 W}{\delta x \delta y} + \frac{\delta^2 W}{\delta x^2}\frac{\delta^2 F}{\delta y^2})]$$

$$+ \frac{2}{1-\upsilon}(\frac{\delta^2 M_T}{\delta x^2} + \frac{\delta^2 M_T}{\delta y^2}) \tag{3.30}$$

There are primarily two structural options in case of diaphragm based sensors, square or circular diaphragms. Under ideal conditions, the center deflection of a square diaphragm can be obtained by substituting these boundary conditions, W=0 dW/dx=0, dW/dy=0 at x=a and y=b into the above equations.. using Levy's method, the center deflection of square diaphragm is given as

$$W = \frac{0.0151 P a^4 (1-\upsilon^2)}{EH^3} \tag{3.31}$$

Similarly, the center deflection for the circular diaphragm is obtained by converting into polar coordinates. Using successive integration and substituting the boundary conditions, W=0 and dW/dr=0 at r=a, the center deflection of a circular diaphragm is obtained as:

$$W = \frac{3(1-\upsilon^2)\,\mathrm{Pr}^4}{16Eh^3} \tag{3.32}$$

r is the radius of the circular diaphragm. On comparing the two equations, we can see for a comparable diaphragm area (2r=a), the square diaphragm has a center deflection which is greater by about 28%. However, it becomes non-linear for larger deflections or pressures. To overcome this, two configurations are proposed in this work: 1) introduction a second diaphragm so that it acts as a reinforced edge, 2) further modification by the addition of a central bossed structure to

both linearize and improve the sensitivity of the output. Keeping in mind the requirements of high sensitivity, high linearity and suitability for micromachining, a stand alone reinforced diaphragm and a reinforced diaphragm with center boss were chosen as the primary diaphragm for implementation. In addition, the reinforced diaphragm avoids high stress concentration points in the corners of the conventional square diaphragm.

A more general quasi-analytical expression for diaphragm deflection across the diaphragm surface can be developed using the coupled partial differential equations (Elagmel et al., 1995). The boundary conditions for determining W and F of built-in edges square diaphragm of Length L are:

$$\begin{aligned} &W = 0 \quad and \quad \frac{\delta W}{\delta x} = 0 \quad at \quad x = \pm\frac{L}{2} \\ &W = 0 \quad and \quad \frac{\delta W}{\delta y} = 0 \quad at \quad y = \pm\frac{L}{2} \\ &u = 0 \quad and \quad \frac{\delta^2 F}{\delta x \delta y} = 0 \quad at \quad x = \pm\frac{L}{2} \\ &v = 0 \quad and \quad \frac{\delta^2 F}{\delta x \delta y} = 0 \quad at \quad y = \pm\frac{L}{2} \end{aligned} \tag{3.33}$$

u and v are the mid-plane displacements of diaphragm with built-in edges in the x and y directions respectively, given as:

$$\begin{aligned} u &= \int_0^x \frac{1}{E}\frac{\delta^2 F}{\delta y^2} - \upsilon\frac{\delta^2 F}{\delta x^2}) - \frac{1}{2}(\frac{\delta W}{\delta x})^2]dx \\ v &= \int_0^x \frac{1}{E}\frac{\delta^2 F}{\delta x^2} - \upsilon\frac{\delta^2 F}{\delta y^2}) - \frac{1}{2}(\frac{\delta W}{\delta y})^2]dy \end{aligned} \tag{3.34}$$

(2) Closed form expression for W(x,y) and F(x,y): The deflection W(x,y), which satisfies the boundary conditions in equation (3.33) can be approximated by (Elagmel et al., 1995):

$$W(x,y) = hf(P_a,T)\cos^2(\pi x/L)\cos^2(\pi y/L) \tag{3.35}$$

Here the general expression of W(x,y) is the form of an infinite series of squared cosine terms can be expressed from equation (3.35) in (3.30)

$$\begin{aligned} &\frac{\delta^4 F}{\delta x^4} + 2\frac{\delta^4 F}{\delta x^4 \delta y^4} + \frac{\delta^4 F}{\delta y^4} = -\frac{\pi^4 h^2 E}{2L^4}\{f(P_a,T)]^2 \times [\cos(\frac{2\pi x}{L}) + \cos(\frac{2\pi y}{L}) + \cos(\frac{4\pi x}{L}) \\ &+ \cos(\frac{4\pi y}{L}) + 2\cos(\frac{2\pi x}{L})\cos(\frac{2\pi y}{L}) + \cos(\frac{4\pi x}{L})\cos(\frac{2\pi y}{L}) + \cos(\frac{2\pi x}{L})\cos(\frac{4\pi y}{L}) \end{aligned} \tag{3.36}$$

Using the boundary conditions (3.33) in the above equation:

$$F(x,y) = -\frac{Eh^2}{32}[f(P_a,T)]^2[\frac{3\pi^2}{12L^2(1-\upsilon)}(x^2+y^2) - \cos(\frac{2\pi x}{L}) - \cos(\frac{2\pi y}{L}) - \frac{1}{2}\cos(\frac{2\pi x}{L})\cos(\frac{2\pi y}{L}) - \frac{1}{16}\cos(\frac{4\pi x}{L}) - \frac{1}{16}\cos(\frac{2\pi y}{L}) - \frac{1}{25}\cos(\frac{4\pi x}{L})\cos(\frac{2\pi y}{L}) - \frac{1}{25}\cos(\frac{2\pi x}{L})\cos(\frac{4\pi y}{L})] \quad (3.37)$$

Since the expression for W(x,y) is an approximate solution, we develop an error function e(x,y)

$$e(x,y) = \frac{\delta^4 W}{\delta x^4} = 2\frac{\delta^4 W}{\delta x^2 \delta y^2} + \frac{\delta^4 W}{\delta y^4} - 12\frac{(1-\upsilon^2)}{Eh^3} \times [P_a + h(\frac{\delta^2 F}{\delta x^2}\frac{\delta^2 W}{\delta y^2} - 2\frac{\delta^2 F}{\delta x \delta y}\frac{\delta^2 W}{\delta x \delta y} + \frac{\delta^2 W}{\delta x^2}\frac{\delta^2 F}{\delta y^2})] - \frac{2}{1-\upsilon}(\frac{\delta^2 M_T}{\delta x^2} + \frac{\delta^2 M_T}{\delta y^2}) \quad (3.38)$$

In order to minimize the error function, using Ritz-Galerkin method, which requires e(x,y) to be orthogonal the deflection W over the range of diaphragm.

$$\iint e(x,y)W(w,y)dxdy = 0 \quad (3.39)$$

$$\frac{3\pi^2 h^2(1-\upsilon^2)}{L^2}[\frac{9}{64(1-\upsilon^2)} + 0.1666][f(P_a,T)]^3 + \frac{2\pi^4 h^2}{L^2}[f(P_a,T) - \frac{3(1-\upsilon^3)}{Eh^2}P_a = 0 \quad (3.40)$$

The above expression is the general cubic equation for a square diaphragm with built-in edges oriented in the (110) plane from which deflection W can be found at any position on the diaphragm. The analytical solutions for diaphragm center deflection W (x=0, y=0) versus applied pressure and the deflection distribution over the diaphragm side W(x, y=0) at pressure of 10 psi respectively are compared with simulation results later in this chapter.

(3) Stress calculations**:** The total stress in the diaphragm parallel to and at a distance z from the middle of the surface are given by (Elagmel et al., 1995):

$$\sigma_{xx} = \frac{\delta^2 F}{\delta y^2} - \frac{Ez}{1-\upsilon^2}(\frac{\delta^2 W}{\delta x^2} + \upsilon\frac{\delta^2 W}{\delta y^3}) \quad (3.41)$$

$$\sigma_{yy} = \frac{\delta^2 F}{\delta x^2} - \frac{Ez}{1-\upsilon^2}(\upsilon\frac{\delta^2 W}{\delta x^2} + \frac{\delta^2 W}{\delta y^3}) \quad (3.42)$$

$$\sigma_{zz} = -\frac{\delta^2 F}{\delta x \delta y} - \frac{E}{1-\upsilon}\frac{\delta^2 W}{\delta x \delta y} \quad (3.43)$$

The first and second term of the above equations represent the diaphragm stress, bending stress and thermal stress respectively. The effect of thermal stress from the dielectric layer on the diaphragm has been ignored. Solving the above partial differential equation for normal stress in the x axis:

$$\sigma_x = -0.51P\frac{L^2}{h^2}[(1-\frac{y^2}{L^2})^2(1-3\frac{x^2}{L^2})^2 + \upsilon(1-\frac{x^2}{L^2})^2(1-3\frac{y^2}{L^2})^2] \tag{3.44}$$

The maximum stresses are at the centers of the edges at (±L,0). The normal stress in x axis is:

$$\sigma_{\max} = 1.23P\frac{L^2}{H^2} \tag{3.45}$$

At the center of the diaphragm (0,0), it is:

$$\sigma_{center} = -0.55P\frac{L^2}{H^2} \tag{3.46}$$

Similarly, maximum deflection at center is given as:

$$W_{center} = 0.22P\frac{L^4}{EH^3} \tag{3.47}$$

The above equations are valid only for small deflections (deflection, < 0.2 times the diaphragm thickness). Beyond this point, diaphragm behaves as a membrane with significant tensile stresses and tends to decrease the amount of deflection, while producing non-linearities.

(4) Large deflection or membrane theory: Upon large deflection, when the thin inner diaphragm moves from state of deformation to state of tension, diaphragm behavior approaches a membrane, with no flexural rigidity. Thus, any approximate characteristic solution to governing equations must consider bending as well as the mid-plane tensile membrane resistance to applied pressure. Apart from the simple reinforced diaphragm, the behavior is also affected by the rigid central boss, which will also be discussed in this section. The pressure sensors that involve diaphragm deflection are often thin enough to be considered as membrane, for first approximation. If the stress term is dominant at small deflections; the structure behaves as a membrane. If the bending term is dominant at small deflections, it behaves as a plate. Now including the component of in-plane tension, the differential equation as:

$$D(\frac{\partial^4 W}{\partial x^4} + 2\frac{\partial^4 W}{\partial^2 x \partial^2 y} + \frac{\partial^4 W}{\partial y^4}) - (N_x^1 \ \frac{\partial^2 W}{\partial x^2} + N_y^1 \ \frac{\partial^4 W}{\partial y^4}) = P \tag{3.48}$$

N_x, N_y are the in-plane tension per unit width in the principal axis x and y. P is the distributed load. If the plate has residual biaxial stress σ, then

$$N_x^1 = N_y^1 = \sigma H \tag{3.49}$$

H is the plate thickness. A tensile in-plate stress increases the bending stiffness of the plate while, a compressive in-plane stress reduces the stiffness and can lead to buckling behavior. For very thin plates, the flexural rigidity can be neglected, so that plate is called a membrane and is described as:

$$(N_x^1 \ \frac{\partial^2 W}{\partial x^2} + N_y^1 \ \frac{\partial^4 W}{\partial y^4}) = -P \tag{3.50}$$

For a particular biaxial tension, $N_x^1 = N_y^1 = N^1$ and this equation becomes:

$$\frac{\partial^2 W}{\partial x^2} + \frac{\partial^4 W}{\partial y^4} = -\frac{P}{N^1} \tag{3.51}$$

As described earlier for square membrane of length L, subject to boundary conditions that the deflection is zero at the boundary and that the moment is zero at the boundary. The differential equations are separable as:

$W - \sin(k_x x)\sin(k_y y)$ for x=L and y=L, we require $k_x = \frac{n_x \pi}{L} and \ k_y = \frac{n_y \pi}{L}$ (3.52)

The complete differential equation by superposition as:

$$\sum C_{n_x n_n}(k_x^2 + k_y^2)\sin(k_x x)\sin(k_y y) = \frac{P}{N^1} \tag{3.53}$$

From which we can conclude that

$$C_{n_x n_n} = -\frac{16L^2 P}{\pi^2 N^1 (n_x^2 + n_y^2) n_x n_y} \tag{3.54}$$

The maximum deflection occurs at the center of membrane,

$$W_{\max} = \frac{-0.45(16)L^2 P}{\pi^2 N^1} \tag{3.55}$$

Therefore, there is a corner stress σc, below which thin plate dominates and above which membrane behavior dominates.

$$\sigma_c = \frac{16D}{L^2 H} \tag{3.56}$$

In case of large deflections, structure becomes nonlinear elastic elements, with an incremental stiffness that increases with the pressure (Sandmaier et al., 1993). The characteristics equation for a diaphragm with a central boss and a large deflection is given as:

$$\frac{PB^4}{EH^4} = \frac{W}{AH} + \frac{BW^3}{H^3}$$

where

$$A = \frac{3(1-\upsilon^2)}{16}\left(1 - \frac{L^4}{B^4} - 4\frac{L^2}{B^2}\log\frac{L}{B}\right) \tag{3.57}$$

$$B = \frac{\frac{7-\upsilon}{3}\left(1 + \frac{L^2}{B^2} + \frac{L^4}{B^4}\right) + \frac{(3-\upsilon)^2 L^2}{(1+\upsilon)B^2}}{(1-\upsilon)\left(1 - \frac{L^4}{B^4}\right)\left(1 - \frac{L^2}{B^2}\right)^2}$$

B is the length of the square boss center. The first term in above equation is due to bending resistance and second term is due to tensile resistance. The equation above is suitable for evaluating load-deflection relationships of simple diaphragms with rigid center but without residual stress. Using P as dependent variable, the equation can be expressed as:

$$P = \frac{EH^3}{AL^3}(W) + B.\frac{EH}{L_4}(W)^3 \tag{3.58}$$

The effect of residual stress is to reduce the center deflection proportional to the residual stress. This stress term can be approximated to a first order as:

$$\sigma_r : \frac{y4\sigma_r L^2}{(EH^3)(1-\upsilon)} \tag{3.59}$$

In this research, deflection to diaphragm thickness ratio has been kept less than 5, the typical ratio where the diaphragm is considered a membrane. Then, this diaphragm can be considered as a thin plate under large deflection. FEA analysis using Coventorware has been performed extensively for optimizing the overall dimensions of the reinforced design. In the later section, these simulation results for conventional single diaphragm and reinforced design are presented.

(5) Load limitation and pressure sensitivity: When the maximum total stress exceeds the fracture stress of 7E6 Pa for silicon, the diaphragm happens to rupture. However actual experimental stress results show failure at much less stress compared to analytical results due to the presence of

very high-density of dislocations on the etched silicon diaphragm. Based on the Griffin fracture criterion, these micro-holes strongly reduce the fracture stress of Si diaphragm. The critical stress for Si diaphragm is less than 291 MPa (Linlin et al. 2006). The pressure sensitivity, S for a piezoresistive sensor is determined by the configuration of the resistors and the stress averaging effects over the resistor dimensions. An approximate relation for diaphragm free from intrinsic stress is:

$$S = \frac{\Delta V}{V_s P} \alpha \; C.(\frac{L}{H})^2 \tag{3.60}$$

ΔV is the resistor bridge output voltage, Vs is the supply voltage, and C depends on the piezoresistive coefficients and geometry of the resistors.

3.4 Design of reinforced diaphragm pressure sensors

3.4.1 Overview

As stated earlier, the reinforced diaphragm pressure sensor makes use of double diaphragm - thinner inner diaphragm and thicker outer diaphragm, instead of the conventional single diaphragm configuration. The inner diaphragm, initially, operates under the small deflection regime, with a linear operating range. Upon reaching a central deflection greater 0.2 times the diaphragm thickness, it enters the large deflection or non-linear regime. At this stage, the outer diaphragm (under small deflection regime) is made operational, thus extending the maximum linear operating range. In general, a square diaphragm of length L and thickness, H, sensitivity, S for input pressure, P is defined as:

$$S = \frac{Vo}{Vs} = C * (\frac{L}{H})^2 P \tag{3.61}$$

It is therefore, advantageous to use much thinner inner diaphragm, H (with adequate reinforcements) to achieve higher sensitivity, S. Also, by using piezo elements in the outer diaphragm operating range can be further increased. In all, by using the reinforced design both the operating range capability and sensitivity are increased at the same time. Schjolberg-Henriksen et al., 2006 fabricated similar double diaphragm pressure sensors with two different thicknesses and a central boss for photo-acoustic gas detection. A resolution of 11 μV/V.Pa (five fold larger than single diaphragm) was achieved with an inner diaphragm of thickness 3 μm, but the maximum burst pressure was limited to ± 1 bar. (14.5 psi). However, in this research, reinforced/double diaphragm pressure sensors are designed (up to 1000 psi) and measured (up to

400 psi) to achieve at the same time both higher sensitivity and wider full scale span) compared to single diaphragm designs.

3.4.2 Generation I: design

The design of the Generation I, as stated earlier, consists of two square (inner and outer) diaphragms with a piezo bridges in each diaphragm. The reinforced piezoresistive pressure sensor design was initially, validated using the finite element analysis software, Coventorware®. Both single and double diaphragm pressure sensors were analyzed for sake of the comparison. Figure 3.12. illustrates the stress distribution in single (a) and inner part of the double diaphragm (b) of dimensions 1500 µm x 1500 µm. As reported by Gotz et al. 1998, in case of single diaphragm sensor, the peak stresses were seen at the sharp diaphragm edges, which will reduce the maximum operating pressure. But in the case of double diaphragm design for the same applied pressure, the outer diaphragm acted as support structure by absorbing all the peak stresses. This is because the stiffness coefficient of the outer diaphragm is higher than that of the inner diaphragm. From simulation analysis, the peak stresses were observed to be about a factor of 2-2.2 higher for the single diaphragm designs (Gotz et al., 1998). It was also found out that for most effective stress transfer from the inner to the outer diaphragm, the ratio of outer to inner diaphragm should be greater than 3. For the sake of completeness, two types of Generation I sensors were designed: 1) outer/inner diaphragm ratio less than 3, 2) outer/inner diaphragm ratio equal to 3. Table 3.3 depicts the design specification for Generation I sensors.

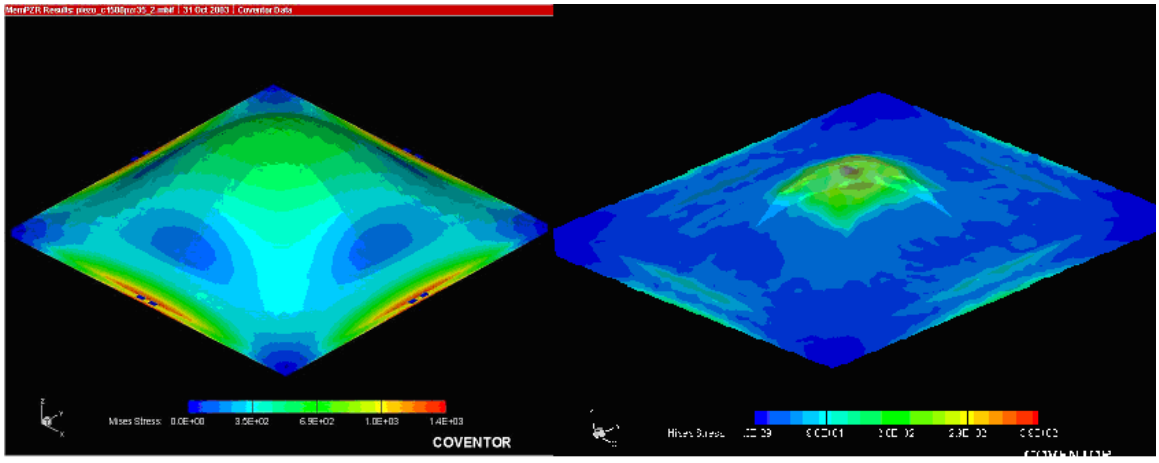

Figure 3.12 Example of stress distribution for single (a) and inner (b) diaphragm designs (1500.x 1500 µm) for an applied load of 1 MPa or 145 psi.

Table 3.3 List of Generation I sensor design parameters.

Parameters	Specifications
Die thickness	250 µm
Inner diaphragm	1000^2, 1500^2
Outer diaphragm	2000^2, 3000^2
Piezoresistance	2 kΩ
Piezo dimensions	100 x 10 μm^2
Inner thickness	5-25 µm
Outer thickness	25-45 µm

Next, the validity of the simulation results was analyzed by comparing against the closed-form analytical equation 3.40 in the stress analysis section. Figure 3.13. shows the comparison of diaphragm center deflection between analytical results and simulation results for a single diaphragm of length 1000 µm and thickness 50 µm, υ = 0.066 and E = 168 GPa under small deflection theory. It was observed that for small deflections, the simulation results correlates well with the analytical solutions (figure 3.13). Next, the diaphragm defection as a function of the position on the diaphragm (x/L) at a pressure of 10 psi was compared, as shown in figure 3.14. The close match between the analytical and simulation values for center deflection validated the simulation boundary conditions, piezoresistor placement and diaphragm dimensions. Due to the complexity in solving analytical equation for the reinforced or double diaphragm, simulated results were used empirically.

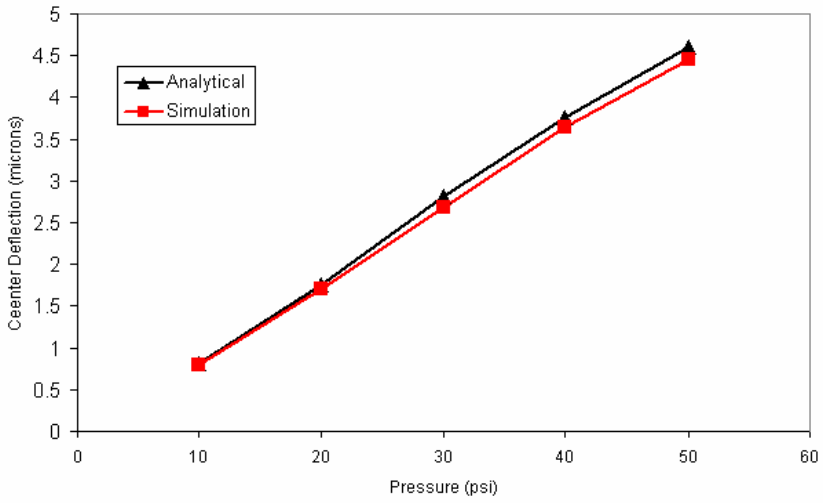

Figure 3.13 Plot of diaphragm center deflection versus applied pressure.

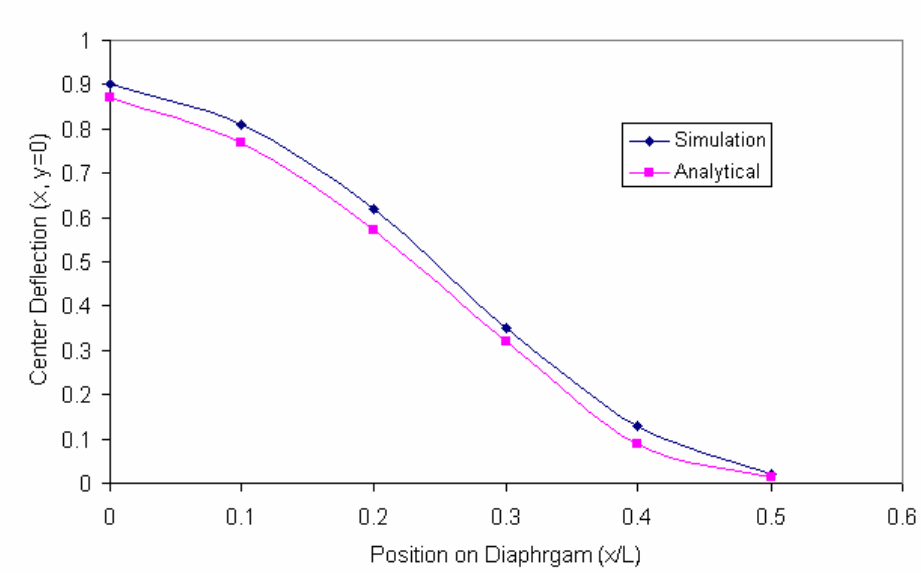

Figure 3.14 Plot of diaphragm deflection at x, y=0 versus position on diaphragm (x/L).

Next, it was important to verify the assumption that the reinforced diaphragm pressure sensors resulted in higher sensitivity and wider operating span at the simulation level before experimental testing. Table 3.4 lists the dimensions for designs in the Generation I sensors.

Table 3.4 List of diaphragm dimensions for Generation I sensors.

Sensor	Inner (L/H in μm)	Outer (L/H in μm)
D1	2000/10	3000/30
D2	1000/13	2000/36
D3	1500/30	2000/45
D4	1000/20	2000/45
S1	1500/30	-
S2	2000/10	-
S3	3000/30	-

Figure 3.15 presents the center deflection as function of applied pressure for sensors D1, D2 and S2. It is evident that the center deflection for both the reinforced diaphragm configurations are about 2-2.5 times higher than that of single diaphragm configuration for same operating range. Similarly, on comparing the stresses at the position of piezoresistors for sensors

D1, D2 and S2, it was found even though peak stresses are transferred from the inner to outer diaphragm, the average stress at the piezoresistor location is about 1.5-2 times higher than in single diaphragm configuration (Figure 3.16). Also, sensor D1, with same outer dimension as single diaphragm sensor S3 exhibited higher stress level and operating pressure range.

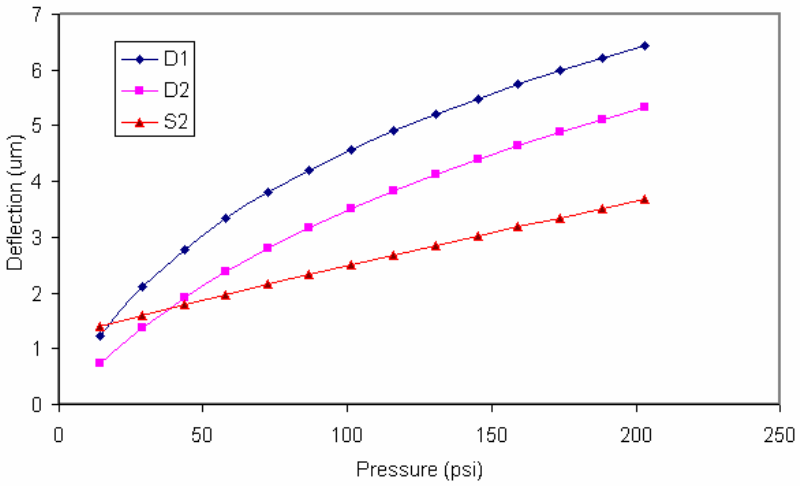

Figure 3.15 Plot of center deflection as function of applied pressure for sensors D1, D2 and S2.

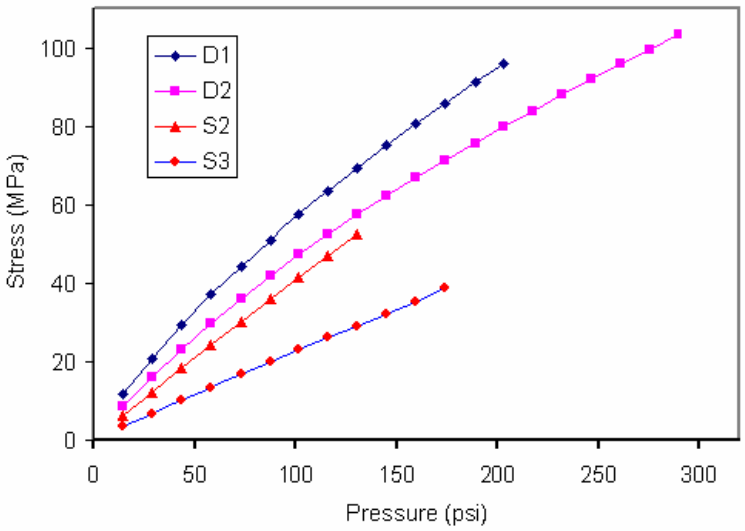

Figure 3.16 Plot of stress at the piezoresistor versus pressure for sensors D1, D2, S2 and S3.

3.4.3 Effect of residual stress

To analyze the effects of any residual stress on the sensing diaphragm, simulations were carried out on different diaphragm dimensions (Chavan et al., 1997). The residual stress on the diaphragm affects the stress distribution o n the diaphragm and hence the response. When the

aspect ratio (length/thickness) was less than 50, no significant (<10% lesser) deflection difference was noticed (Chavan et al., 1997)..There may be two types of stress on a diaphragm: (1) stress due to diaphragm deflection, (2) residual stress. Any residual stress will superimpose on the original stress distribution, thus making the stress distribution unsymmetrical. Before, the effects of residual stress, it is important to understand the origin of residual stress. Boron-doped piezoresistors in silicon diaphragm predominately display a tensile stress in the range of 40-160 MPa (Chavan et al., 1997). Boron atoms have a smaller radii of 0.88Å as compared to 1.17Å for Si atoms. The stress arises because the high doping densities (above 1E20/cm^3) may cause a lattice mismatch. Reports in literature indicate that compressive stress can occur in boron-doped layers, which will manifest itself on high temperature oxidation or drive-in step. Chavan et al., 1997 showed that for diaphragm length more than 400 μm, even a 25 MPa of residual stress causes appreciable difference (less) in center deflection.

(1) Effect of residual stress under small deflection: Implanted boron atoms into the diaphragm cause tensile residual stress (Petersen et al., 1982). This residual stress influences the total diaphragm stress and hence, affects the load limitation on the diaphragm. Ding et al., 1990 confirmed that very high-density of dislocations was generated during boron diffusion process. After the wet etch process, many micro-etch holes were observed on the boron-doped silicon diaphragm surface. Both these effects need to be accounted for load limitation on diaphragm using Griffith fracture criterion. The deflection w(x,y) of diaphragm considering the residual stress, σ_0 and flexural rigidity, D is given by

$$D\Delta^2 w - \sigma_0 H \Delta w = P \tag{3.62}$$

Considering both load stress and residual stress on load-deflection equation:

$$P = 3.41\frac{\sigma_0 H^2}{(L/2)^2}\left(\frac{w_o}{H}\right) + 4.13\frac{EH^4}{(L/2)^4(1-\upsilon)^2}\left(\frac{w_0}{H}\right) \tag{3.63}$$

σ_0 is the residual stress on the diaphragm, P is the uniform load pressure, w_0 is the maximum deflection. The maximum total stress of the diaphragm under small deflection can be written as:

$$\sigma_{total\,\max} = \frac{1.76P}{3.41\frac{\sigma_0}{E} + 4.54\frac{H^2}{(L/2)^2}} \tag{3.64}$$

Residual stress due to boron implants has been measured to be between 30 MPA and 100 MPa (Chau et al., 1987; Palik et al., 1988; Maseeh et al., 1990). By accounting for residual stress in equation 3.64, with residual stress much greater than bending stress.

$$\sigma_{total\max} = 0.52\frac{E}{\sigma_0}P \quad (only\ residual\ stress) \tag{3.65}$$

Therefore, the residual stress should not be neglected.

(2) Effect of residual stress under large deflections: The total maximum stress can be obtained as:

$$\sigma_{total\max} - \sigma_{tensile} + \sigma_{bend} + \sigma_0 \tag{3.66}$$

$\sigma_{tensile}$, σ_{bend} and σ_0 are the mid-plane tensile, bending and residual stresses respectively. The relationship between mid-plane maximum tensile stress and maximum deflection can be expressed under transverse uniform pressure as:

$$\sigma_{tensile\max} = \frac{0.864EH^2}{(L/2)^2}(\frac{w_0}{H})^2 \tag{3.67}$$

According to Chia et al., 1980, the bending stress at the middle of the edge can be expressed as:

$$\sigma_{bending\max} = \frac{6.5EH^2}{(L/2)^2}(\frac{w_0}{H}) \tag{3.68}$$

Tensile stress (being proportional to $(w_0/H)^2$) compared to (w_0/H) dependence for bending stress, is more dominant to total stress under large deflection. Therefore, the residual stress should not be neglected in this case too.

3.4.4 Temperature compensation bridge

One of the main disadvantages of piezoresistive sensors is their strong cross-sensitivity to temperature. The output sensitivity of the sensor decreases with increase in temperature.

$$R(T) = R(0)(1 + \alpha T + \beta T^2), \tag{3.69}$$

R(0) is the value of the piezoresistors at the referential temperature; α and β are the temperature coefficients (TCR) of the first and second power of T , respectively (Bonkabache et al., 2000). An important parameter of interest is the temperature coefficient of sensitivity (TCS).

$$TCS = \frac{1}{S}.\frac{\Delta S}{\Delta T} \tag{3.70}$$

ΔS is the change in sensitivity, S is the room temperature sensitivity and ΔT is the change in sensitivity. A wheatstone bridge network is therefore used to compensate for these temperature effects and improve sensitivity. However, even with all piezoresistors evenly matched, change in temperature can be manifested as change in span and offset in measurement. Most temperature compensation techniques use either laser trimming of resistors or digital compensation technique. However, in this research, the temperature compensation technique was established at the wafer or process-level. Apart from the two sensing bridge networks, a third piezoresistive bridge will be incorporated away from the stress regions to compensate for temperature offsets. Akbar et al., 1992 showed that by placing the temperature bridge in silicon bulk, 100 μm away from the sensing diaphragm, effective temperature compensation can be achieved. Because, both the sensing bridge and temperature bridge will experience the same temperature and tracking errors, a differential output of the two bridge response will eliminate all erroneous signals.

3.5 Design of Generation II reinforced diaphragm pressure sensors

3.5.1 Overview

The development of the reinforced diaphragm pressure sensor involves two bulk etching steps to create the double level structure. It was noticed that the second silicon etching step involved etching of both a maskless (111) edge and masked region, as shown in figure 3.17. This combination of steps is termed as masked-maskless etching process (Li et al., 2001).

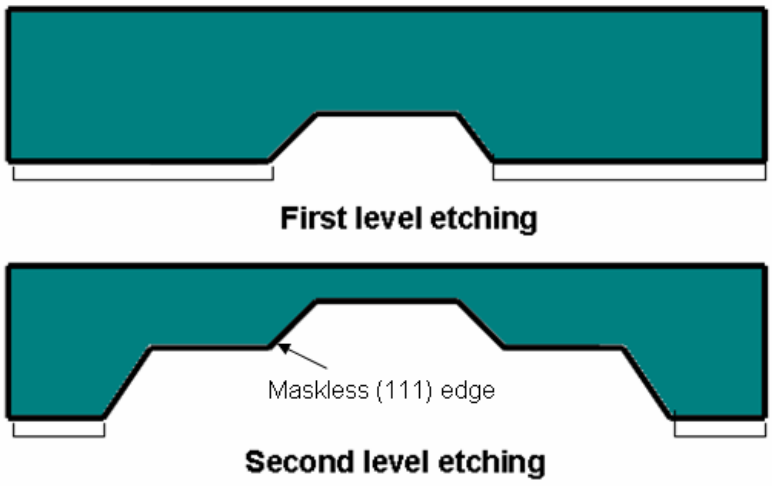

Figure 3.17 Illustration of multi-level structure etching. Adapted from Li et al., 2001.

3.5.2 Description of masked-maskless etching process

Normal anisotropic etching is always processed with a mask, thus it is called masked etching. In the masked etching process only one structural level, i.e. the etched bottom, can be created. Three-dimensional or multi-level structures of more complexity are difficult to form by using normal masked etching (figure 3.17). However, in the reinforced design, two-level structures are formed. At first, normal masked etching is processed for a certain depth. After the mask pattern on the previously etched step is stripped, maskless etching is resumed for the final formation of the structure. Further, the convex-corner undercutting under maskless etching is found to be far different compared with that of normal masked etching. In this section, the different stages in the maskless etching process, and evolution of new planes, namely, (311) plane instead of the conventional (111) plane will be discussed.

Firstly, in this section we explain the formation of (311) plane. According to Resnik et al, 2000 it is evident that the most sensitive point where etching commences is the exposed outposting corner of the (111) and (100) plane intersection. A new situation appears when the (111) and (100) planes are both exposed to the etching solution at once. By taking into account the microscopic view, why the outer silicon atoms at the edge are attacked more rapidly can be explained. The removal of an atom from a rough surface requires less energy than removal of an atom from an atomically flat surface. The backbonds of the outposting atoms probably exhibit lower bonding energy and are easily removed from the edge (Resnik et al., 2000). A measurement of this angle was seen to be around 25˚ (corresponding to (311) plane, formed at an angle of 25.24 to (100)). This can be further explained by the nature of (311) plane and adhering surface energy.

A sketch of the cross-sectional evolution of a single step along the _<110> orientation in the (100) wafer is shown in figure 3.18. the stages in the etching process are:

(1) The step with a height of *h*, previously formed by masked etching, consists of a (111) sidewall, and top and bottom (100) planes.

(2) The mask on the top of the step is stripped and the structure then undergoes a maskless etching in TMAH, the overall step height, *h*, will remain constant as both the top and the bottom planes are etched at the same rate, R-100 (etch rate for (100).plane).

(3) The sidewall of the step changes due to the emergence of a fast etching (311) plane (with an etch rate *R*-311) starting at the top convex edge of the (111) sidewall. The (311) plane will replace the previous (111) sidewall by a fast undercutting effect.

(4) The ratio, r = R-311/R-100, will be a function of etchant concentration. and for 25% TMAH, it has been experimentally determined to be 2.028 (Resnik et al., 2000).

(5) The line in the middle shows the profile when the (111) plane is partly replaced by (311) The top edge of the sidewall recedes due to the (311) fast etching.

(6) Maskless etching is divided into two stages. In the first stage, d_1 (<d, final depth) is called the critical depth, complete replacement of (111) by (311). In the second stage, d is larger than d_1, (111) sidewall is completely replaced by the fast etching (311) plane.

$$d_1 = \frac{h}{\frac{r\sin\alpha}{\sin(\alpha-\theta)}-1} = \frac{h}{1.66r-1}, \quad \alpha = 54.74^\circ, \theta = 25.24^\circ \quad (4.1)$$

The (311) sidewall moves laterally by L with time

$$L = (\frac{r}{\sin\theta} - \frac{1}{\tan\theta})d = 2.35r - 2.12)d \quad (4.2)$$

where d is the maskless etching depth and $\theta \approx 25.24^\circ$ is the included angle between the (311) sidewall and the {100} bottom, $\alpha \approx 54.74^\circ$ is the included angle between the original {111} sidewall and the {100} bottom.

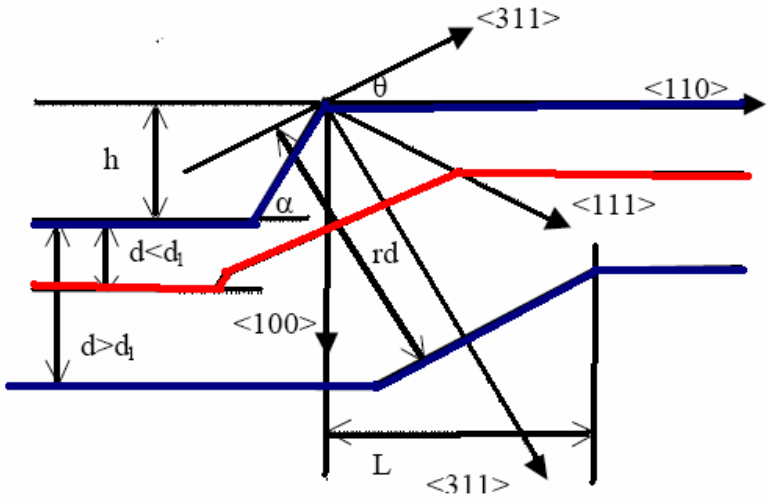

Figure 3.18 Cross-sectional evolution of (311) plane during maskless etching. Adapted from Bao et al., 1998.

3.5.3 Design of Generation II sensors

As stated earlier, because of the evolution of the (311) plane at an angle of 25.24˚ to (100) plane and a lateral movement of (311) plane. The two important parameters that need to be considered for diaphragm design, depending on the etchant concentration and etching temperature are 1) critical depth, d_1 and recession length, L. In the next chapter, these have been experimentally determined for different etchants and temperature. Using the above stated equations for recession distance and critical depth, new design specifications were developed. These new mask dimensions accounted for the masked-maskless etching process.

Table 3.5 Design parameters for Generation II sensors.

Sensor	Initial Inner (L/H in μm)	Outer (H/L in μm)	Calculated d_1 (in μm)	Calculated Recession, L (in μm)	Final Inner (L/H in μm)
II-D5	500/15	3000/45	12.65	543.35	1502/15
II-D6	1000/10	4000/30	8.44	583.11	2109/10
II-D7	500/15	4000/45	12.66	543.35	1502/15
II-D8	400/15	4000/30	6.33	583.11	1523/15

It is important to note that because of the longer recession distance and (311) angle, at 25.24˚ the Generation II devices are expected to have higher sensitivity and even wider operating span. This is because of better transfer of peak stresses through a less sharp 25.24˚ angle instead of the normal 54.74˚. This evolution of (311) plane was further, studied using Etch3D™ simulation tool (see next chapter). In addition, Conventoware simulations were performed to manifest this effect. Figure 3.19. shows reinforced diaphragm stresses at lower (a) and higher pressures (b). In (a) it is seen that maximum stresses at the inner diaphragm, while in (b) the maximum stresses are transferred to the outer/reinforced diaphragm

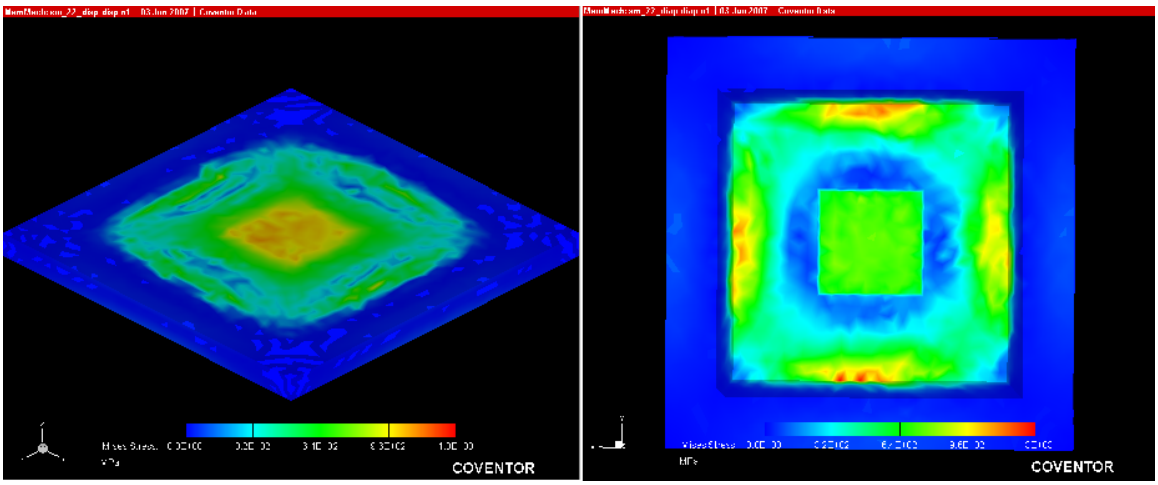

Figure 3.19 Conventorware stress map of a) low pressure (100 psi) peak stress at inner diaphragm, b) high pressure (300 psi) peak stress at outer diaphragm.

3.6 Design of Generation III reinforced diaphragm pressure sensors

The Generation III reinforced pressure sensors were designed with a central square bossed structure in addition to the reinforced edge. The use of central boss will increase the sensitivity and widen the linear operating span (Sandmaier et al., 1993). Therefore, central boss structure was added to the Generation II sensors (Figure 3.20). The incorporation of the central boss adds mass to the inner diaphragm and eventually acts as a stress concentrator focusing stress fields more toward the location of inner diaphragm piezoresistors. The resulting structure suppresses the non-linearity of the inner diaphragm (in addition to reinforced edge) and increase the sensitivity.

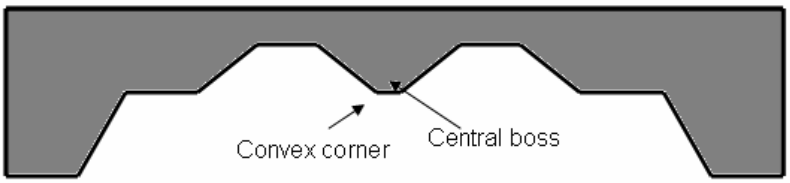

Figure 3.20 Illustration of Generation III sensor with central boss.

However, a new situation arises because of the presence of masked-maskless etching process and exposure of two convex corners in addition to concave corners during this etching. A detailed Etch3D™ simulation analysis, experimental results and corner compensation structure used are discussed in the next chapter. At this point, by adding a central boss to Generation II sensors, new diaphragm design specifications are tabulated in table 3.5.

Table 3.6 Design parameters for Generation III diaphragm structures.

Sensor	Inner (H/L in μm)	Square boss (H/L in μm)	Outer (H/L in μm)
III-B1	1505/15	200/30	3000/45
III-B2	2090/10	200/20	4000/30

3.7 Summary

In summary, this chapter described the sensing mechanism used in this research, namely, the theory of piezoresistivity as applicable to pressure sensors. Then, mechanical deformation and stress analysis of thin diaphragms and significance of reinforced/double diaphragms were discussed. This theoretical background led to the design of three generation of reinforced diaphragm pressure sensors. The Generation II sensors, by accounting for the masked-maskless etching process improved on the sensitivity and operating span over the Generation I sensors. While the Generation III sensors incorporated a central bossed structure to minimize the inner diaphragm non-linearities and further improve the output sensitivity. In addition, in this chapter, a detailed mathematical description to the evolution of (311) plane during maskless etching was presented.

CHAPTER 4

REINFORCED PRESSURE SENSOR FABRICATION AND PACKAGING

4.1 Overview

The reinforced pressure sensor fabrication process followed three variations. In the first approach, referred to as Generation I, the double diaphragm was fabricated without accounting for the masked-maskless etching process, while in the second approach; referred to as Generation II, this was taken into account at the stage of mask design. The third approach (called as Generation III) incorporated a square central boss structure on the inner diaphragm. Later, the packaging process also followed two approaches. In the first approach (packaging I), the zeroth-level package was accomplished by routing electrical connections outside the glass reference cavity. This was later system packaged by integration through Anisotropic Conductive Film (ACF) to flexible printed circuit board (Figure 4.1). In the second approach (packaging II), the zeroth-level package involved electrical interconnections drawn through the reference pressure cavity. This was accomplished by drilling through-holes through the glass substrate and later filling it with conductive epoxy paste. Then, system packaging was realized by integrating printed circuit boards with signal conditioning circuit on the pressure sensor package (figure 4.2). Figures 4.1 and 4.2 show the two packaging approaches followed in this research. The sensing side (bottom side) in both cases was first coated with protective coatings and then attached to bottom boards either Plexiglas or glass substrates with inlet and outlet ports.

In this chapter, the following topics will be discussed: 1) Fabrication process for Generation I of reinforced pressure sensors, 2) Fabrication process of Generation II devices, where process of masked-maskless etching in silicon (100) will be presented. The significance and challenges in the evolution of (311) crystal plane during this process will be discussed, 3) packaging process I, where both the zeroth-level and system-level integration schemes will be presented, 4) packaging process II (zeroth and system-level package) for pressure sensors,

and finally 5) fabrication process for Generation III devices with central boss and corner compensation structures will be discussed.

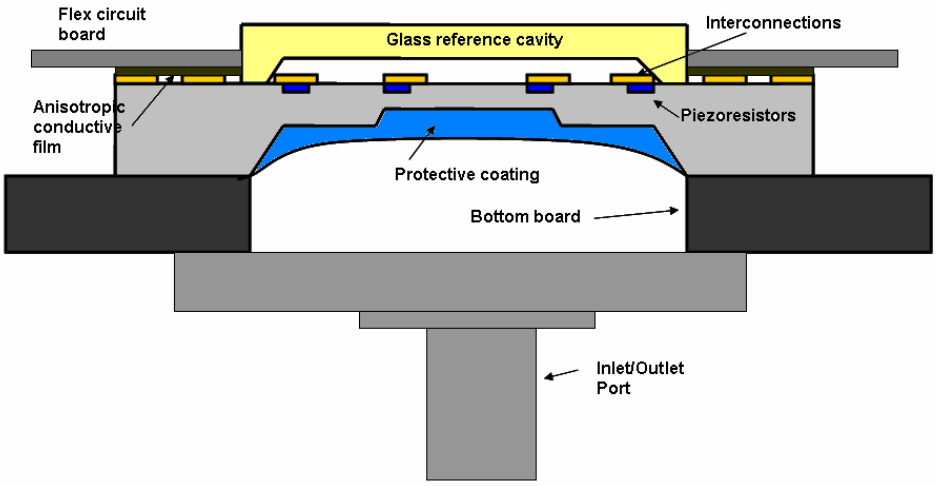

Figure 4.1 Schematic of system-level packaging of pressure sensors following packaging approach I.

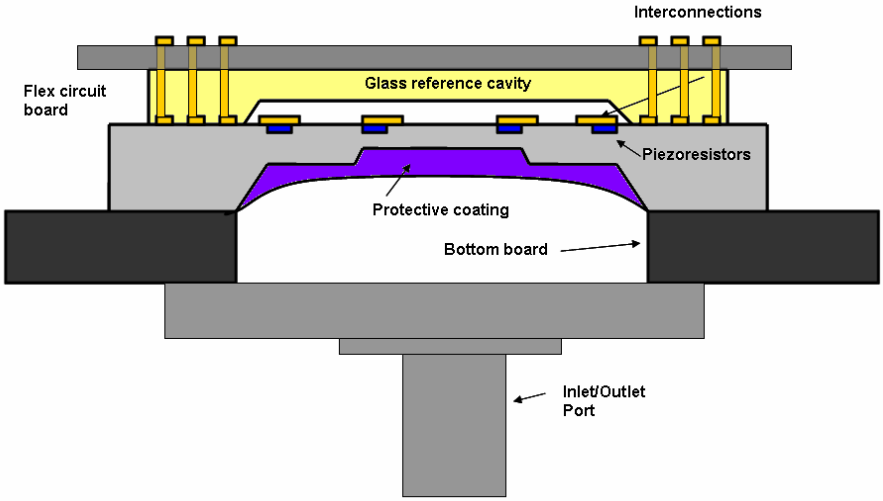

Figure 4.2 Schematic of system-level packaging of pressure sensors following packaging approach II.

4.2 Generation I: fabrication process

The fabrication of the reinforced diaphragm pressures sensors followed the classical bulk micromachining process, as illustrated in Figure 4.3. First, the bare 2" Si (100) wafers of resistivity 10-20 Ω-cm were RCA cleaned, in a bath of base and acid solutions at 70 ˚C for 10

minutes each. This process was done to remove any organic, particulate, ionic or metallic contaminants present on the bare silicon. This was followed by thermal oxidation to grow 3000Å of oxide. The thermal oxidation was performed at 1050 ˚C in an open tube furnace following dry-wet-dry oxidation sequence to reduce internal stresses in the film growth. Then, using conventional photolithography (Shipley 1818) and wet etching of oxide (10:1 Buffered oxide etch), openings for p-type boron implants were created. Ion-implantation technique was used to create shallow boron implants in silicon using the grown oxide as a hard mask. Boron implantation was carried at Nu ions with a energy of 40 KeV, dose of $8.5x10^{12}$ cm^{-2} and 7˚ tilt to obtain a peak concentration of $1.7x10^{18}$ cm^{-3}. Implantation created a p-type boron dopant of resistivity around 2 K Ω (figure 4.4a). Later, these implants were diffused by limited-source diffusion to a junction depth of 1 μm. Then, wafers were deglazed in 10:1 HF by removing all boron-implant contaminated oxide. The next step was to activate/anneal the boron-implants in silicon. At the same time, a thick layer of wet oxide about 5000Å was grown at 1000 ˚C in the open tube furnace, followed by annealing in nitrogen to getter any defects or traps in the oxide. Next, using the back-side alignment capability, photolithography (Shipley 1818) was done to define the inner diaphragm in oxide. Then, wet silicon etchant namely, TMAH was used to etch the first trench in silicon (figure 4.4b). The depth of this trench was the height difference between the inner and outer diaphragm. Next, photolithography was again done to define the outer diaphragm in oxide, followed by TMAH Si etch at 80-85 ˚C to fully etch the required diaphragm thicknesses (figure 4.4c). Finally, metal lines (contacts) in the form of Wheatstone bridge were defined by standard lift-off process of Cr/Au (100/3000 Å) using Futurex 3000PY negative resist.

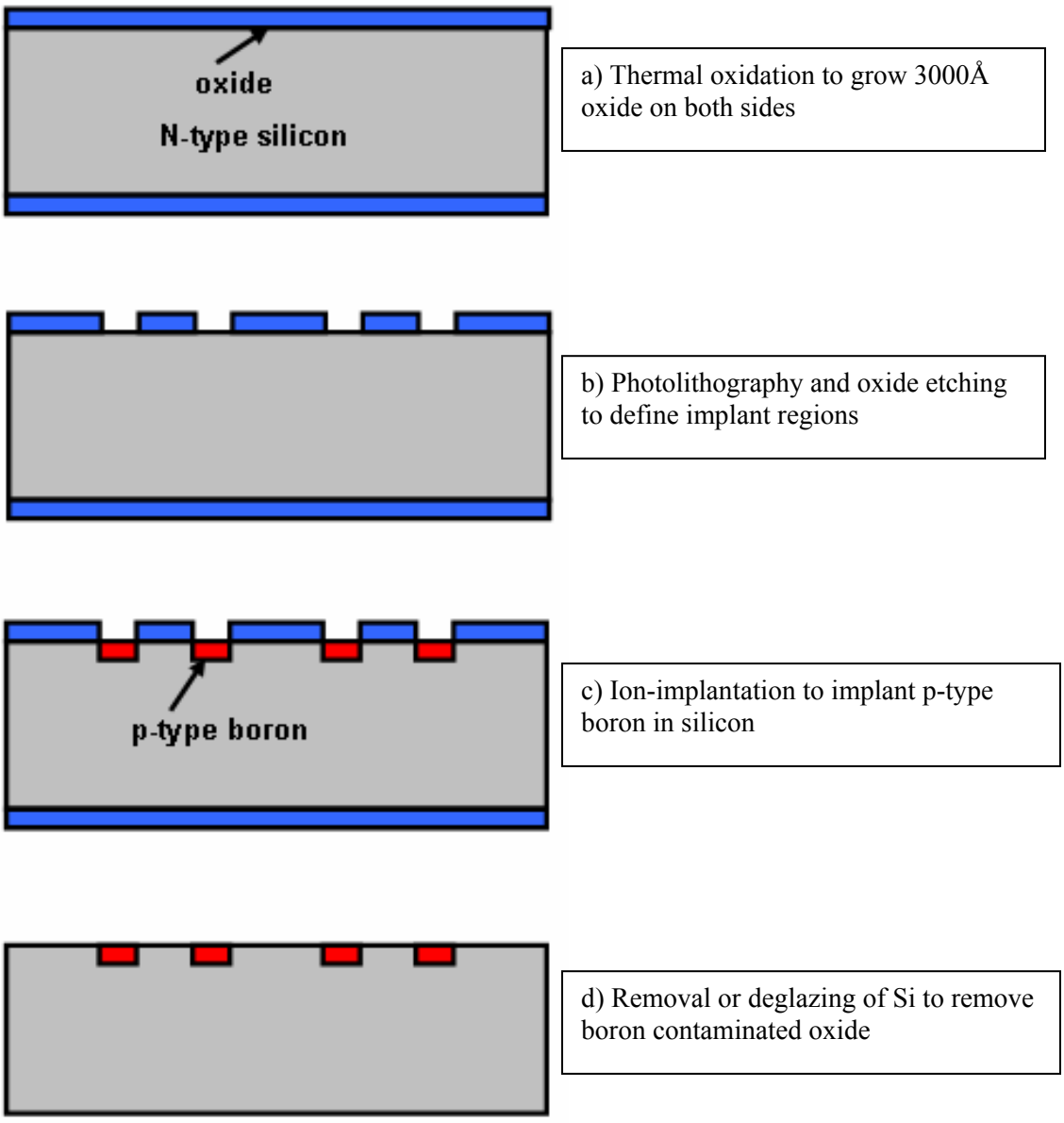

Figure 4.3 Illustration showing process flow for Generation I sensors.

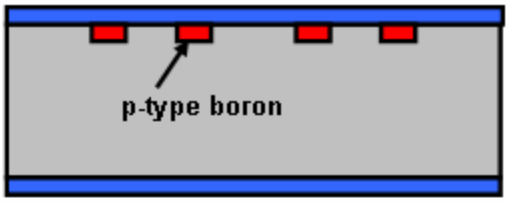

e) Boron activation and thermal oxidation to grow 5000 Å of oxide

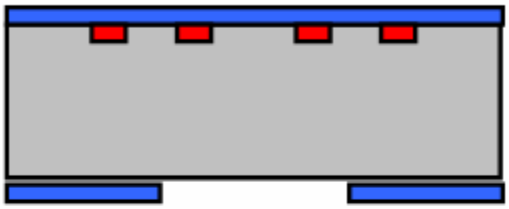

f) Photolithography and wet etching to define inner diaphragm in oxide

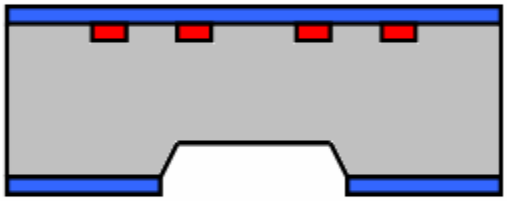

g) TMAH Si etching to etch desired depth for inner diaphragm

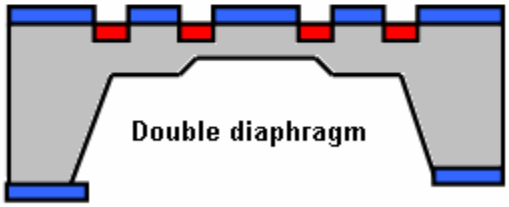

h) Photolithography and oxide etching to define outer diaphragm, followed final Si etching

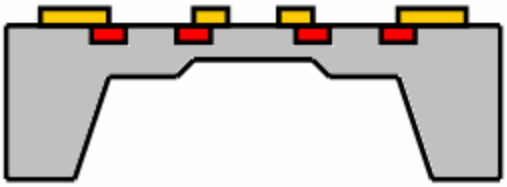

i) Metal lines definition to form Wheatstone bridge by photolithography and lift-off process

Figure 4.3 (continued)

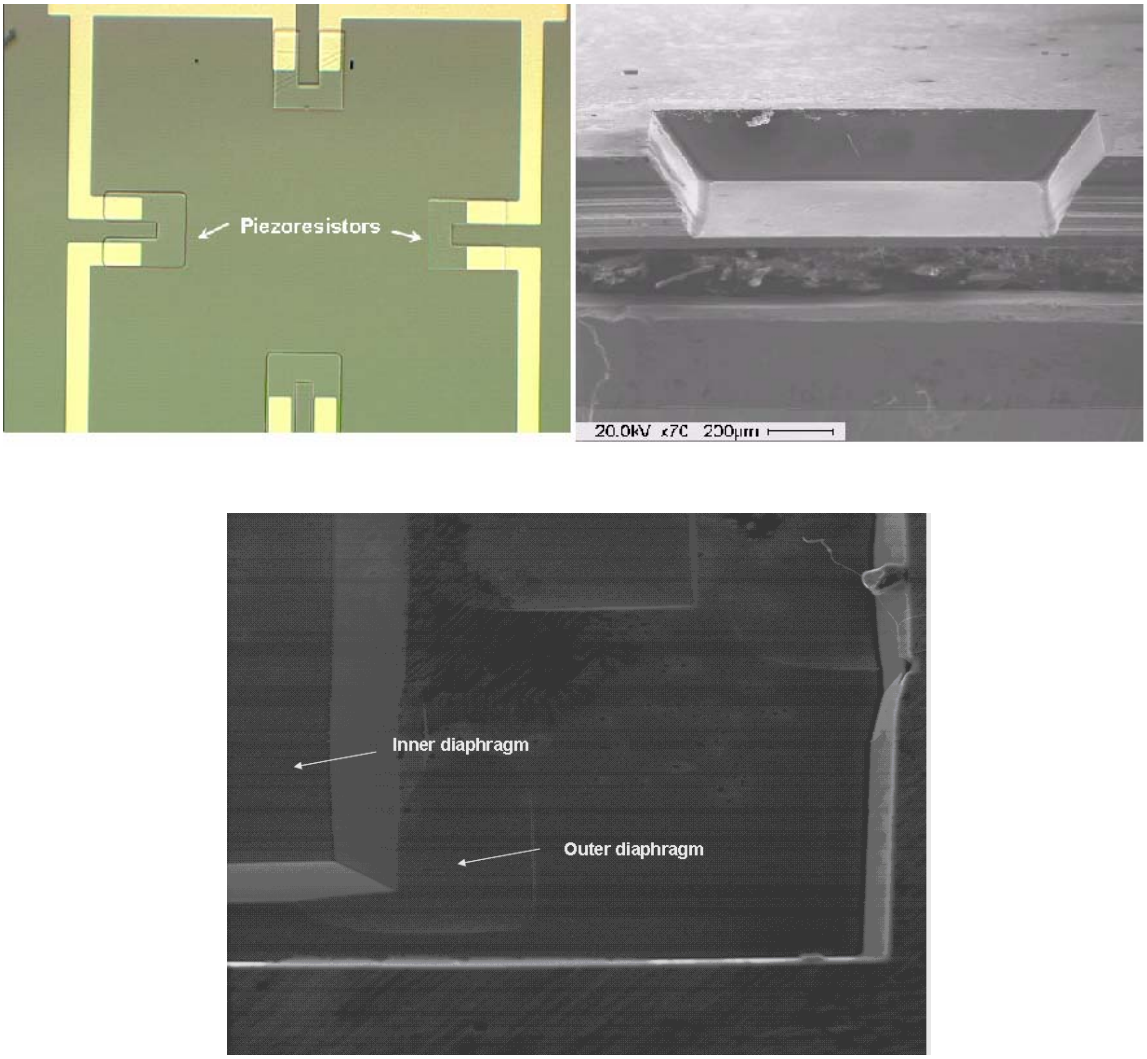

Figure 4.4 Image of a) piezoresistors (boron), b) after first etch (inner diaphragm), c) inner and outer diaphragm.

4.3 Generation II: fabrication using masked-maskless process

4.3.1 Introduction

During the fabrication of Generation II devices, it was noticed that the second silicon etching step involved etching of both a maskless (111) edge and masked region, as shown in figure 4.5. This process is termed as masked-maskless etching; wherein at first, normal masked etching is processed to a certain depth (Lin et al., 2001). After which the mask pattern of the etched step is removed, and maskless etching is resumed for the formation of double or reinforced diaphragm (even multiple is possible) structures. Using this masked-maskless dual-stage etching

sequence, theoretically multilevel structures can be realized. The process was discussed in detail in Chapter 3 and the characterization results of this process are presented here.

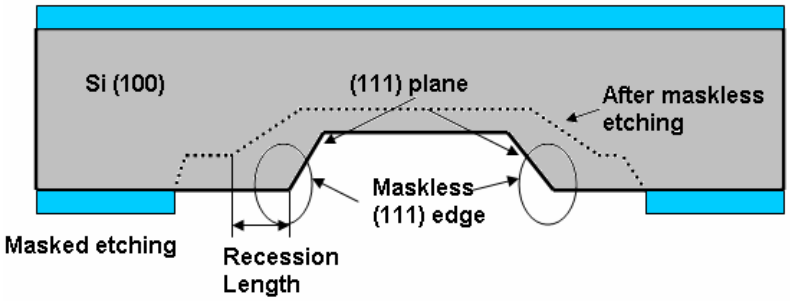

Figure 4.5 Illustration of the maskless etching edge.

4.3.2 Characterization of masked-maskless etching process

The two important parameters to be experimentally determined, which depend on the etchant concentration and etching temperature are 1) critical depth, d_1 and recession length, L (illustration shown in Chapter 3, figure 3.18). In this research, these two parameters have been experimentally measured for 25% TMAH and 45% KOH etchant at 90 ˚C for a range of initial depths as shown in figures 4.6 and 4.7.

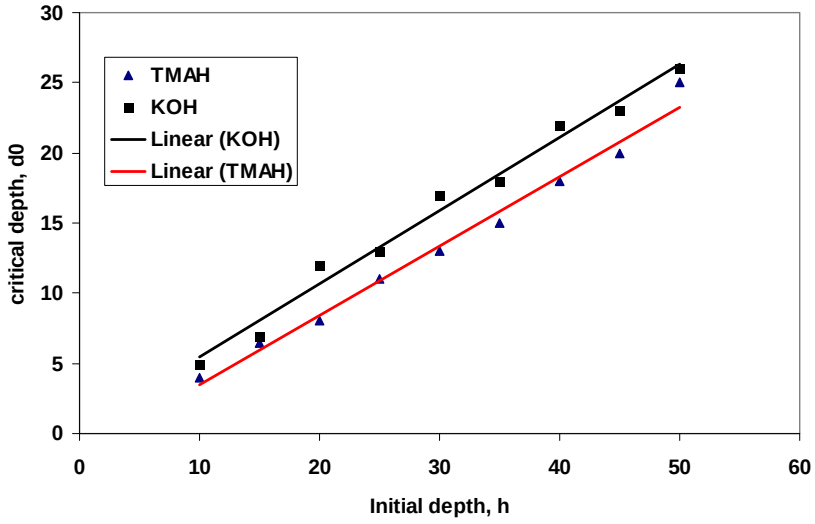

Figure 4.6 Experimentally determined critical depths for a range of initial masked depth.

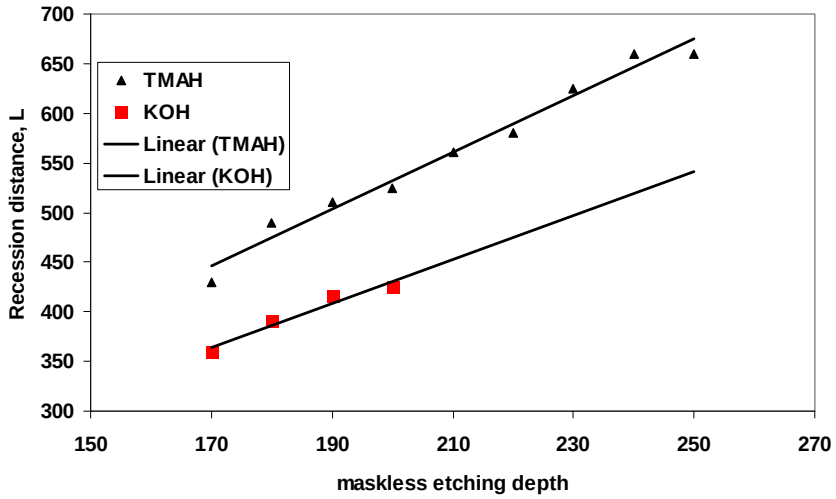

Figure 4.7 Experimentally determined recession distance for a range of maskless etching depth.

Using these data, new mask designs were incorporated into the Generation I devices, taking into account the evolution of (311) plane during the masked-maskless etching process (figure 4.8). It was expected that designs incorporating recession distance due to (311) plane will improve the overall sensitivity of individual sensors, as the angle between (311) and (100) bottom is 25.24º, which meant much less sharp corner edge (hence better reinforcement). This in turn will increase the operating range of the reinforced diaphragm pressure sensors, incorporating evolution of (311) plane. To further optimize the effect of masked-maskless etching process and to study convex and concave corner behavior during maskless etching, Etch3D™ simulation tool from Coventorware® was used.

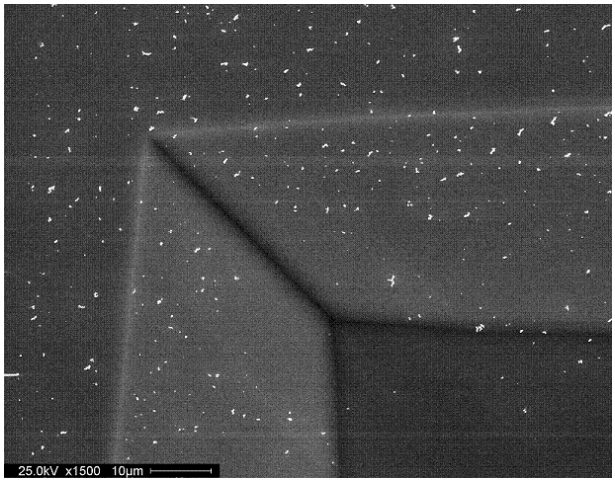

Figure 4.8 Image showing the evolved (311) plane during maskless etching.

4.3.3 Etch3D™ simulation analysis

According to Etch3D™ user guide, "*Etch3D simulation tool is based on first-principles, atomistic simulation method. The wafer is represented by a matrix of "atoms" arranged with the same geometry and connectivity as the 18-atom cells in crystalline silicon. After initialization, which usually involves applying a mask to one or both sides of the wafer, the simulation goes through a series of time steps (also called frames). During each frame, the simulator computes the removal probability for each atom on the wafer surface that is exposed to the etchant (i.e. not masked). The simulator uses a Monte Carlo approach; it compares the removal probability to a random number between 0 and 1. If the removal probability is greater than the random number, the atom is removed from the surface or, in effect, etched away. With the Monte Carlo approach, the surface of the wafer develops some roughness as the simulation proceeds. Using this approach, it is possible to duplicate certain microscopic topographies that occur in actual anisotropic etching*." To set up simulation using Etch3D, a python script and mask file were created. The python script used for both conventional single diaphragm design and reinforced diaphragm design are presented in Appendix B.

Initial simulations were carried out to form single diaphragm using the masked etching process. Figure 4.9 shows mask etched diaphragm in TMAH with (100) bottom bounded by (111) sidewalls.

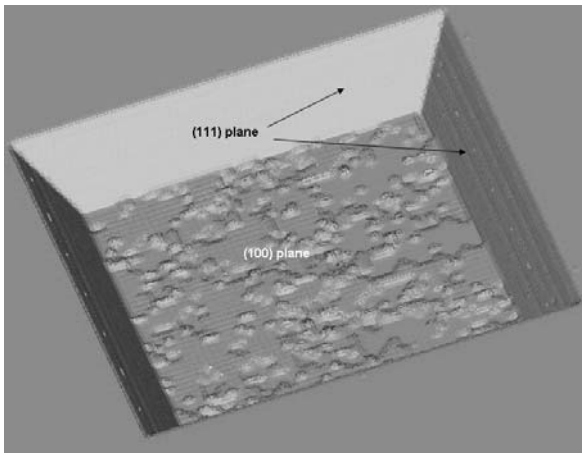

Figure 4.9 Etch3D™ image of conventional single etched trench.

The next set of etch simulations were carried out on reinforced diaphragm configurations with a combination of masked and maskless etching process in 25% TMAH solution. Figure 4.10 a-c show the top and cross-sectional view of the dual etching process. Apart from (111) seen

during masked etching, evolution of (311) plane can be clearly seen during these etching simulations. Simulation were carried out to verify the (311) plane evolution and effect of undercutting on reinforced edge.

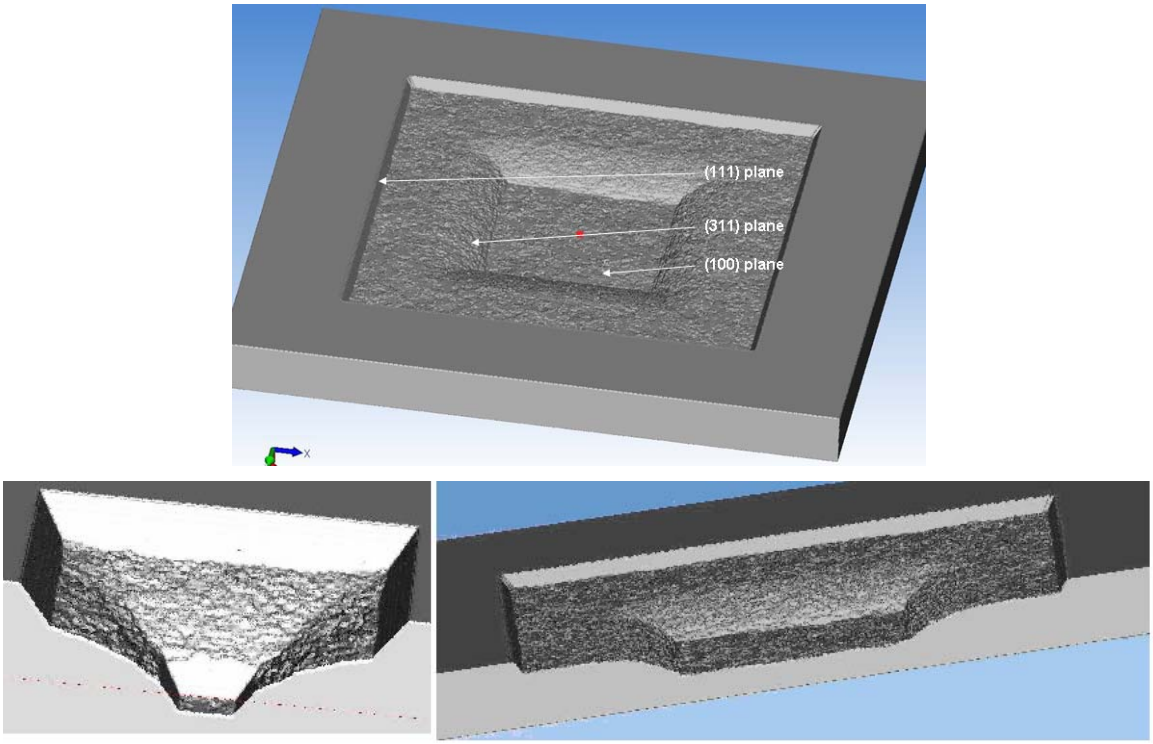

Figure 4.10 a) Top view of double diaphragm etching, b) and c) cross-sectional view of double etched diaphragm.

In this research, two kinds of reinforced diaphragm structures as shown in figure 4.11 are considered. Figure 4.11a shows typical reinforced diaphragm structure, with only exposed concave corners, while figure 4.11b shows the reinforced diaphragm structure with a square central boss and both convex and concave corners. Since the 1980s, there have been many investigations on convex corner undercutting in masked etching process and techniques to compensate for them. Bao et. al., 1998 found that similar convex corner undercutting will occur during maskless etching, however etching rate and process are far different compared to normal masked etching. In the following simulation, the geometrical evolution of this undercutting contour and compensation scheme are investigated.

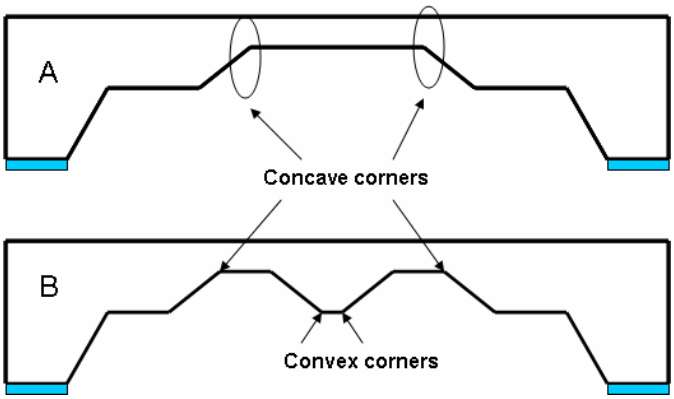

Figure 4.11 Illustration of a) exposed concave corner during maskless etching, b) exposed convex and concave corner during maskless etching.

Firstly, we will investigate undercutting in reinforced diaphragm structures with a square central boss. As stated earlier, these types of structures have both convex and concave corners. After masked etching for a convex corner without a compensation scheme, the undercutting inevitably exists. Following which maskless etching is conducted. It has been reported by Bao et al., 1998 that no matter whether a compensation scheme is used or not for the masked etching, the corner will finally show a perfect right-angle as long as the maskless etching is deep enough. Moreover the maskless etching formed corner shows structural perfection from the top plane to the bottom. Generally this can be explained by the even faster movement of the (311) plane merging the corner-undercutting effect of the relatively slow etching planes. However, this will happened only when too deep a maskless etching is done to eliminate the corner undercutting if the masked-etched undercutting is too big. However, since the maskless etching depth is fixed for the formation of a reinforced structure. Such a limited maskless etching depth is more often than not inadequate to change the existing undercut corner to a right one. Therefore, it is necessary to investigate the evolution of the convex-corner undercutting during maskless etching and to compensate for it. Figure 4.12 shows the evolution of the undercutting contour at the tope edge U versus the masked etching depth from Etch3D™ simulation. It can be seen that undercutting depth increases with etching time, meaning need for compensation structure during convex corner etching (Figure 4.15). On investigating the convex corner under maskless etching regime, the following conclusions were drawn. Figure 4.13 shows the evolution of the undercutting size at the top edge, U, versus the maskless etching depth. It was found that in this mode, the general tendency for TMAH solution is a very slight increase of undercut obtained in the masked mode, while for KOH, the undercut of a convex corner decreases from the initial value and tends to

compensate for the initial undercut. If sufficient time is allowed, the convex corner reaches self-compensation, a sharp edge. If the initial undercut is too severe (etched too deep in the masked mode without any convex corner compensation, then self-compensation cannot be achieved at the end of the required etching depth, even with KOH.

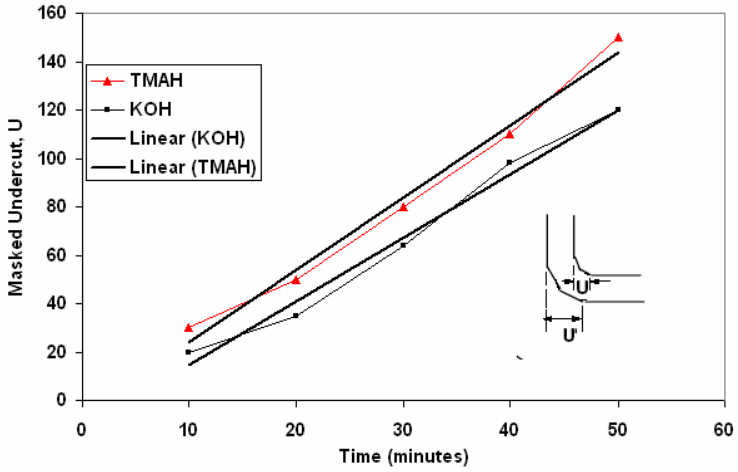

Figure 4.12 Relationship of masked undercutting versus time (simulated).

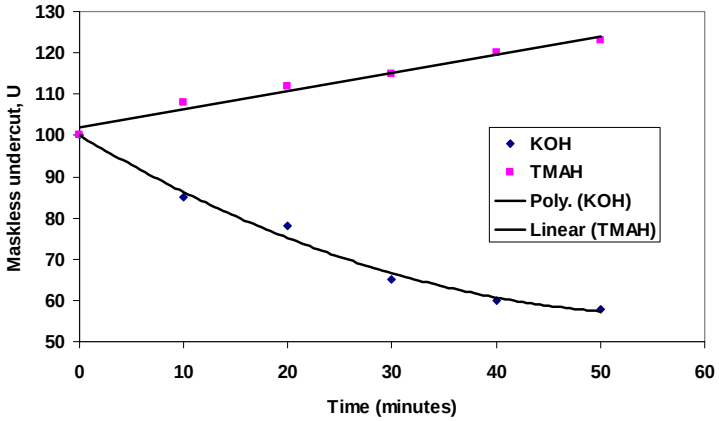

Figure 4.13 Relationship of maskless undercutting versus time (simulated).

Since, in this research, most of the etching was conducted using TMAH solution, we will investigate properties of (311) plane obtained with TMAH solution. TMAH has a significant undercut of convex corners compared to KOH for the same depth. The relationship between maskless undercutting *U* versus time with TMAH etchant for the normalized depth is shown in figure 4,12 and 4,13. The undercutting is mitigated to a great extent but could not be compensated for in a specific undercut. When the TMAH etchant used in the maskless etching mode, the

roughness was not as severe as on samples etched in KOH. The surface quality was evaluated by SEM and optical microscopy. Figure 4.14a shows AFM surface map illustrating the etch quality. The surface profile is presented in figure 4.14b. The roughness of both the inner and outer diaphragm is less than 70 nm. It has been reported earlier that the (311) surface is locally smooth with R_a values around 10-30 nm, comparable with (111) roughness, but it exhibits a convex bow across the whole scan in contrast to samples etched in KOH. Another very important observation is, however, the behavior of the bottom and the top transition regions between the (100) and (311) planes. The bottom transition was found to be smoothly curved, while the top transition between the (100) and (311) planes is abrupt (Bao et. al., 1998). It is clear from the above observations that the compensation pattern should be designed for both masked and the first stage of maskless etching. The compensation condition for a masked-maskless two stage convex etched corner is that the compensation pattern must not be used up when the maskless etching has reached the moment of $d = d_1$. So width of compensation structure is increased by $2d_1$ to prevent undercutting of both top and bottom convex corners. Figure 4.16 shows the corner compensation scheme which is required on all four corners of the central bossed structure in the reinforced diaphragm configuration (Enoksson et al., 1997). d refers to the maskless etching depth

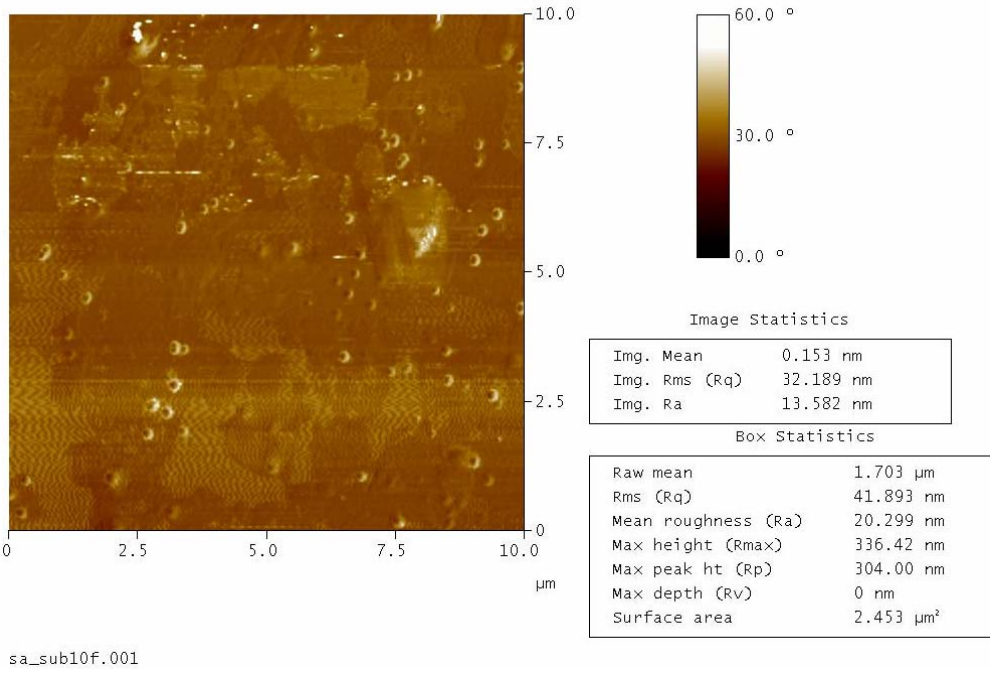

a

Figure 4.14 a) AFM surface map. Average roughness 32 nm. b) Surface profile of inner and outer diaphragm. Average roughness was less than 70 nm, after several line scans.

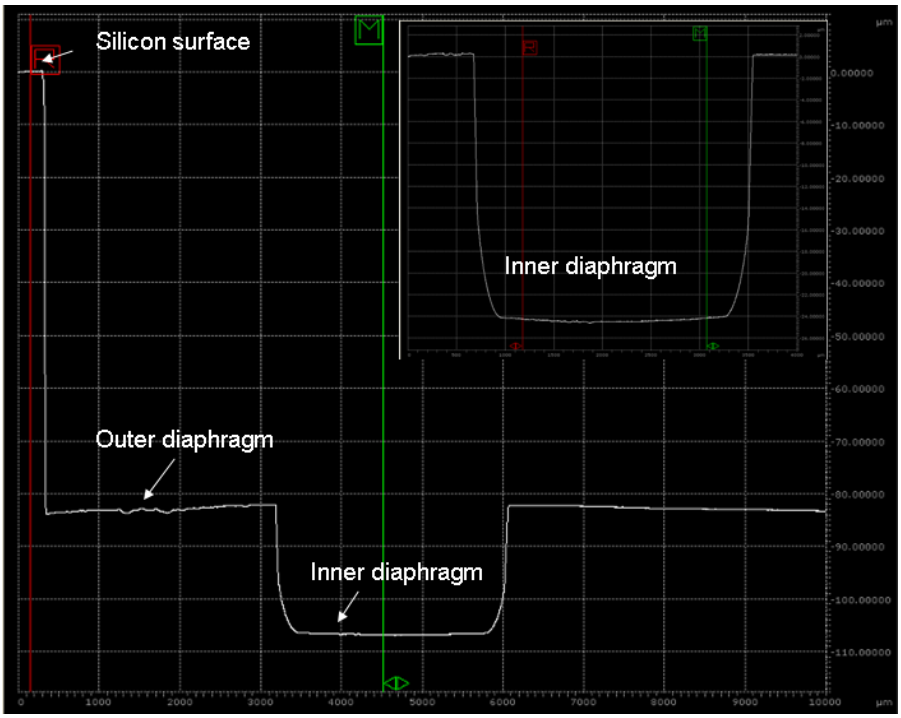

b

Figure 4.14 (continued)

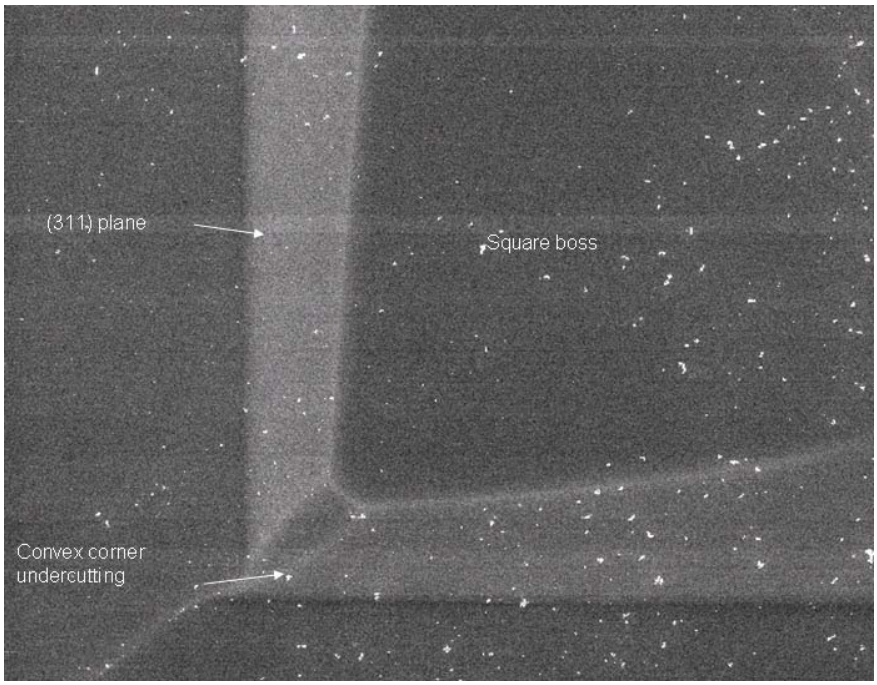

Figure 4.15 Image showing convex corner undercutting in Generation III devices.

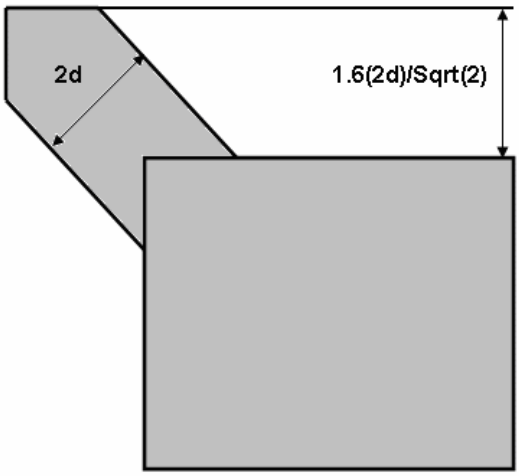

Figure 4.16 Corner compensation structure in Generation III sensors. d is the etching depth. Adapted from Enoksson et al., 1997.

Next, the behavior of concave corner during maskless etching process was considered. During masked etching process, it is known that no etching conditions influence the sharp concave corner shape. It is due to the orthogonal intersection of smooth {111} planes regardless of the etch depth or etch condition. This situation is changed in maskless etching process where the concave corner tends to round once it is not constrained by the top surface mask. Rounding occurs gradually as the lateral shrinkage increases and becomes severe, as shown in the figure 4.15. It has been reported that the rounding can be attributed to the lower accessibility of the etching species to the silicon concave corner surface and to the energy needed for breaking the backbonds of the silicon atoms to the underlying bulk at the concave corner position. According to Holke et al., 1999 the slowest etching planes govern the shape of the internal corners. Rounding not only occurs at the top (100) plane, but also vertically towards the bottom (100) planes with this showing almost isotropic behavior. Also, it has been shown that TMAH causes less concave corner rounding compared to KOH,

4.4 Packaging approach I

A two-level packaging approach was followed in this research. First, the zeroth or wafer-level package was developed to ensure a hermetic sealing followed by system-level package, which involves integration with printed circuit board on the top plane. Figure 4.18 illustrates the complete sensor/package integration scheme. The zeroth-level packaging started with etching of 10 μm cavity in 500 μm glass (Corning 7740 Pyrex) substrate. The dimensions of the glass cavity

were 3.5 x 3.5 mm^2. Glass etching was done using 10 μm AZ4620 as the masking layer and the etching solution was a mixture of HF/HNO_3/DI water (7:3:10). The etching rate was around 1.6 - 1.8 μm/min. Next, patterned glass substrate was aligned and anodically bonded to the silicon carrier, containing the reinforced pressure sensor die. Anodic bonding was either done under low pressures or at 1 atmospheric pressure (Figure 4.17). The two substrates are bonded at an elevated temperature of around 400-450 ˚C) by placing and clamping them between two metal electrodes. A high DC potential was applied between the glass substrate (cathode) that contains sodium ions and silicon carrier (anode). On application of high electric field, the sodium ions are displaced from the bonding surface, causing depletion near the surface. This caused an electrostatic force of attraction between the glass and silicon and they form a solid covalent chemical bond. Generally, one places the glass substrate on top of the Si wafer and pin-point contact to the uppermost surface of the glass piece which is held at constant negative bias with respect to the electrically grounded silicon. Looking through glass, the bonded region moves from the contact cathode point outward and can be detected visually though the glass, by disappearance of interference fringes. When the whole area displays a gray color, the bonding is completed. Bonding was done typically for 10-15 minutes depending on size of the substrate. For bonding, the chamber was pumped down to 0.1 mTorr. This resulted in a glass cavity which was absolutely hermetic so that that the diaphragm deflection is consistently translated into the proportional electrical output.

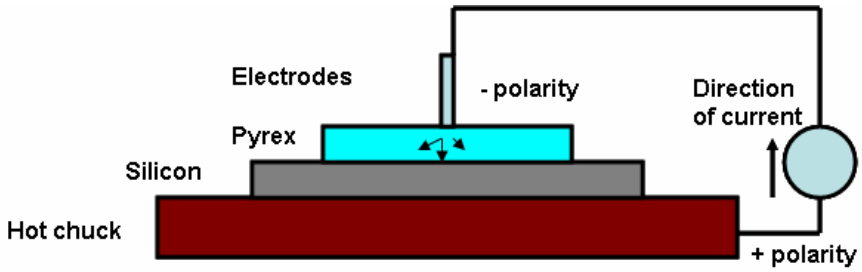

Figure 4.17 Illustration of anodic bonding process.

Now it can be observed from the process flow that metal interconnections have been routed outside the glass cavity in this scheme of packaging. The glass cavity bonded on the silicon carrier serves two purposes: 1) act as reference/absolute pressure chamber, 2) provides over-pressure protection for the diaphragms. Next, protective coatings were either deposited or spun-on on the exposed regions (backside of the diaphragms) to prevent bio-growth or bio-fouling. The list of protective coatings tested in actual marine conditions is discussed later in this chapter. This was followed epoxy bonding of bottom broad (either Plexiglas or FR-4) with

inlet/outlet opening onto the entire package. This process completes the zeroth-level package (figure 4.19). Next, two approaches were devised at this point: 1) Metal wires were directly epoxy glues onto the contact pads and testing was performed (Figure 4.20), or b) System-level packaging was accomplishes by integrating flexible circuit boards with signal conditioning microcontroller though the use of Anisotropic Conductive Film (ACF). Details on system-level process integration and signal conditioning microcontroller are presented later in this chapter.

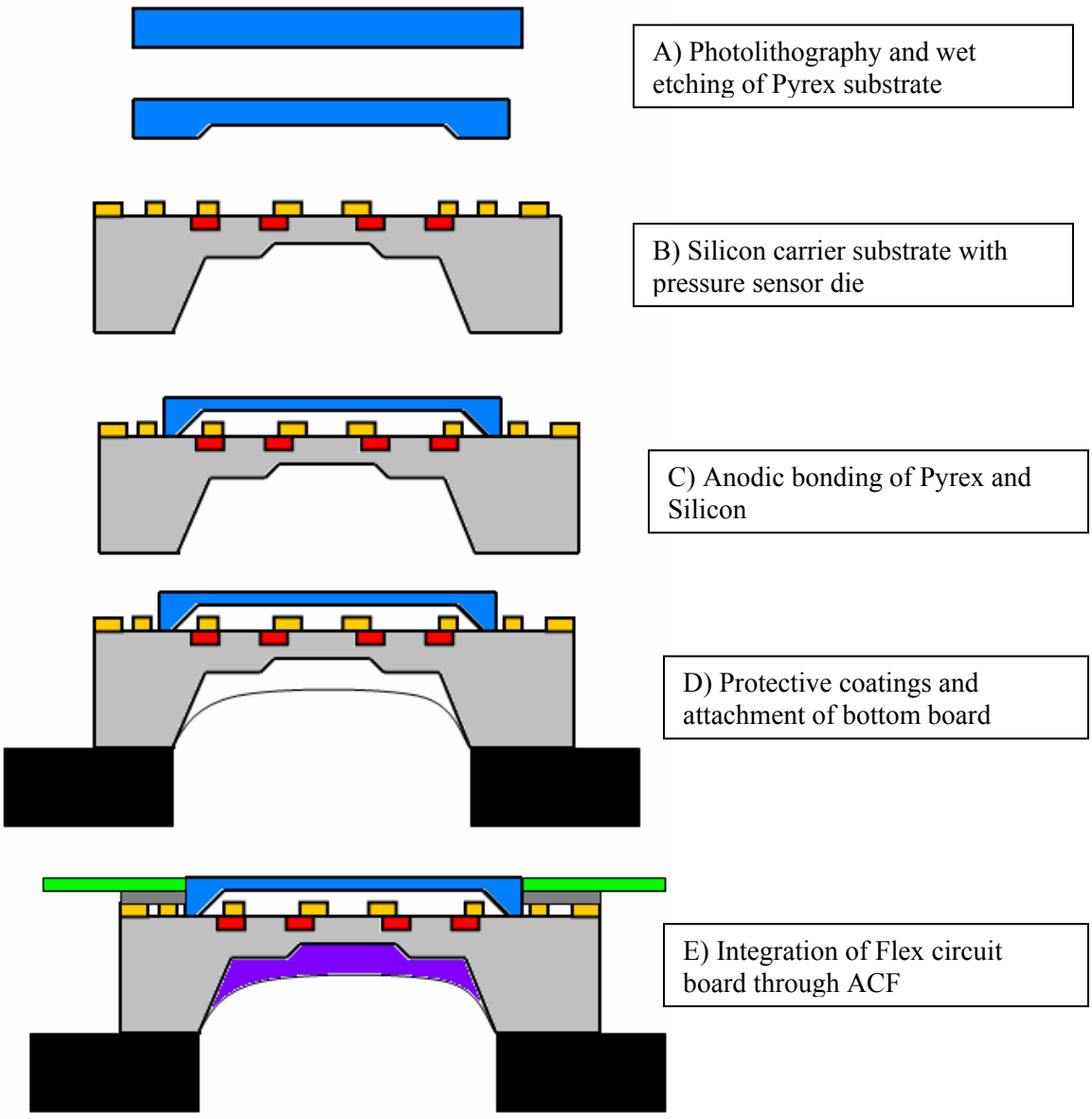

Figure 4.18 Illustration of the packaging I process flow.

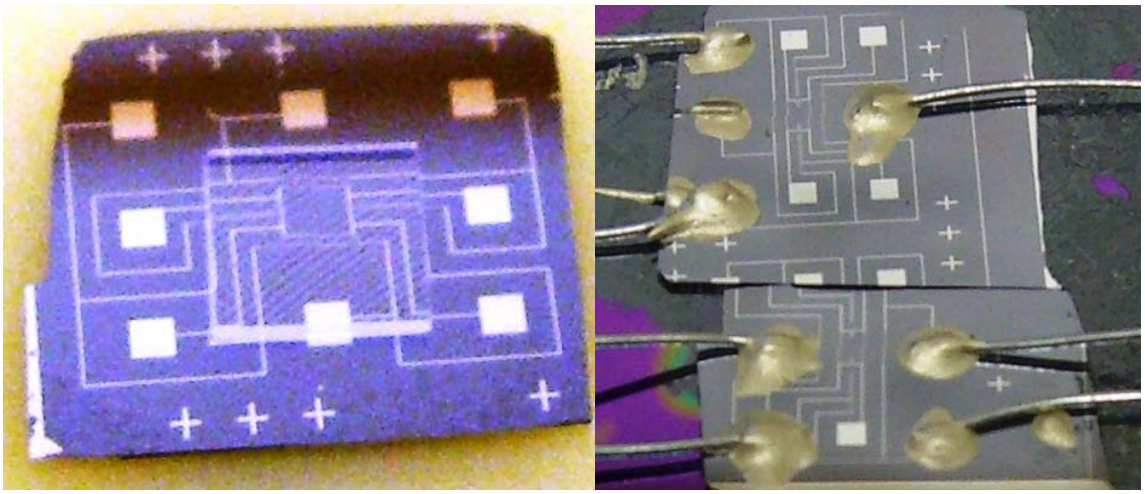

Figure 4.19 Image of a) zeroth-level package on pressure sensors, b) contacts through conductive epoxy.

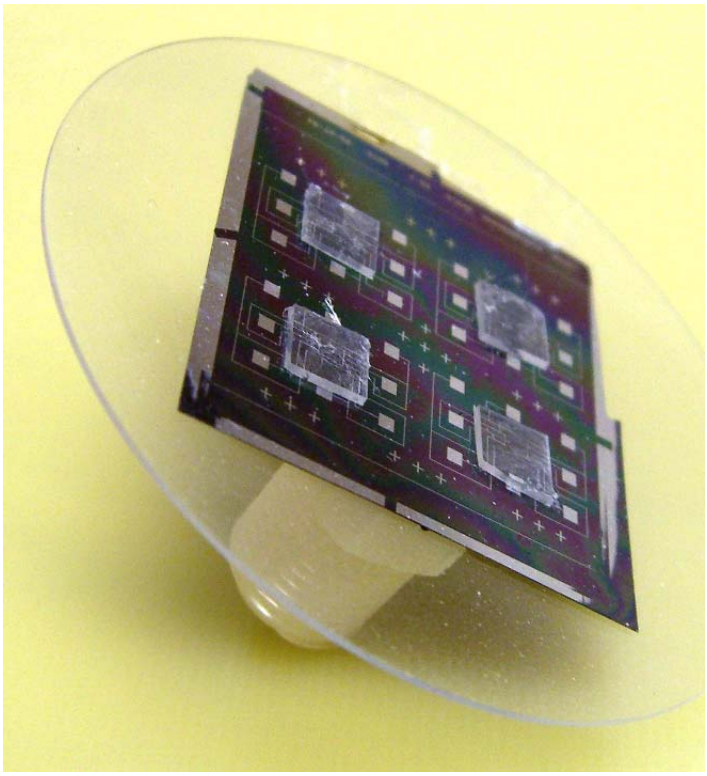

Figure 4.20 Image of system-level package (array of pressure sensors).

4.5 Packaging approach II

In this packaging scheme, as illustrated in figure 4.21, instead of routing the metal interconnections outside the reference pressure cavity, through-hole metal interconnections will be adopted. First, the 10 μm deep cavities were etched on 2" Pyrex wafers. Next, alignment markers (metal pads, similar to the bottom silicon wafer) were patterned onto these Pyrex wafers to accurately position the drill bits. Then, plated solid drill (Lnnzer, 0.040" OD and ¼"DL) was used to mechanically drill (using CNC machine) through holes on these metal pads on a water-cooled Pyrex wafer. After drilling hoes through Pyrex, the Pyrex and Silicon wafer were anodically bonded (similar to previous package), either under low pressures or at 1 atmospheric pressure. Next, conductive epoxy was filled into the holes that would eventually contact the bottom silicon metal pads and enable the routing of electrical signal lines. Then, the wafers were diced into individual dies in a K&S wafer dicing saw. Similar to the previous approach, protective coatings were either deposited or spun coated on the backside of the package. Then, finally, bottom boards (Plexiglas or FR-4) were attached by using a cold weld resin (Aliphatic Polyamine/Polyamide/Epoxy resin from J-B Weld company). This step completes the zeroth-level package (Figure 4.24). The system-level packaging was done similar to previous approach by attaching integrating printed circuit boards onto the zeroth-level packaged device.

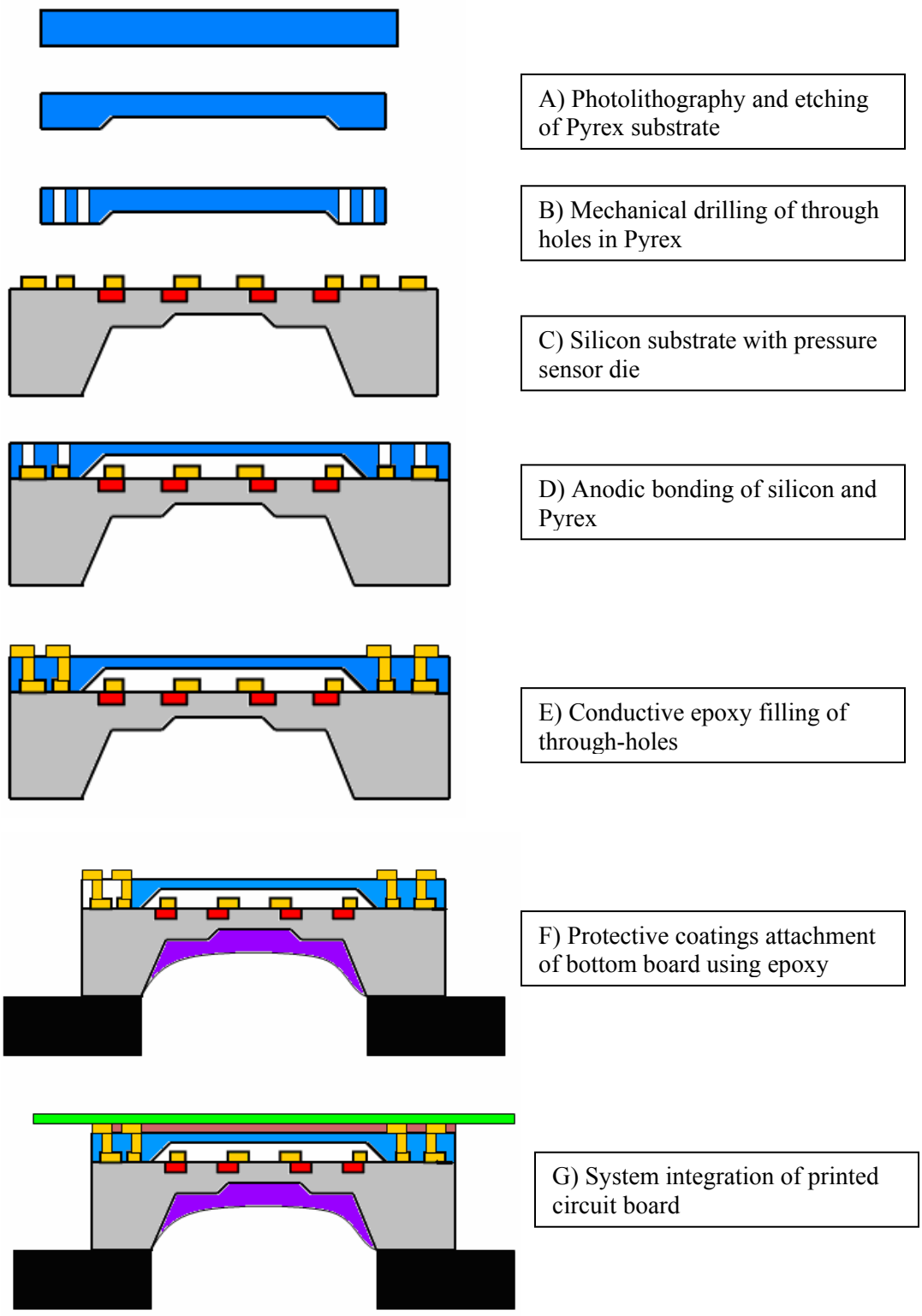

Figure 4.21 Illustration of packaging approach II process flow.

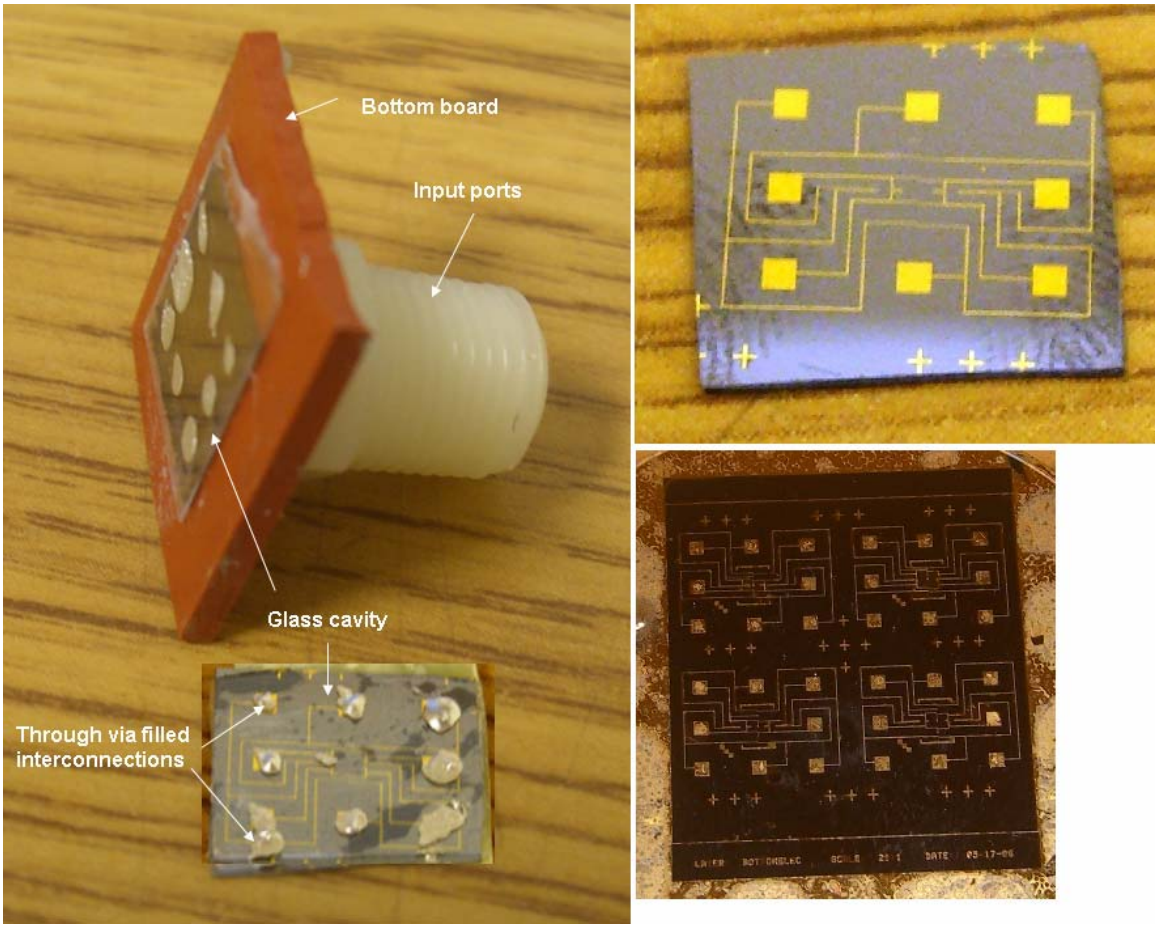

Figure 4.22 Images of pressure sensors packaged using approach II.

4.6 Description of packaging elements

4.6.1 Protective coatings

The critical challenge in any ocean sensor is how to minimize the effects of bio-fouling and long-term degradation to the sensor components. Bio-foulants can build-up on the sensor surface to cause both drift and reliability problems. In an effort to find a suitable film or coating to minimize this sensor degradation, we evaluate various materials for long-term reliability (1 week) in actual marine conditions (St. Petersburg harbor, FL). Different materials such as oxide, nitride, parylene-C, epoxy resin-SU-8, Lumiflon®, CYTOP®, BCB, and PDMS were evaluated in ocean conditions. The results of the measurement are presented in the next chapter.

4.6.2 Flip chip technology with anisotropic conductive films (ACF)

To address challenges in development of suitable packaging and interconnect strategies for MEMS and packaging of MEMS devices, an approach of chip scale or flip chip technology

with anisotropic conductive films (ACF) was proposed by Walsh et al., 2005. In this research, this ACF flip chip technology will be used for sensor chip-to-board assembly. The flip chip technology utilizing anisotropic conductive film (ACF) combines stable mechanical attachment, electrical connectivity and scaling/isolation in a single processing step. In general, flip chip technology is a highly-compact microelectronic assembly strategy involving direct electrical connection of 'flipped' chips onto patterned substrates by means of conductive bumps. It offers the ability to package a chip with dense connections in a very limited area. With ACF interconnections, electrical connectivity is provided through the conductive particles trapped between the corresponding bonding pads of the flipped device and bottom substrate when an appropriate combination of heat and pressure is applied. ACF material consists of a very stable adhesive polymer matrix containing polymer spheres of plated gold, silver or nickel-gold and then coated with a final insulating layer that protects them against shorting through contact with neighboring particles. During the bonding process, the applied pressure 'strips' off the insulating layer on the particles in only the *Z*-direction (normal to applied bonding force) while the applied temperature cures the epoxy. The cured epoxy provides mechanical attachment and immobilizes the deformed conductive particles, thus forming reliable electrical connections between the chip and the substrate. The electrical connection only occurs in the *Z*-direction, thus the name anisotropic conductive film (ACF).

As stated earlier, the ACF interconnects may be formed by the application of lower forces at moderate temperatures in comparison to thermosonic assembly where lot of heat, force and ultrasonic energy are applied to form Au-to-Au metallic bonds without any adhesives. ACF has the further advantage over other adhesive-based methods of requiring no underfill, even for very large die, thus eliminating the time-consuming and expensive step. Additionally, it offers others advantages such as extreme fine pitch capability (pitch: 50 μm), lead-free processing, low-temperature assembly (<190 ˚C), mechanical and thermal stability, low contact resistance (around 15 mΩ), and cost effectiveness. The bump that provides the electrical conduction from the ACF to the bonding pad of the chip also serves to produce enhanced compression in the z-direction, thermal conduction, maintains space between chip and substrate without shorting, and acts as a mechanical stress reliever in the flip chip assembly.

Anisotropic conductive films used in this work were obtained from Creative Materials Inc Model No. 121-24. 121-24 is a B-staged, anisotropically conductive, epoxy adhesive film

with silver/polymer particles of size around 20 μm. The process starts with the formation of Au stud bumps on the sensor chip contact pads using a wire bonder (figure 4.24). This coining process was performed using flip chip bonder at room temperature and under 10 N force, to achieve flat Au bumps for better contact and higher surface area. Then, ACF were cut into appropriate sizes and laminated onto the flexible printed circuit board, where the sensor chip will be flip chip bonded. A typical example of wafer-level package integrated to flexible circuit board using ACF is shown in figure 4.23. Similar, integration will be implemented with signal conditioning unit ZMD31050 in future (Chapter 8). The procedure for ACF flip chip assembly includes several steps: (1) ACF placement and lamination onto the circuit board, (2) alignment of circuit board and sensor chip, (3) pre-bonding to avoid misalignment, (4) final bonding with heat and pressure, thus forming electrical interconnections between board and sensor chip. Alignment and bonding was performed on a Finetech Flip Chip bonder with 2N of applied pressure and a temperature of 175 ˚C for 30 minutes.

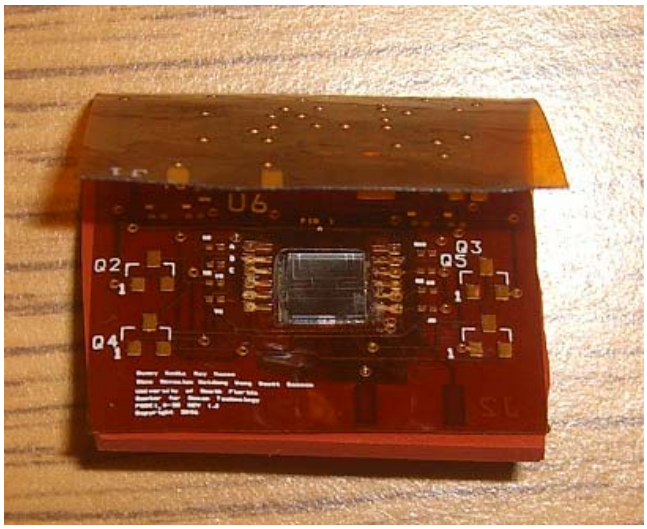

Figure 4.23 Typical system-level package with ACF and flexible circuit board.

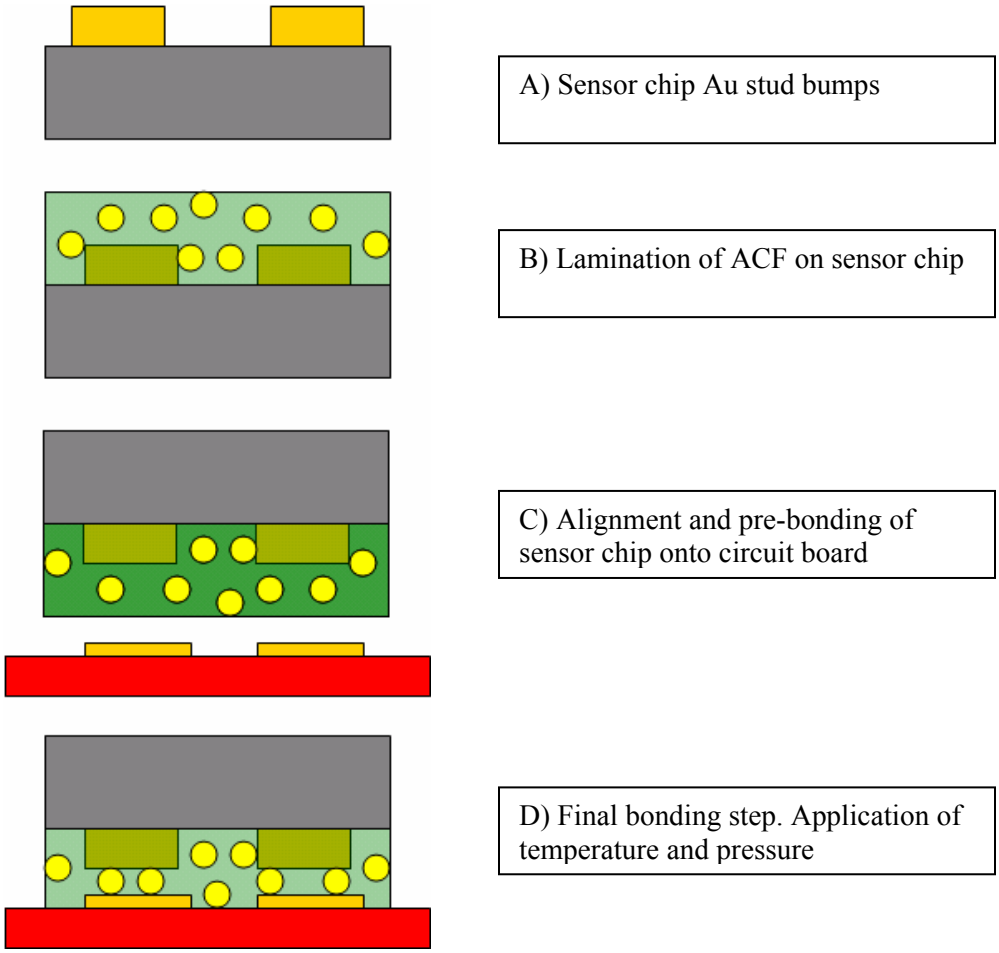

Figure 4.24 Process flow for bonding sensing chip with flexible electronics using ACF.

4.7 Summary

In summary, this chapter described the fabrication process and packaging approaches used to develop the three generations of reinforced pressure sensors. Generation II pressure sensors accounted for the masked-maskless etching process at stage of mask design, unlike Generation I sensors. Generation III sensors added an additional central bossed structure to the Generation II design. On the packaging side, two approaches were followed for both zeroth and system-level integration. The system-level package was implemented using the flip chip technology with anisotropic conductive film for integrating the sensor chip and flexible circuit board. The long-term goal of the system-level package was to develop an all integrated remotely deployable pressure transducer with electronics, on-board calibration and protective housing for ocean deployment.

CHAPTER 5

PERFORMANCE OF REINFORCED DIAPHRAGM PRESSURE SENSORS

5.1 Overview

This chapter analyzes the experimental results of the reinforced diaphragm pressure sensors fabricated in the manner described in the last chapter. Broadly, the experimental results have been divided into: a) Performance of Generation I devices, b) Effect of temperature sensitive bridge, c) Package analysis, d) Performance of Generation II devices (accounting for masked-maskless etching process), e) Performance of Generation III devices (with central boss). Also, in certain cases, the experimental results have been compared with the (simulation) modeling results to accurately predict the sensor behavior.

5.2 Generation I: results and discussion

This section presents the experimental results obtained with the Generation I pressure sensors. Firstly, the maximum burst pressure or high pressure package testing was performed on these devices, compared with the conventional single diaphragm configuration.

5.2.1 Maximum burst pressure and sensor calibration testing

The Generation I sensors were tested in a special pressure chamber filled with sea water, shown in figure 5.1. The chamber was pumped up to pressures of 1000 psi. The testing was performed in three stages: 200 psi (141 m of water), 500 psi (351 m of water) and 1000 psi (703 m of water) for about 10 minutes each. The tests were performed to both evaluate the burst pressure capability and also the mechanical integrity of the package. Table 5.1 summarizes the maximum operating pressure capability for the different sensor designs. In summary, the maximum operating pressure range of reinforced diaphragm (D3) was more than two times than that of single design (S1). Both designs had same inner or single diaphragm dimensions. These results compare well with the simulation results on peak stresses, which were about 2-2.2 times lower in the reinforced diaphragm configuration. The integrity of package was evaluated by

inspecting under a high magnification optical microscope. The optical images showed no traces of water inside the package or degradation to the bonding interfaces. Pressures up to 200 psi were generated from gas cylinder connected to the test rig. Later, to simulate water pressure conditions, tests were conducted by mounting the sensor test rig on a water filled chamber, pumped by a pressure pump. The voltage excitation to the wheatstone bridge was the range of 4.5-6 V, along with the measurement of output voltage. The input pressure was determined by connecting a high resolution reference pressure transducer (from GE Druck sensing) across the input line.

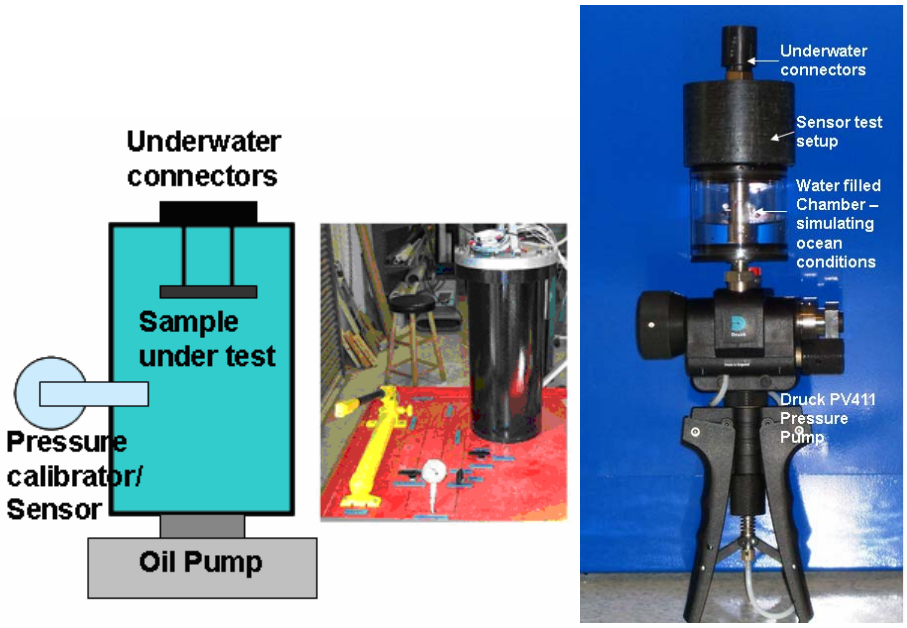

Figure 5.1 Custom-built pressure chamber to simulate ocean conditions (left), sensor testing setup: pressure pump, water chamber and test rig (right).

Table 5.1 Summary of maximum burst pressure for different sensor designs.

Sensor	Inner (L/H in µm)	Outer (L/H in µm)	Maximum burst pressure (psi)
D1	2000/10	3000/30	200-500
D2	1000/13	2000/36	>1000
D3	1500/30	2000/45	500-1000
D4	1000/20	2000/45	200-500
S1	1500/30	-	< 200

5.2.2 Sensitivity analysis of single diaphragm configuration

First, two configurations of single diaphragm sensors were tested to obtain the baseline response. Sensor S1 was designed as a square diaphragm of length 1500 µm and thickness 30 µm and sensor S2 consists of a diaphragm of length 2000 µm and length 10 µm. Figure 5.2 shows the linear output voltage response of S1 and S2 up to an input pressure of 100 psi. Sensor S2 was more sensitive (higher slope) compared to S1; because of much higher length/thickness ratio (stress varies as square of diaphragm length/thickness ratio).

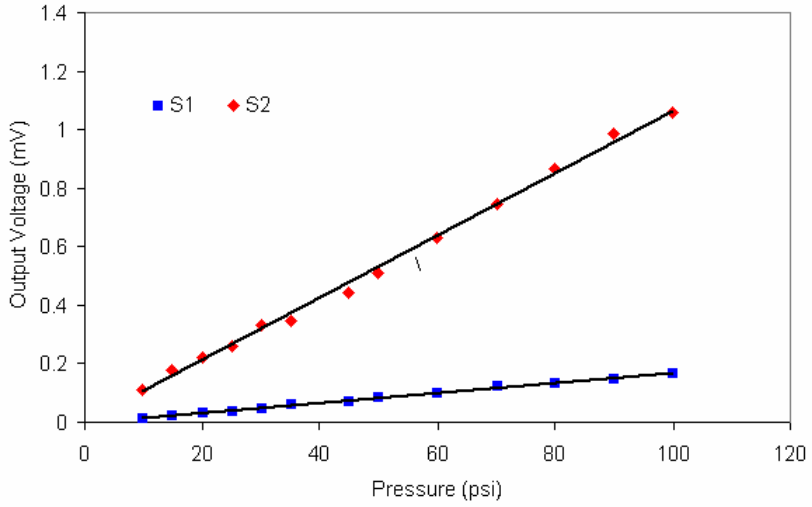

Figure 5.2 Variation of output voltage to input pressure for single diaphragms (S1, S2).

5.2.3 Sensitivity analysis of reinforced diaphragm configuration

Next, two configurations of two-element reinforced diaphragm pressure sensors were tested. Sensor D1 was designed with a square inner diaphragm of length 2000 µm and thickness 10 µm and outer supporting diaphragm of length 3000 µm and thickness 30 µm. Sensor D2 consisted of inner diaphragm of length 1000 µm, thickness 13 µm and outer rim of length 2000 µm and thickness 36 µm. In both sensor configurations, the temperature compensating bridge was placed at 4000 µm from the center (away from the stressed regions). Figure 5.3 shows the linear output voltage response for Sensor D1 versus input pressure up to 120 psi for the inner diaphragm and up to 190 psi for the outer diaphragm. It is evident that the inner diaphragm is more sensitive compared to the outer diaphragm. However, in either case, the obtained voltage output is a differential signal from the sensing bridge (inner/outer) and temperature compensation bridge. Similarly, figure 5.4 plots the output voltage response for sensor D2 versus the input pressure up to 300 psi.

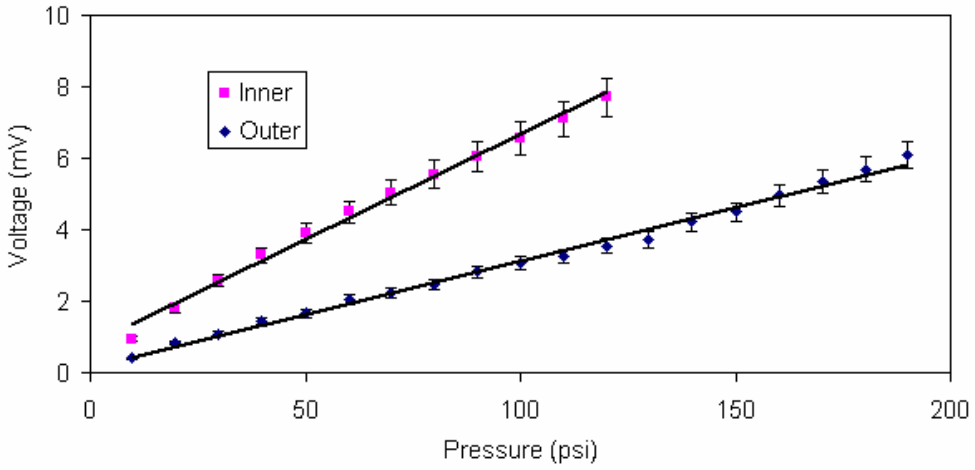

Figure 5.3 Variation of output response to input pressure variations for sensor D1.

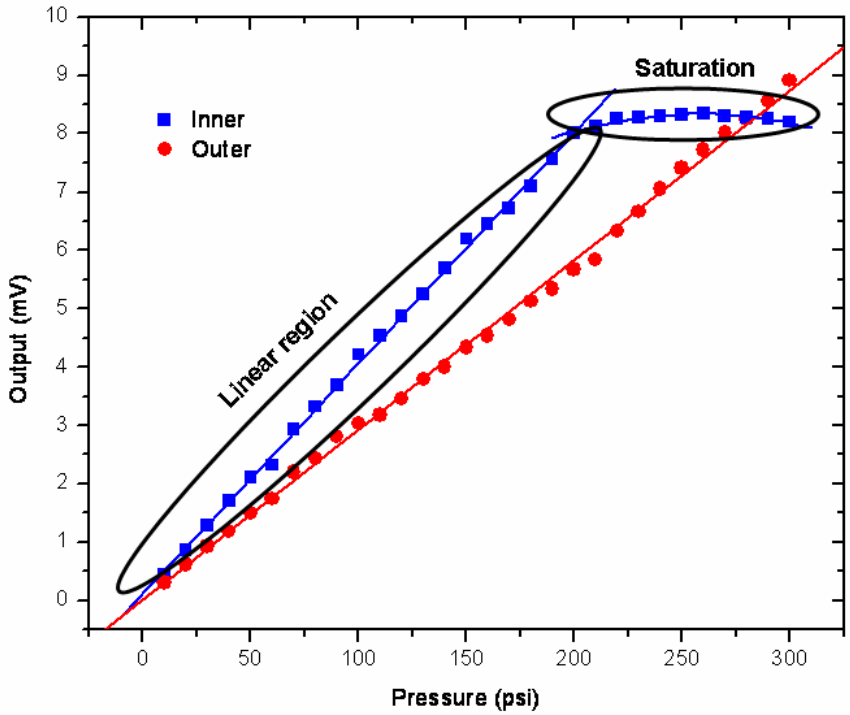

Figure 5.4 Variation of output response to input pressure variations for sensor D2.

It is evident that both inner and outer diaphragm respond quasi-linearly (up to 200 psi in case of D2 inner) to pressure variations, with sensitivity between 0.03-0.059 mV/psi for the different configurations. The pressure hysteresis was within ±6% of the measured output for 3 cycles. The output variation may be mainly due to source pressure and process variations, along with initial diaphragm creep. In the case of inner bridge in Sensor D2, beyond 200 psi, the output

voltage entered the saturation or large deflection regime. At this pressure (called as the transition pressure for D2), the inner thin diaphragm reaches a state of dominant tensile stress. In this state, the inner diaphragm can support larger pressures, without breaking. The transition can be thus, explained as the stress in the piezos passing from compressed (bending) stress state to dominant tensile stress. The signal from the outer bridge was increasing monotonically throughout this pressure range (up to 300 psi),

Next, we compare the experimental sensitivities for the conventional single (S1 and S2) and the reinforced (double) diaphragm pressure sensors (Figure 5.5). In the first case, the ratio of outer to inner was 2. The dimensions of the single diaphragm and inner diaphragm of the reinforced design were both 1500 µm in length and 20 µm thick (actual dimensions were 1-2 µm thicker). However, we find that the reinforced configuration (with smooth transition regions) was about 5-10% more sensitive than the (sharp) single diaphragm configuration of the same dimensions (Figure 5.5). However, as stated in the design chapter, for most effective stress transfer from the inner to the outer diaphragm, the ratio of outer to inner diaphragm thickness was found to be greater than 3. So, in the next case, the reinforced sensor D1 (ratio >3) was compared with conventional single diaphragm (S2) of length 2000 µm and thickness 10 µm (Figure 5.6). The reinforced diaphragm design was found to be about 20-22% more sensitive (from slope) compared to the single diaphragm design for the same pressure range. Therefore, it may be concluded that by using the reinforced configuration, even higher sensitivity (by further diaphragm thinning) can be achieved without compromising on the operating range.

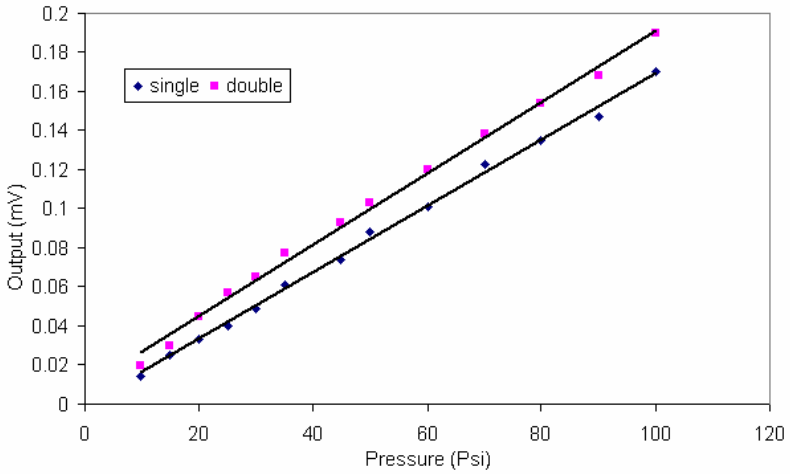

Figure 5.5 Comparison of output response to input pressure variations for single and reinforced sensors (ratio of outer/inner less than 3).

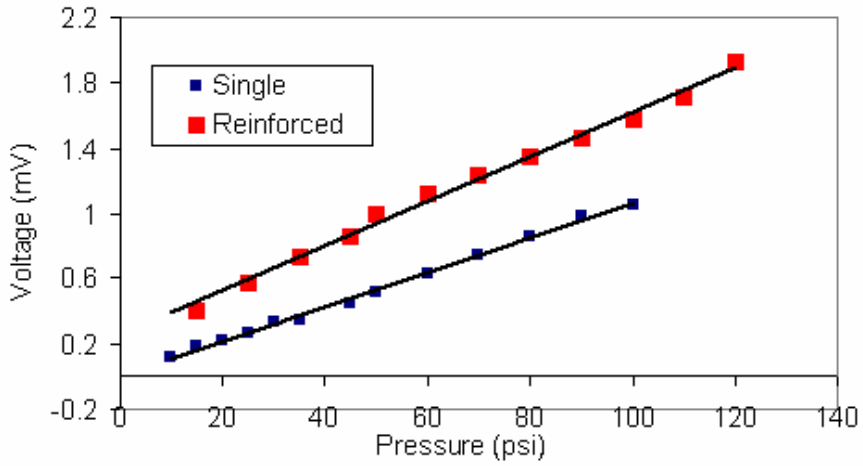

Figure 5.6 Comparison of output response to input pressure variations for single and reinforced sensors (ratio of outer/inner greater than 3).

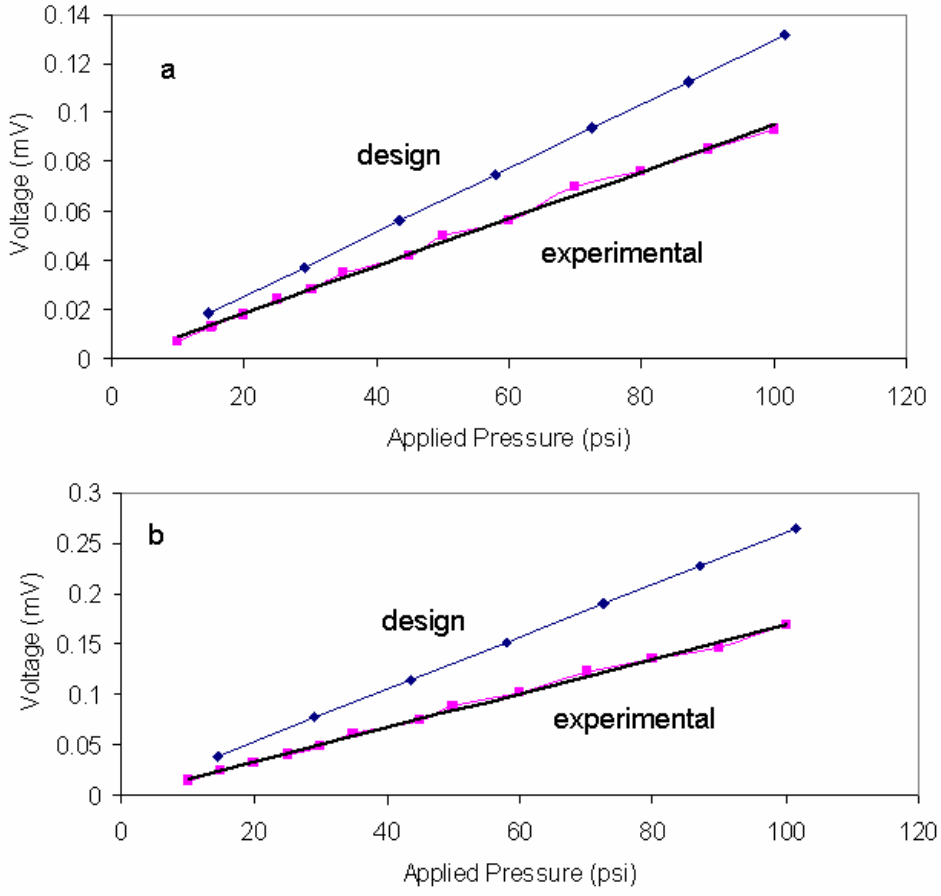

Figure 5.7 Comparison of design and experimental (same dimensions) output response a) sensor D3, b) sensor D4.

5.2.4 Comparison of experimental and simulation results

Figure 5.7 a and b show the comparison between the simulated and experiments (from designed dimensions) results for the two sensor configurations. Sensor D3 consists of a square inner diaphragm of: length 1000 µm and thickness 20 µm (design). While, sensor D4 consists of inner diaphragm of length 1500 µm, thickness 30 µm (design). The dimensions of the outer diaphragm in both cases were 2000 µm in length and 45 µm thick (design). The experimental output response is 25-50% lower than that of simulation/designed specifications. Even though, the experimental data fits well with the simulation trend, the discrepancy mainly arises due to variations in pressure sensor fabrication (difference in actual and designed diaphragm dimensions, smoothing of inner diaphragm edges during bulk etching (masked-maskless etching process), misalignment in placement of piezoresistors from the diaphragm edge, effect of diaphragm residual stress from ion-implantation process, and averaging of stress and piezoresistance values. Re-simulation or modeling taking in account these actual dimensions was then performed to confirm the measured sensitivity loss.

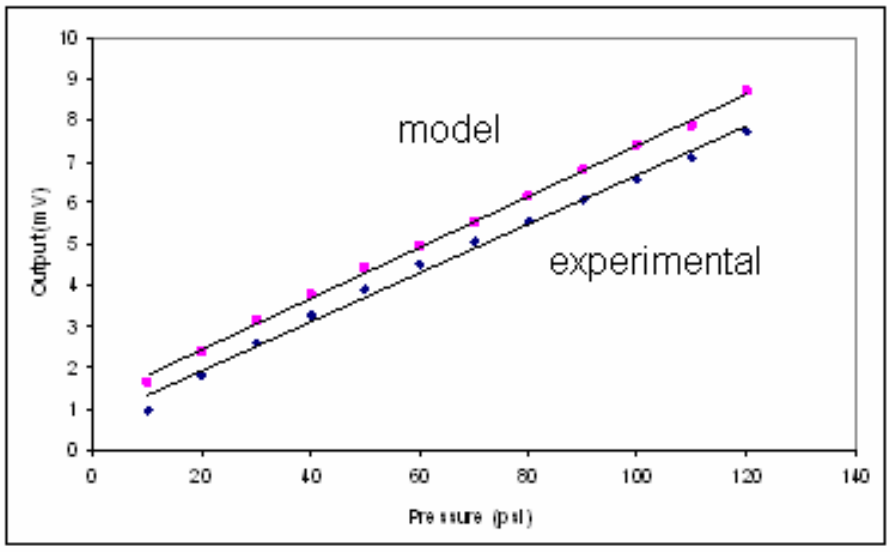

Figure 5.8 Comparison of experimental results with re-simulated (model) data accounting for process variations.

Modeling or re-simulation was performed using the experimental data (from Sensor D1). Figure 5.8 shows the modeled data matched (within 5-10%) against the inner diaphragm results from Sensor D1 (Figure 5.8). The model incorporated a) 1.3 µm thicker inner diaphragm and 2.4 µm thicker outer diaphragm with same length dimensions (profilometer measurements as first

approximation), b) 25.24 ˚ as the sidewall angle between (311) and (100) plane, c) piezoresistor averaging effects due to finite resistor dimensions (20% lower effective resistances), d) front-to-back misalignment in piezoresistors (up to 4 µm), e) skew of up to 5º. The effect of diaphragm residual stress was not taken into account. Figure 5.9 shows the modeled data (within 5%) compared to the experimental results from inner bridge of Sensor D1 by accounting for residual stress in the small deflection regime. The diaphragm residual stress was assumed to be about 50 MPa (from literature) due to the energetic ion-implantation and diffusion process. The rest of the disagreement could be due to process variations.

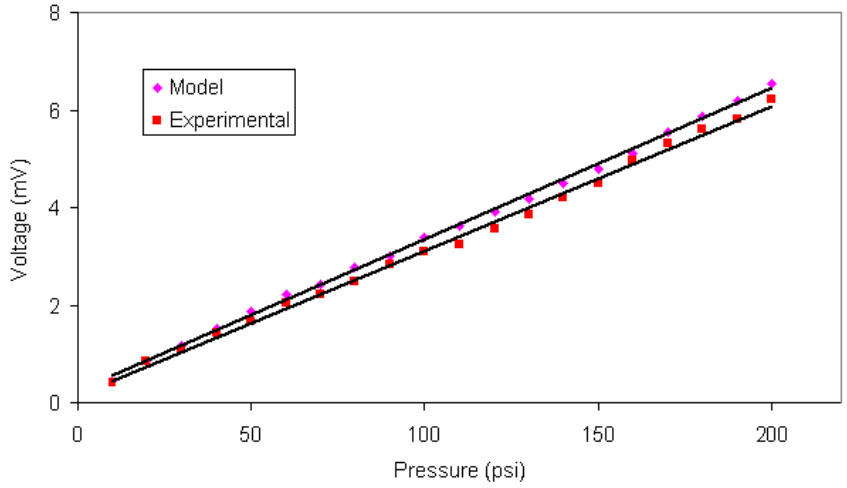

Figure 5.9 Comparison of experimental results with re-simulated (model) data accounting for process variations and residual stress on diaphragm.

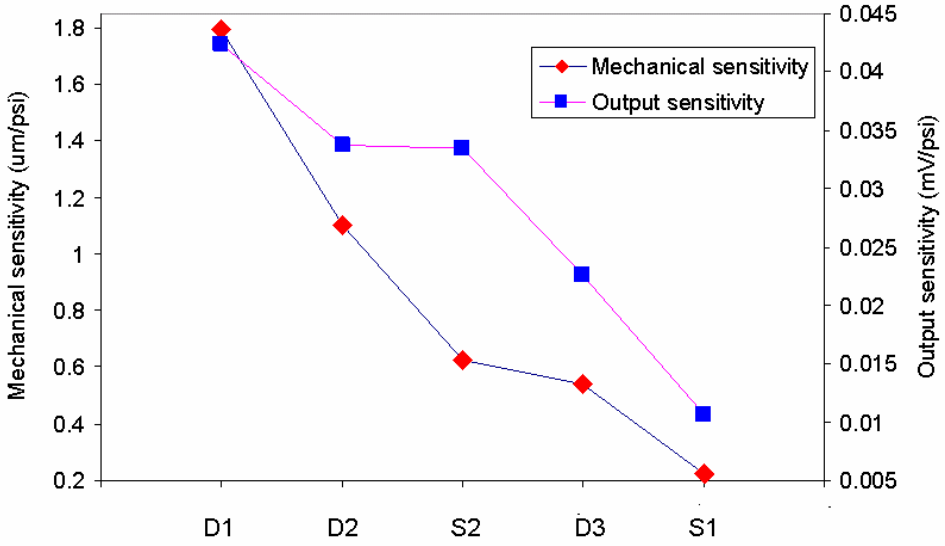

Figure 5.10 Mechanical and output sensitivity for Generation I sensors.

5.2.5 Mechanical and output sensitivity

Figure 5.9 summarizes the Generation I reinforced diaphragm pressure sensor configurations in terms of output and mechanical sensitivities. These results were obtained from re-simulation, after accounting for experimental dimensions variations from fabrication process The mechanical sensitivity S_m was obtained by measuring the central deflection of the inner diaphragm under a known applied pressure. It can be seen that even in case of Sensor D3 and S1, (same dimensions - inner and single), the reinforced diaphragm design has higher mechanical and output sensitivity compared to the conventional single diaphragm design due to the reinforced edge structure. Further, sensors D1 and D2 (with outer/inner thickness ratio greater 3) show even improved sensitivity and wider operating range because of better transfer of peak stresses.

5.3 Effect of temperature sensitive bridge

A third wheatstone bridge in the form of piezoresistors was embedded 4000 μm away from the outer sensing bridge to compensate for temperature variations and also act as a temperature sensor. Because the temperature bridge was placed near the pressure sensing bridges, similar temperature effects on piezoresistors (and no stress effects) will be encountered. By simply subtracting the outputs of pressure sensing bridge and temperature bridge, a reduction in offset and temperature drifts were realized. Figure 5.11 shows the piezoresistance values for variation in temperature. Even though, temperature sensitivity is not high (0.14 Ω/°C), this method reduces offset and temperature drift by more than 95% (Lee et al., 1995).

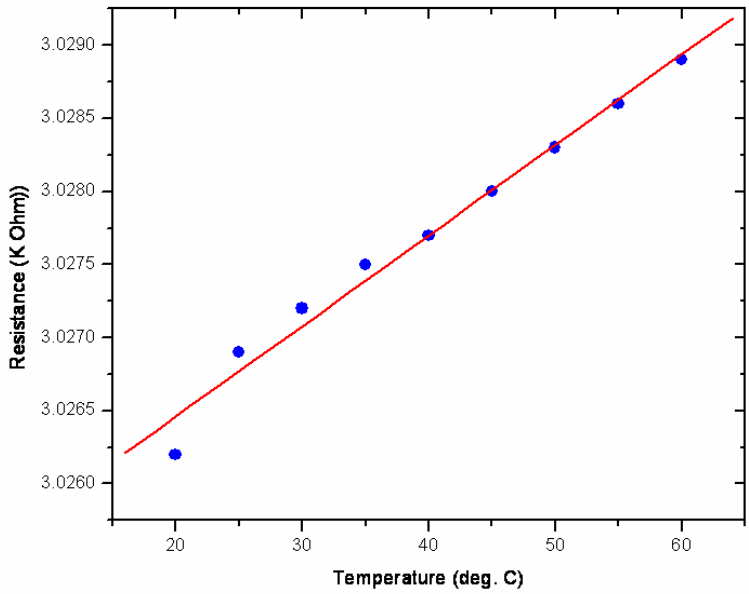

Figure 5.11 Variation of piezoresistance values for a temperature range.

5.4 Package and protective coatings analysis

As discussed earlier in this chapter, high pressure package testing was conducted in custom-built pressure chamber to evaluate the mechanical integrity and hermeticity of the package under stress. After exhaustive tests, the integrity of package was evaluated by inspecting under a high magnification optical microscope. The optical images showed no traces of water inside the package or degradation to the bonding interfaces. Next, the critical challenge in any ocean sensor is how to minimize the effects of bio-fouling and long-term degradation to the sensor components. Bio-foulants can build-up on the sensor surface to cause both drift and reliability problems. Therefore, the reliability of the protective coatings (Lumiflon®, SU-8, BCB, CYTOP®, Parylene, Oxide, and Nitride) was evaluated for one week in real ocean conditions at depth of 5 m (Center for Ocean Technology St. Petersburg harbor, FL). These tests were conducted both during winter (December) and summer (May) months to better understand the seasonal ocean conditions. Figure 5.12 shows the image of sensor surfaces coated with different protective coatings tested for a week in winter. Lumiflon® and SU-8 showed no/minimal effect on their mass (water uptake), delamination, de-coloration or bio-growth. Figure 5.13 shows images of similar experiments conducted for a week during summer. With summer being the period of greater bio-activity, all sensor surfaces showed some form of bio-growth (Figure 5.13).

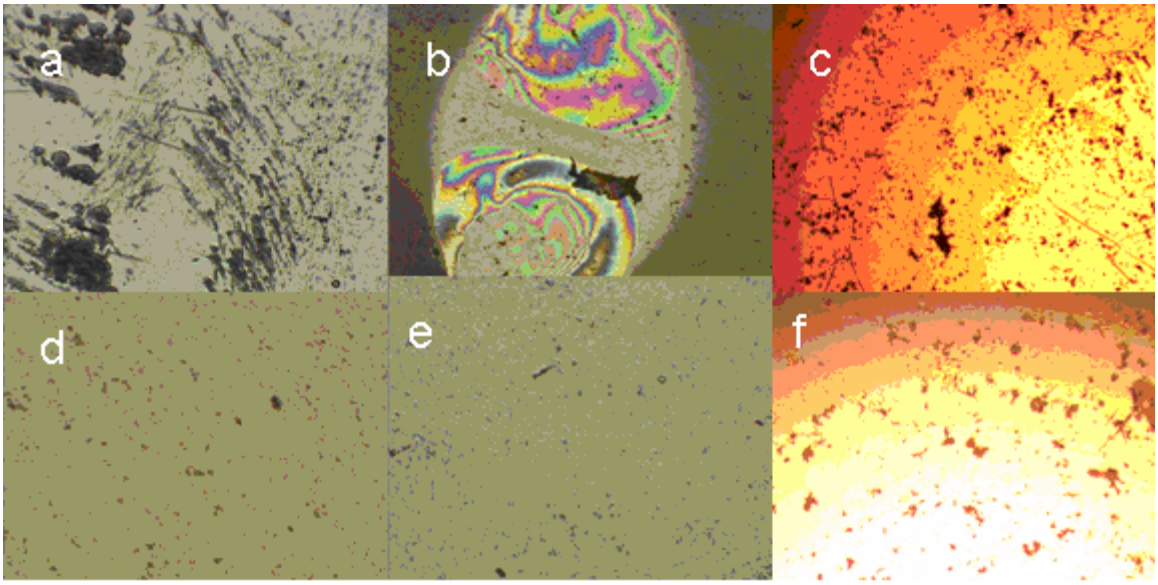

Figure 5.12 Images of sensor surface after exposure for one week in winter a) CYTOP®, b) BCB, c) oxide, d) SU-8 50, e) lumiflon®, f) nitride.

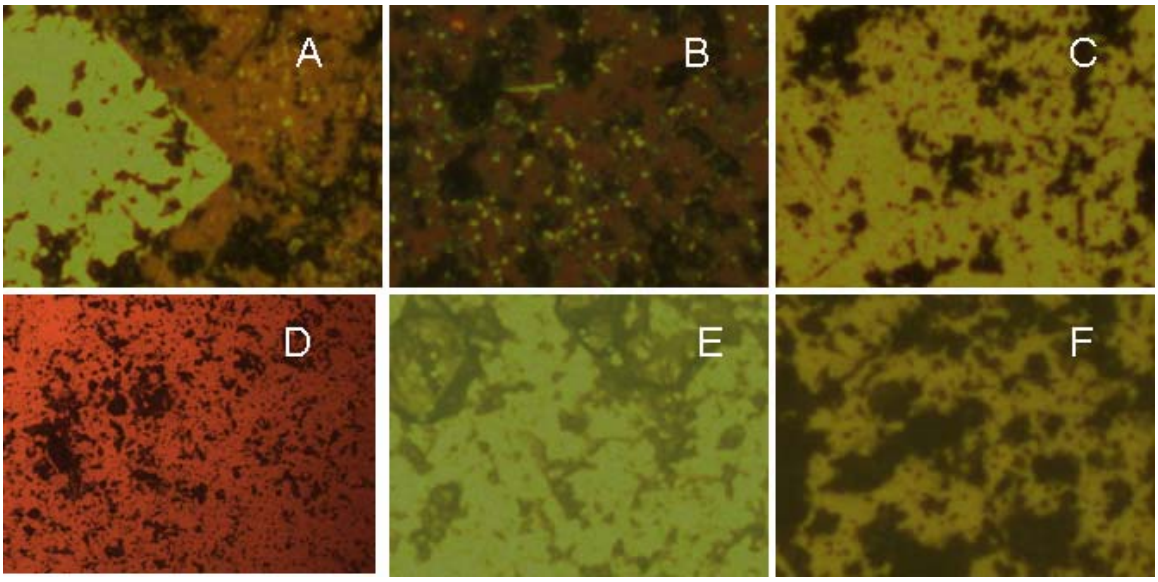

Figure 5.13 Images of sensor surface after exposure for one week in summer a) parylene, b) CYTOP®, c) lumiflon®, d) oxide, e) SU-8 50, f) nitride.

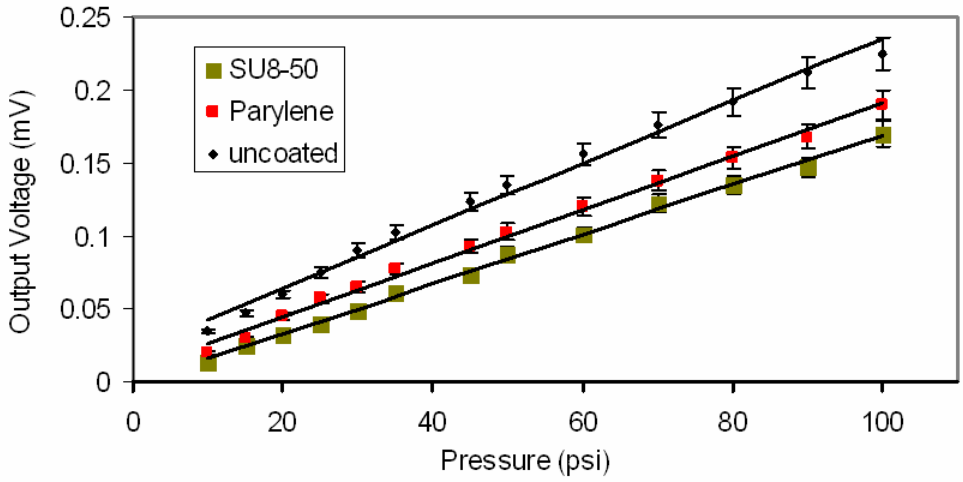

Figure 5.14 Effect of package and protective coatings on output voltage.

Next, the effect of package-induced stress and protective coatings on sensor response was evaluated. Figure 5.14 shows the voltage output response versus input pressure for packaged sensors coated with a) SU-8, b) Parylene, and c) uncoated or package. It is evident that package stresses and protective coatings, in all, reduced the output response by up to 34%. In particular, packaged device with parylene coating showed 16% lower output, while SU-8 coated packaged device showed 33.75% lower output sensitivity compared to uncoated devices of same diaphragm

dimensions (thickness and length). Modeling of packaged-induced stresses and effect of protective coatings will need to be performed in future.

5.5 Generation II: results and discussion

5.5.1 Overview

In the Generation II devices, the masked-maskless etching process was taken into account during the stage of mask design. Table 5.2 summarizes the initial and final Generation II designs after masked-maskless etching process.

Table 5.2 Summary of Generation II device dimensions (measured).

Sensor	Initial Inner (L/H in μm) (design)	Outer (L/H in μm) (design)	Measured d_0 (in μm)	Measured recession, l (in μm)	Final Inner (L/H in μm) (measured)
II-D5	500/15	3000/45	14	550	1505/15
II-D6	1000/10	4000/30	9.5	590	2090/10
II-D7	500/15	4000/45	12	550	1505/15
II-D8	400/15	4000/30	7	580	1520/15

Generation I devices didn't account for the recession distance, l and hence the increase in inner diaphragm length, which also meant decrease in the length of reinforcement edge. In the case of Generation I devices, because of the masked-maskless etching process, the size of the reinforcement edge was consumed by the fast lateral movement of (311) plane. Therefore, in the Generation II devices, care was taken during the mask design to retain an effective reinforcement edge (design chapter), even after the masked-maskless etching process. By accounting for such behavior, it was possible to design reinforced diaphragm devices (Generation II) with even wider operating range and higher sensitivity. The actual thicknesses of inner diaphragm were about 1-2 μm higher, while outer diaphragm was about 2 μm thicker.

5.5.2 Sensitivity analysis of Generation II sensors

As shown in table 5.2, three representative Generation II reinforced diaphragm pressure sensors, referred to as II-D5, II-D6, II-D7 were analyzed. Figure 5.15 shows the output response of II-D5 versus applied input pressure. The outer bridge exhibited a linear response up to 220 psi

with a sensitivity of 0.018 mV/V/psi. The response of the thin inner diaphragm can be broken into two parts: a) linear region up to 120 psi, with a sensitivity of 0.029 mV/V/psi, and b) saturation region, where the inner bridge is in a state of uniaxial tension. Further, the pressure hysteresis was within ±4-5% of the measured output.

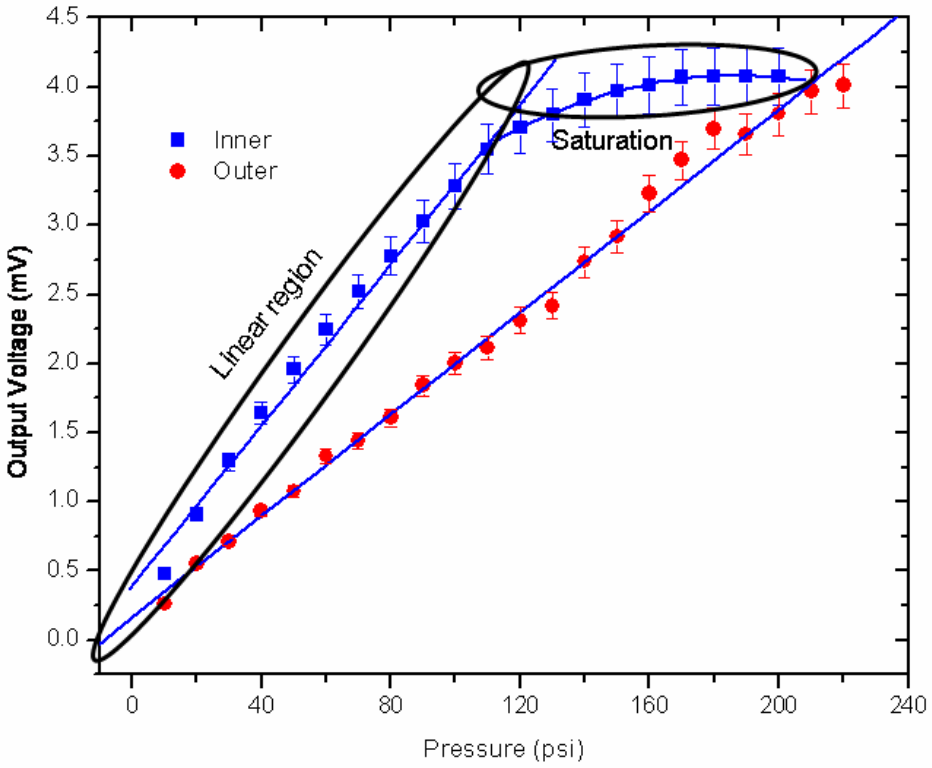

Figure 5.15 Variation of output response to input pressure variations for sensor II-D5.

Figure 5.16 shows the response of II-D6 versus input pressure. As in the case of II-D5, the outer bridge exhibited a quasi-linear response up to 350 psi, with a sensitivity of 0.044 mV/V/psi. While, the inner bridge exhibited two regions: a) linear region up to 260 psi, with a high sensitivity of 0.067 mV/V/psi, and b) saturation region up to 350 psi. It is worth noting that even though the inner diaphragm is inoperable after 260 psi, it doesn't break or buckle because of transfer of peak stresses to the outer diaphragm after the transition point.

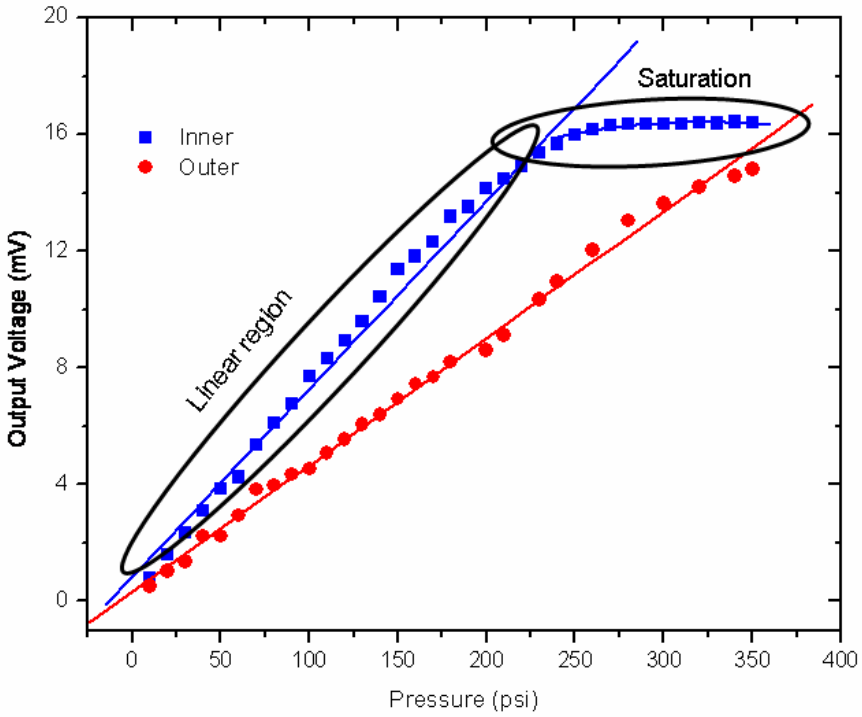

Figure 5.16 Variation of output response to input pressure variations for sensor II-D6.

Figure 5.17 shows the output response versus input pressure for II-D7 devices. The outer bridge exhibited a linear response up to the maximum measured pressure of 440 psi (310 m of water), with a sensitivity of 0.012 mV/V/psi. The thin diaphragm similarly had two distinct regions: a) linear region up to 160 psi, with sensitivity of 0.023 mV/V/psi, and b) a saturation region beyond the transition point, where the diaphragm was in a state of tension. Further, the pressure hysteresis for the inner diaphragm was ±4-5% of the measured output, while the output bridge showed large hysteresis up to ±7%, probably due to source pressure, process or piezoresistance variations along with in-built diaphragm creep effects.

Figure 5.18 and 5.19 summarizes the Generation II devices showing the 3D plot for sensitivity and inner diaphragm transition point with respect to the reinforced (outer) edge length and thickness. From these plots, we can draw the following conclusions:

(1) Effect of inner diaphragm length and thickness: As shown earlier (design chapter), stress varies as square of diaphragm length to diaphragm thickness. Therefore, sensor II-D6

showed maximum output sensitivity, while other inner diaphragms with the same ratio of length to thickness (1505/15), further depended on the dimensions of the outer diaphragm.

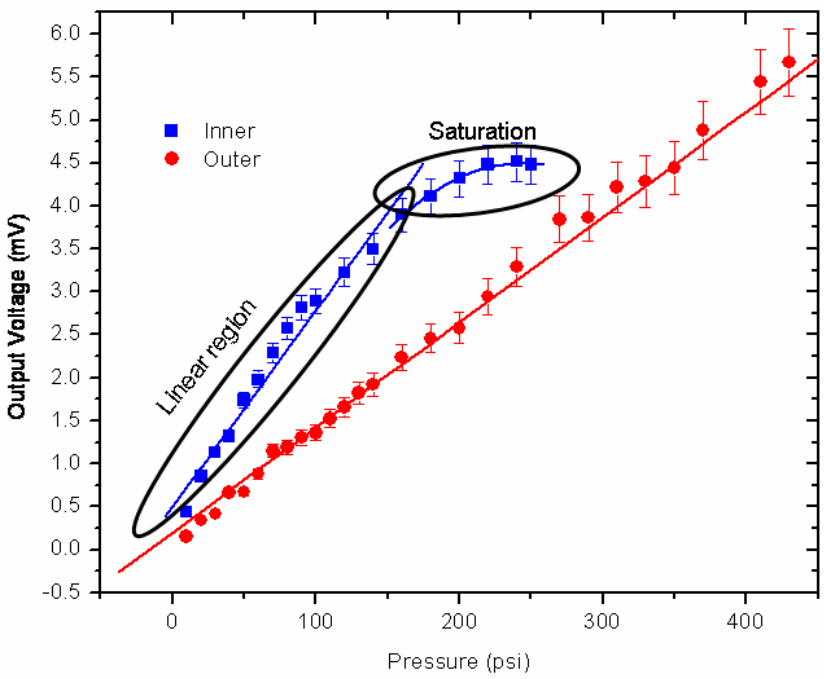

Figure 5.17 Variation of output response to input pressure variations for sensor II-D7.

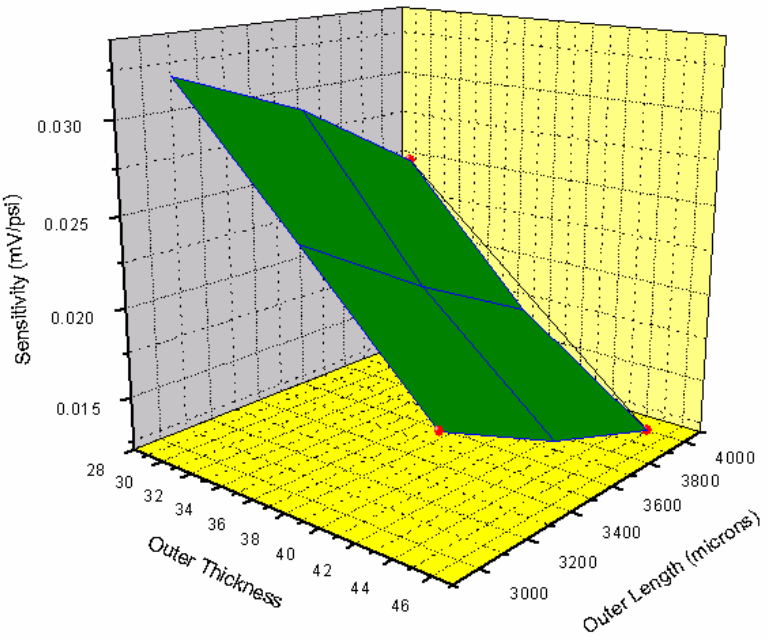

Figure 5.18 3D plot of variation of outer bridge sensitivity to outer diaphragm dimensions for constant inner dimensions.

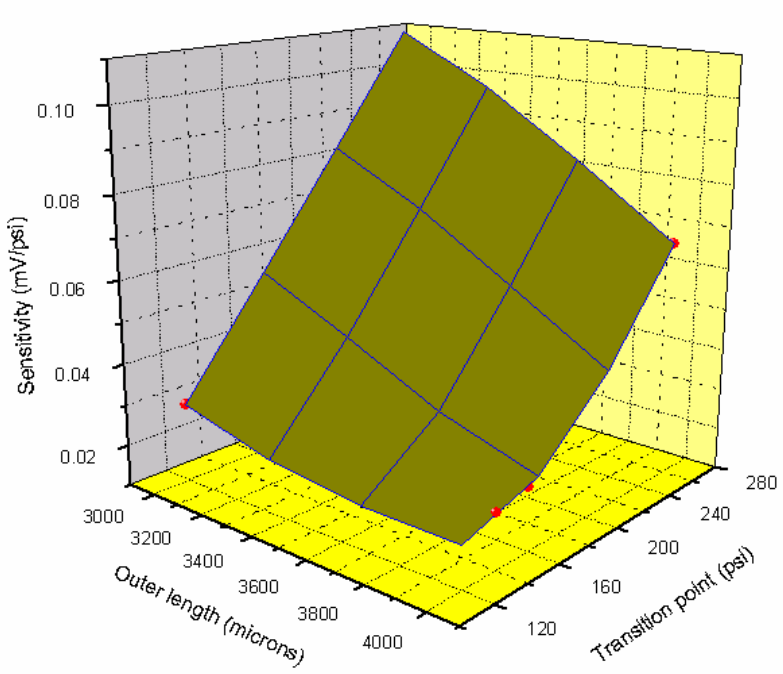

Figure 5.19 3D plot of variation of inner bridge sensitivity and transition point to outer diaphragm length.

(2) Effect of reinforced edge thickness: It can be seen that outer diaphragms with same length and different thicknesses, affected both outer bridge sensitivity and inner bridge transition point. Outer diaphragms of lower thickness deflected more easily and hence had higher sensitivity. In case of the transition point, however, lower outer thickness caused lower transition point as inner diaphragm reached large deflection regime much earlier. The other contributing factor was the inner diaphragm dimensions, sensor II-D6 with outer dimensions (4000/30) and inner dimensions (2090/10) had higher sensitivity, higher transition point and wide range compared to II-D8 with outer (4000/30) and inner (1520/15).

(3) Effect of reinforced edge length: Diaphragm with shorter reinforced edge length showed lower sensitivity and lower transition point compared to other designs. This may be mainly because of higher stiffness to deflection and ineffective transfer of peak stresses. Table 5.3 summarizes sensitivities and transition pressure points for the different diaphragm configurations.

Table 5.3 Summary of experimental results for Generation II devices.

Sensor	Inner (L/H in µm)	Inner sensitivity (mV/V/psi)	Transition point (psi)	Outer (L/H in µm)	Outer sensitivity (mV/V/psi)
II-D5	1505/15	0.029	120	3000/45	0.018
II-D6	2090/10	0.067	260	4000/30	0.044
II-D7	1505/15	0.023	160	4000/45	0.012
II-D8	1520/15	0.025	140	4000/30	0.025

5.5.3 Comparison of Generation I and Generation II sensors

Next, the experimental output response and sensitivity of Generation I (D2) and II (D6) devices of comparable diaphragm dimensions were plotted (Generation II: 2090/10±1 µm, Generation I: 1000/13, changed to 2000/13±1 µm, due to masked-maskless etching). From figure 5.20, by accounting for the masked-maskless process and recession length, Generation Ii sensors showed much improved sensitivity and wider linear operating range. The sensitivity was improved from 0.037 mV/V/psi to 0.067 mV/V/psi and the linear range from 200 psi to 260 psi, even though the inner diaphragm is thinner than the Generation I device. It should be noted that thinner diaphragms exhibit non-linear behavior at lower pressure compared to thicker diaphragms.

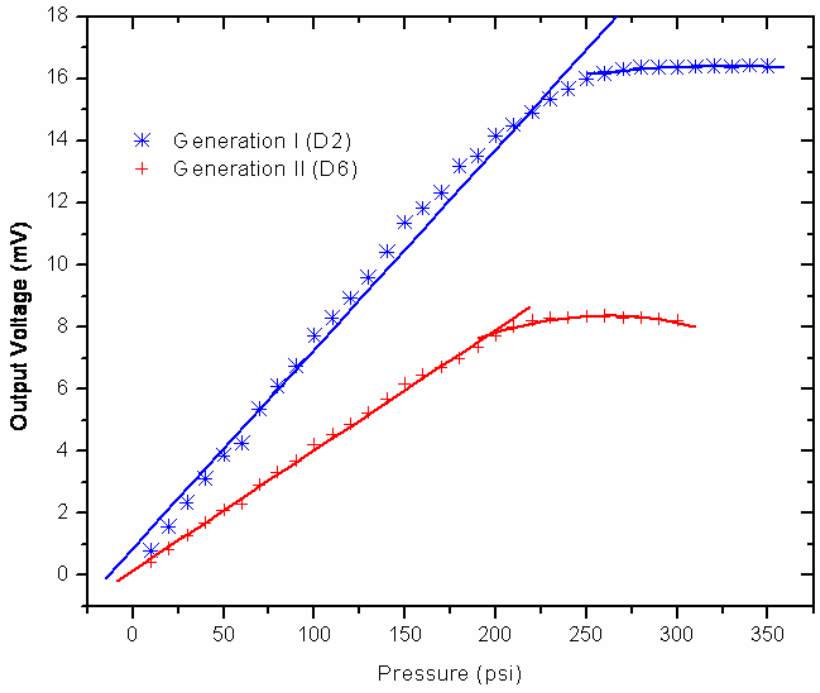

Figure 5.20 Comparison of experimental results of Generation I-D2 and II-D6 sensors.

Even though, experimental responses of different pressure sensor generations were compared (figure 5.20), the actual improvement in inner bridge sensitivity was measured by re-simulation/modeling using actual dimensions. Figure 5.21 shows the output response of Generation I, Generation II and single diaphragm designs of same inner/single diaphragm dimension (length 2000 μm and thickness 10 μm) to input pressure. Generation I sensor showed about 21% improvement, while Generation II showed about 27% improvement in the inner bridge sensitivity compared to single diaphragm design. The outer diaphragm for Generation I (length 3000 μm and thickness 30 μm) and for Generation II (length 4000 μm and thickness 30 μm). The operating range was not measured in this comparison because of non-repeatable process variations between fabrication and design.

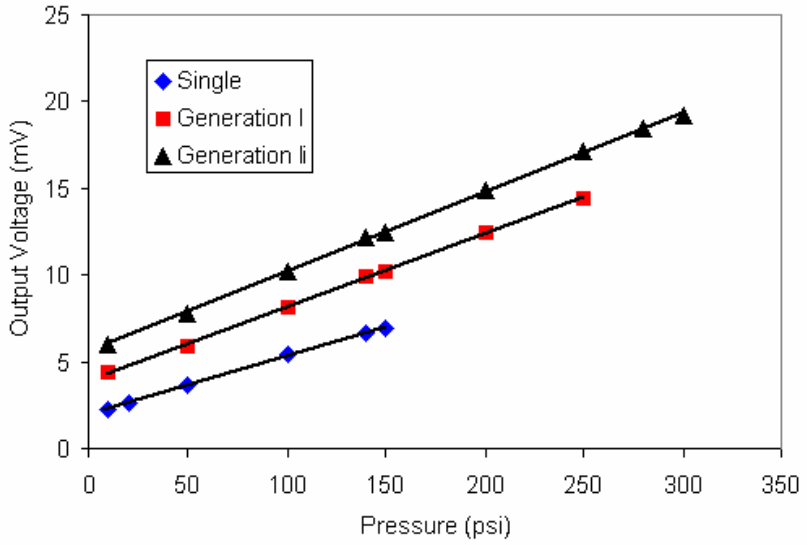

Figure 5.21 Re-simulated output response for input pressure variation for single, Generation I and Generation II sensors. Inner/single diaphragm dimensions length, 2000 μm, thickness, 10 μm.

5.6 Generation III: results and discussion

5.6.1 Overview

In this research, two configurations of Generation III device were measured. Table 5.4 illustrates the designed dimensions for Generation III devices. Generation III devices accounted for both the masked-maskless etching process and incorporated a central bossed structure to improve the linear operating range. It is worth mentioning here that central boss will add mass to the center of the diaphragm, which will essentially act as an additional stress concentrator focusing the stress fields more toward the location of the inner piezoresistors.

Table 5.4 Summary of Generation III sensors.

Sensor	Measured inner (L/H in µm)	Square boss (L/H in µm)	Outer (L/H in µm)
III-B1	1505/15	200/30	3000/45
III-B2	2090/10	200/20	4000/30

5.6.2 Sensitivity analysis of Generation III sensors

Figure 5.22 shows the inner bridge response to input pressure for III-B1 and III-B2 sensors. The response varied quasi-linearly with pressure, with sensitivity of 0.028 mV/V/psi for III-B1 and 0.056 mV/V/psi for III-B2. The response was fairly linear up to 260 psi for III-B1.

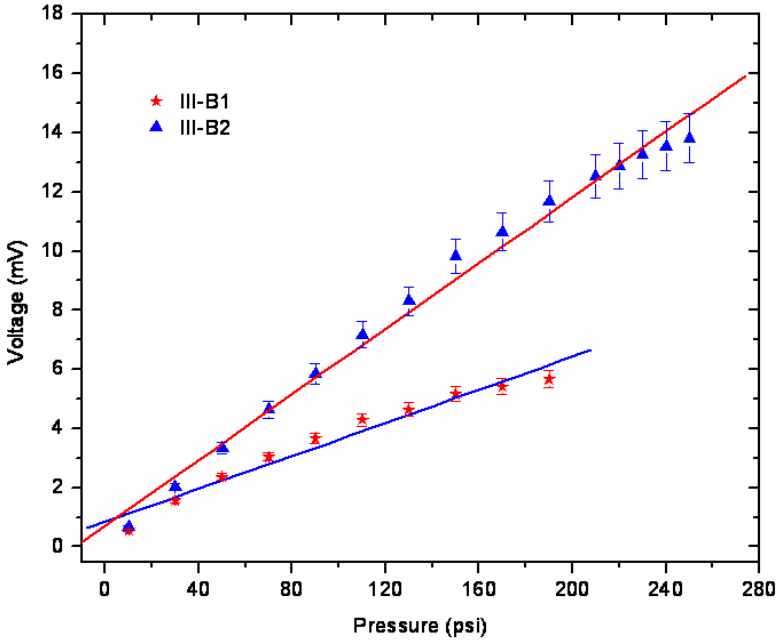

Figure 5.22 Variation of output response to input pressure variations for Generation III sensors (inner diaphragm).

From the output responses (Figure 5.23) for all three Generation devices (III-B2, III-D6 and I-D2), the following conclusions were drawn: (1) Transition pressure point of Generation III sensors are much higher than Generation I or II sensors. (2) Wider linear operating range is possible with Generation III sensors (up to 320 psi in case of III-B2) compared to III-D6 (up to 260 psi). (3) Output sensitivity of Generation III sensor is comparable to Generation II sensor. (4) Realization of a operating range of 430 psi (300 m) is possible, by the combination of inner and

outer bridges. For example in II-D6, up to 320 psi inner bridge is operable, beyond which the output bridge is measured. (5) A single element pressure sensor (Generation III) with both high sensitivity (> 0.05 mV/V/psi) and long operating range (> 300 psi) is also possible.

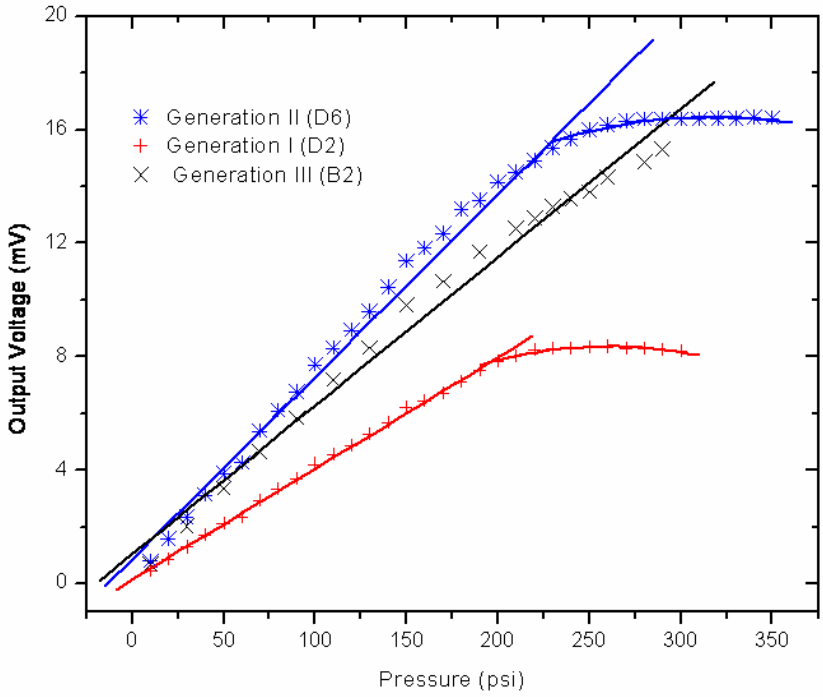

Figure 5.23 Comparison of output response of Generation I-D2, II-D6, III-B2 sensors.

5.7 Summary

In summary, Generation I, II and III of reinforced pressure sensors were measured progressively. It was observed that, in accordance to design specifications, the reinforced pressure sensors showed more than two times wider operating pressure range compared to conventional single diaphragm sensors. Further, the output sensitivity (from re-simulated date) was 27% higher in case of Generation II devices. All the bridge circuits were temperature compensated by third stress-free piezoresistive bridge. In case of Generation III sensors, the central bossed structure provided additional stress concentration effects to further, widen the linear operating range for the bridge (up to 320 psi). The reinforced edge structure, range up to 430 psi and sensitivity between 0.02-0.07 mV/V/psi were measured in the three Generation of reinforced pressure sensors. Work on measuring system-level packaged pressure sensors (with signal conditioning chip) is currently underway. The signal conditioning circuit will aid in digitally compensating for pressure offsets, drifts, noise and non-linearity between inner and outer bridge circuits.

CHAPTER 6

NANOWIRE-BASED ELECTROCHEMICAL DETECTION-ON-CHIP

6.1 Introduction

The ultimate goal of Lab-on-a-cable systems is to integrate analytical procedures into one microsystem that can perform sequential sampling, pretreatment, separation, analyte detection and data analysis. As a result, the development of micro-detection modules with high sensitivity, high signal-to-noise ratio, high selectivity fast response time and multiple functions is an important issue to be addressed. There are numerous studies to integrate detection schemes with microfluidic Lab-on-Chip (LoC) systems. Among these detection methods, optical and electrochemical detection techniques are the most frequently employed. Optical detectors are commonly used due to their accessibility in laboratories and the simplicity of the microfluidics–sensor interface. Electrochemical sensors are simple, robust and offer good detection limits for various analytes of biological interest and so it is advantageous to integrate such a detector with other microfluidic components within a microsystem (Hanrahan et al., 2004). They have also shown great potential for the extremely sensitive detection of selected analytes which avoids the need for extensive sample pretreatment and derivatization. Furthermore, microfabrication is well suited for the construction of electrochemical sensors.

The objective of this chapter is to introduce electrochemical sensors integrated on a microfluidic platform for detection of chemical and biological specimens in environmental samples. The attraction in integrating an electrochemical sensor module into microfluidic systems stems from its inherent portability and ease in fabrication of micro/nanoelectrodes. The electrochemical sensors' electrodes, in this research are based on one-dimensional (1-D) nanostructures, namely nanowires, which act as the transduction element. Nanowires as sensing electrode is gaining recognition in microfluidics due to its inherent advantages, such as their dimensions are similar to the dimensions of targets (which could dramatically reduce background noise), and ability to use multiple nanoelectrodes (resulting in a magnified signal).

However, nanowire electrodes in microfluidics are still in their infancy; much work needs to be done for practical applications.

6.2 Electrochemical sensors

Electrochemical sensors represent an important subclass of chemical sensors in which an electrode is used as the transduction element. The purpose of any chemical sensor is to provide real-time, continuous and reliable information about the chemical composition of its surrounding environment. Ideally, such a device provides a certain type of response directly related to quantity of a specific chemical species continuously and reversibly and does not perturb the sample. All chemical sensors consist of a transduction element covered with a biological or chemical recognition layer, which transforms the response into a detectable signal and also isolates the response from its immediate environment. In the case of electrochemical sensors, the analytical information is obtained from the electrical signal that results from the interaction of the target analyte and the recognition layer. Figure 6.1 illustrates the characteristics of electrochemical sensors: high sensitivity and selectivity towards the electroactive species, rapid and accurate response, compactness, portability and lower cost (Bret et al., 2001). Such capabilities have already made a significant impact on environmental, clinical, industrial and agricultural analyses. Electrochemical devices have been used depending on the nature of the analyte, the character of the sample matrix, and sensitivity or selectivity requirements. Electrochemical devices such as pH or oxygen electrodes have been used routinely for years in environmental analysis (Rajeshwer et al., 1994). These sensors fall into three major categories (nature of the electrical signal): potentiometric, conductometric and amperometric (Hanrahan et al., 2004).

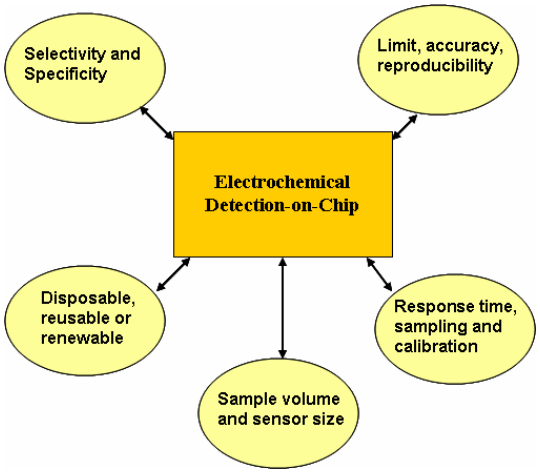

Figure 6.1 Aspects of an electrochemical sensor for environmental monitoring. Adapted from Bret et al., 2001.

For potentiometric sensors, a local equilibrium is established at the sensor interface, where the electrode potential is measured, and information about the composition of a sample is obtained from the potential difference between two electrodes. Such devices rely on the use of ion selective electrodes for obtaining the potential signal. The response is measured under conditions of essentially zero current. Potentiometric sensors are very attractive for field operations because of their high selectivity, simplicity and low cost. They are, however, less sensitive and often slower than their amperometric counterparts (Hanrahan et al., 2004 and Bret et al., 2001). Amperometric sensors exploit the use of a potential applied between a reference and a working electrode, to cause the oxidation or reduction of an electroactive species; the resultant current is measured. On the other hand, conductometric sensors are involved with the measurement of conductivity at a series of frequencies. Given the importance of each type of sensor, it would be impossible to review and compare the different electrochemical sensors. Therefore, the main emphasis of this section would to study and understand amperometric sensors or controlled potential electroanalytical techniques (technique mainly implemented in this work).

6.2.1 Controlled-potential techniques

Controlled-potential (potentiostatic) techniques deal with the study of charge transfer processes at the electrode-solution interface, and are based on the non-zero current (dynamic) situations (Wang et al., 2000). Here, the electrode potential is used to derive an electron-transfer reaction and the resultant current is measured. The controlled parameter, namely potential forces the chemical species to gain or lose an electron (reduction or oxidation). Accordingly, the resulting current reflects the rate at which electrons move across the electrode. They can thus measure any species that is electroactive, in other words, that can be made to reduce or oxidize. The advantages of controlled-potential techniques include high sensitivity and selectivity towards the electroactive species, wide linear range of operation, low cost instrumentation, wide range of electrodes, extremely low detection limits (up to 10^{-15} mol) with small sample volumes (5-10 μL). Improved selectivity may also be achieved by incorporation of chemical recognition elements or by specific enzymes.

The objective of controlled-potential techniques is to obtain a current response that is proportional to the concentration of the target analyte. This is accomplished by monitoring the transfer of electrons during the redox process of the analyte:

$$O + ne^- \leftrightarrow R \qquad (6.1)$$

where O and R are the oxidized and reduced forms, respectively, of the redox couple. From laws of thermodynamics, the potential of the electrode establishes the concentration of the electroactive species at the surface [$C_O(0,t)$ and $C_R(0,t)$] according to Nernst equation:

$$E = E^0 + \frac{2.3RT}{nF}\log\frac{C_O(0,t)}{C_R(0,t)} \tag{6.2}$$

E^0 is standard potential for the redox reaction, R is universal gas constant (8.314 J/K/mol), T is the Kelvin temperature, n is the number of electrons transferred in the reaction, F is the Faraday constant (96,487 coulombs). The current resulting from a change in oxidation state of the electroactive species is termed as faradaic current. This current is the direct measure of the rate of the redox reaction. The resulting I-V plot, is known as the voltammogram. The total current is the addition of the faradaic currents for the sample and blank solutions, as well as the nonfaradaic background currents.

The faradaic current that flows at any time in the system is a direct measure of the rate of the electrochemical reaction taking place at the electrode. This depends mostly on two reactions: 1) the rate at which the electroactive species gets from bulk to the electrode surface, called as the mass transport reaction; 2) the rate at which electrons transfer from electrode to solution species and vice versa, called as the charge transfer reaction (Wang et al., 2000). Whether a given reaction is controlled by the mass transport or electron transfer is usually determined by the type of species being measured and experimental conditions (electrode material, media, potential, time scale etc.). Actually these two rate-limiting processes are inexorably intertwined. Mass transport takes place by the following three modes: (1) diffusion-the spontaneous movement under the influence of concentration gradient; (2) migration-the movement of charged particles in an electric field; and (3) convection-movement to the electrode by gross physical movement.

The basic instrumentation requirement for an amperometric sensor is a controlled-potential instrument and an electrochemical cell with two or three-electrodes immersed in an electrolyte. While the working electrode is the electrode at which the reaction of interest occurs, the reference electrode (Ag/AgCl or Hg/Hg_2Cl_2) provides a stable potential compared to the working electrode and an inert conducting material (Pt or graphite) is usually used as auxiliary electrode. The performance of these kinds of sensors is strongly influenced by choice of working electrode.

6.2.2 Working electrodes

Since 1022, when Heyrovsky invented the dropping mercury electrode for electrochemical measurements, various solid electrodes constructed of noble metals and carbon has been implemented. Mercury was very attractive as an electrode material because of its extended cathodic potential range, high reproducibility and renewable surface. Solid electrodes (carbon, platinum, gold, silver, nickel, copper) have also been popular because of their versatile potential window, low background current, low cost, chemical inertness and suitability. Immobilization of chemical elements onto electrode surfaces has been a major growth area in electrochemistry in recent years (Wang et al., 2000). Chemically modified electrodes (CME) result from a deliberate immobilization of a modifier agent onto the electrode surface though chemical reactions, chemisorption, composite formation or polymer coating (Murray et al., 1984). Compared to conventional electrodes, greater control of electrode characteristics and reactivity is achieved by surface modification, since the immobilization transfers the physicochemical properties of the modifier to the electrode surface. The important benefits to electroanalytical applications include acceleration of electron transfer reactions, preferential accumulation, and interferent exclusion. Such steps can impart higher selectivity, detectability and stability to amperometric sensors.

In the recent years, with the advent of microfabrication and nanotechnology miniaturization of the working electrode has gained much attention and micro/nanoelectrodes have been developed, increasing the possibility of in vivo and in vitro measurements. This has resulted in a predictable boon for the development of amperometric sensors for real and continuous sample analysis. An example of this advance is was the development of electrochemical biosensors (Wang et al., 2005). Micro/nanoelectrodes exhibit several attractive possibilities, including the exploration of microscopic domains, detection in microflow system, time-resolved probing of processes in single cells or molecules, and analyses of very small sample volumes. Furthermore, with the electrode dimensions significantly smaller than the diffusion layer at their surface, the double layer capacitance is greatly reduced and the signal–to-noise characteristics are much better than with conventional electrodes. Also, because of their geometries and low current intensities, it is possible to work in highly resistive electrolytes. In the following section, research efforts in fabrication, assembly, functionalization and electrochemical sensing applications of one-dimensional nanostructures (nanoelectrodes) will be discussed.

6.3 One-dimensional (1-D) nanostructures (nanowires)

6.3.1 Properties at nanoscale

1-D nanostructures such as nanowires, nanotubes and nanosprings have been attractive due to their unique electrical, mechanical, chemical, optical and thermal properties and their potential for fabrication into high-density nanoscale devices including sensors, electronics and optoelectronics. In this research focus is mainly devoted to 1-D nanostructures, namely nanowires. In addition to their novel characteristics, nanowires, nanorods and nanotubes have unique properties, not found in other nanostructured materials, namely nanoparticles. They exhibit an additional degree of freedom associated with their shape anisotropy and ability to incorporate different components along their length.

Nanostructures are fabricated using a number of advanced techniques such as e-beam or focused-ion beam writing, proximity probe patterning, X-ray or extreme-UV lithography, Vapor-Liquid-Solid (VLS) method and some non-conventional methods based on electrochemical deposition. Furthermore, nanowires can be used for both efficient transport of electrons and for optical excitation, which are critical to the function and for integration into nanoscale devices. Because of their high surface-to-volume ratio and tunable electron transport properties due to quantum confinement effect, their electrical properties are strongly influenced by minor perturbations. Compared to bulk thin films where binding to the surface leads to depletion or accumulation of charge carriers only on the surface, the charge accumulation or depletion in the nanowires takes place in the “bulk” of the structure thus giving rise to large changes in the electrical properties that potentially enables the detection of a single cell or molecule (Wanekaya et al., 2006). 1-D nanostructures thus avoid the reduction in signal intensities and give rise to high signal-to-noise ratio that is inherent in thin films as a result lateral current shunting. This property of the nanowires provides a sensing modality for label-free and direct electrical readout when the nanostructures are used as electrochemical sensors (Wanekaya et al., 2006) . Such direct detection is particularly desirable for rapid and real-time monitoring of receptor-ligand interaction. This is critical for the detection of environmental targets, clinical diagnosis and bio-warfare agents. In addition, the sizes of chemical or biological targets, such as enzymes, proteins or nucleic acids are comparable to nanowires and any interaction between such targets should induce significant changes in the electrical properties of nanowires.

So far in this section, some of the unique properties of nanowires have been discussed, The focus of the next section will be on: 1) the methods for fabricating 1-D nanostructures, with primarily focus on electrochemical synthesis of metallic nanowires, 3) address issues in assembly of 1-D nanostructures and 3) illustrate their unique properties by building prototype functional electrochemical sensing devices.

6.3.2 Synthesis techniques for nanowires

The preparation of nanostructures can be categorized into two broad approaches. The first approach is called the "bottom-up" method and the second approach is called the "top down" method. The bottom-up approach is to place, consolidate, and pattern individual atoms or molecules into the structure wanted. It occurs very often in nature, such as the nano sized protein is built-up of amino acids and the building blocks for DNA, which has the structure of a compacted nanowire, are four nucleotide molecules. The top-down approach starts with a large scale object and gradually reduces its dimension to the nanometer scale. In general, the basic process of nanowires formation is crystallization. The evolution of solid, vapor or liquid phase involves two fundamental steps: nucleation and growth (Xia et al., 2003). As the concentration of building blocks (atoms, ions or molecules) of a solid becomes sufficiently high, they aggregate into small clusters through homogenous nucleation. With a continuous supply of the building blocks, these nuclei can serve as seeds for further growth to form larger structures. The most important issue that needs to be addressed is the simultaneous control over dimensions, morphology, and monodispersity. Several chemical methods have been demonstrated as the "bottom up" approach for producing nanowires. Figure 6.2 illustrates some of these synthetic techniques: 1) use of intrinsically anisotropic crystallographic structure of a solid to accomplish 1-D growth (fig 6.2A), 2) introduction of a liquid-solid-interface to reduce the symmetry of seed (fig 6.2B), 3) use of various templates with 1-D morphology to direct the formation of 1-D nanostructures (fig. 6.2C). 4) Use of supersaturation control to modify the growth of a seed, 5) use of capping reagents to kinetically control the growth of seeds (fig. 6.2D), 6) self assembly of 0-D nanostructures (fig.6.2E), 7) size reduction of 1-D microstructures (fig.6.2F).

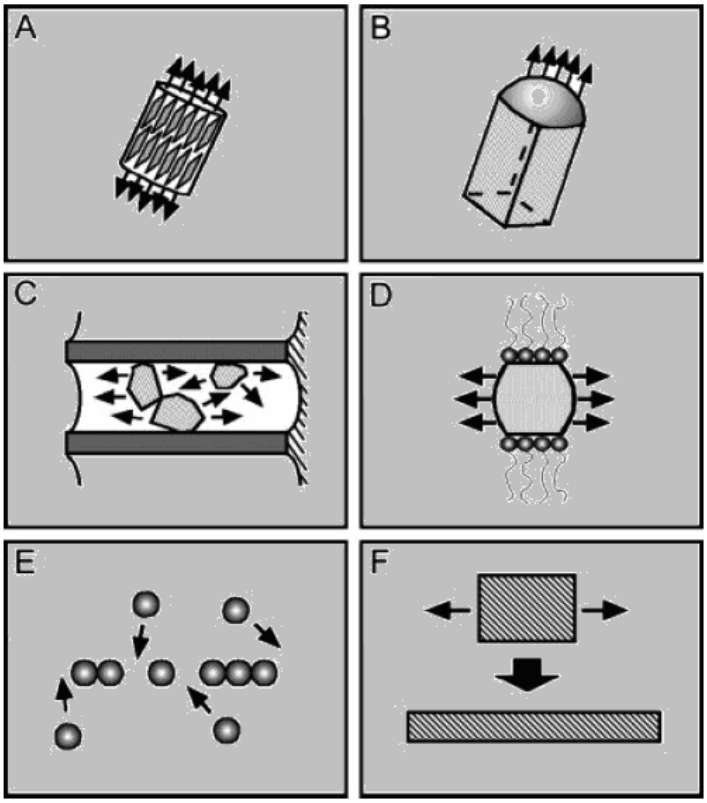

Figure 6.2 Illustration of the six different techniques for obtaining nanowire growth. Adapted from Xia et al., 2003.

Of the various methods, this work will primarily focus on the use of nanotemplates with 1-D morphology to direct the formation of nanowires by electrochemical means. This involves direct nano-fabrication by selective deposition into the openings of a self-organized templates. In this case the size and shape of the nano-objects are controlled by the size and shape of the openings in the nanotemplates, and may vary over a wide range depending on the template used. This flexibility also extends to the range of materials deposited in the template's openings. This approach is particularly attractive since it circumvents the lithographic limitations altogether by making use of naturally occurring nano-templates. Examples of such nanotemplates are zeolites and molecular sieves, mica sheets, diblock polymer, polymer nuclear track membranes, porous anodic aluminum oxide (AAO) films or porous silicon (Martin et al., 1994; Foss et al., 2002).

.

6.4 Template-directed synthesis of nanowires

6.4.1 Overview

The template synthesis of nanostructures by electrodeposition is an elegant low-cost, high yield alternative to sophisticated methods such as molecular beam epitaxy, nanolithography and vapor-liquid-solid growth mechanisms (Martin et al., 1994). The key feature of the templating technique is ones' ability to control the size, length, shape and morphology of the material deposited by (a) controlling the template morphology and (b) controlling the synthesis parameters (Aravamudhan et al., 2007). In addition, electrodeposition provides the ability to introduce composition modulation or different functionalities (two-segment Ni-Fe/Au) along the wire length. In this approach, the template serves as a scaffold within (or around) which a different material is generated in-situ and shaped into a nanostructure with its morphology complementary to that of the template. This can be classified into: 1) negative template, 2) positive template, 3) surface step templates. Negative template methods use prefabricated cylindrical nanopores in a solid material as templates. By depositing metals into the nanopores, nanowires with a diameter predetermined by the diameter of the nanopores are fabricated. The positive template method uses wire-like nanostructures, such as DNA and carbon nanotubes as templates, and nanowires are formed on the outer surface of the templates. Unlike negative templates, the diameters of the nanowires are not restricted by the template sizes and can be controlled by adjusting the amount of materials deposited on the templates. By removing the templates after deposition, wire-like and tube-like structures can be formed. Atomic-scale step edges on a crystal surface can also be used as templates to grow nanowires. This method takes the advantage of the fact that deposition of many materials on a surface often starts preferentially at defect sites, such as surface step-edges. For this reason, this method is sometimes called "step edge decoration."

The templated fabrication of nanowires was first realized by Possin in the late 1960, who reported forming wires with 40 nm diameter by electrodepositing tin, indium and zinc in pores of mica (Possin et al., 1970). Martin and Maskovits popularized this technique by creating electrically conductive polymers and metallic nanowires in nanoporous polycarbonate and alumina templates (Martin et al., 1994). To fabricate nanowires, the template's pores must be filled with the desired nanowire material. A number of approaches namely, electroless deposition, in-situ polymerization, pyrolysis, electroploymerization and electrodeposition have been developed. Of these methods, electrodeposition is the most common and versatile method to produce metallic nanowires. Figure 6.3 illustrates template synthesis via electrodeposition of

metallic nanowires. Firstly, one face of the template is coated with conductive material and the template's pores are then filled with one or more metals via electrodeposition. The templates are then chemically etched to remove the nanowires. The nanowires formed are uniform in diameter and length and can have high aspect ratios (>100).

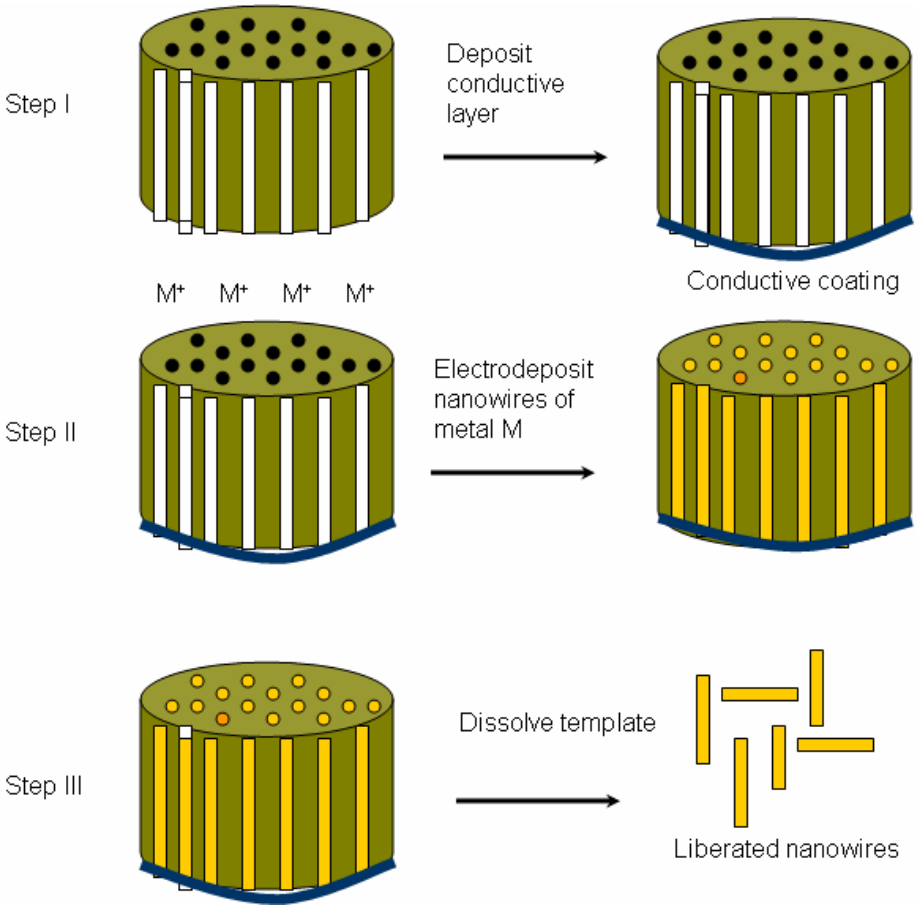

Figure 6.3 Illustration of template synthesis method of creating metallic nanowires.

6.4.2 Template fabrication

As stated earlier, many kinds of porous templates can be used to create nanowires, including alumina, polycarbonate and porous silicon. The nanopores in alumina template are formed by anodizing aluminum films in an acidic electrolyte. The individual nanopores in the alumina can be ordered into a close-packed honeycomb structure (Hornyak et al., 1997). The diameter of each pore and the separation between two adjacent pores can be controlled by changing the anodization conditions. The diameter and depth of each pore, as well as the spacing between adjacent pores can be also controlled by the anodizing conditions. Both the pore diameter and the pore spacing are proportional to the anodizing voltage with proportional

constants of 1.29 nm/V and 2.5 nm/V, respectively. The dependence of the diameter and the spacing on the voltage is not sensitive to the electrolyte, which is quite different from the optimal voltage for ordered distribution of the pores as discussed above. This property has been exploited to make size-selective microfiltration membranes and to control the diameter of nanowires formed in the pores. By properly controlling the anodization voltage and choosing the electrolyte, one can make highly ordered nanopores in alumina with desired pore diameter and spacing.

Another type of nanowire template is formed by etching pores in polymer materials such as polycarbonate. When the material's surface is bombarded with nuclear fission products, damage is caused chemical etchants such as NaOH can preferentially etch the material at these damage sites, creating pores in the material. However, polycarbonate templates are not stable at high temperatures, and pores are randomly scattered across the template surface and pore densities are lower than that of alumina template (Scho1nenberger et al., 1997). Other problems include the angle between the pores and the template surface (up to 34º) and cigar shape of pores due to pore widening under the surface. The third type of template for nanostructure formation is porous silicon. In this research, a wide variety of nanowires (single segment: Au, Ni-Fe, and two-segment Au/Ni-Fe) have been formed in porous silicon. There are only few reports in literature on nanowire formation in porous silicon. Porous silicon (PS) was discovered in 1956 by Uhlir while performing electropolishing experiments on silicon wafers using an HF-containing electrolyte. He found that increasing the current over a certain threshold, a partial dissolution of the silicon wafer started to occur. PS formation is then obtained by electrochemical dissolution of Si wafers in aqueous or ethanoic HF solutions (Lehmann et al., 2002).. A detailed study of porous silicon template and nanowire formation is presented in Appendix D.

6.4.3 Nanowire synthesis via electrodeposition

Electrodeposition is an economical and versatile method for fabrication of nanowires. However, a layer of conductive material is required on side of the template for electrodeposition. The electrodeposition conditions play a critical role in determining the crystallinity of the deposited nanowires. A distinct advantage is the availability of various process parameters (electrolyte composition, bath pH, and mode of deposition- DC, AC or pulse) that can be varied to get the desired material properties. During electrodeposition, there is a competition between the growth of existing grains (resulting in single-crystal nanowires) and nucleation followed by the growth of new crystallites (resulting in polycrystalline nanowires). Further, either constant

potential or constant current methods can be used to reduce the cations into the template. If a constant potential deposition is used, the template is placed in a three-electrode cell comprising of counter, reference and working electrodes (figure 6.4). The reference electrodes potential doesn't fluctuate in response to changes in current. The potential between the working and reference electrode is held constant as current between the counter and working electrode. The metal ions are reduced as the working electrode.

The time dependence of the current curves recorded during the electrodeposition process reveal three typical stages (figure 6.4) (Valizadeh et al., 2001). Stage I corresponds to the electrodeposition of metal into the pores until they are filled up to the top surface of the membrane. In this stage, the steady-state current at a fixed potential is directly proportional to the metal film area that is in contact with the solution, after the pores are filled up with deposited metal, metal grows out of the pores and forms hemispherical caps on the membrane surface. This region is called stage II. Since the effective electrode area increases rapidly during this stage, the electrochemical current increases rapidly. When the hemispherical caps coalescence into a continuous film, stage III starts, which is characterized by a constant value again. By stopping the electrodeposition process before stage I ends, an array of nanowires filled in the pores is formed.

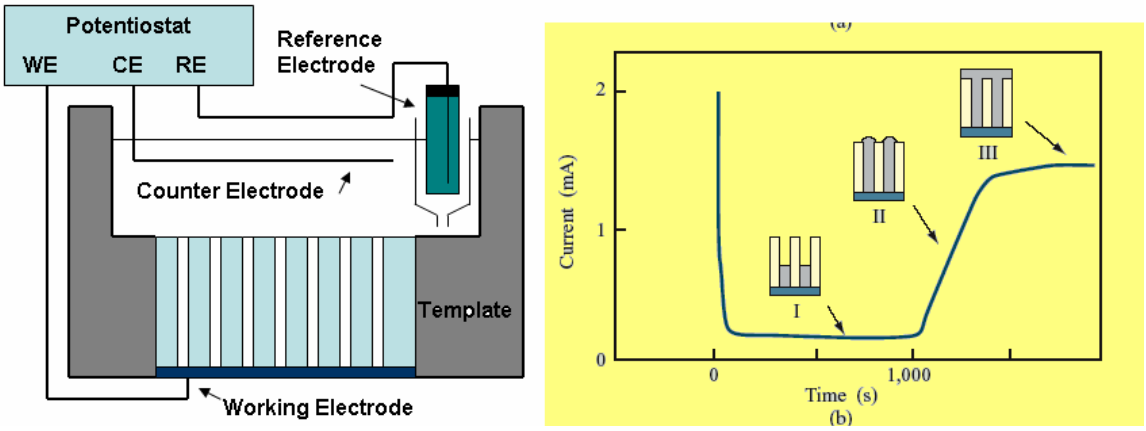

Figure 6.4 Illustration of the electroplating setup and the different regimes in the electroplating process. Adapted from Valizadeh et al., 2001.

After the formation of nanowires, the next step is to assemble or integrate the synthesized nanowires onto sensor surfaces such as the electrochemical detection-on-chip. To accomplish this, different sensing modalities have been explored based the metallic species deposited and assembly techniques used to align them. In the next section, firstly, the different sensing elements

(nanowires) formed using template approach will be discussed, followed by their assembly procedures. Finally, a prototype biosensor built on the principles of electrochemical detection-on-chip (nanoelectrodes, assembly on MEMS platform) will be presented.

6.5 Sensing modalities

6.5.1 Fabrication of nanosensor elements

In this section, the synthesis of nanosensor elements, namely single segment Au and Ni-Fe and two-segment Au/Ni-Fe nanowires in nanoporous templates will be discussed. As stated earlier, arrays of ordered nanowires are attractive in the field of electronics, storage, chemistry and biology: ranging from bio-sensing to cell manipulation to cancer therapy (Reich et al., 2003; Fert et al., 1999). In order to be suitable for chemical or bio-sensing element, the material to be adopted should be compatible with and have a good affinity to targets and should be stable in air or aqueous solution for reliable measurements. Gold is a good candidate for this purpose. It is well known that gold has good affinity to biomolecules, because functional groups such as thiol (-SH) or amine (-NH2) can chemically adsorb onto gold surface. In particular, Au nanowires, as sensing elements can be covalently modified to attach thiols, dithiols and thioacetates, or amines. In the case of Ni-Fe, the magnetic properties of Ni-Fe nanowires in suspension can be used to assemble them magnetically and then, they can be selectively bound to specific ligands (Reich et al., 2003). A combination of Au and Ni-Fe nanowires produces two-segment nanowires with the ability to functionalize multiple ligands specific each material and in addition to, magnetic based assembly procedures (Aravamudhan et al., 2007).

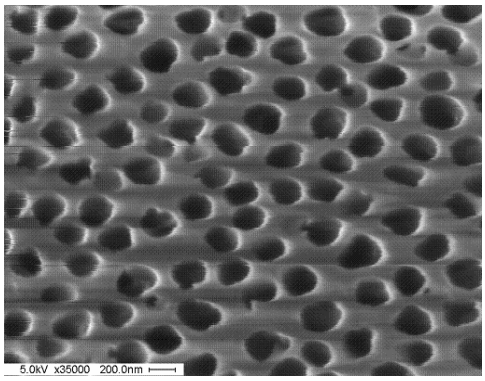

a

Figure 6.5 a) SEM image of alumina template with 200 nm diameter pores. b) SEM image of strands of Au nanowires of diameter 200 nm and length up to 30 μm.

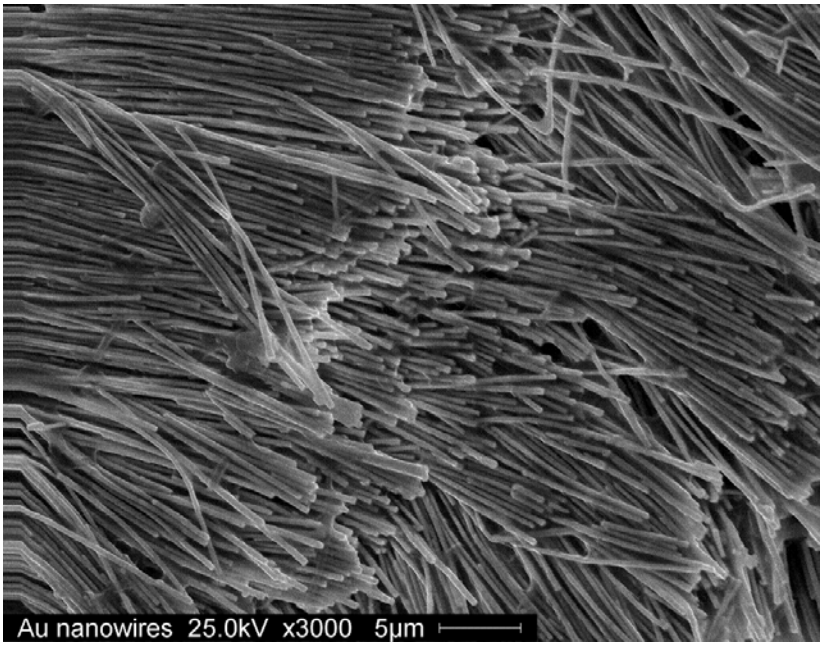

b

Figure 6.5 (continued)

First, the fabrication and release of Au nanowires (Au-NWs) will be discussed. The Au nanowires were fabricated by a one-step electroplating process inside the 200 nm pores of commercial alumina template (Figure 6.5a, Whatmann Inc). A 1 µm aluminum layer was evaporated on one side of the alumina template to act as an electrode for electroplating. The electroplating was performed at a current density of 2.5-4 mA/cm^2 and 55 ºC using Technic 25E plating solution. Techni-Gold 25 ES plating solution (Technic Inc., RI, USA) for 2 h. Techni-Gold 25 ES is a ready-to-use neutral sulfite based (noncyanide) gold plating formulation (8.2-16.4 g/L of gold, 45 g/L of anhydrous sodium sulfite, 132 ml/L of DI water and rest is made of propriety makeup and stabilizer solutions). Platinum mesh acted as anode and alumina template (with one side coated with aluminum) acted as cathode. After electroplating for about 1 hour, the sample was thoroughly rinsed in DI water. Then, to liberate the Au nanowires, alumina template with aluminum on one side was dissolved in warm 45% KOH with periodic agitation. This resulted in release of Au nanowires in solution. Then, the Au nanowires were collected from KOH by centrifugation at 7000-9000 RPM. The supernatant was decanted and replaced with clean methanol. The nanowires were sonicated for 1 min and this protocol of collection-solvent addition-sonication was repeated three times to completely wash the nanowires. Figure 6.5 shows the SEM image of the Au-NWs. Nanowires released from alumina template have a diameter of

about 175 ± 25 nm and length up to 30 µm. In the top view, a large number of free standing nanowires are observed. The nanowires deposited in the pores are uniform in diameter throughout the length.

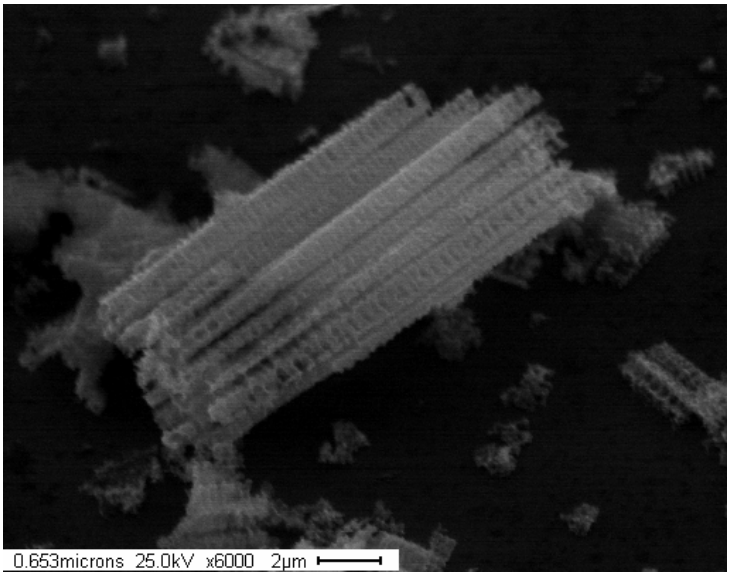

a

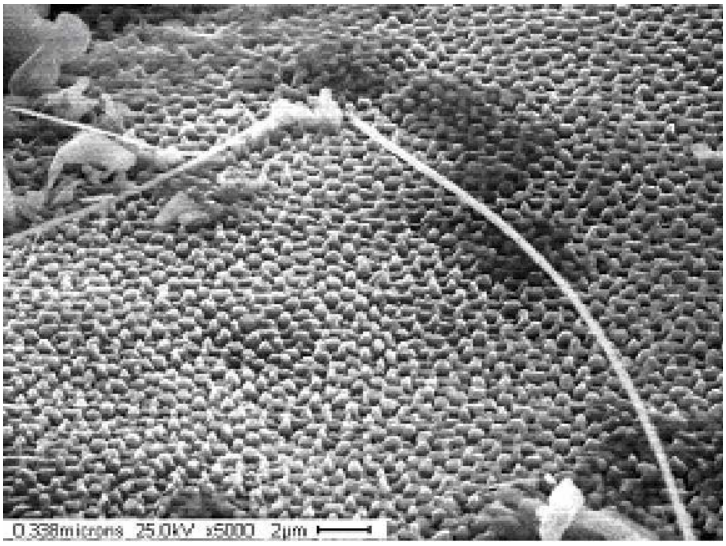

b

Figure 6.6 a) SEM image of a cluster of 275±25 nm Ni-Fe nanowires partially released by 10 µm. b) Typical single strand of fully released Ni-Fe nanowire.

Next for the purpose of magnetic based assembly, magnetic material namely Ni-Fe nanowires were studied. Many magnetic nanowire arrays (metals, alloys, or multi-layer structures) have been investigated in the past (Fert et al., 1997). Amongst the materials studied,

Ni-Fe is attractive because of its superior ferromagnetic properties, high magnetization behavior and invar effect in certain compositions compared to other magnetic materials (Ni, Co, or Fe). Ni-Fe nanowires, being high aspect ratio structures, have large remanent magnetizations at small external magnetic fields compared to superparamagnetic beads (Reich et al., 2003). This distinct advantage makes ferromagnetic nanowires suitable for cell separation experiments, by using them (in a magnetic field) to apply force on mammalian cells or bio-molecules. In case of Ni-Fe, a sulfate based electroplating bath of composition 200 g/L $NiSO_4.6H_2O$, 8 g/L $FeSO_4.6H_2O$, 5 g/L $NiCl_2.6H_2O$, 25 g/L H_3BO_3, 3 g/L Saccharin was used. A Ni foil was used as anode to maintain constant metal ion composition and the electroplating was performed under current density of 3.5 mA/cm^2. A detailed structural, compositional and magnetic characterization of Ni-Fe nanowires deposited in templates such as porous silicon, alumina and polycarbonate is discussed in Appendix E. However, a typical bunch of Ni-Fe nanowires electrodeposited and partially released in porous silicon is shown in figure 6.6. Figure 6.6a shows a cluster of 10 μm long nanowires partially released from the silicon template. Figure 6.6b shows the morphology of a typical fully released Ni-Fe nanowire strand of diameter 275±25 nm and length 100 μm. The length of the nanostructures was initially calculated from the deposition charge and time and later verified using the SEM. The Ni-Fe nanostructures' aspect ratio was calculated as between 330 and 400. The SEM micrograph also shows the Ni-Fe nanostructures to be textured and faceted with multiple grain boundaries

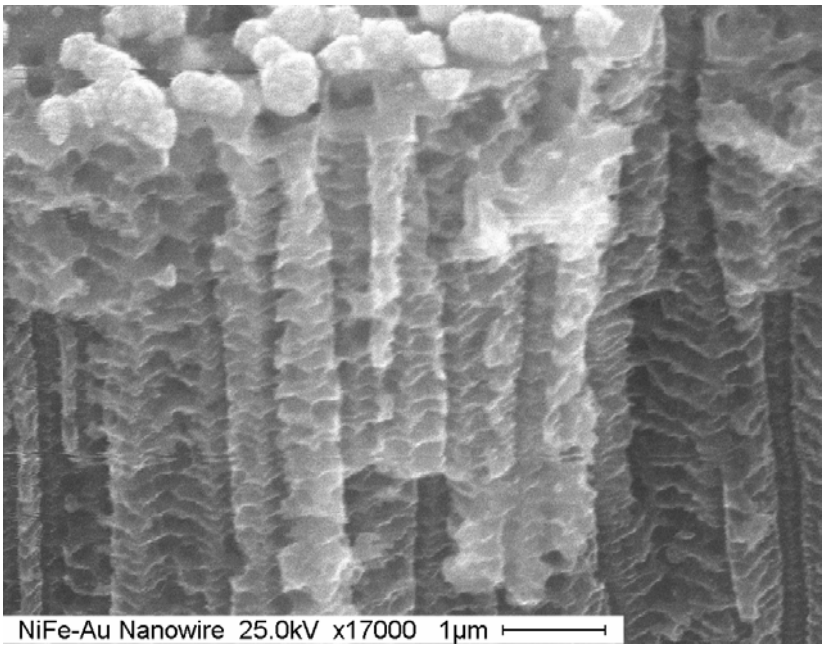

Figure 6.7 SEM image of two-segmented Ni-Fe/Au nanowires.

Next, a combination of Au and Ni-Fe nanowires were deposited. In the case of two-segmented (Ni-Fe/Au) nanostructures, electrodeposition was done sequentially, first Ni-Fe and then Au was electrodeposited, with thorough cleaning with DI water in between the two electroplating steps. The nanowires were about 250-300nm in diameter. Figure 6.7. shows the image of two-segment Ni-Fe/Au nanowires. The two-segmented wires have about 0.5 μm top layer of Au, while the rest is Ni-Fe, of the same length as the single-segment wires. The Au cap can be seen clearly as discrete entities deposited on top of Ni-Fe wires.

The fourth kind of nanostructure deposited was conducting polymers namely polypyrrole in alumina template. A detailed synthesis and assembly of polypyrrole nanowires is presented in the next chapter.

6.5.2 Assembly of nanowires on silicon substrate

Although considerable progress has been made in the synthesis of nanowires, sensor fabrication is still hindered by the lack of efficient processes that can assemble the materials with the desired connectivity into useful architectures and functional sensing devices. Controlled assembly of nanowires is necessary to realize any useful applications. A good nanoscale assembly technique should be affordable, fast, defect tolerant and compatible with a variety of materials in various dimensions. In fact, the key to the future success of nanotechnology will depend on the availability of facile techniques for assembly and alignment. In this work, three different assembly techniques including magnetic, through wafer interconnection and electric field have been explored.

Magnetic alignment: The magnetic properties of Ni-Fe nanowires, namely perpendicular shape anisotropy due to their large aspect ratios are exploited in this method. Magnetic nanowires exhibit interesting behavior when placed in fluid suspensions. Their large magnetic shape anisotropy and high remnant magnetization make suspended nanowires highly orientable and easily manipulated in small external magnetic fields (Bauer et al., 2003). This property can be used to control the interwire dipolar forces and hence obtain ordered structures. The multi-segmented nanowires with Ni-Fe ends and Au central portion can be assembled as illustrated in figure 6.8. Additionally, the different segments of the nanowire can be functionalized differently

and this influences how they interact with the environment. A detailed study of the perpendicular shape anisotropy property of Ni-Fe nanowires is presented in Appendix E.

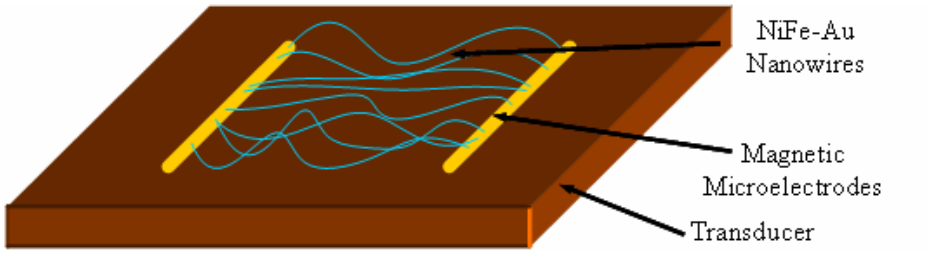

Figure 6.8 Illustration of magnetic alignment process showing NiFe-Au-NiFe nanowires assembled using magnetic field.

Through wafer interconnection: The fabrication of porous silicon by electrochemical etching of silicon is a well-established technique. Until now, porous silicon was used either as a sacrificial material to fabricate free-standing structures and cavities or in photonic crystals and as sensors. However, in this work, the ultra-high aspect ratio nanoscale pores created by electrochemical etching of silicon have been used as a "nano-template" to create one-dimensional nanostructures, namely nanowires. This ability to create controlled and uniform pores in silicon at "areas of interest" enables nanowires to be always physically and electrically addressable through the silicon substrate (Figure 6.9). Currently, there are only few methods to assemble and organize nanostructures on sensor surfaces. However, these techniques which involve tedious fabrication, transfer and alignment procedures externally on the sensor surface. In other methods, a two step process of first forming the porous alumina on silicon substrate and then depositing nanowire arrays were used. In contrast, porous silicon template based method will use a single process to directly integrate nanowires as functional in-situ structures in silicon electronics, optical, sensing or lab-on-chip (LOC) components, without contaminating the sensing surface (Aravamudhan et al., 2003). The templating and synthesis of nanowires can be localized at "regions of interest" using masking layers, thus enabling a rigid pathway for seamless integration with sensor arrays and CMOS circuits on the same wafer. Furthermore, the pore dimensions and morphology can be easily controlled by varying doping (n- or p-type) or applied current for electrochemical etching. The length of the nanowire can also be effectively controlled by varying the etching time. A detailed processing conditions and experimental results are presented in Appendix D.

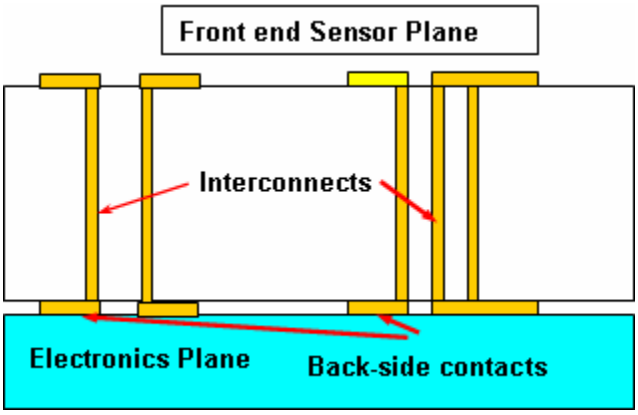

Figure 6.9 Illustration of the through wafer interconnection scheme for assembly on nanowires deposited in porous silicon.

Electric field alignment: The next method, which is implemented throughout this work, is by using electric field to assemble the metallic nanowires. When an electric field is applied to a nanowire suspension, it polarizes the nanowires, which forces them to align with their length oriented parallel to the direction of the electric field (Boote et al., 2005). The alignment quality is dependent on many factors, including the field strength and thermal energy. Additionally, the length of the nanostructures has also been found to be a factor because of its dependence on the anisotropy in electric polarizability. Electric field assisted assembly has been used to align individual Au nanowires from solvent suspensions onto interdigitated electrodes. Figure 6.10. illustrates the alignment of Au nanowires on the Pt lines, achieved using electric field assisted or dielectrophoresis (DEP) technique. The Pt lines were fabricated as interdigitated fingers of width and spacing 50 μm and 10 μm respectively (figure 6.10B). Using the alignment process described by Boote et al. 2005, dilute suspensions (200 μL, approximately 10^7 wires/mL) of the Au-NWs in methanol were dispensed on the interdigitated Pt lines. An alternating electrode voltage of 30 V_{rms} at a frequency of 20 KHz was applied to the left Pt lines (represented as 1 in figure 6.10A) relative to the right grounded Pt lines (represented as 2 in figure 6.10A) for about 20-60 seconds. The nanowires experience a dielectrophoretic force that produces a net movement in the direction of increasing electric field strength, which occurs at the periphery of the Pt lines. It is this large near-field force that results in alignment of Au-NWs between the interdigitated Pt lines. The alignment was monitored by studying the series current and later verified by microscopy (figure 6.10C). Due to the random distribution of Au-NWs, as shown in figure 6.10C, along the interdigitated Pt lines, the number of nanowires aligned could not be measured.

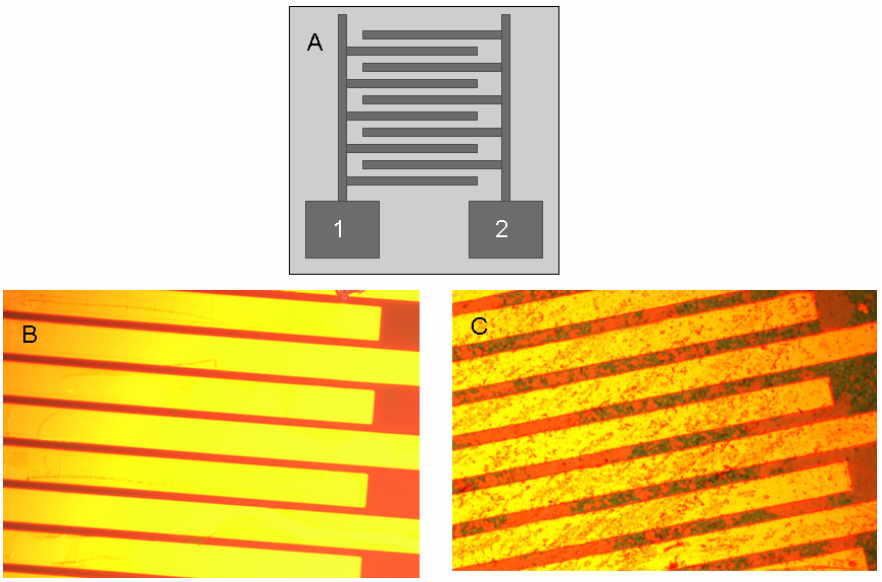

Figure 6.10 Schematic top view of the interdigitated Pt lines for dielectrophoresis. a) Au nanowires with AC voltage of 30 V_{rms} at frequency of 20 KHz is applied on electrode 1 relative to grounded electrode 2. b) Image of interdigitated Pt lines (50 µm width and 10 µm spacing) before dielectrophoresis process, c) Image of interdigitated Pt lines with random alignment of Au nanowires after dielectrophoresis for 20 seconds.

Thus far in this chapter, the different fabrication techniques, assembly procedures and electrochemical techniques for building an electrochemical detection system have been discussed and reviewed. To illustrate the practicality of the proposed approaches, a prototype electrochemical biosensor on a MEMS/microfluidic platform using enzymes modified Au nanowire electrodes to detect biomarkers (such as cholesterol levels) in biological fluids (such as blood) have been developed. The blood system was chosen because of the presence of multiple interferences, similar to seawater. The following section will present in detail the design, fabrication, experiments and testing of this prototype electrochemical biosensor.

6.6 Microfluidic electrochemical biosensor for targeted detection using Au nanowires

6.6.1 Introduction

Recent efforts have been focused on using enzymes immobilized on electrodes for electrochemical detection (Charpentier et al., 1995; Allain et al., 1974; Martin et al., 2003). Immobilization of enzymes is generally carried out either by direct physical adsorption or through mediators or entrapment in polymers. The simple design, specificity and high sensitivity provided by a particular enzyme appears promising. Metallic nanowires, in particular Au nanowires (Au-

NW) are very promising as smart building blocks in emerging electronic and sensing applications (Kovtyukhova et al., 2002). They offer higher capture efficiency, faster response time due to their large adsorption surface (large surface to volume ratio > 1000 m^2/g), high electrical conductivity and small diffusion time. More specifically, as a bio-sensing material they can be covalently modified with functional groups like –SH, -COOH and $–NH_2$, which can be linked further to a specific enzymes such as cholesterol oxidase (COX) and cholesterol esterase (CE). Moreover, as an electrode material it is not easily reduced/oxidized over a range of potentials. It also promotes electron transfer and demonstrates catalytic activity for many electrochemical reactions. Additionally, the size similarity between the nanowires and the redox enzymes can be used effectively for developing a highly sensitive biosensor. Accordingly, in this work, selective and sensitive electrochemical detection of cholesterol in blood serum in a microfluidic platform (figure 6.11) using aligned Au-NW immobilized with specific enzymes, on-chip deposited platinum electrode and Ag/AgCl (3M KCl) as the working, the counter and the reference electrodes, respectively. The cholesterol determination was performed through direct physical adsorption of specific enzymes namely cholesterol oxidase (COX) and cholesterol esterase (CE).

6.6.2 Importance of cholesterol detection in blood

Sensitive and selective detection of a particular bio-marker in a multi-component blood system is a challenging task in clinical analysis/diagnosis. Cholesterol is one such bio-marker found in blood, linked to a number of clinical and heart disorders. Its higher accumulation in blood is strongly correlated with coronary heart disease, arteriosclerosis, myocardial infarction, brain thrombosis, lipid metabolism dysfunction, hypertension, etc (Fredrickson et al., 1972). Further, it is also a major component of proteins and lipid assemblies in cell plasma membranes that are involved in signal transmission among cells, cell infection, and immune response. The normal human blood serum contains about 5.2 mM/L of total cholesterol, along with various interfering species such as uric acid, glucose and ascorbic acid. Cholesterol level is commonly determined by employing non-enzymatic spectrophotometric techniques, using colored substances. This method, however, involves complex procedures for precipitation of lipoproteins fractions and suffers from various drawbacks such as low specificity, instability of reagents and high cost (Aravamudhan et al., 2007). It is thus desired and crucial to develop techniques for cost-effective, convenient, rapid, sensitive and selective estimation of cholesterol levels in blood.

6.6.3 Materials and instruments

DL-Thioctic acid (100%) was purchased from MP Biomedicals (Irvine, CA). EDC(1-ethyl-3 [3dimethylaminopropyl]carbodiimide hydrochloride), Sulfosuccinimidyl-6-(biotin-amido)hexanoate (EZ-link Sulfo-NHS-LC-Biotin) and Streptavidin conjugate were obtained from Pierce Biotechnology (Rockford, IL). Cholesterol oxidase (COX) from *Pseudomonas fluorescens* (10-50 U/mg), Cholesterol esterase (CE) from *Pseudomonas fluorescens* (> 10 U/mg), cholesterol (> 98%) and Triton X-100, and 0.1 M Phosphate buffered saline (PBS) (pH 7.2) were purchased from Sigma-Aldrich (St. Louis, MO). All chemicals were analytical reagent grade and used without further purification. Square wave voltammetry measurements were performed using an Autolab PGSTAT30 from Eco chemic N.V. All electrochemical measurements were performed in the standard three-electrode format. The modified Au nanowires acted as the working electrode, an Ag/AgCl (3 KCl) acted as reference electrode and a platinum strip deposited on the silicon chip acted as the counter electrode. All measurements were performed at room temperature. Scanning Electron Microscopy (SEM) images were obtained on a Hitachi S800 Scanning electron microscope. Atomic force microscopy was done on a Digital Instruments AFM with Nanoscope III software. Fourier transform infrared spectroscopy (FTIR) analysis was performed on a Nicolet Avatar spectrometer in the range of 400-4000 cm^{-1} with the main focus in the range of 1200-1800 cm^{-1} at a resolution of 1 cm^{-1}

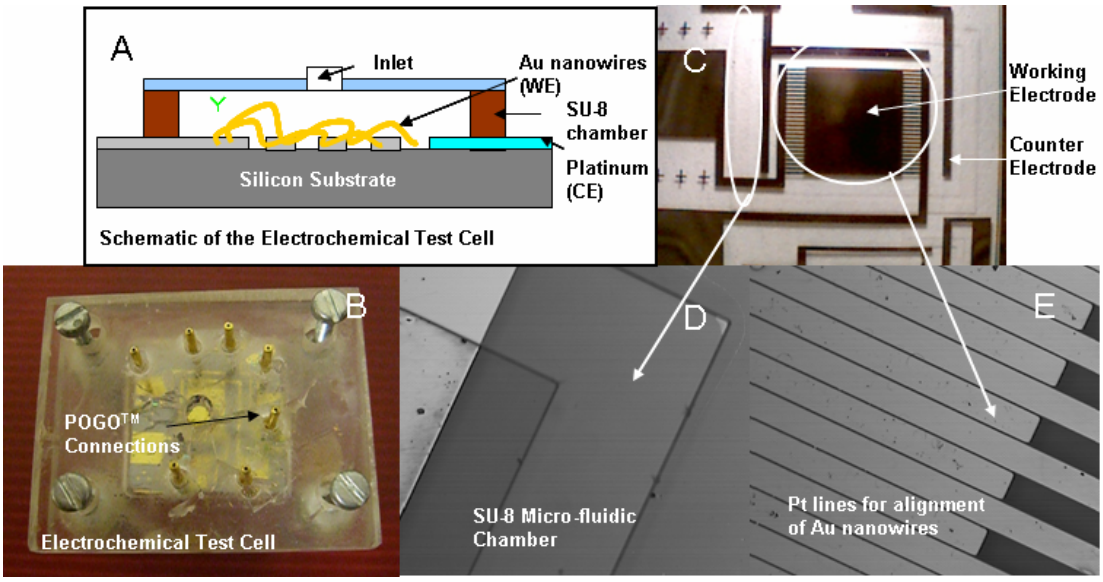

Figure 6.11 Cross-sectional schematic of the electrochemical test cell. a) With nanowires on the Pt lines, b) picture of the electrochemical test set up, shown with the silicon chip, inlet for reagents and electrical connections using Pogo™ pin technology, c) actual image of the microfluidic platform in silicon with Pt lines (Au nanowires between them) and SU-8 chamber, d) image of the hard-baked SU-8 chamber e) Magnified image of Pt lines for nanowire alignment.

6.6.4 Electrochemical cell fabrication

First, Au nanowires (Au-NWs) were synthesized by electrodeposition procedures discussed earlier. Next, the electrochemical chip was fabricated on oxidized (100) silicon substrate. Figure 6.10. shows the microfluidic device with electrodes and electrical connections drawn using Pogo™ pins (Everett Charles Technologies, CA, USA). The interdigitated patterns for nanowire alignment and the counter electrode were fabricated in Platinum (Pt) (figure 6.11E). This was accomplished by photolithography, subsequent e-beam evaporation and lift-off of Ti/Pt layers. Ti was used as the adhesion layer for Pt. Then, 60 µm tall microfluidic chamber in SU-8 (Microchem Corp. Newton, MA) was fabricated to hold the reagents (Figure 6.11D). The SU-8 chamber was then hard baked at 180 ºC for 3 minutes to prevent any out-gassing or contamination. This was followed by electric field assisted assembly of Au nanowires on the interdigitated patterns.

6.6.5 Enzyme immobilization on Au-NWs

The enzyme immobilization on the Au nanowires surface is a critical step in the performance of the electrochemical biosensor. Aligned Au-NWs in the electrochemical cell were

first cleaned in piranha solution to remove any trace organics and contaminants and then, rinsed in excess of DI water. Au-NWs were then activated with 2% (w/w) thioctic acid in absolute ethanol with shaking and were immobilized using carboxyl-terminated chemistry in 0.2 M EDC and 0.05 M NHS-LS biotin in DI water. Lastly, 250 µg/mL of streptavidin in PBS was immobilized on the NW surface and incubated at 4 ºC overnight. The biotin/avidin linkage is one of the strongest known biological interactions (Diamandis et al., 1991). and this linkage has been further used to bind Au nanowires to specific enzymes namely COX and CE. Because of the in-solubility of cholesterol in PBS solution, Triton X-100 (nonionic surfactant) was used to dissolve cholesterol. First, 0.1 M cholesterol oxidase, prepared in.25 µL of 0.1 M PBS solution. (pH 7.2) and 2 µL of Triton X-100 was immobilized on the functionalized Au-NW. Then, 25 µL of 0.1 M cholesterol esterase in 0.1 M PBS and 2 µL of Triton X-100 was immobilized on the NW surface. Finally, the un-reacted reagents were washed in standard PBS solution.

6.6.6 Electrochemical measurements

Square wave voltammetry (SWV) was performed using an Autolab PGSTAT30 from Eco chemic N.V at room temperature in blood serum. The measurements were performed in the standard three-electrode format with enzyme modified Au-NW, Ag/AgCl (3 M KCl) and a platinum line deposited on the silicon chip as the working, the reference and the counter electrode, respectively. The electrochemical response of the modified Au-NWs to varying levels of cholesterol (10-60 µM) and interfering species such as ascorbic acid, uric acid and glucose was studied using SWV. Normal blood serum was used as a baseline electrolyte and known quantities of cholesterol (> 98%) dissolved in PBS, Triton X-100 and interferences were added to this baseline to study the current response. The voltammogram of cholesterol were measured by applying the negative going potential scan with frequency of 30 Hz, amplitude 20 mV and potential step of 4 mV. The responses were recorded after 2 minutes of immobilization (stabilization time) with the cholesterol. All responses were recorded under identical conditions.

6.6.7 Structural and morphological results

Figure 6.12 shows the SEM top and cross-sectional view (inset) of the Au nanowires of diameter 175±25 nm and length up to 20 µm released from alumina template. The structure of the Au nanowires can be clearly observed in the SEM top view, while the cross-sectional view further illustrates the uniform nature of nanowires deposited in the alumina template. Figure 6.13 shows the immobilization of biotin-streptavidin linkage on the Au nanowires. Finally, the

enzymes immobilized on the Au nanowire surface were characterized. Figure 6.14 shows the atomic force microscopic (AFM) image of the nanowires (a) before and (b) after immobilization with COX and CE (seen as bright spots). AFM image shows globules of COX/CE molecules on the electrode surface. The size of the globules is much larger than that of one molecule because of non-spherical shape of the globules after adsorption. FTIR spectra, further confirmed the functionalization of COX/CE on Au nanowires (Figure 6.15), The FTIR spectra shows amide I band through stretching vibrations of carbonyl (C=O) carboxylic group (1712 cm^{-1}), amide II band (1442) through bending vibrations of the N-H bond and peak at 1554 cm^{-1} is attributed to C=C stretching. The characteristics bands around 1650 (amide I) and 1554 cm^{-1} (carbonyl group) further confirm the binding of cholesterol oxidase and esterase on the Au nanowires. The broad stretching (not shown in figure) around 3000-3500 cm^{-1} is attributed to OH stretch from water.

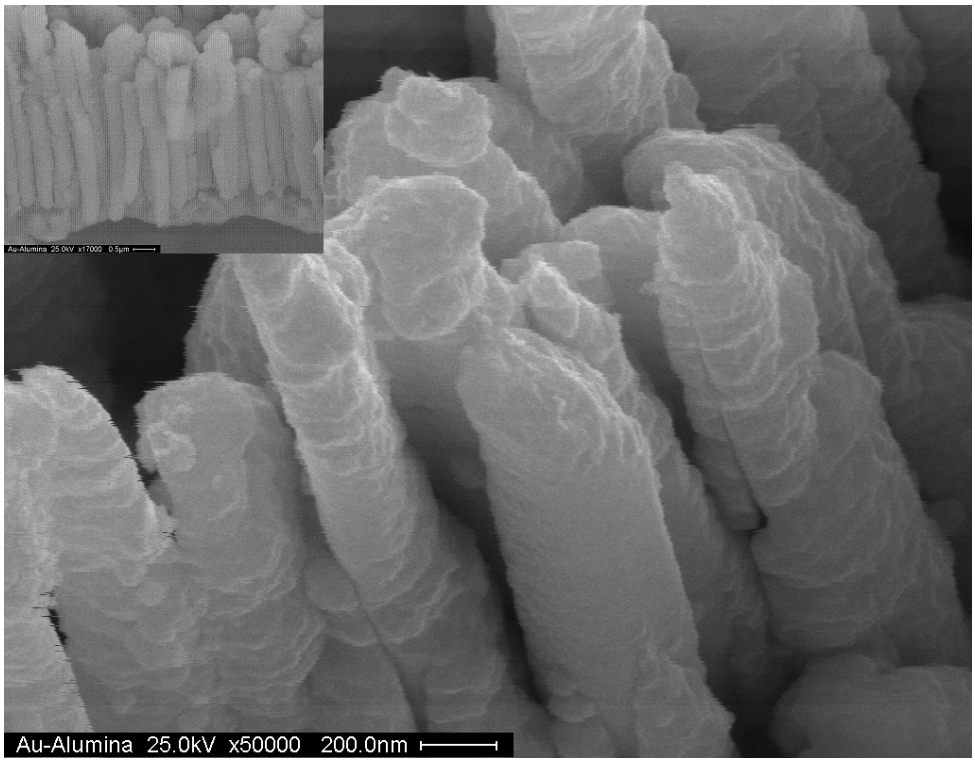

Figure 6.12 SEM images showing the top view and cross-sectional view (inset) of the 175±25 nm Au nanowires released from alumina template.

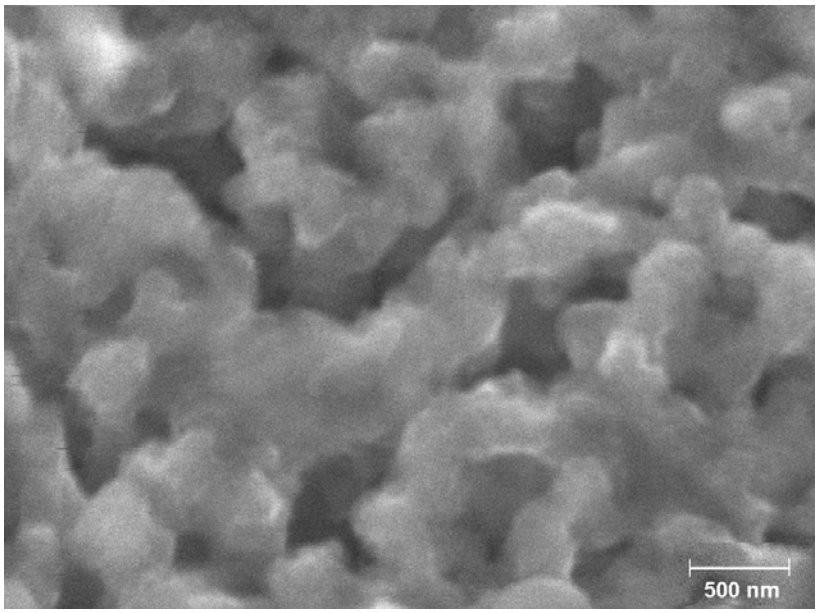

Figure 6.13 SEM image of Au nanowires specifically modified with biotin/avidin linkage**.**

6.6.8 Calibration results

As stated earlier, cholesterol is determined via direct physical adsorption of enzymes – COX and CE. COX catalyzes the oxidation of cholesterol, while CE catalyzes the hydrolysis of esterase esterified cholesterol, which is important for determination of total cholesterol. These enzymes help in monitoring both native and esterified cholesterol levels. More specifically, the cholesterol estimation is based on:

a) Hydrogen peroxide determination, as a result of COx reaction (6.3)

$$\text{Cholesterol} + O_2 \rightarrow \text{4-cholesten-3-one} + H_2O_2 \quad (6.3)$$

b) Cholesterol esterase reaction:

$$\text{Cholesterol ester} + H_2O \rightarrow \text{cholesterol} + \text{fatty acids} \quad (6.4)$$

Hydrogen peroxide is detected by the current response at the enzyme electrode as per the equation:

$$H_2O_2 \rightarrow O_2 + 2H^+ + 2e^- \quad (6.5)$$

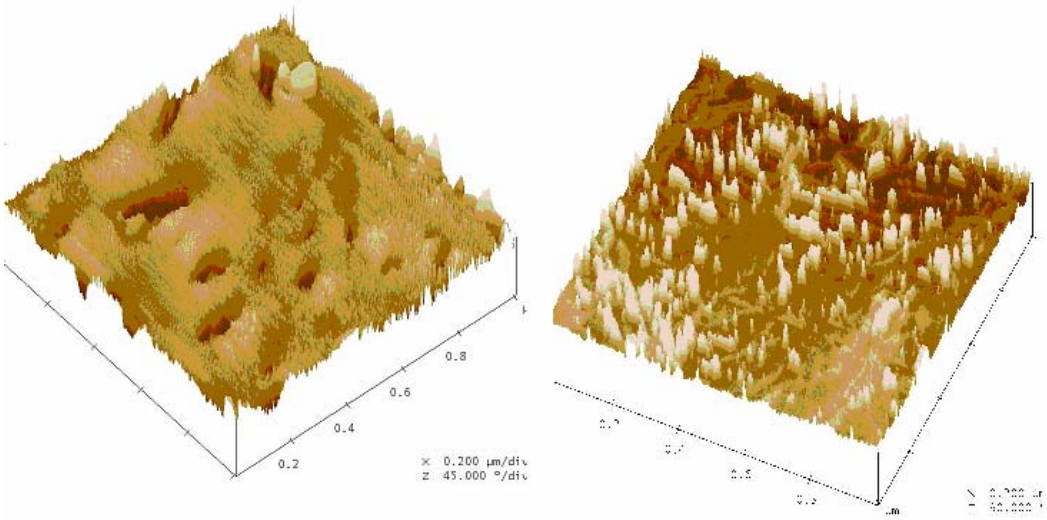

Figure 6.14 AFM images of Au nanowires a) before modification (left), b) after enzyme immobilization (right), showing the modified working electrode.

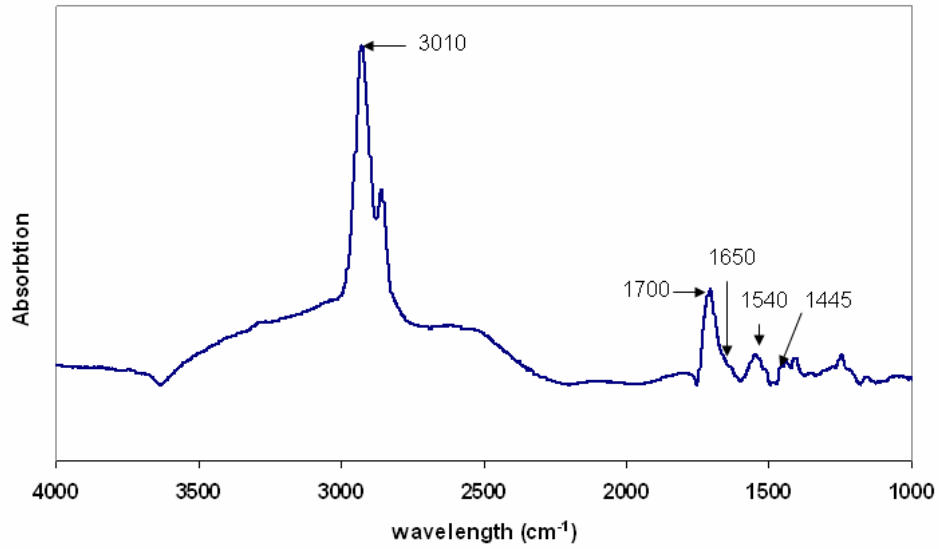

Figure 6.15 FTIR spectra of the Au nanowires after immobilization with enzymes COX and CE.

After numerous preliminary scans at different scan rates, the working potential range was optimized and set as -0.08 to 0.10 V and scan rate to 100 mV/s, respectively. Figure 6.16 shows the SW voltammograms recorded for varying concentrations of cholesterol (between 10 and 60 µM) at a step of 10 µM over the baseline blood serum. A very small background noise with the main activity between 0.01 and 0.09 V were observed. Interestingly, an increase in both the anodic peak at around 0.06 V and full width at half maxima (FWHM) were observed. The base

line blood serum also contains normal level of interferences such as ascorbic acid (2 µM), uric acid (10 µM), glucose (20 µM), lactic acid (50 µM), apart from varying levels of cholesterol. Figure 6.17 shows the calibration line created by taking the anodic peak currents for each concentration level. The linear response fits well in the following equation with an accuracy of ± 4 %, where the linearity coefficient, R^2 is 0.99.

$$I\ (nA) = 0.6054 * [\text{cholesterol}\ (\mu M)] + 0.2411 \quad (6.6)$$

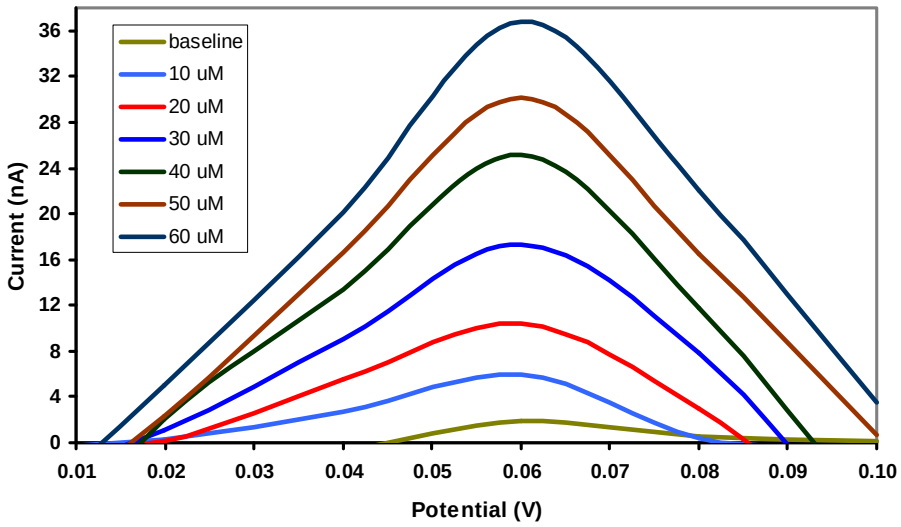

Figure 6.16 Square wave voltammograms (0.01 to 0.10 V) recorded at different concentration of cholesterol, from 10 to 60 µM with step of 10 µM.

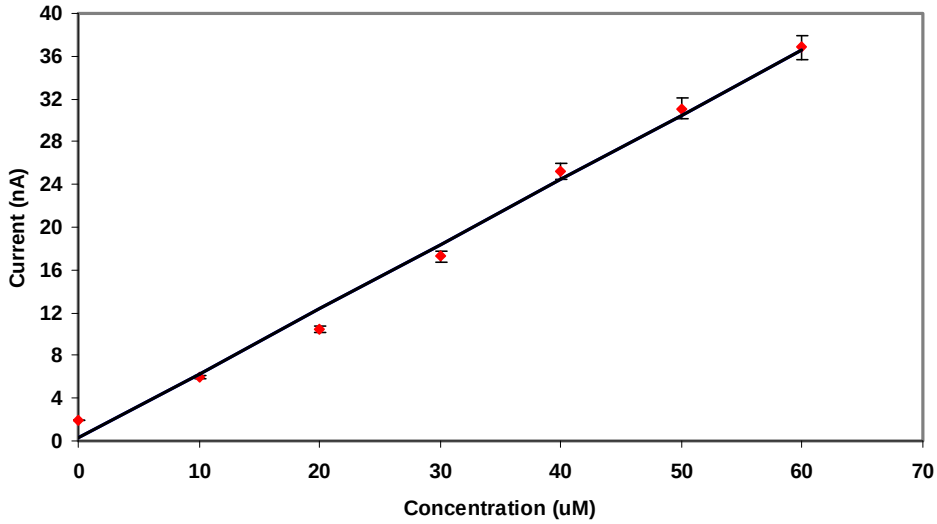

Figure 6.17 Calibration plot for cholesterol levels (10 to 60 µM with step of 10 µM).

The slight deviation in response could be attributed to the partial loss of enzymatic activity on the Au-NW. In the linear range, the sensitivity is estimated to be about 0.85 nA/μM better than the reported values for other materials such as metals or polymers (Roy et al., 2006; Brahmin et al., 2001). Moreover, when similar experiments were performed with Au microelectrodes (instead of nanowires) of width 100 μm and length 2 mm, it resulted in less than half the sensitivity and current response, further signifying the role of Au-NWs in enhancing sensor sensitivity (figure 6.18). The presence of Au nanowires, with large surface area (greater than 1000 m^2/g) causes a large amount of enzymes (COX and CE) to be functionalized. This large amount of functionalized enzymes yields a higher current response compared to the Au microelectrodes. In addition, the presence of Au nanowires enhances the electron transfer between the enzymes and the electrode and among the enzymes, similar to carbon nanotubes based sensors (Roy et al., 2006), resulting in further increase in current response and higher sensitivity.

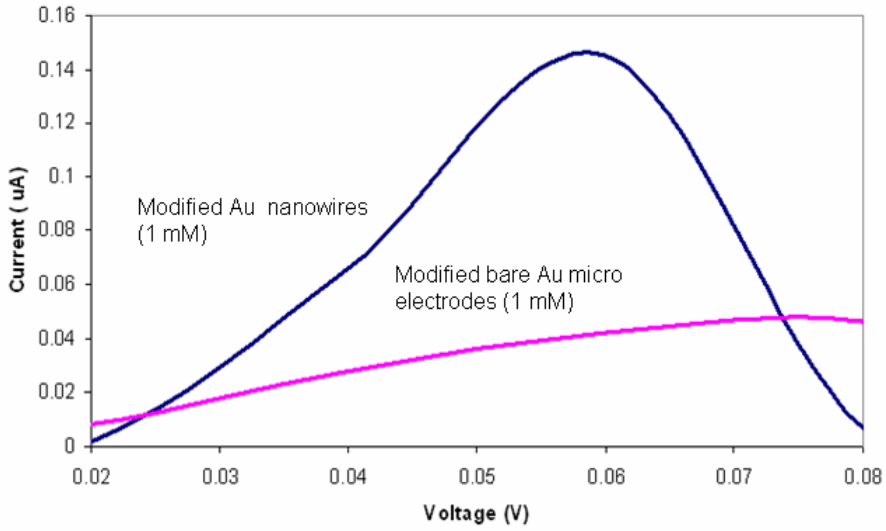

Figure 6.18 Comparison of current response between Au nanowires electrode and Au microelectrode.

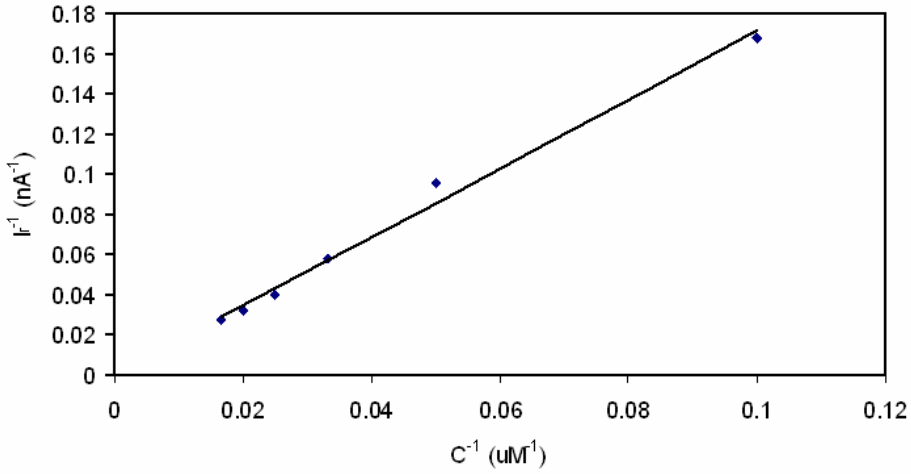

Figure 6.19. Lineweaver-Burk Plot of I_r^{-1} versus C_s^{-1} for the results shown in calibration plot of cholesterol biosensor.

Additionally, the apparent Michaelis-Menton constant (K_m^{app}), which gives an indication of the enzyme-substrate affinity and the maximum current response of the cholesterol biosensor was estimated from the Lineweaver-Burk equation (Figure 6.19) as,

$$I_r^{-1} = (1 + K_m^{app} C_s^{-1}) I_{\max}^{-1} \quad (6.7)$$

where, I_r is the steady state current obtained at cholesterol concentration level Cs. K_m^{app} is the apparent Michealis-Menten constant for the electrode and I_{max} is the maximum current response. Through linear regression, K_m^{app} and I_{max} were estimated to be 17.1 mM and 10 µA, respectively. This value of K_m^{app} is better than that reported for many multi-enzymatic/nanoelectrode cholesterol biosensors (about 7 mM) implying higher bioactivity, reliability and sensitivity of the present approach.

6.6.9 Selectivity and storage stability

From the above calibration plot, it can be seen that normal levels of interfering species had no significant effect on the anodic current peaks. Figure 6.20 shows the SW voltammogram response for two higher cholesterol levels, 30 µM and 50 µM, with 20 µM of urea, 50 µM of glucose and 4 M of ascorbic acid. Interestingly, the current response was within the error range of ± 4% implying no significant contribution. This high selectivity can be attributed to the Au-NW and low working potential (0.06 V). At these low potentials neither uric acid nor ascorbic acid is expected to oxidized, leading to highly selective and sensitive cholesterol detection.

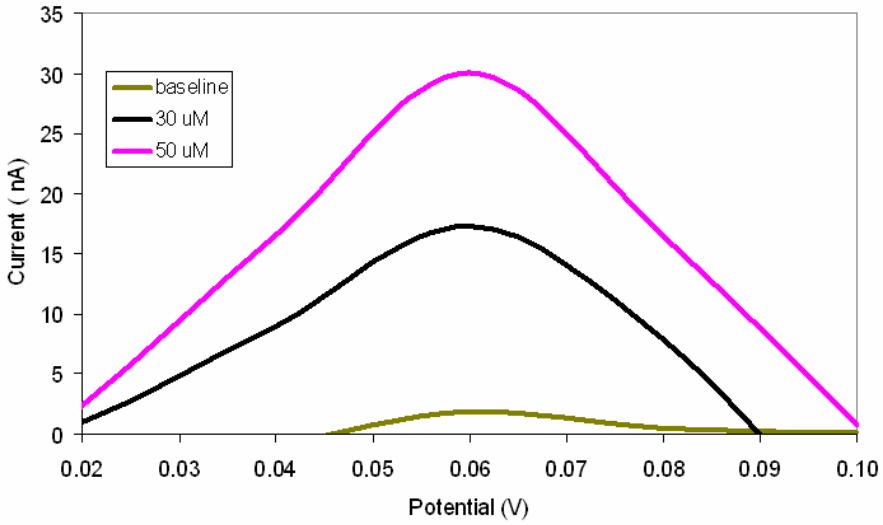

Figure 6.20 Interference study for cholesterol levels (30 and 50 µM) and higher level of interfering species (20 µM of urea, 50 µM of glucose and 4 M of ascorbic acid).

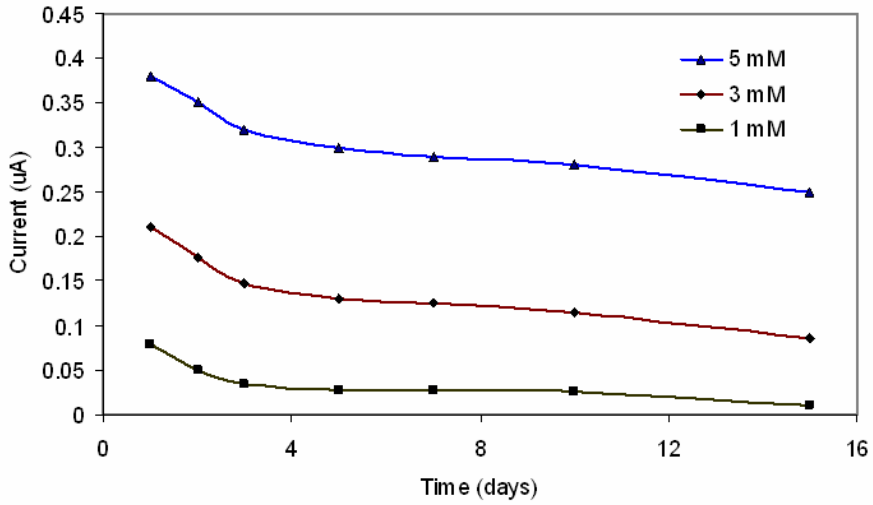

Figure 6.21 Storage stability study of current response as a function of time in days for three different concentrations (1, 3, 5 mM).

The operational and storage stability for the cholesterol biosensor was also evaluated. Twenty runs conducted at 3 mM cholesterol concentration yielded a very stable response that changed an indiscernible amount. The storage stability was tested by measuring the response for the modified electrode which was stored dry at 4 ºC at different time intervals. Accordingly, figure 6.21 shows the current response for three different cholesterol concentration levels (1, 3,

and 5 mM) recorded as a function of time (days). After an initial decrease in current response (20-25%) in the first two days, the sensor response was fairly constant up to ten days. This initial decrease in current may be attributed to the deactivation of immobilized enzymes from the electrode surface. The storage stability can also be improved further by other mechanisms such as lyophilization treatment and trehalose immobilization, which are currently underway.

6.7 Summary

In conclusion, in this chapter a prototype Electrochemical detection-on-Chip (EoC) module utilizing nanowire electrodes, electrochemical techniques and MEMS/microfluidic platform was demonstrated. In particular, an electrochemical biosensor for estimation of targeted species such as blood cholesterol was developed successfully using modified Au-NWs - based MEMS microfluidic platform. The Au-NWs, modified using enzymatic assays - cholesterol oxidase and cholesterol esterase, promotes better electron transfer, operates at low potentials and show enhanced sensitivity. A good linear relationship between current response and cholesterol level was observed within the testing range of 10-60 μM of cholesterol. Further, no significant contribution of the interfering species such as ascorbic acid, urea, and glucose were observed on the current response. On studying the storage stability, it can be concluded that these kind of modified electrodes seem useful as disposable sensors. Tests conducted with Au electrodes yielded poor detection limits towards nitrate ions. Furthermore, due to the assembly of the Au-NWs in the microfluidic device and its compatibility to MEMS technology, the proposed scheme can be integrated in Lab-on-Chip systems.

CHAPTER 7

ELECTROCHEMICAL NITRATE SENSOR WITH INTEGRATED MICROFLUIDICS

7.1 Introduction

This work describes the development of a nitrate-selective electrochemical sensor using doped polypyrrole (PPy) nanowires on a microfluidic platform. Determination and estimation of nitrate ion is important for a variety of applications in different fields, including environmental engineering, marine cycles, food analysis, water management, biology and medicine (Moorocroft et al., 2001). In addition, precise nitrate concentration management is needed for growing field of precision agriculture. Federal health and environmental agencies, ecological scientists, oceanographers, and farmers have a great need for small, low-power reliable and yet sensitive nitrate sensors that can be remotely operated and measure concentrations in the range of 1 μM to 1 mM.

In spite of the increase in current understanding of their role within environmental matrices, a substantial degree of uncertainty and speculation still remains. Nitrate is a widespread contaminant of groundwater and surface waters worldwide, because of being in such diverse materials such as fertilizers, foods, livestock feeds, wastewater and drinking water. The extensive use of nitrate fertilizers in agriculture negatively impacts fresh water, ground water and marine ecosystems by simulating the occurrence of eutrophication and algae blooms (Addiscott et al., 1991). In general, nitrate concentration in surface and ground water are mainly induced by the following factors: a) domestic sewage effluent and animal effluent from farms, b) discharge of domestic and industrial waste waters, c) runoff and seepage water from land containing nitrified products of decayed vegetation and animal matter, d) fixation of atmosphere by bacteria present in leguminous plant and lightning process, e) excess use of nitrogenous fertilizers and f) geological deposits of nitrogen rocks.

About 78% of earth's surface is nitrogen. Biotic and abiotic processes are involved in nitrogen cycle in the ecosystem. Bacteria both free living and in plants, assimilate atmospheric nitrogen. For example, Rhizobium bacteria living in the roots of plants and cyanobacteria are the most common nitrogen-fixing bacteria. This path is considered the major natural rote for capture of atmospheric nitrogen. Another pathway for atmospheric nitrogen transfer to earth is through lightning, when nitrogen and oxygen combine to form nitric oxide. Followed by reactions with water and oxygen, they become nitrate and nitrite. In other cases, there are also natural deposits of nitrate salts.

The presence of nitrate ions in environment or food samples has potential human health threat, especially in infants, causing blue-baby syndrome, some forms of cancer and congenital defects (Kurzer et al., 1981). Chronic consumption of high levels of nitrate may also cause other health problems; including some forms of cancer and teratogenic effects. Even though, current data are inconclusive, there are causes for concern. A contentious health concern is possible formation of carcinogenic nitrosamines within the acidic conditions of stomach and their subsequent implication in the pathology of gastric cancer. Upon reaching the stomach, nitrite is converted into nitrous acid, which can act as a powerful nitrosating agent. Because of its role in ecosystem dynamics and its potential impact on human health, nitrate level is carefully monitored in municipal water lines, engineered and environmental systems worldwide to prevent exposure of populations to harmful levels. To address these concerns, US EPA and European Community have set limits of nitrate (10 ppm nitrate-N or 0.7 mM/L and 11.3 mg/L nitrate-N respectively) in potable water.

The other significant area, which also forms the basis for this research is ocean research and monitoring. Plant nutrients such as nitrate, phosphate, silicate and ammonia play a key role in controlling ocean, in particular costal ecosystem. These chemicals are essential nutrients that are required by phytoplankton and benthic plants for growth. In natural ecosystems, all of these nutrients are generally the factor that limits the accumulation of plant biomass (Johnson et al., 1991). The increase flux of nitrates can led to number of negative impacts on ocean ecosystem. Elevated concentrations of plant nutrients caused eutrophication or the increased production of plant organic carbon. Further, the increased concentrations may lead to a shift in ecosystem structure. Such rapid shifts in ecosystem structure may favor increase in the concentration of

phytoplankton that produces toxic compounds such as Harmful Algae Blooms (HAB) or "red tides."

7.2 Current methods of nitrate detection

The current methods of determination of nitrate can be divided into three main categories: direct, through a reduced nitrogen species, and indirect (Glazier et al., 1998). Table 7.1 summarizes a variety of techniques which fall into these categories.

Table 7.1 Methods for nitrate determination. Adapted from Glazier et al., 1998.

Direct	
	Nitration of phenols and colorimetry
	Oxidation of organics and colorimetry
	Ion-selective electrode detection
	Direct UV-absorbance spectrophotometry
	Gas chromatography after derivatization
	Electrophoretic
	Nitration of salicylic acid
	Ion chromatography
Reduced nitrogen species	
	Reduction to nitrite and
	Spectrophotometry
	Electrochemistry
Reduction to ammonia and	
	Colorimetry
	Potentiometry
	Conductimetry
Reduction to nitric oxide and	
	Chemiluminescence
Indirect	
	Atomic absorption spectrophotomety
	Polarography

Traditionally, air segmented continuous flow analyzers were used for determination of nitrates. Such devices are costly to buy and to operate (technical staff and chemists are required) and are not selective (Moorocroft et al., 2001). Sampling is also necessary and this has two major disadvantages: 1) sample can change in composition from time of sampling to analysis; 2) the information on sample is not available immediately. Other approaches involve reduction of relatively inert nitrate to more reactive nitrite before initiating the detection sequence. A variety of reducing agents have been investigated to facilitate this conversion, which include zinc, amalgamated cadmium, hydrazine copper, copperised cadmium or by photo-induced reduction (Goff et al., 2003). The other popular method is spectroscopic detection due to the excellent limits of detection and facile assay-type protocols (Moorocroft et al., 2001). While compositional complexities offered by real samples often preclude such direct UV determination of nitrate. Satlantic's ISUS v2 nitrate sensor uses the absorption characteristics of inorganic compounds in the UV light spectrum. By using UV absorption technology, the ISUS instrument yields the nitrate absorption spectrum and directly computed concentration. Fourier-transform infra-red (FT-IR) spectroscopy and raman spectroscopy have also been utilized for spectroscopic determination of nitrate in aerosols (Moorocroft et al., 2001).

However, the focus of this work was to develop an electrochemical sensor such as amperometric or potentiometric using the technology already developed (chapter 6) with integrated microfluidics. The important advantages are its simplicity, ease in miniaturization and microfabrication, low power consumption and yet sensitive enough for targeted applications. Various electrodes such as copper, nickel, copper-nickel alloy, cadmium, platinum, glassy carbon, gold, lead, and boron-doped diamond have been used to reduce nitrate electrochemically. Despite thermodynamic feasibility of the reduction, the kinetics of the charge transfer is slow and such, direct reduction of nitrate has been characterized by poor sensitivity and often marked irreproducibility through cumulative electrode passivation effects. The need to apply large over potential can also affect the selectivity of this approach. Later approaches involved surface modifications and conditioning steps. In recent times, nitrate determination via the selective reduction of nitrate to nitrite by nitrate reductase enzyme (biological catalysts) is gaining credence (Glazier et al., 1998). Transduction of this reaction involves the monitoring of reduction current of an electron mediator, methyl viologen, which shuttles electrons between the enzyme and an electrode. There have been also few reports of nitrate biosensors in the literature (Moorocroft et al., 2001; Glazier et al., 1998). Nitrate reduction was achieved with a nitrate

reductase-based electrode which utilized a polythiophene bipyridinium film as the electron mediator. The enzymatic reaction could be observed in this system only through prolonged electrolysis, which resulted in an accumulation of nitrite in solution. Catalytic reduction currents could not be distinguished from background, presumably due to low enzymatic activity at the electrode surface A similar study reported the ability of a bipyridinium thiol bound to a gold electrode to act as an electron mediator for nitrate reductase.

The most common and commercial potentiometric approach is to use ion-selective electrodes (ISEs), whereby the selective passage of charged species from one phase to another, typically from solution to membrane, gives rise to potential difference, which varies with a Nernstian fashion with the activity of the ionic species (Pretsch et al., 1988). A calibration graph for potential versus nitrate concentration can thus be obtained. ISEs offer attractive features as nitrate sensors, including ease with which they can be coupled with continuous flow systems such FIA and in flow systems with sample injection. However, ISEs posses no inherent anion recognition functionalities and they respond based on the anion's lipophilicity (Pretsch et al., 1988). They typically respond to ions according to Hofmeister series: large lipophilic anions > ClO_4^- > SCN^- > I^- > NO_3^- > Br^- > Cl^- > $H_2PO_4^-$ (Hofmeister et al., 1888). This series implies that commercial nitrate ISEs is more selective to prechlorates and iodides than nitrates. Therefore, it is necessary to incorporate selective interactions between ionophores and nitrate using chemical recognition principles. This would enable truly selective nitrate-sensor development, one not limited by the Hofmeister series. Selectivity is a major concern in electrochemical sensors and many surface modifications including immobilized enzymes, freshly deposited electrode surfaces, and complexing metal-ions have been used. In this work, selective chemical recognition sites towards nitrate are achieved in amperometric-based electrochemical sensors through the use of novel sensing modalities. Amperometry usually offers simpler analyses and lower detection limits than potentiometry.

7.3 Sensing modality

7.3.1 Nanosensor elements: polypyrrole nanowires

The advantage in applying nanosensor elements in electrochemical sensing has been emphasized enough in the last chapter. It is also known that increased sensitivity in electrode response can be achieved by maintaining a large and highly active surface area. Nanowires, being one-dimensional structures have a large surface-to-volume ratio and lower diffusion resistance,

thus enhancing the capture cross section. Recently, the use of conducting electroactive polymers such as polypyrrole, polythiophene, polyacetylene, polyaniline as the active component of electrochemical sensors has attracted much attention (Wang et al., 2000). The ability to incorporate and expel ionic species during the switching of the polymer from the oxidized to reduced state has been used to produce analytically useful signals from conducting polymer sensors.

$$P^0 + A^- \rightarrow P^+A^- + e^- \quad (7.1)$$

P and A represent the polymer and the "dopant" atom anion respectively. The latter serves to maintain electrical neutrality, which is to counterbalance the positive charge of the polymer backbone. Further, conducting polymers are emerging as promising material for synthesis of nanostructured devices, because they exhibit electrical, electronic, magnetic, and optical properties similar to metals or semiconductors while retaining their flexibility, ease of processing, and tailored electrical conductivity (Martin et al., 1994; Cheng et al., 2005). The electrical conductivity of these polymers can vary from an insulator to almost the metallic state and can be reversibly modulated over fifteen orders of magnitude by controlling the dopant type and level (Duchet et al., 1998). Their porous structures are very amenable to entrapping biomolecules. A variety of conducting polymers have shown promise as sensor materials, including chemical and biosensors, because their properties can be tailored to detect a wide range of chemical compounds (Wanekaya et al., 2006).

Polypyrrole (PPy) is one of the widely studied conducting polymers because of its high conductivity, ease of preparation, flexibility, and stability as ion-selective electrode material (Martin et al., 1994). Furthermore, polypyrrole-doped nanowires show high selectivity and rapid reactivity towards the dopant ion and integration ability as sensor elements (Hutchina et al., 1995; Bendikov et al., 2005). In its oxidized state, polypyrrole exists as a polyradical cation and at the oxidation stage; nitrate anions are attracted electrostatically into the PPy matrix as dopants or counter ions, as illustrated below (Bendikov et al., 2005)

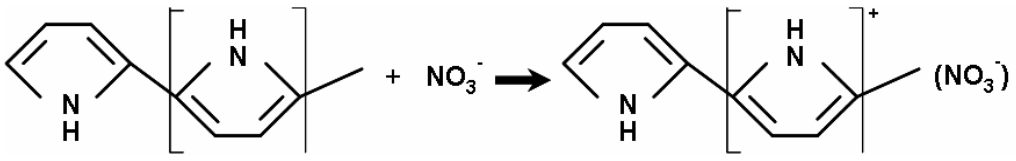

(7.2)

7.3.2 Synthesis of polypyrrole nanowires

Among the methods that have been used to fabricate conducting polymers on the nanometer scale are electrochemical dip-pen lithography, mechanical stretching, electrospinning, template-directed electrochemical synthesis and electropolymerization (Wangekaya et al., 2006). Dip-pen nanolithography (DPN) is a nano-patterning technique in which an AFM tip is used to deliver molecules to a surface via a solvent meniscus. Doped polyaniline and polypyrrole lines down to 310 nm and 290 nm line-widths, respectively, have been formed using ionically charged conducting polymers as the "ink". In the mechanical stretching procedure, conducting polymer nanowires are fabricated by electrochemical polymerization of the corresponding monomer onto a sharp scanning tunneling microscope (STM) tip that is held between 20-100 nm from an electrode followed by the reduction of the diameter of the deposited polymer by stretching by moving the STM tip (Wangekaya et al., 2006). Like other nanowires, 1-D conducting polymer nanowires can also be synthesized by template-directed methods (Cheng et al., 2005; Martin et al., 1994). Porous anodic alumina oxide (AAO), track-etched porous polymer membranes, and mica are the three types of templates that are commonly used with and electrochemical deposition. Electrochemical deposition is accomplished by coating one face of the template with an inert conducting film (gold and platinum) and using this inert conducting film as the anode. The polymer is then electrochemically synthesized within the pores of the membrane. The length of the nanowires is determined by the current density and deposition time. Chemical template synthesis can be similarly accomplished by simply immersing the membrane into a solution of the desired monomer and its oxidizing agent. The diameter of nanowire is determined by the pore diameter of template. In other methods, PPy nanowires can also be obtained at the edge of lipid-tubules or at the steps and pit defects of highly-oriented pyrolytic graphite (HOPG). It is noteworthy that the nanowires synthesized by this template method have shown higher conductivity and strength over conventional bulk-synthesized polymers.

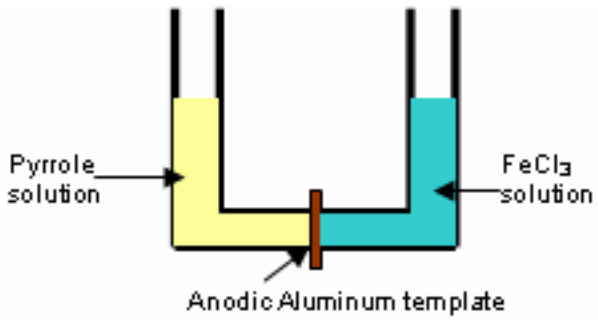

Figure 7.1 Two compartment cell for synthesis of polypyrrole nanowires.

In the present work, PPy-NWs were synthesized in a two-compartment cell (as shown in figure 7.1) (Zhang et al., 2005; Duchet et al., 1998). The nanoporous alumina template (pore diameter: 200 nm, thickness: 60 μm) was placed between the two compartments, with 0.2 M of pyrrole monomer and 0.2 M of $FeCl_3$ oxidant on each side. Initially, only pyrrole monomer was allowed to diffuse through the template for 20 minutes. Then, the oxidant, $FeCl_3$ was added in the second compartment. Both monomer and oxidant diffused towards each other through the pores of the template, resulting in polymerization of polypyrrole nanowires. The entire polymerization reaction was carried out for 4 hours with new solution added every 1 hour. Figure 7.2 shows the SEM front (7.2a) and back-side (7.2b) images of the nanoporous alumina template with pores filled with polymerized polypyrrole. The template was then removed from the cell and thoroughly rinsed in DI water. Next, the PPy-NWs were released by dissolving the template in warm 45% KOH with periodic agitation and centrifugation at 7000 rpm. The supernatant was decanted, replaced with clean methanol and ultra-sonicated for about 1 min. This protocol of nanowire collection/solvent addition/ultra-sonication was repeated three times to completely clean the PPy-NWs. Figure 7.3 show the SEM cross-sectional view of bunch of 200±25 nm PPy-NWs released from template. It can be observed that the released PPy-NWs have a smooth surface and are uniform in diameter, but tend to aggregate when left free in solution. Figure 7.4 shows the FTIR spectrum of polypyrrole nanowires in alumina template. The bands around 1567 and 1452 cm^{-1} may be assigned to typical polypyrrole ring vibrations. The bands at 1312, 1051 cm^{-1} may correspond to C–H band in-plane vibration. The broad band around 1203 cm^{-1} may be due to N–C stretching band. The peak observed around 878 cm^{-1} may be assigned to the C–H out of plane vibration indicating polymerization of pyrrole.

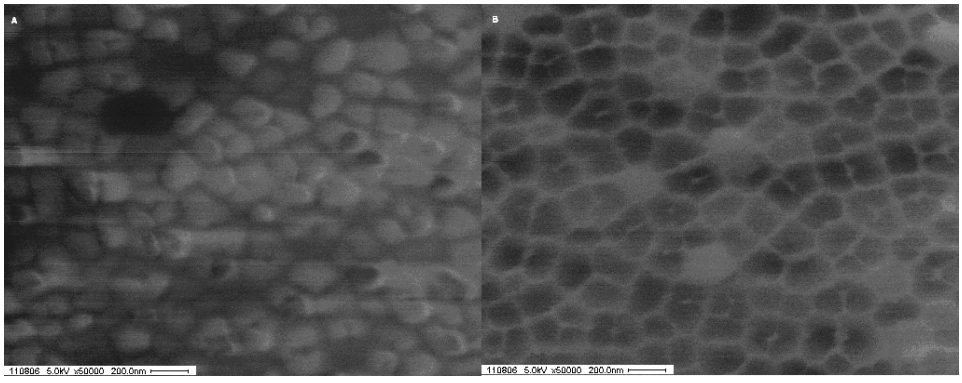

Figure 7.2 a) SEM image of alumina template (front side) with 200-250 nm PPy nanowires polymerized in the nanopores, b) SEM backside view of alumina with pores partially filled with PPy nanowires.

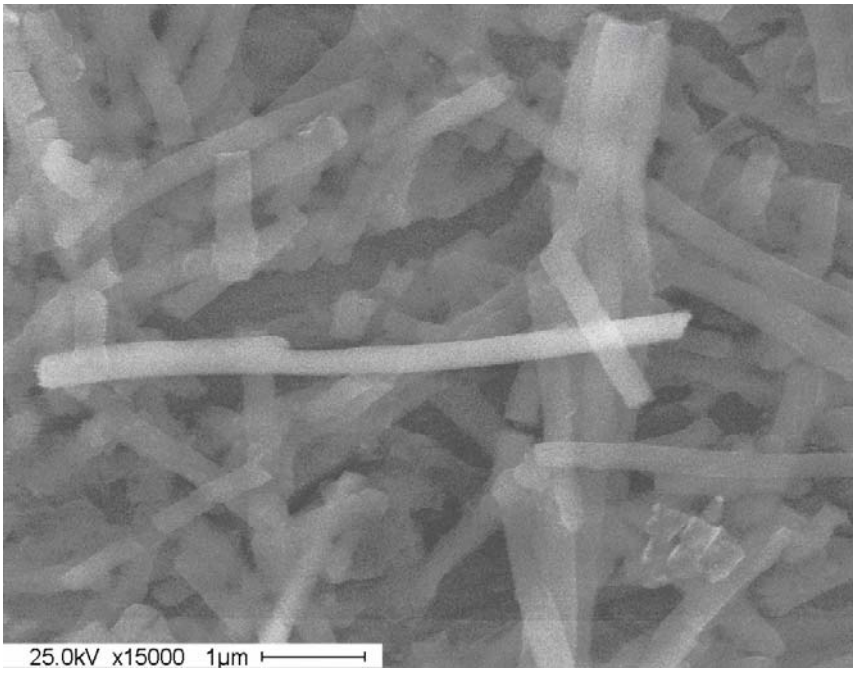

Figure 7.3 SEM view of bunch of 200±25 nm PPy nanowires after released from alumina template.

7.3.3 Incorporation of chemical recognition sites

The next step is to achieve selective chemical recognition for nitrate by electrochemical polymerization (doping) of an appropriate monomer (pyrrole) under controlled conditions to allow generation of selective recognition sites in the PPy layers (Lu et al., 1989; Pearson et al., 1992). On polymerizing PPy layers in presence of $NaNO_3$, pores that are complimentary to the size of the target nitrate ion are produced. The size of the pore and charge distribution within the doped polypyrrole form a host cavity for nitrate, thus providing enhanced selectivity over conventional nitrate-selective ISEs (Bendikov et al., 2005). An example for application of chemical recognition elements in development of selective ISEs is chloride-selective electrodes prepared by doping chloride into polypyrrole films (Dong et al., 1988). Another type of recognition element involves metal-ligand interactions. Such interactions have been used in development of phosphate and nitrate-selective electrodes based on organotin, porphyrin or corrin ionophores (O'Reilly et al., 1991). In this manner, both lower detection limit and improved sensitivity are achieved by utilizing doped polypyrrole nanowires, instead of conventional polypyrrole films.

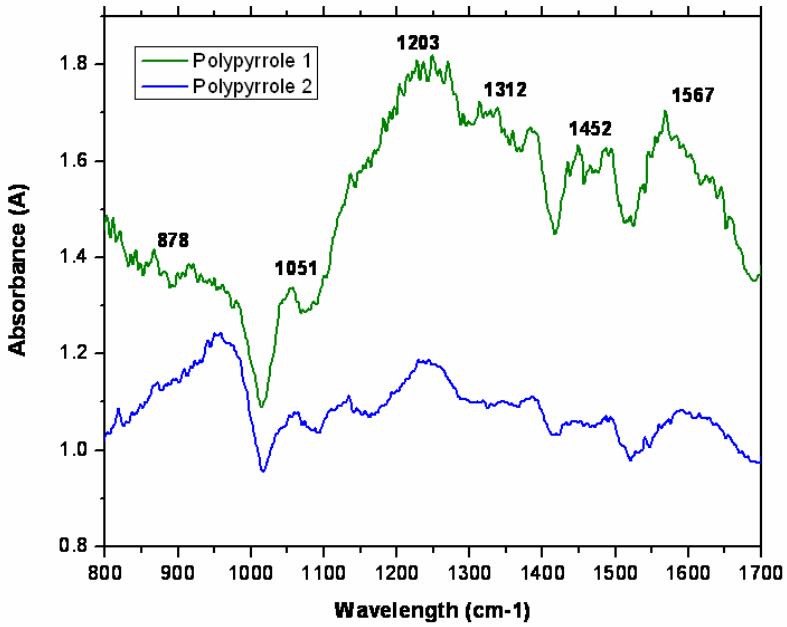

Figure 7.4 FTIR spectra of polypyrrole nanowires in alumina template. Polypyrrole 1 refers to the front side of template, 2 refers to the other side.

Polymerization of polypyrrole-doped with nitrate was performed galvnostatically (Bendikov et al., 2005). The electropolymerization solution, composed of 0.5 M pyrrole and 0.5 M $NaNO_3$, which were deoxygenated before the experiment by purging with N_2. Autolab PGSTAT30 potentiotat/galvanostat was used to supply constant current at 2 mA/cm^2 for 10-20 minutes. Silver wire and on-chip deposited platinum electrode were used as reference and counter electrodes respectively. After the polymerization reaction, the doped PPy-NW electrode was conditioned in 0.1M $NaNO_3$ for either 2 or 24 hours. Having established the sensing modality in the form of nanosensor elements and selective chemical recognition sites, the next step was to integrate these doped-sensor elements onto a integrated microfluidic electrochemical sensor platform.

7.4 Development of electrochemical sensor with integrated microfluidics

7.4.1 Overview

The objective of this present work was to develop nitrate-selective and highly sensitive electrochemical sensor, implemented on a microfluidic platform, as illustrated in Figure 7.5. The integrated sensor was built and tested in three stages:

Generation I: In the Generation I, sensor calibration was done under standing or static conditions with micromachined electrodes and microfluidic chambers.

Generation II: In the Generation II, the sensor was implemented and tested under dynamic conditions involving a flow through microfluidic platform with flow channels, micromachined sample chamber and fluidic inlet/outlet and syringe pump. No microscale packaging was performed, however, the platform was packaged using Plexiglas housing. Microfluidic integration of the electrochemical sensor: a) enabled working at low sample volumes with better control over chemical reactions, b) lowered fabrication cost, c) enhanced analytical performance and resolution, d) eliminated need for sampling, e) speed up analysis times, and f) ensured portability.

Generation III: During the Generation III, sensor platform would be fully packaged with microscale packages such as PDMS lids along with Nanoport™ inlet/outlet assembly, micro control valves and on-chip potentistat. The long-term goal of this project is to develop a remotely-operable, field-deployable, network of microsensors to monitor chemical species in large volumes of ocean in time-space scales.

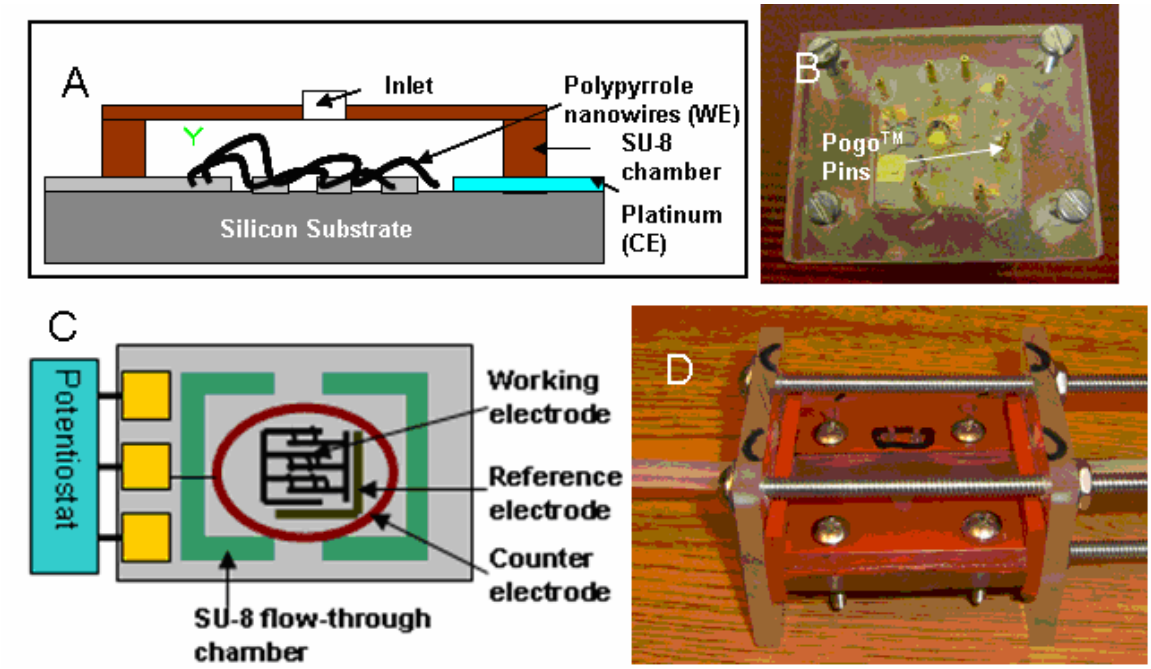

Figure 7.5 Electrochemical nitrate sensor chip. a) illustrative view, b) actual picture of the electrochemical cell, c) illustration of the flow through electrochemical test cell, d) picture of through flow cell shown with inlet/outlet and Pogo™ pin connectors.

7.4.2 Materials

Standard and buffer solutions were prepared using deionized water of resistivity 18.2 MΩ. Pyrrole monomer, ferric chloride, sodium salts of nitrate, chloride, sulfate, phosphate and perchlorate were obtained from Sigma-Aldrich (St. Louis, USA). All chemical reagents were analytical grade and used without purification, except pyrrole. Pyrrole was purified by distillation under nitrogen before use and stored at 4 ºC in dark. IAPSO standard seawater (salinity 34.996) was obtained from Ocean Scientific International (Hampshire, UK). Nanoporous alumina templates were obtained from Whatmann Inc. (NJ, USA).

7.4.3 Fabrication of electrochemical sensor chip and microfluidic platform

The construction of the microfluidic platform includes the fabrication of electrochemical sensor chip, assembly of PPy-NWs on the chip, and integration of micromachined fluidic paths and microfluidic components (Figure 7.5). The fabrication of the electrochemical sensor and nanowires assembly were similar to electrochemical biosensor (Chapter 6). Figure 7.6 illustrates the assembly of PPy-NWs nanowires on the Pt lines, achieved using dielectrophoresis (DEP) technique. The interdigitated assembly lines and the counter electrode were fabricated in Pt, with

Ti as adhesion layer on 7740 Pyrex substrate (2.5 x 2.5 mm) (Figure 7.6A). The microfluidic flow paths and reagent chamber were then patterned using 100 μm thick SU-8 film (MIcrochem Corp, Newton, MA). The SU-8 film was hard baked at 180 ºC for 10 minutes to prevent any out-gassing or contamination. The Pt lines, as described earlier were fabricated as interdigitated fingers of width and spacing 50 μm and 10 μm respectively (Figure 7.6C). Figure 7.6B shows the microfluidic chamber to house the reagents. Dielectrophoresis is the selective assembly of neutral particles in a liquid dielectric medium by non-uniform electric field (Boote et al., 2005). Using the alignment process described in previous works (Aravamudhan et al., 2005), dilute suspensions (100 μL, approximately 10^6 wires/mL) of the PPy-NWs in methanol were dispensed on the interdigitated Pt lines. An alternating electrode voltage of 10-20 V_{rms} at a frequency of 20 KHz was applied to the left Pt lines (represented as 1 in Figure 7.6A) relative to the right grounded Pt lines (represented as 2 in Figure 7.6A) for about 60-90 seconds. The assembly was monitored by studying the series current and later verified by microscopy (Figure 7.6C). Due to the random distribution of PPy-NWs, as shown in Figure 7.6C (inset), along the interdigitated Pt lines, the number of nanowires assembled was not measured. The PPy-NWs on the interdigitated Pt lines act as the working electrode in the subsequent electrochemical measurements. Finally, the PPy-NWs and electrochemical sensor chip was cleaned thoroughly to remove any excess nanowires and left overnight for drying. Gen I sensor is illustrated in figure, testing was done under static conditions.

Generation II sensor for dynamic testing was built as follows. The microfluidic components, tubing and fluidic connectors were integrated to the electrochemical sensor chip, as shown in Figure 7.7. The electrical connections were drawn using Pogo™ pins (Everett Charles Technologies, CA, USA). The primary objective of this flow through setup is to mimic a steady, unidirectional effluent flow in water systems. The setup is a representative of a flow analysis system with inlet/outlet flow rates controlled using PHD 2000 Syringe pump (Harvard Apparatus Inc., Holliston, MA, USA). A continuous flow of nitrate was introduced into the system via a syringe pump; along with intermittent nitrate spikes injected using a conventional syringe. The description of the Generation III of all micromachined nitrate sensors (Gen III) is described in the last section.

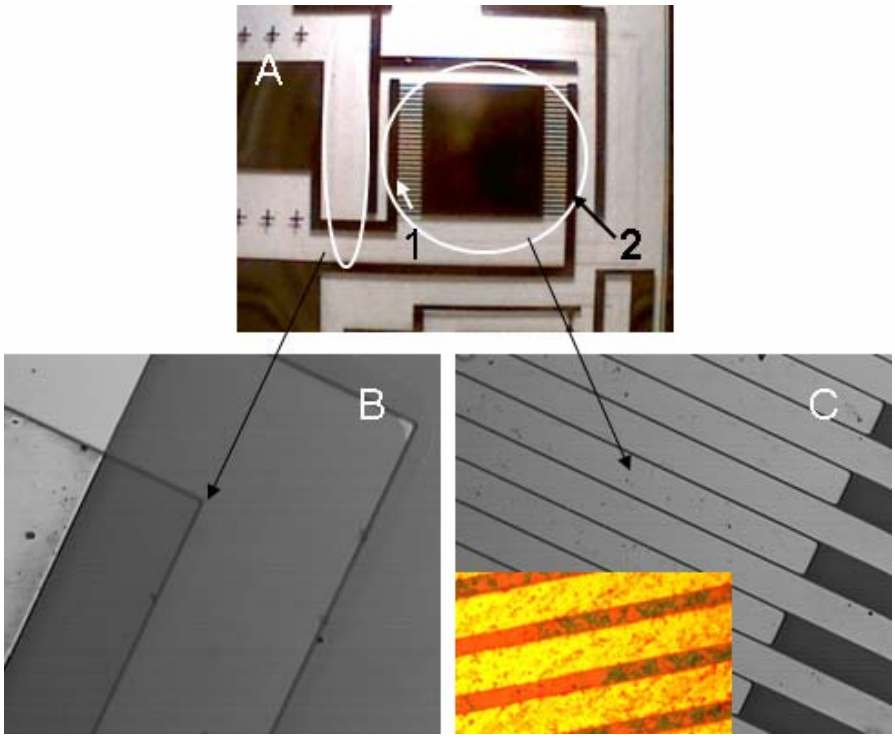

Figure 7.6 Test cell with Pt assembly lines and counter electrode. a) Full view, b) picture of the SU-8 microfluidic chamber, b) close-up view of the assembly lines with PPy nanowires (inset) assembled on them.

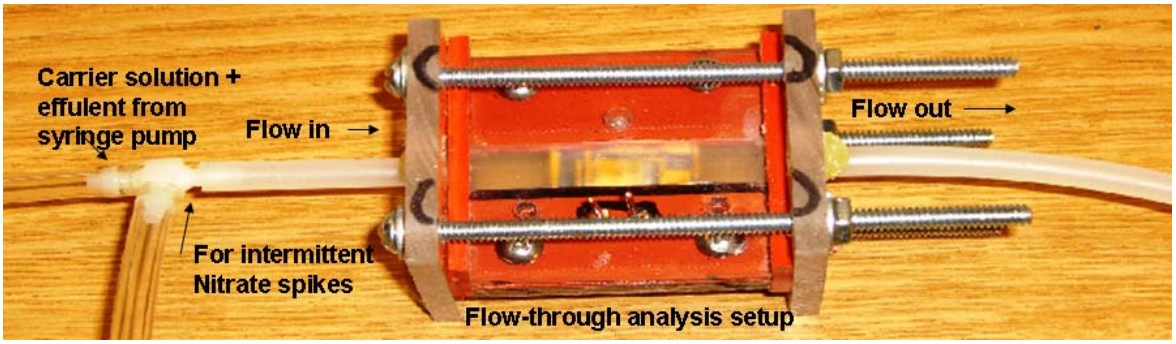

Figure 7.7 Picture of the flow through analysis setup with assembled microfluidic components, connectors and tubing.

7.4.4 Electroactivity of doped PPy nanowires

Electroactivity or electrochemical reactivity of doped PPy-NWs towards nitrate ion was tested using cyclic voltammetry (CV) technique. A CV result rapidly provides qualitative information about the thermodynamics of redox processes, or the kinetics of heterogeneous electron-transfer reaction and on coupled chemical reactions or adsorption processes (Wang et al.,

2000). It offers a rapid location of the redox potentials and convenient evaluation of the effect of media upon the redox reaction. CV consists of scanning linearly the potential of stationing working electrode using a triangular potential waveform with single or multiple cycles. During the potential sweep, the potentistat measures the current resulting from the applied potential. The resulting plot of current versus potential is termed as cyclic voltammogram, which is time-dependent function of large number of chemical and physical processes. Four of the observables, the two peak currents and tow peak potentials provide the basis for the diagnostics developed by Nicholson and Shain.

Figure 7.8 shows the cyclic voltammograms of doped PPy-NWs for three different $NaNO_3$ solutions (0.1, 0.2, 0.5 mM) at scan rate of 25 mV/s. The voltammograms indicate the PPy-NWs to be electroactive for $NaNO_3$ concentrations with nitrate reduction peak at about -0.1 V. Based on these experiments, the determination of nitrate ions using doped PPy-NWs was considered feasible.

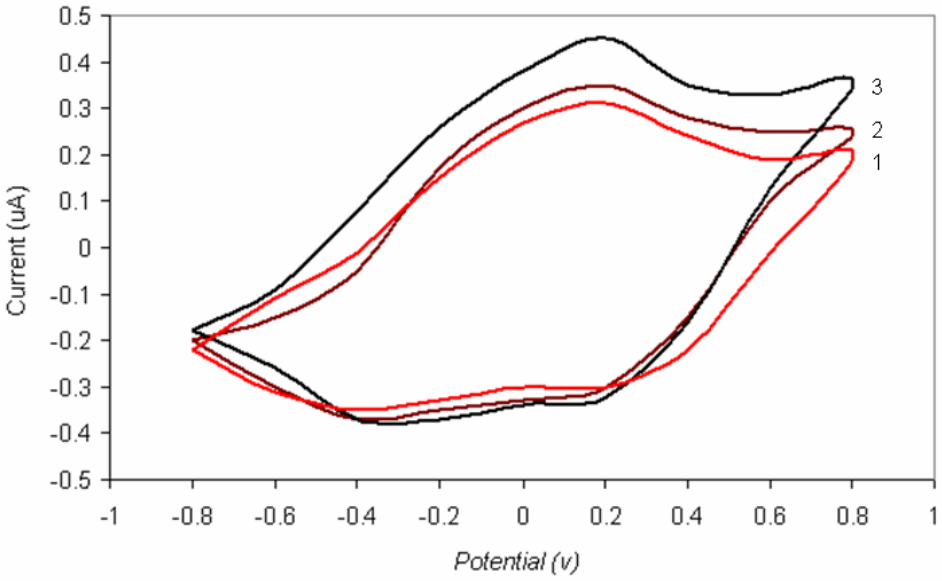

Figure 7.8 Cyclic voltammogram of PPy-NWs electrodes. Curves show 1) 0.1 mM, 2) 0.2 mM, and 3) 0.5 mM of $NaNO_3$ electrolyte solution at scan rate of 25 mV/sec.

7.4.5 Generation I: electrochemical measurements under static conditions

Constant-potential or amperometric sensors are ideally suited for monitoring analytes that are electroactive at moderate potentials. Such devices are characterized by remarkable sensitivity, high selectivity, wide linear range, low dead volumes, fast response, and relatively simple and

inexpensive instrumentation. Amperometric static measurements were performed with Autolab PFSTAT30 potentiostat/galvanostat (as shown in figure 7.9). The measurements were performed in the standard three-electrode format with doped PPy-NWs, Ag/AgCl double junction electrode and on-chip deposited platinum electrode as the working, the reference and the counter electrode, respectively. Initially, the electrochemical response of the doped PPy-NWs to varying levels of nitrate (10-1000 µM) was recorded to obtain the calibration plot. Two sets of effluent carrier solutions were used in these measurements. In the first set of experiments referred to as *DI-cal*, de-ionized water was used to obtain baseline calibration and nitrate (10-200 µM) was progressively added to the baseline solution. In the second set of experiments, referred to as *Ocean-cal*, IAPSO standard seawater (salinity 34.996) was used to obtain the baseline calibration and nitrate (20-1000 µM) was progressively added to the standard solution. Then, sensor response was measured under flow through conditions. The flow rate was set between 1-5 mL/min. Next, the pulsed potential waveform was optimized using the double potential step process. At the first potential, optimized at 0.65 V, the PPy-NWs were preoxidized, and the second potential step at -0.15 V was to reduce the nitrate ions. All experiments were carried under identical conditions at room temperature

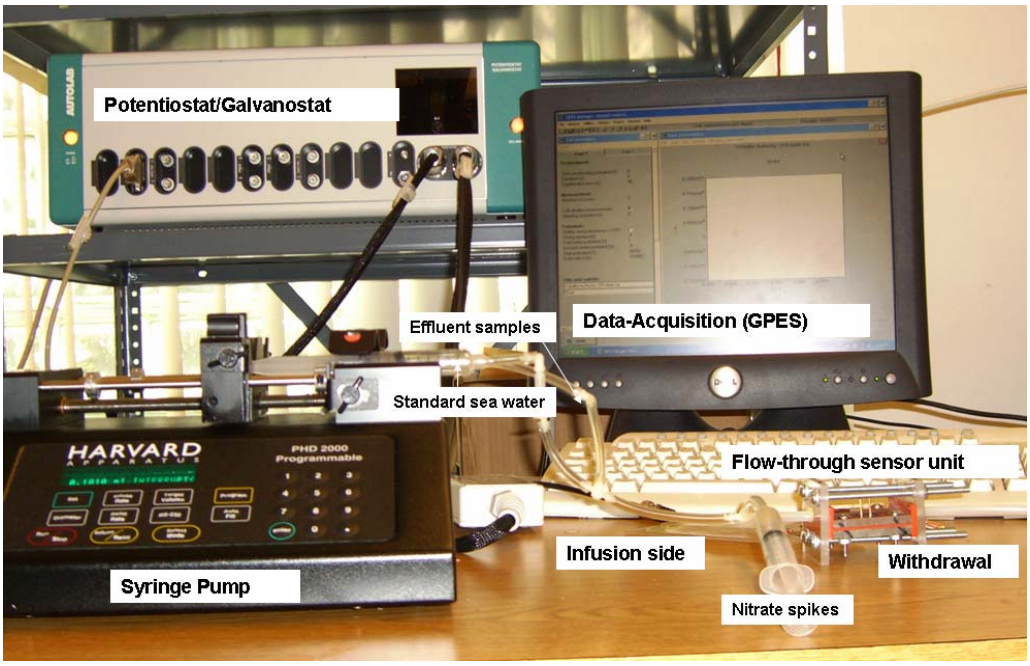

Figure 7.9 Complete experimental set up for measuring nitrate concentration in flow through conditions.

Calibration of doped PPy-NWs electrodes**:** The response of the doped PPy-NWs electrodes were tested for nitrate ions in two sets of calibration solutions, *DI-cal* and *Ocean-cal*. A steady state current was reached within 60 seconds of application of working potential, with a response time of less than 20 seconds. Figure 7.10 shows the calibration plot for *DI-cal* baseline solution for two conditioning time (2 and 24 hours), created by taking the peak currents for each nitrate concentration level (10-200 μM). There is a linear fit of the form:

$$I(\mu A) = 0.0028[concentration(\mu M) - 0.012 \quad (7.3)$$

with accuracy of ±5%, and linearity coefficient of 0.995. From the slope of the calibration plot, sensitivity was found as 1.65 nA/μM. The operational stability was then evaluated. Twenty runs performed at 100 μM nitrate level yielded a stable response that changed an indiscernible amount. For 2 hours of conditioning time, the sensors were unstable with lower peak currents and sensitivity, reflecting on poor chemical recognition properties. However, for 24 hours conditioning, the plots show a quasi-linear relationship between peak current and nitrate level (20-1000 μM). Figure 7.11 shows O*cean-cal* calibration plot tested with PPy-NWs electrodes conditioned in $NaNO_3$ for 24 hours after electroploymerization. The plot shows a quasi-linear relationship between peak current and nitrate level (20-1000 μM) with accuracy of ±4% and linearity coefficient R^2 of 0.96. The sensor exhibited high peak currents and rapid response times compared to other doped PPy electrodes (Bendikov et al., 2005; Quan et al., 2001). This may be due to the presence of PPy nanowires with large effective surface area and lower diffusion resistance. From the slope, the sensitivity was found to be 1.17 nA/μM. The PPy-NWs electrodes had a detection limits of 4.5±1 μM/L (n = 8). This detection limit for nitrate is more than two orders of magnitude lower the safe limits as regulated by United States Environmental Protection Agency (US-EPA) or European Commission (EC) directive. PPy-NWs electrodes conditioned for only 2 hours after electropolymerization showed an unstable response and lower peak currents compared to 24 hour conditioned electrodes, probably due to ineffective chemical recognition properties (Hutchina et al., 1995)

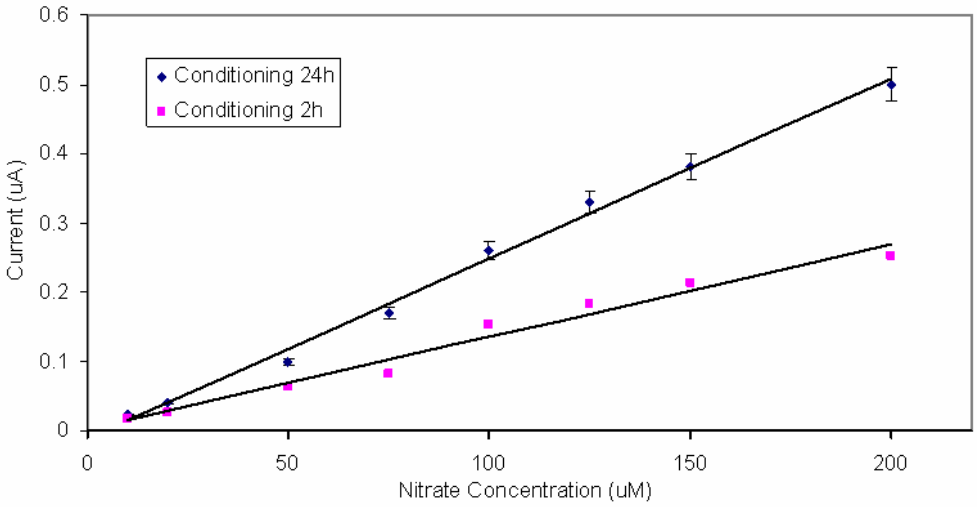

Figure 7.10 Calibration plot for *DI-cal* baseline solution; peak current response versus nitrate concentration (10-200 µM*)*.

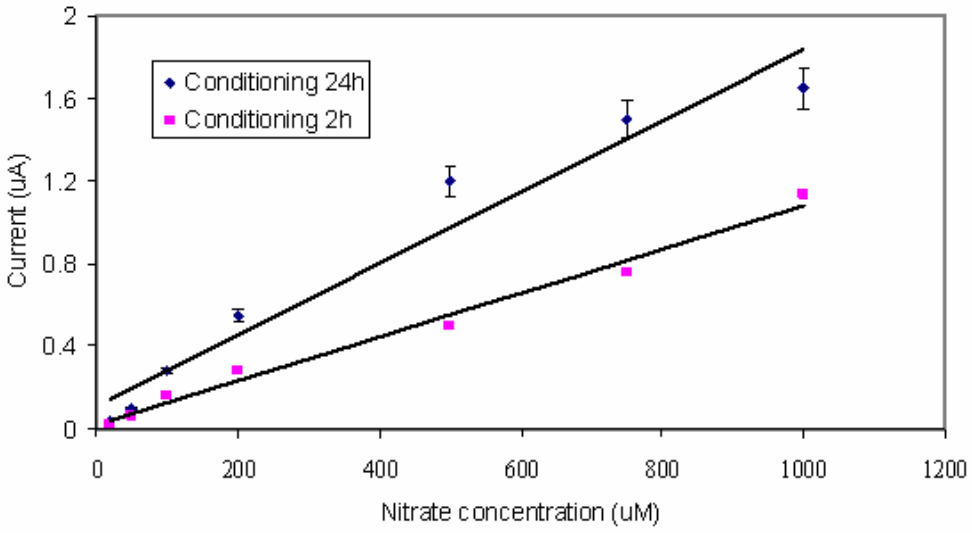

Figure 7.11 Calibration plot for *Ocean-cal* baseline solution; peak current response versus nitrate concentration (20-1000 µM*)*.

7.4.6 Generation II: flow cell analysis under dynamic conditions

Principle of Detection: After successful calibration testing of PPy-NWs electrodes under static conditions, the electrodes were tested in the integrated microfluidic platform. The microfluidic platform represented a more realistic and controlled environment mimicking

conditions in water systems. As in the case of static measurements, constant-potential technique is used for flow analysis under dynamic conditions. The detection is performed by controlling the potential of the working electrode at a fixed value and monitoring the current as function of time. The current response thus generated reflects the concentration profiles of these analytes as they pass through the sensor. These systems result in sharp current peaks (reflecting the passage of effluent), further indicating the measure of concentration. The flow cell design must fulfill the requirements of high signal-to-noise ratio, low dead volume, well-defined hydrodynamics, small ohmic drop and ease of maintenance (figure 7.12). In addition, the reference and counter electrodes should be located in the downstream side of the working electrode, so that the reaction products at the counter electrode do not interference with working electrode. In the present design, flow channels were formed using SU-8 molds with Teflon gasket and Plexiglass top cover, which defines a small dead volume.

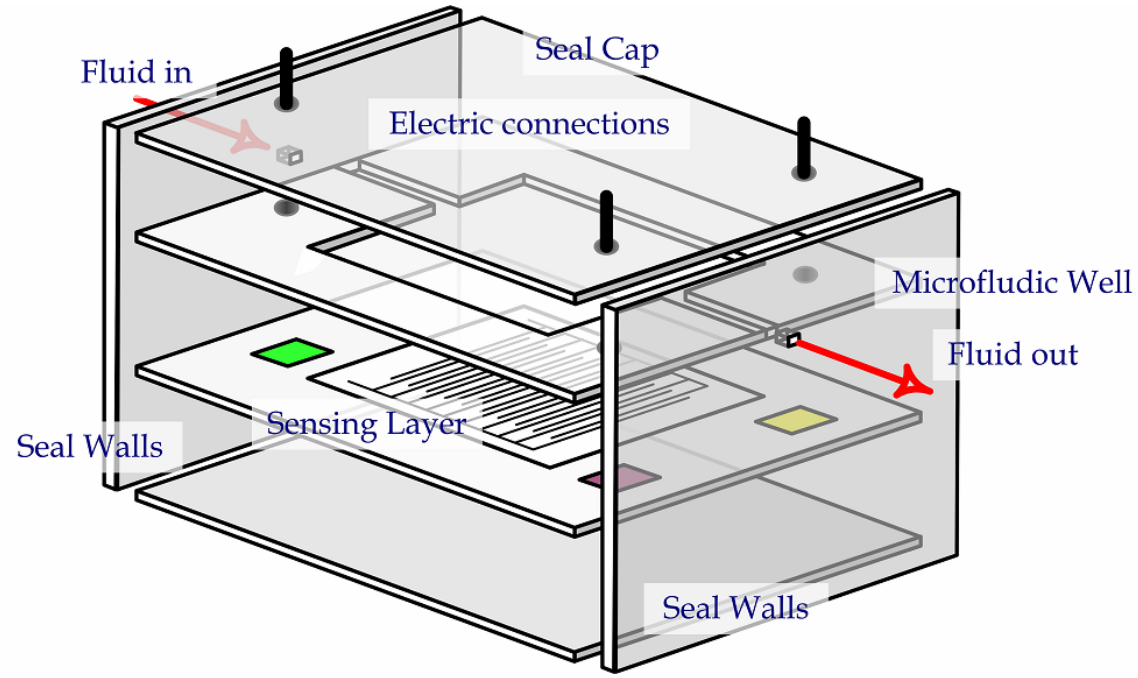

Figure 7.12 Illustration of the flow through set up for measuring nitrate concentration under realistic and controlled environment.

Flow analysis and current response. Flow channel hydrodynamics and inlet/outlet stream pressure can be calculated using the following theoretical equations or modeled using CFD tools such as COMSOL multiphysics or microfluidics subsystem in Coventorware®. A well-defined hydrodynamic condition with a high rate of mass transport is essential for successful application

of electrochemical sensors. Based on Nernst approximate approach, the thickness of the diffusion layer (δ) is empirically related to the solution flow rate (U) via

$$\delta = \frac{B}{U^{\alpha}} \tag{7.4}$$

B and α are constants for a given set of conditions, α ranging between 0.33 and 1.0. By substituting the above equation in the general current response for mass transport controlled reactions ($i_l = nFADC/\delta$) one obtains the limiting state response of flow through electrodes

$$i_l = nFAK_m CU^{\alpha} \tag{7.5}$$

K_m is the mass-transport coefficient, A is electrode area, F is faraday constant, C is concentration (mM), n is number of electrons. A more rigorous treatment takes into account the hydrodynamic characteristics of the flowing effluent. By solving the three-dimensional convention diffusion equation, expressions for the limiting currents (under steady-state conditions) for various electrode geometries can be arrived at.

$$\frac{\partial C}{\partial t} = D\left(\frac{\partial^2 C}{\partial x^2} + \frac{\partial^2 C}{\partial y^2} + \frac{\partial^2 C}{\partial z^2}\right) - \left(U_x \frac{\partial C}{\partial x} + U_y \frac{\partial C}{\partial y} + U_z \frac{\partial C}{\partial z}\right) \tag{7.6}$$

Then, by substituting the appropriate initial and final boundary conditions, the resulting equation for limiting current in the case of a tubular and thin-layer cell are obtained respectively

Tubular: $$i_l = 1.61 nFC(DA/r)^{2/3} U^{1/3} \tag{7.7}$$

Thin-layer cell: $$i_l = 1.47 nFC(DA/r)^{2/3} U^{1/3} \tag{7.8}$$

Sensing Mode: The simplest detection scheme is to measure current at a constant potential. Such fixed-potential amperometric measurements have the advantage of being free of double-layer charging and surface-dominant effects. As a result extremely low detection limits can be achieved. Also by recording numerous voltammograms of potential scans during the elution, a three-dimensional response of the current against potential and time. In addition, by using more than one working electrodes (in this present work an array of nanowire electrodes is used), detection confidence and discrimination with irreversible redox chemistry can be achieved.

.

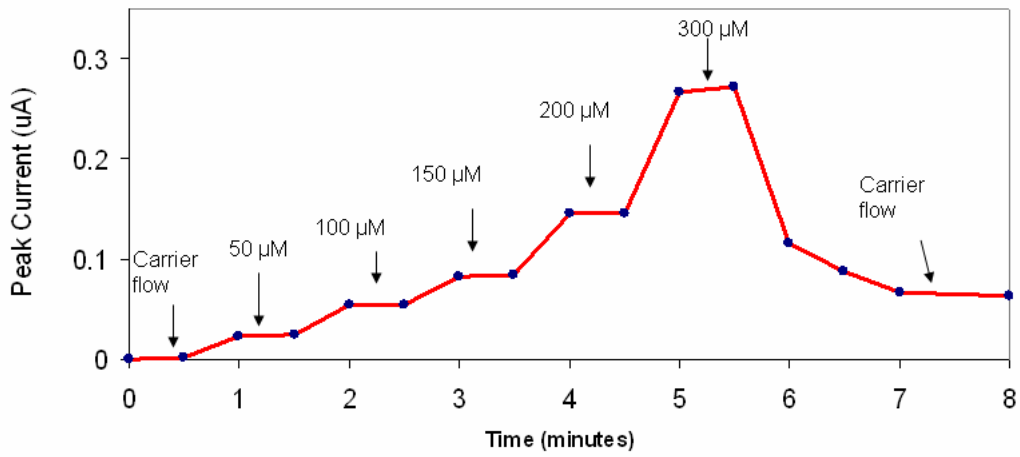

Figure 7.13 Flow through analysis plot of peak current response at regular time intervals for successive nitrate increments (50-300 µM). Carrier solution was IAPSO standard seawater at 1-5 mL/min.

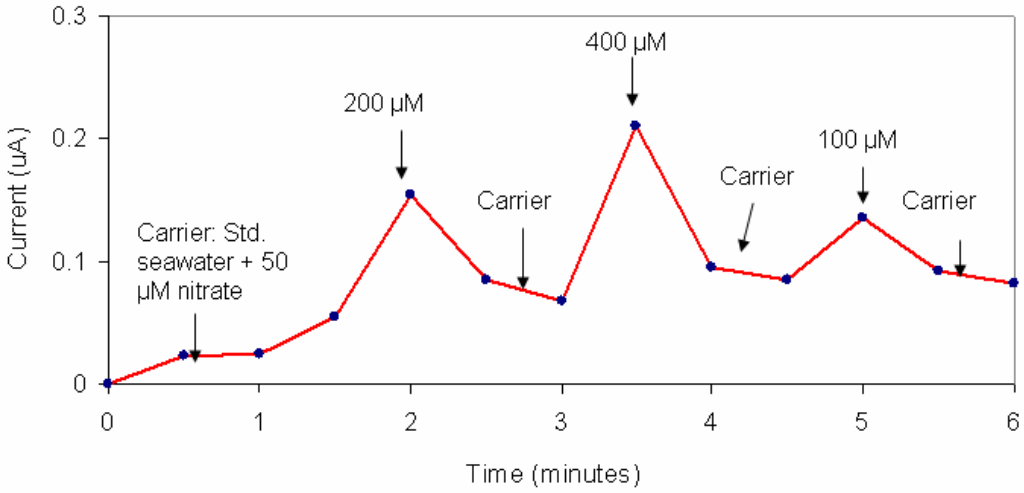

Figure 7.14 Flow through analysis plot of peak current response for intermittent nitrate spikes. Baseline carrier solution was IAPSO standard seawater and 50 µM nitrate effluent.

In the first set of experiments, the carrier effluent contained only IAPSO standard seawater to give baseline stability. Numerous experiments were carried out to optimize the carrier flow rate, and pulsed voltammograms as the response intensity depended on the carrier conditions. An optimal flow rate was chosen between 1-5 mL/min, and was used in all further experiments. Figure 7.13 shows a typical peak current response at regular intervals of time for successive higher nitrate flow into the system. It can be observed that for successive higher nitrate levels, the

peak current also increased linearly, maintaining a stable current response. In the next set of experiments, the baseline carrier effluent contained IAPSO standard seawater and 50 μM nitrate ions with intermittent nitrate spikes injected into the system at certain time intervals (Figure 7.14). After every sudden nitrate spike for about 30 seconds, the baseline carrier effluent was flown for 2 minutes to test sensor recovery. It can be observed even though sensor responded very well to nitrate spikes; the initial baseline current was not obtained. This is may be due to the presence of residual nitrate ions in the system and the absence of control valve mechanism to completely eliminate back flows. Investigations on sensor regeneration by further optimizing the electropolymerization parameters, modeling flow dynamics using Finite Element Method (FEM) tools, and integration of off-the-self solenoid control valves are currently underway.

7.4.7 Effect of interfering ions and storage stability

The selectiveness of the doped PPy-NWs electrodes and effect of interfering ions on current response was investigated for various anions. When the effluent solution contains interfering ions, these ions will compete for the adsorption sites with nitrate ions, and the determination of nitrate may be affected. We find that up to 0.2 mM of chloride, sulfate, phosphate and perchlorate ions in baseline IAPSO seawater solution, no significant effect was found in the current response. However, at higher levels of interfering ions (tested at 0.2, 0.25, 0.4 mM), the peak current response decreased by only about 15-20%. Therefore, in this study, the PPy-NWs electrodes demonstrated significant deviation from the Hofmeister series with regards to selectivity towards nitrate ions. This nitrate-selective response is a result of the electrochemically mediated nitrate doping, which created nitrate specific chemical recognition sites. In addition, these electrodes are known to be insoluble in organic solvents, where conventional ISEs are unusable (Hutchina et al., 1995). Even though, in this work, effects of standard interfering ions such as chlorides, sulfates, phosphates and perchlorates have been avoided, other ions such as thiocyanates can still affect the current response. Thiocyanate ions, with equal or smaller radii as nitrate ions can still pose interference problems. To further improve the selectivity of doped PPy-NWs electrodes, techniques such as deposition of solvent polymeric membranes (Quan et al., 2001) and selective coordination interaction (Hutchina et al., 1995) can be investigated.

Next, the lifetimes of the nitrate doped PPY-NWs electrodes were studied. In between experiments, the electrodes were placed in 1 mM $NaNO_3$. Figure 7.15 shows the results of this

experiment. All electrodes showed gradual ageing and deterioration in current response, decreasing up to 50% after the 10th day. This may be due to polymerization and loss of chemical activity in PPy-NWs, due to extended exposure to light. Improved lifetimes have been reported, when electrodes were stored in dark or by optimizing the conditioning solution (distillation on the day of electropolymerization). It was shown that even after 5 months; the slope of nitrate calibration plot was still 90% of its original response (Hutchina et al., 1995).

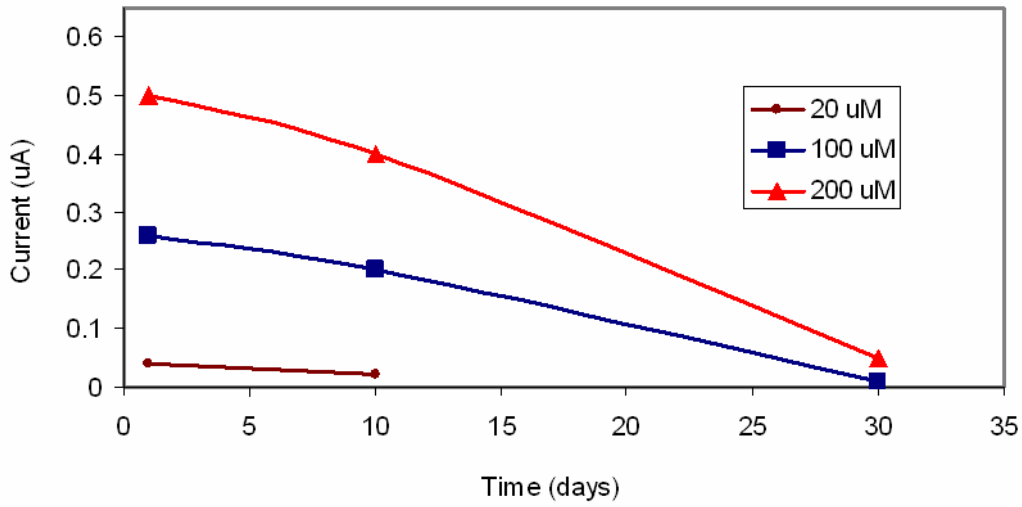

Figure 7.15 Lifetime study of nitrate doped PPy-NWs electrodes at different nitrate concentrations (50, 100, and 200 µM).

7.4.8 Generation III: all micromachined flow cell

In the Generation III of the nitrate electrochemical sensor, the Plexiglas housing was replaced by PDMS mold as top lid with Nanoport™ assembly as inlet/outlet connections. In this manner, all micromachined nitrate flow cell was constructed. Figure 7.16 shows the schematic of the Generation III electrochemical nitrate sensor. The fabrication process followed all steps as described in Generation II. Then, PDMS top lid fabrication and inlet/outlet assembly were performed (Figure 7.17).

PDMS is a flexible elastomeric polymer with excellent microfluidic material properties such as transparency to visible wavelengths and ability to modify surface properties (for example from Si-CH_3 to Si-OH). The PDMS fabrication process is as follows. First, 55 g of 1:10 PDMS (Sylgard 184 curing agent and polymer base) was mixed thoroughly. Then, the pre-cured PDMS was poured onto 2" Si master mold in a flat Petri dish. Next, the degaussing was performed by

placing this in a vacuum chamber, until all bubbles have been removed from the surface. Then, the covered Petri dish was placed at 80 ˚C for 3-6 hours. Next, the PDMS casting was released by peeling it from the Si surface using a knife and then was cut into required dimensions. At the same time, fluidic ports (Nanoport™ assembly) were punched into the walls of SU-8 in the flow cell. The next step was to bond the cut PDMS onto the flow cell. Both surfaces of flow cell and PDMS mold were treated with oxygen plasma (100 mW, 1% oxygen, 1 min). Then, they were immediately placed in contact to bond the surface irreversibly. Finally, the flow cell was baked at 70 ˚C for 10 minutes.

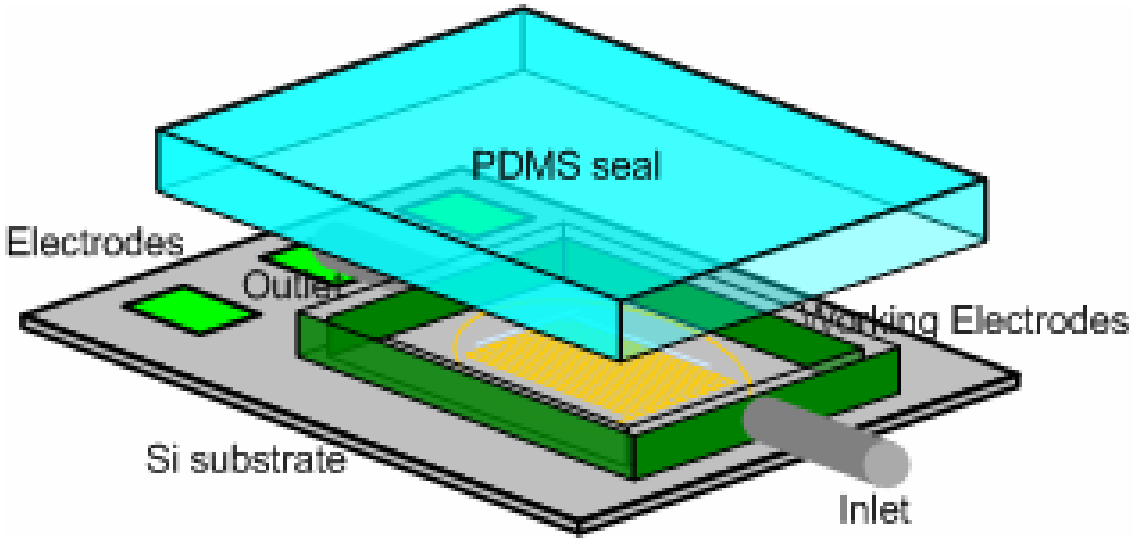

Figure 7.16 Schematic of the all micromachined electrochemical flow cell.

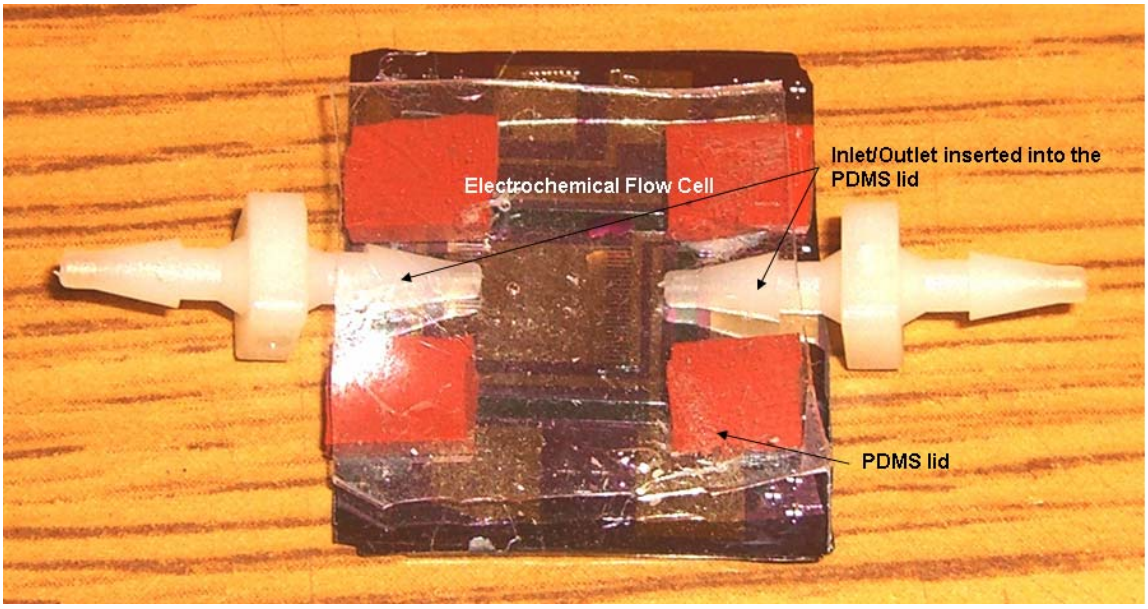

Figure 7.17 Image of all micromachined electrochemical sensor with integrated microfluidics.

7.5 Summary

In summary, by using electrochemical doping approach on polypyrrole nanowires, a highly sensitive and selective nitrate sensor has been demonstrated on MEMS microfluidic platform. The PPy-NWs electrodes exhibited 4.5±1 µM detection limit on standard seawater samples and rapid response to changing nitrate concentrations in a flow through system. The sensor further showed a linear response to nitrate (10-1000 µM) with a sensitivity of 1.17-1.65 nA/µM. More importantly, the sensor exhibited good selectivity to nitrate ion, with only 15-20% decrease in current due to interfering ions. In future, we will investigate the effect of electropolymerization parameters on sensor characteristics and integration on-chip potentiostat, control valves and micropumps to assemble a truly field-deployable sensor.

CHAPTER 8

CONCLUSIONS AND FUTURE OUTLOOK

8.1 Conclusions

This dissertation described the implementation of micro and nanosensor elements and their associated packages for measurement of physical, chemical and biological parameters of interest in the environment. The first part of the dissertation focused on the development of novel reinforced diaphragm MEMS piezoresistive pressure sensors for high resolution pressure (depth) measurements in the ocean. An accurate knowledge of pressure/depth (up to 1000m of water) is a key requirement for any underwater observatory or measurement system. However, conventional MEMS single diaphragm piezoresistive pressure sensors are limited in their operating range and sensitivity. When thin bulk micromachined diaphragm is subjected to high pressure, it may result in large deflections (membrane theory) and hence non-linearities in measurement. To overcome this limitation, in this research, a novel reinforced diaphragm piezoresistive pressure sensor was proposed and implemented as Generation I, Generation II, Generation III pressure sensors.

The Generation I sensors used a thin inner diaphragm (with piezoresistors) and a thicker outer diaphragm (with piezoresistors) as the sensing bridges and a third piezoresistive bridge for temperature compensation. By transferring the peak (overload) stresses from the inner diaphragm to the outer diaphragm, the thick outer diaphragm acted as reinforcement or edge smoothing structure. This in turn improved the operating pressure range of the sensor. In addition, the higher stiffness coefficient of the outer diaphragm provided mechanical support for the inner diaphragm. On the other hand, this opened the possibility of designing inner diaphragms much thinner than that possible with conventional single diaphragm designs. In summary, the reinforced diaphragm design improved both sensitivity and operating range at the same time. The Generation I sensors showed up to 21% higher sensitivity (from re-simulated data) and more than two times wider operating range than conventional single diaphragm designs. It was noticed during the fabrication

of Generation I sensors that the process involved a masked-maskless etching step. By accounting for this effect, Generation II sensors were designed, fabricated and measured. These sensors exhibited a sensitivity of up to 0.067 mV/V/psi (and 27% higher from re-simulated data) and a linear operating range up to 430 psi (300 m of water), with a combination of inner and outer bridges. The inner bridge reached its transition point around 260 psi, beyond which the outer bridge was used. To further improve on the inner bridge operating range, the third generation (Generation III) was designed, fabricated and measured. These sensors incorporated a central bossed structure on the inner diaphragm. This bossed structure, further, helped in linearizing the response up to a measured pressure of 320 psi. Apart from design and fabrication of these sensors, two-levels of packaging and protective coating testing was performed during the course of the research. First, the zeroth or wafer-level, involving glass cavity (top), interconnection routing, pressure ports (bottom) was developed. This was followed by the system-level package with flexible circuit board (signal conditioner) integrated through Anisotropic Conductive Films (ACF) and protective coatings to withstand bio-fouling effects.

The second part of this dissertation involved development of nanowire-based Electrochemical detection-on-Chip (EoC) to measure biological and chemical markers, especially nitrate in the environment. Different sensing modalities, involving a variety of nanosensor electrodes (single element Au and Ni-Fe, two-segment Au/Ni-Fe and conducting polypyrrole nanowires) and different assembly techniques (magnetic, through wafer interconnects and dielectrophoresis) were investigated for integration as electrochemical nitrate sensors in a MEMS/microfluidic platform. A prototype MEMS based electrochemical biosensor using Au nanowires was developed to detect biomarkers (cholesterol) in biological fluids (blood). In the detection range of 10-60 μm, the sensitivity was estimated to be 0.85 nA/μM with a high apparent Michaelis-Menton constant of 17.1 mM. However, this sensor exhibited poor detection limits towards nitrate ions. Doped polypyrrole nanowires based electrochemical sensor with integrated microfluidics proved effective as a ocean nutrient sensor. This sensor was packaged and tested as an representation of a flow through system using seawater samples. A detection limit (4.5±1 μM), sensitivity (1.65 nA/μM) and stability (<15% variation to interfering ions) was achieved.

8.2 Future outlook

The ultimate goal of this research is to develop an integrated physical, chemical and biological measuring system, which can be readily deployed as a network of distributed sensors

to continuously sample along temporal and spatial scales. Towards this long-term objective, the following short-term objectives will need to be addressed. With the successful development of the reinforced diaphragm pressure sensor configuration and integration with flexible circuit board (signal conditioner), the next steps involve calibration and testing of the system-level package in ocean condition using a cable approach (figure 8.1).

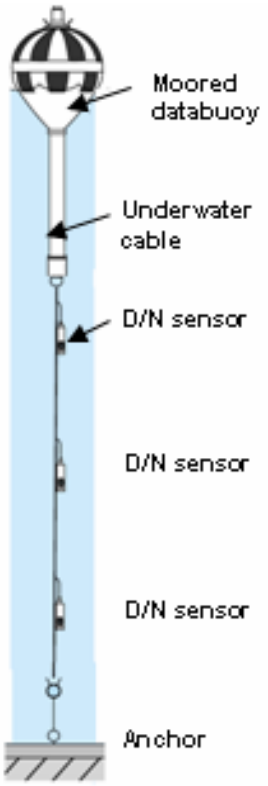

Figure 8.1 Cable deployment strategy for pressure/depth sensors. Adapted from Anderaa.

The signal conditioner (ZMD31050, advanced differential signal conditioner**)** will be used to digitally compensate for pressure offset, drift, noise and non-linearity between inner and outer bridge outputs. The resolution of the pressure sensor depends on the type of readout circuitry and various fundamental noise limits. Noise consists of Brownian noise, which is caused by the intrinsic nature of physical bombardment of molecules against the diaphragm and electrical noise generated by the transduction element and its readout circuitry (piezoresistor thermal, kT/C, shot). In addition, offsets and drifts due to temperature, hysteresis will significantly degrade the pressure accuracy. Chau et al., 1987 showed that Brownian noise is the least significant among the noise mechanisms. While, other noises in order of increasing

magnitude are piezoresistive thermal noise, kT/C noise, and circuit noise. The piezoresistor thermal noise scales as:

$$p_n^2 = \frac{4kTR.BW}{(V_s S_{piezo})^2} \alpha \frac{h^4}{a^4} \tag{8.1}$$

R is the equivalent bridge resistance, h, and a are the thickness and length of diaphragm. Digital compensation using signal conditioning circuits offers significant advantages over conventional analog trims. Signal conditioning and signal amplification of the Wheatstone bridge output was done using ZMD31050 microcontroller. ZMD31050 is a CMOS integrated circuit for highly accurate amplification and sensor-specific correction of piezoresistive bridge sensor signals. The device provides digital compensation of sensor offset, sensitivity, temperature drift and non-linearity by a 16-bit RISC microcontroller running a correction algorithm with correction coefficients stored in non-volatile EEPROM. The circuit was operated in a typical ratiometric measurement mode with voltage output, temperature compensation via external diode, internal VDD regulator and active sensor connection check (Figure 4.25). The ZMD31050's signal path is partly analog and partly digital. The analog part is realized differential, this means internal is the differential bridge sensor signal also handled via two signal lines, which are rejected symmetrically around a common mode potential (analog ground = VDDA/2). Consequently it is possible to amplify positive and negative input signals, which are located in the common mode range of the signal input. The differential signal from the bridge sensor is pre-amplified by the programmable gain amplifier (PGA). The Multiplexer (MUX) transmits the signals from bridge sensor, external diode or separate temperature sensor to the ADC in a certain sequence. Afterwards the ADC converts these signals into digital values. The digital signal correction takes place in the calibration micro-controller (CMC). It is based on a special correction formula located in the ROM and on sensor-specific coefficients (stored into the EEPROM during calibration). Dependent on the programmed output configuration the corrected sensor signal is output as analog value, as PWM signal or in digital format (SPI, I2C, ZACwire™). The output signal is provided at 2 flexible I/O modules (FIO) and at the serial interface (SIF). The configuration data and the correction parameters can be programmed into the EEPROM via the digital interfaces.

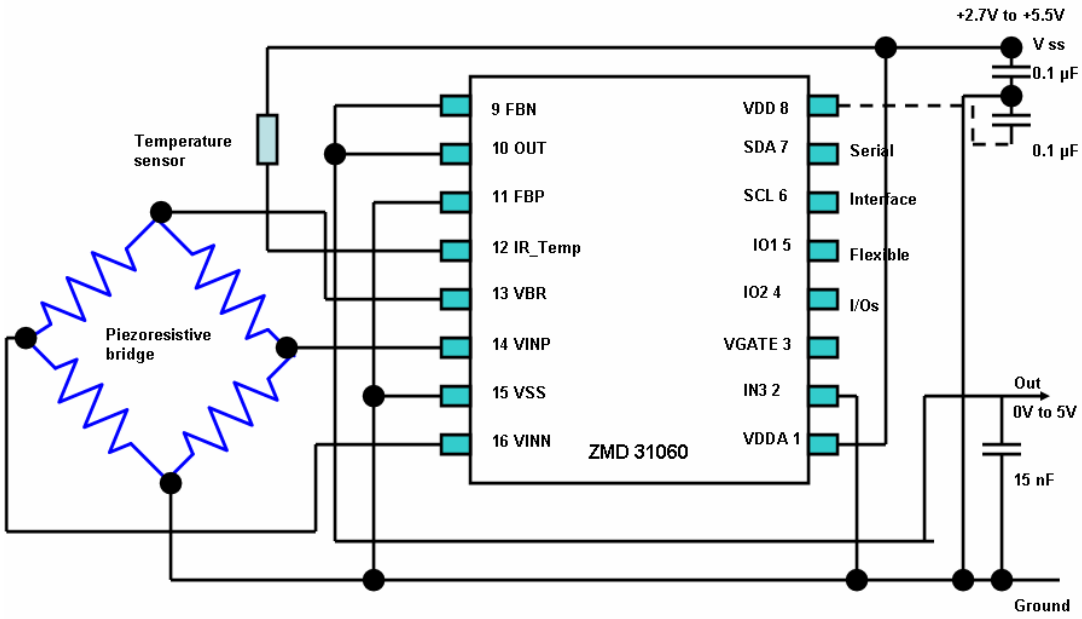

Figure 8.2 Illustration of signal conditioner ZMD31050 and bridge network mode of operation.

Later, improvements (increase the operating range) to the Generation III sensors will need to be performed, without compromising on sensitivity to ultimately reach 1000's m of water. Measurements at these depths are significant for instrument or platform leveling, ocean currents and tides/tsunami detection. In addition, an array based sensor approach can be developed, where a set of sensors will operate up to a particular depth, following which another set of sensors can be electronically switched for operation. One deployment strategy, which could be implemented in short-term, is the cable approach (Figure 8.1). Here, the pressure (depth) sensor along with other sensors (say nitrate sensor) can be connected to a underwater cable (with power and data lines) and anchored on to the seabed. This deployment method will help in continuous monitoring of ocean currents and chemical fluxes at that particular spatial scale.

On the chemical or biological measurement platform, an approach, similar to Lab-on-a-cable concept (Wang et al., 2000) could be adopted. This involves, as shown in Figure 8.3, system integration of analyte collection, sample holding, micropump, flow connectors, power unit, and the electrochemical detection-on-chip module along with a on-chip potentiostat in a scaled – down sealed cylindrical unit, connected to a long-shielded underwater cable. Deployment of such submersible microlaboratories will help in continuous monitoring, while avoiding errors and costs associated with collection of discrete samples and maintains sample integrity.

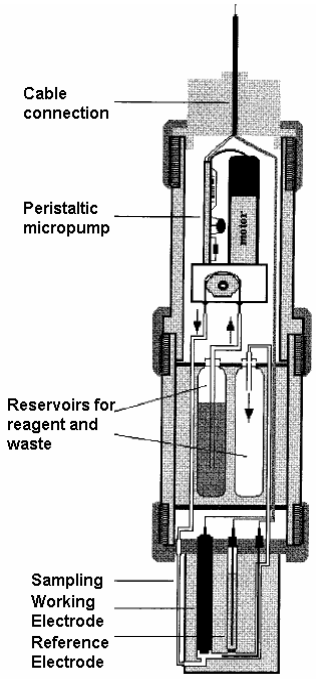

Figure 8.3 Schematic diagram of Lab-on-a-cable concept. Adapted from Wang et al., 2000.

Apart from the system integration, various optimization experiments will need to be performed before a full-fledged ocean deployment. First, a more effective and reliable nanowire assembly scheme has to be developed. One strategy would be to use electrodes, as shown in Figure 8.4 to electrically assemble nanowires. This method will enable one or few tens of nanowires to assemble, thereby making this technique run-to-run reliable. Next, the flow through analysis experiments clearly showed the need for microfluidic modeling using Computational Fluid Dynamics (CFD) tools. Figure 8.5 illustrates the effectiveness of modeling to accurately predict flow hydrodynamics and stream pressures at inlet/outlet. The figure shows the movement of pressure-driven liquid along a straight and T-channel at different instances of time.

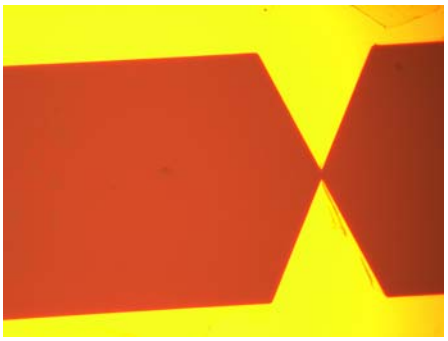

Figure 8.4 Single pair of electrodes for nanowire assembly.

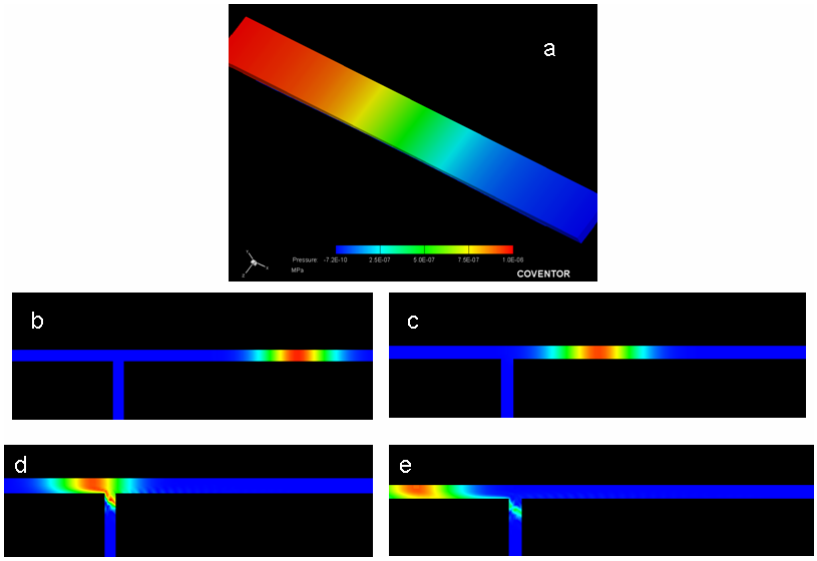

Figure 8.5 Pressure-driven fluid flow through a) straight micro-channel, b) T-channel at time t_1, c) time t_2, d) time t_3 and e) time t_4.

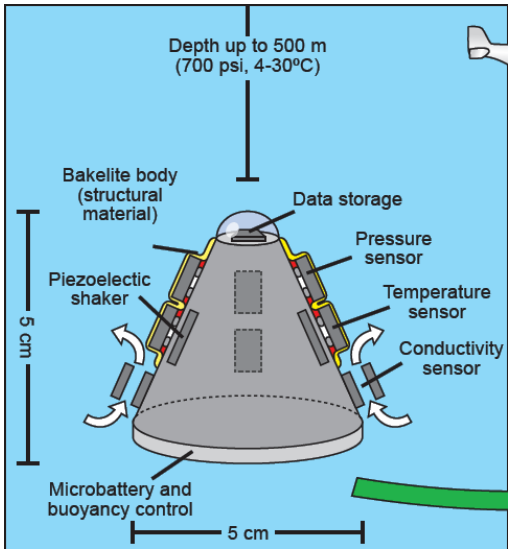

Figure 8.6 Integrated sensors in a single package (patent pending).

Finally, as stated earlier, the long-term objective of this research is to potentially integrate all the micro/nanosensor elements, into a tennis ball package, as shown in Figure 8.6 (where conductivity, temperature and depth sensors are schematically integrated), along with electronics, data storage, (wireless) communication, microbattery (Appendix F) and buoyancy control. However, any system deployed in the ocean for long-term monitoring will ultimately, be limited by bio-fouling effects.

REFERENCES

Addiscott, T. M., Whitmore, A. P., Powlson, D. C. (1991). *Farming Fertilizers and Nitrate Problems*. CAB International Oxford.

Akbar, M., Shanblatt, M. A. (1992). *Temperature compensation of piezoresistive pressure sensors*. Sens. Actua. A 33 155-162.

Alliance for Coastal Technologies. (2003). *State of technology in the development and application of nutrient sensors*. Proc. Workshop. Savannah, Georgia.

Allain, C. C., Poon, L. S., Chan, C. G. S., Richmond, W., Fu, P. C. (1974). *Enzymatic determination of total serum cholesterol.* Clin. Chem. 20 470-475.

Aravamudhan, S., Bhat, S., Bethala, B., Bhansali, S., Langebrake, L. (2005). *MEMS based conductivity-temperature-depth (CTD) sensor for harsh oceanic environment***.** Proc. IEEE Oceans 3 1785-1789.

Aravamudhan, S., Bhansali, S. (2004). *Design and Simulation of a Piezoresistive MEMS Pressure Sensor for Marine Applications*. Digest of 133rd TMS Annual Meeting, Multiphase Phenomena and CFD Modeling and Simulation of Engineering Processes. 347-355.

Aravamudhan, S., Bhansali, S. (2007). *Reinforced Piezoresistive Pressure Sensor for Ocean Depth Measurement*s. Sens. Actua. A in press.

Aravamudhan, S., Kumar, A., Mohapatra, S., Bhansali, S. (2007). *Sensitive estimation of total cholesterol in blood using Au nanowires based microfluidic platform.* Biosens. Bioelectron. 22 2289=2294.

Aravamudhan, S., Ramgir, N., Bhansali, S. (2007). *Electrochemical biosensor for targeted detection in blood using aligned Au nanowires.* Sens. Actua. B 127 29-35.

Bauer, L. A., Reich, D. H., Meyer, G. J. (2003). *Selective functionalization of two-component magnetic nanowires*. Langmuir 19 7043-7048.

Bendikov, T. A., Kim, K., Harmon, T. C. (2005). *Development and environmental application of a nitrate selective microsensor based on doped polypyyrole films*. Sens. Actua. B 106 512-517.

Bendikov, B., Harmon, T. (2005). *A sensitive nitrate ion-selective electrode from a pencil lead*. J Chem. Education 82 439-441.

Boote, J. J., Evans, S. D. (2005). *Dielectrophoretic manipulation and electrical characterization of gold nanowires.* Nanotechnology 16 1500-1505.

Brahmin, S., Narinesingh, D., Guiseppi-Elie, A. (2001). *Amperometric determination of cholesterol in serum using a biosensor of cholesterol oxidase contained within a polypyrrole-hydrogel membrane.* Anal. Chim. Acta. 448 27-36.

Brett. C. M. A. (2001*). Electrochemical sensors for environmental monitoring: strategy and example*s. Pure Appl. Chem. 73 1969-1977.

Brewer, P. G., Malby, G., Pasteris, J. D., White, S. N., Peltzer, E. T., Wopenka, B., Freeman, J., Brown, M. O. (2004). *Development of a laser Raman spectrometer for deep-ocean science*. Deep Sea Res. I 51 739-753.

Broecker, W. S., Denton, G. H. (1989). Geochim. Cosmochim. Acta. 53 2465.

Brown, N. (1987). *New generation CTD sensor systems*. IEEE Oceans 19 280-286.

Bryzek, J., Petersen, K., Mallon, J. R., Christel, L., Pourahmadi, F. (1990). *Silicon Sensors and Microstructures.*

Cai, W. J., Reimers, C. E. (1995). *Benthic oxygen flux, bottom water oxygen concentration and core top organic carbon content in the deep Northeast Pacific Ocean*. Deep Sea Res. I 42 1681-1699.

Callow, M., E., Callow, J. A. (2002). *Marine bio-fouling: a sticky problem*. The Biologist 49 10-14.

Chan, M. A., Collins, S. D., Smith, R. L., (1994). *A micromachined pressure sensor with fiber-optic interferometric readout.* Sens. Actua. A 43 196-202.

Charpentier, L., Murr, I. E. (1995). *Amperometric determination of cholesterol in serum with use of a renewable surface peroxidase electrode*. Anal. Chim. Acta. 318 89–93.

Chavez F. P., Strutton, R. G., Friederich, G. E., Feely, R. A., Feldman, G. C., Foley D. G., McPhaden. M. J. (1999). *Biological and chemical response of the equatorial Pacific to the 197-98 El Nino*. Science 286 2126-2131.

Cheng, F., Zhang, M., Wang, H. (2005). *Fabrication of polypyrrole nanowire and nanotube arrays.* Sensors 5 245.

Clark, S., Wise, K. (1979). *Pressure sensitivity in anisotropically etched thin-diaphgram pressure sensors*. IEEE Tran. Elect. Dev. 26 887-1895.

Clark Jr., L. C., Wolf, R., Granger, D., Taylor, Z. (1953). *Continuous recording of blood oxygen tensions by polarography*. J. Appl. Physiology 6 189-193.

Coale, K. H., Chin, C. S., Massoth, G. J., Johnson K. S., Baker, E. T. (1991). *In-situ chemical mapping of dissolved iron and manganese in hydrothermal plumes*. Nature 352 325-328.

Collar, P. G., Cartwright, D. E. (1972). *Open sea tidal measurements near the edge of the northwest European continental shelf.* Deep Sea Res. I 19 673-689.

Connolly, S., Cobbe, S., Fitzmaurice, D. (2001). *Effects of ligand-receptor geometry and stoichiometry on protein-induced aggregation of biotin-modified colloidal gold*. J. Phys. Chem. B 105 2222-2226.

Daly, K., Byre, R., Dickson, A., Gallager, S., Perry, M. Tivey, M. (2004). *Chemical and biological sensors for time series research: current status and new directions*. Marine Tech Soc. 38 121-143.

Daly, K. L. (2000). *Meeting explores sensor technology for remote, interactive aquatic experiments*. EOS Trans. Am. Geophys. Union 81 580.

DeGrandpre, M. D., Hammar, T. R., Wallace D. W. R., Wirick. C. D. (1997). *Simultaneous mooring-based measurements of seawater CO_2 and O_2 off Cape Hatteras, North Carolina*. Limnol. Oceanogr. 42 21-28.

Diamandis, E. P., Christopoulos, T. K. (1991). *The biotin-(strept)avidin system: principles and applications in biotechnolo*gy. Clin. Chem. 37 625-636.

Dickey, T. D. (2001). *The role of new technology in advancing ocean biogeochemical research*. special issue JGOFS Oceanography 14 108-120.

Dong, S., Sun, Z., Lu, Z. (1988). *Chloride chemical sensor based on an organic conducting polypyrrole polymer***.** Analyst 113 1525-1528.

Duchet, J., legras, R., Demoustler-Champagne, S. (1998). *Chemical synthesis of polypyrrole:structure-properties relationship*. Syn. Metals 98 113-122.

Eaton, W. P., Smith, J. H. (1007). *Micromachined pressure sensors: review and recent developments*. Smart Mater. Struct. 6 530-539.

Eble, M. C., Gonzalez F. I. (1991). *Deep-Ocean Bottom Pressure Measurements in Northeast Pacific*. J. Atmos. Oceanic Technol. 8 221-233.

Elgamel, H. E. (1995). *Closed form expressions for the relationship between stress, diaphragm deflection, and resistance change with pressure in silicon piezoresistive pressure sensors*. Sens. Actua. A 50 17-22.

Emerson, S., Stump, C., Johnson B., Karl, D. M. (2002). *In-situ determination of oxygen and nitrogen dynamics in the upper ocea*n. Deep Sea Res. I 49 941-952.

Enoksson, P. (1997). New structure for corner compensation in anisotropic KOH etching. J. Micromech. Microeng. 7 141-144.

Feely, R. A., Wanninkhof, R., Goyet, C., Archer D. E., Takahashi, T. (1997). Variability *of CO_2 distributions and sea-air fluxes in the central and eastern equatorial Pacific during the 1991-1994 El Nino*. Deep Sea Res. II 44 1851-1867.

Fert, A., Piraux, L. (1999). *Magnetic nanowires*. J. Magn. Magn. Mater. 200 338-355.

Filloux, J. H. (1969). *Bourdon tube deep-sea tide gauges. Tsunami in the Pacific Ocean*. W. M. Sams, Ed., East-West Center Press 223-238.

Föll, H., Christophersen, M., Carstensen, J., Hasse, G. (2003). *Formation and application of porous silicon*. Mat. Sci. Engin. R 39.

Foss, C. A. J. (2002). *Metal nanoparticles synthesis characterization and applications*. Marcel Dekker.

Fredrickson, D. S., Levy, R. I. (1972). *The metabolic basis of inherited disease*. Ed Stanbury . J.B., Wyngaarden. J.B., Fredrickson, D.S, McGraw-Hill Book New York 545.

Gallager, S. M., Whelan, J. eds. (2004). *The next generation of in-situ biological and chemical sensors in the ocean: a workshop report*. WHOI 85.

Glazier, S. A. (1998). *Construction and characterization of nitrate reductase-based amperometric electrode and nitrate assay of fertilizers and drinking water*. Anal. Chem. 70 1511-1515.

Goff, T., Braven, J. Edbon, L., Scholefield, D. (2003). *Automatic continuous monitoring of nitrate using a novel ion-selective electrode.* J. Environ. Monit. 5 353.

Gonzalez, F. l., Bernard, E. N., Milburn, H. B., Castel, D., Thomas, J., Hemsley, J. M. (1987). *The Pacific Tsunami Observation Program (PacTOP)*. Proc. International Tsunami Symp. IUGG. Vancouver. 3-19.

Gotz, A., Campabadal, F., Cane, C. (1998). *Improvements of pressure sensor performance and process robustness through reinforcement of the membrane edges.* Sens. Actua. A 67 138-141.

Gieles, A. C. M., Somers, G. H. J. (1973). *Miniature pressure transducers with a silicon diaphragm*. Philips Tech Rev. 33 14-20.

Grasshoff, K., Kremling K., Ehrhardt, M. (eds). (1999). *Methods of Seawater Analysis*. 3rd ed. Wiley 632.

Gwilliam, T. J. P., Collar, P. G. (1974). *A strain gauge pressure sensor for measuring tides on the continental shelf*. Institute of Ocean Sciences Report 14 27.

Harris, M. J., Tucker, M. J. (1963). *A pressure recorder for measuring sea waves.* Instrument Practice 17 1055-1059.

Hanrahan, G., Patil, D. G., Wang, J. (2004). *Electrochemical sensors for environmental monitoring: design, development and applications*. J. Environ. Monit. 6 657-664.

Hofmeister, F. (1888). *Naunum-Schneidebrgs*. Arch. Exp. Pathol. Pharmacol. 24 247-260.

Holke, A., Henderson, H. T. (1999). *Ultra-deep anisotropic etching of (110) silicon*. J. Micromech. Microeng. 9 51-57.

Hornyak, G. L., Patrissi, C. J., Martin, C. R. (1997). *Fabrication, characterization, and optical properties of gold nanoparticle/porous alumina composites: The nonscattering Maxwell-Garnett limit*. J. Phys. Chem. B 101 1548-1555.

Houston, M. H., Paros, J. M. (1998). *High accuracy pressure instrumentation for underwater applications*. IEEE Oceans 307-311.

Hutchina, R. S., Bachas, L. G. (1995). *Nitrate-selective electrode developed by electrochemically mediated imprinting/doping of polypyrrole*. Anal. Chem. 67 1654-1660.

Hyldgaard, A., Hansen, G., Thomsen, E. (2005). *Fish & Chips: single chip silicon MEMS CTDL for use in fisheries research*. Proc. IEEE MEMS 303.

Johnson, C. J., Kross, B. C. (1990). *Continuing importance of nitrate contamination of groundwater and wells in rural areas*. Am. J. Ind. Med. 18 449-456.

Johnson, K. S., Coletti, L. J. (2002). *In-situ ultraviolet spectrophotometry for high resolution and long-term monitoring of nitrate, bromide and bisulfide in the ocean*. Deep Sea Res. I 49 1291-1305.

Johnson, K. S. (2003). *Chemical sensors for autonomous and langrangian platforms*. Workshop for Autonomous and Langrangian Platforms.

Johnson, K. S., Coale, K. H., Jennasch, H. W. (1992). *Analytical chemistry in oceanography*. Anal. Chem. 64 1065-1075.

Johnson, K. S., Coletti, L. J., Chavez, F. P., (2006). *Diel nitrate cycles observed with in-situ sensors predict monthly and annual new production*. Deep Sea Res. I 53 561-573.

Kanda, Y. (1982). *Graphical representation of piezoresistance coefficients in silicon*. IEEE Tran. Elect. Dev. 19 64-70.

Kovtyukhova, N. I., Mallouk, T. E. (2002). *Nanowires as Building Blocks for Self-Assembling Logic and Memory Circuits*. Chem. Eur. J. 8 4355-4363.

Kroebel, W. (1987). *A New Type of Pressure Sensor for Very Fast Measurements in Fast CTD-Probes.* Proc. IEEE Oceans 19 331-334.

Kroger, S., Law, R. (2005). *Biosensors for marine applications – We all need the sea, but does the sea need biosensors?* Biosens. Bioelectron. 20 1903-1913.

Kurzer, M. S., Wollenhaupt, J., Calloway, D. H. (1981). *Nitrate and nitrogen balance in men*. Am. J. Clin. Nutrition 34 1305-1313.

Larsen, L. H., Kjar, T., Revsbech, N. P. (1997). *A microscale NO_3^- biosensor for environmental applications*. Anal. Chem. 69 3527-3531.

Lefcort, M. D. (1968). *Vibrating wire pressure transducer technology*. J. Atmos. Oceanic Technol. 2 37-44.

Lehmann, V. (2002). *Electrochemistry of silicon – instrumentation, science, materials and application*s Wiley-VCH. New York.

Li, X., Bao, M. (2001). *Micromachining of multi-thickness sensor-array structures with dual stage etching technology.* J. Micromech. Microeng. 11 239-244.

Li, X., Lin, R., Miao, J., Bao, M. (2000). *Study on convex-corner undercutting formed by masked-maskless etching in aqueous KOH*. J. Micromech. Microeng. 10 309-313.

Lin, L., Chin, H., Li, Y. (1999). *A simulation program for the sensitivity and linearity of piezoresistive pressure sensors*. J Microelectromech. Syst. 8 514-522.

Liu, Z., Searson, P. C. (2006). *Single nanoporous gold nanowire sensors*, J Phys. Chem. B 110 4318-4322.

Lu, Z., Sun, Z., Dong, S. *Study of ClO_4^- selective electrode based on a conducting polymer polypyrrole*. Electroanalysis 1 271–277.

Malone, T., C. (2006). *Research to operations and back again*. IEEE Oceans 1-4.

Martin, S. P., Lamb, D. J., Lynch, J. M., Reddy, S. M. (2003). *Enzyme-based determination of cholesterol using the quartz crystal acoustic wave sensor*. Anal. Chim. Acta. 487 91-100.

Martin, C. R. (1994). *Nanomaterials: A Membrane-Based Synthetic Approach*. Science 266 1961-1966.

Martin, J. H., Fitzwater, S. E., Gordon, R. M. (1990). *Iron deficiency limits phytoplankton growth in Antarctic waters.* Global biogeochem. Cycles 4 5-12.

Mohan, A, Malshe, A., Aravamudhan, S., Bhansali, S. (2004). *Piezoresistive MEMS pressure sensor and packaging for harsh oceanic environment***.** Proc. IEEE Electronic Components and Technology 948-950.

Moorocroft, M. J., Davis, J., Compton, R. G. (2001). *Detection and determination of nitrate and nitrite: a review*. Talanta. 54 785-803.

Murray, R. W. (1984). *Electroanalytical Chemsitry: A series of advances*; Bard, a. J., ed., Marcel Dekker. New York 13 191.

Murphy, T., Lucht, S., Schmidt, H., Kronfeldt, H.-D. (2000). *Surface enhanced Raman scattering (SERS) system for continuous measurements of chemicals in sea-water*. J. Raman Spectrosc. 31 943-948.

Oliver, F. J. (1971). *Practical Instrumentation Transducers*. Hayden Books.

O'Reilly, S. A., Daunert, S., Bachas, l. G. (1991). *Nitrogen oxide gas sensor based on nitrite-selective electrode*. Anal. Chem. 63 1278-1281.

Pearson, J. F., Slater, J. M., Jovanovich, V. (1992). *Coated-wire and composite ion-selective electrodes based on doped poly(pyrrole)*. Analyst 117 1885–1890.

Petersen, K. E., Pourahmadi, F., Brown, J., Parsons, Skinner, M., Tudor, J. (1991). *Resonant beam pressure sensor with silicon fusion bonding*. Int. Conf. on Solid-State Sens.Actua. 664-667.

Possin, G. E. (1970). *A method for forming very small diameter wires.* Rev. Sci. Instr. 41 772-774.

Pourahmadi, F., Bart, P., Petersen, K. (1990). *Modeling of thermal and mechanical stresses in silcion microstrutures*. Sens. Actua. A 21-23 850-853.

Pretsch, E., Badertschen, M., Welti, M., Marnizumi, T., Morf, W. E., Simon, W. (1988). *Design features of ionophores for ion selective electrodes*. Pure Appl. Chem. 60 567-574.

Prien, R. (2007). *Technologies for new in-situ chemical sensors*. IEEE Oceans 1-6.

Quan, D. P., Lewis, T. W., Wallace, G. G., Viet, P. H. (2001). *A conductive polypyrrole modified microelectrode for selective amperometric detection of nitrate in a flow-injection system.* Anal. Sci. 17 i745-i748.

Rajeshwar, S., Ibanez, J. G., Swain, G. M. (1994). *Electrochemistry and envirornment*. J. Appl. Electrochemistry. 24 1077-1091.

Reich, D. H., Tanase, M., Hultgren, A., Bauer, L. A., Chen, C. S., Meyer, G. J. (2003). *Biological applications of multifunctional magnetic nanowires.* J. Appl. Phys. 93 7275.

Resnik, D., Vrtacnik, D., Amon, S. (2000). *Morphological study of {311} crystal planes aniostropically etched in (100) silicon: role of etchants and etching parameters*. J. Micromech. Microeng. 10 430-439.

Sander, C. S., Knutt, J. W., Meindl, J. D. (1980). *A monolithic capacitive pressure sensor with pulse-period output*. IEEE Tran. Elect. Dev. ED-27 927-930.

Sandmaier, H., Kuhl, K. (1993). *A square-diaphragm piezoresistive pressure sensor with a rectangular central boss for low pressure ranges*. IEEE Tran. Elect. Dev. 40 1754-1759.

Sarmiento, J. L., Sundquist, E. T. (1992). *Revised budget for the oceanic uptake of anthropogenic carbon- dioxide.* Nature 356 589-593

Sato, K., Shikida,, M., Yamashiro, T., Tsunekawa, M., Ito, S. (1999). *Roughening of single-crystal silicon surface etched by KOH water solution*. Sens. Actua. A 73 122-130.

Scho1nenberger, C., van der Zande, B. M. I., Fokkink, L. G. J. (1997). *Template synthesis of nanowires in porous polycarbonate membranes: electrochemistry and morphology* J. Phys. Chem. 101 5497-5505.

Schjolberg-Henriksen, K., Wang, D, T., Rogne, H., Ferber, A., Brida, S. (2006). *High resolution pressure sensor for photo acoustic gas detection*. Sens. Actua. A 132 207-213.

Senturia, S, D. (2001). *Microsystem design*. Kluwer Academic.

Seyfried, W. E., Johnson, K. S., Tivey, M. K. (2000). *In-situ sensors: Their development and application for the study of chemical, physical and biological systems at Mid-Ocean Ridges*. RIDGE workshop report 56.

Short, R. T., Fries, D. P., Toler, S. K., Lembke, C. E., Byrne, R. H. (1999). *Development of an underwater mass-spectrometry system for in-situ chemical analysis*. Meas. Sci. Technol. 10 1195-1201.

Sieracki, M. E. Verity P. G., Stoecker, D. K. (1993). *Plankton community response to sequential silicate and nitrate depletion during the 1989 North Atlantic spring bloom*. Deep Sea Res. II 40 213-225.

Smith, C. (1954). *Piezoresistance effect in silicon and germanium.* Phys. Rev. 94 42.

Smith, P. A., Nordquist, C. D., Jackson, T. N., Meyer, T. S., Martin, B. R., Mbindyo, J., Mallouk, T. E. (2000). *Electric field assisted assembly and alignment of metallic nanowires*. Appl. Phys. Lett. 77 1399-1402.

Snodgrass, F. E. (1968). *Deep-sea instrument capsule*. Science 162 78-87.

Takahashi, T., Sutherland, C. S. Sweeney, C. Poisson, A., Metzl, N., Tilbrook, B., Bates, N., Wanninkhof, R., Feely, R. A., Sabine, C., Olafsson J., Nojiri, Y. (2002). *Global sea-air CO_2 flux based on climatological surface ocean pCO_2, and seasonal biological and temperature effects*. Deep Sea Res. II 49 1601-1622.

Taniyasu, Y., Kasu, M., Makimoto, T. (2006). *An aluminum nitride light-emitting diode with a wavelength of 210 nanometres*. Nature 1 325-328.

Tercier, M. L., Buffle, J., Graziottin, F. (1998). *A novel voltammetric in-situ profiling system for continuous real-time monitoring of trace elements in natural waters*. Electroanalysis 10(6) 355-363.

Tengberg, A., Hovdenes, J., Andersson, H. J., Brocandel, O., Diaz, R., Hebert, D., Arnerich, T., Huber, C., K6rtzinger, A., Khripounoff, A., Rey, F., Ronning, C., Schimanski, J., Sommer, S., Stangelmayer, A. (2006). *Evaluation of a lifetime-based optode to measure oxygen in aquatic systems*. Limnol. Oceanogr. Methods 4 7-17.

Timoshenko, S., Woinosky-Krieger, S. (1959). *Theory of plates and shells*. McGraw Hill.

Toriyama, T., Sugiyama, S. (2002). *Analysis of piezoresistance in p-type silicon for mechanical sensors*. J Microelectromechanical Sys. 11 508-604.

Tufts, O., Chapman, P. (1962). *Silicon-element diffused piezoresistive diaphragms.* J. Appl. Phys. 33 3322.

Valizadeh, S., George, J. M., Leisner, P., Hultman, L. (2001). *Electrochemical deposition of Co nanowire arrays; quantitative consideration of concentration profiles*. Electrochim. Acta 47 865-874.

Virta, M., Lampinen, J., Karp, M. (1995). *A luminescence-based mercury biosensor*. Anal. Chem. 67 667-669.

Vitousek, M., Miller, G. (1970). *An instrumentation system for measuring tsunamis in the deep ocean.* Tsunamis in the Pacific Ocean. East-West Center Press 2 39-252.

Wagner, D., Frankenberger, J., Deimel, P. (1994). *Optical pressure sensor using two Mach–Zehnder interferometers for TE and TM polarizations*. J. Micromech. Microeng. 4 35-39.

Wanekaya, A. K., Chen, W., Myung, N. V., Mulchandani, A. (2006). *Nanowire-based Electrochemical biosensors*. Electroanalysis 6 533-550.

Wang, J. (2000). *Analytical Electrochemistry*. 2nd ed. Wiley-VCH. New York.

Wang, J. (2001). *In-situ electrochemical monitoring: From remote sensors to submersible microlaboratories.* Laboratory Robotics and Automation 12 178-182.

Wang, J. (2000). *Lab-on-a-cable for Electrochemical monitoring of phenolic contaminants.* Anal. Chem. 72 2659-2663.

Wang, J. (2005). *Electrochemical biosensors: Towards point of care cancer diagnostics*. Biosens. Bioelectron. 21 1887-1892.

Watkins, J. D. et al. (2004). *An ocean blueprint for the 21st century.* United States Commission on Ocean Policy.

Wearn, R. B., Jr. (1985). *Year long stability measurements on paroscientific atmospheric pressure transducers.* Tech. Note, Paroscientific Inc. 6.

Weisberg, S., Ruberg, S. (2004). *Developing technologies for environmental micro-chemical sensors*. Alliance for Coastal Technologies Workshop Proceedings. Technical Report Series. 21.

Wren, G., May, D. (1997). *Detection of Submerged Vessels using Remote Sensing Techniques*. Australian Defense Force J. 127.

Xia, Y., Yang, P., Sun, Y., Wu, Y., Mayers, B., Gates, B., Yin, Y., Kim, F., Yan, H. (2003). *One-dimensional nanostructures: synthesis, characterization, and applications.* Adv. Mater. 15 353-389.

Yamada, K., Nishihara, M., Matsuoka, Y. (1982). *Nonlinearity of the piezoresistance effect of p-type silicon diffused layers*. IEEE Tran. Elect. Dev. 29 71- 77.

Zhang, X., Wang, J., Wang, Z., Wang, S. (2005). *Improvement of amperometric sensor used for determination of nitrate with polypyrrole nanowires modified electrode*. Sensors 5 580.

APPENDICES

APPENDIX A

CONVERSION OF PRESSURE TO DEPTH

To determine the linear depth in seawater from hydrostatic pressure measurements, it is recommended to measure hydrostatic pressure in pressure units of [decibar], which is about 1 [meter] of depth (source: DigiQuartz® Transducers).

The ocean depth formula, according to UNESCO International State of Equation (IES 80) is:

$$z = D \diagup < g > \tag{A.1}$$

Where z is the depth in meter, D is the geopotential distance fitted to the fourth order polynomial in pressure and <g> is the average gravity.

$$\begin{aligned} D &= C_1 + C_2 P^2 + C_3 P^3 + C_4 P^4 \\ < g > &= g(\theta) + 1 \diagup 2\, \gamma P \end{aligned} \tag{A.2}$$

Where P is in decibar, g(θ) is the local gravity at latitude θ, and C1, C2, C3, C4, γ are constants

Table A.1 List of values for constants in pressure and gravity calculations.

Parameter	Value	Units
P	Measured gauge pressure	[decibar]
C_1	9.72659	[J/kg/decibar]
C_2	-2.2512 E-5	[J/kg/decibar^2]
C_3	2.279 E-10	[J/kg/decibar^3]
C_4	-1.82 E-15	[J/kg/decibar^4]
g(θ)	Local gravity at latitude θ	[m/s^2] - see formula below
γ	2.226 E-6	[m/s^2/decibar]

Table A.2 Typical depth-pressure conversion at different latitudes.

Pressure/Latitude	θ = 0 [deg]	θ = 30 [deg]	θ = 45 [deg]	θ = 60 [deg]
500 [decibar]	496.65 [m]	496.00	495.34	494.69
1000	992.12	990.81	989.50	988.19
2000	1979.55	1976.94	1974.33	1971.72
5000	4915.04	4908.56	4902.08	4895.60
10000	9725.47	9712.65	9699.84	9687.03

Gravity varies with latitude. The standard gravity correction used in the standard ocean depth formula is $g(\theta) = 9.780318\ (1.0 + 5.2788\text{ E-}3\ \sin^2\theta + 2.36\text{ E-}5\ \sin^4\theta)$ [m/s^2] (A.3)

APPENDIX B

ETCH3D™ SIMULATION CODE FOR DOUBLE DIAPHRAGM ETCHING

Python script for first etching step

```
#<div class="moz-text-flowed" style="font-family: -moz-fixed">
#! python
# -*- coding: utf-8 -*-
# Copyright (c) 2006, Coventor, Inc. All rights reserved.
# Autogenerated by Proc2Py on 1/23/2007, 9:14:27
# SEMulator3D-MEMulator 2006.500.1022.2
# This script was generated from the process file:
# AnisoEtch.vproc
# This python script can be modified by the user.
# However, if you regenerate this python script using the process to python writer
# your changes will be lost.
#============================================================
# import modules
from voxelModeler      import *
from time              import *
from etch3dx           import *
import math
startTime = time()
#============================================================
# Setup Masks
layoutFileName = "Model3.gds"
topCellName = "trench"
maskFileObj = MaskFile(layoutFileName, topCellName)
L0D0 = maskFileObj.GetLayer(0)
Aniso = maskFileObj.GetLayer(1)
substratemask = maskFileObj.GetLayer(2)
modelUnits = MICRONS
```

APPENDIX B (continued)

```
# Setup the required Modeler Objects
modelResolution = 4
doc = VoxelDocument("Model3_"+MEMulatorRoot.dateTime, modelResolution)
doc.SetProcessFilename("AnisoEtch.vproc")
doc.SetMaskFile("Model3.gds")
doc.SetModelUnits(modelUnits)
modelerObj = VoxelModeler(doc)
modelerObj.SetMaskUnits(maskFileObj.GetUnitsPerMicron())
modelerObj.SetBounds(GetMaskBounds(modelUnits))
lithographyResolution = 50
modelerObj.SetLithographyResolution(lithographyResolution)
#============================================================
# setup model output parameters
doc.SetOutputEnabled(True)
#============================================================
# Setup Materials
# Using Materials Database File:
C:\work\Etch3D\common\apps\SemulatorMaterialsDatabase.vmpd
Silicon = doc.AddMaterial("Silicon", (192,192,192), DIELECTRIC)
Air = doc.AddMaterial("Air", (), CONDUCTOR)
#============== Step : 0  ( Wafer Setup ) ==============#
print "Step 0 (Wafer Setup) : Create a new wafer (Wafer)"
waferBound = substratemask.GetBounds(modelUnits)
modelerObj.SetBounds(waferBound)
waferThickness = 250
Wafer = modelerObj.CreateRectangularWafer(Silicon, waferThickness, modelResolution, False)
if doc.IsOutputEnabled():
   Wafer.Save(doc.GetModel(),"Wafer Setup",0)
#============== Step : 3  ( Anisotropic Wet Etch ) ==============#
print "Step 3 (Anisotropic Wet Etch) : Anisotropic etch on wafer (Wafer)"
temperature = 350
```

```
concentrationFactor = 0.2
waferType = Wafer100
angle,xax,yax,zax = getWaferRotation(waferType, 0)
anisoetch = getEtch3D(MonteCarlo)
anisoetch.setWafer(Wafer)
anisoetch.setWaferRotation(angle, xax, yax, zax)
anisoetch.setMask(cvar.kBottomSide, L0D0, False)
anisoetch.setEtchFrom(cvar.kTopSide, False)
anisoetch.setEtchFrom(cvar.kBottomSide, True)
anisoetch.setTemperature( temperature )
rpf = RPF_Cinterp(concentrationFactor)
# The following code shows how to modify rpf parameters
print "default value of a21 = ",rpf.getParameterA( 2, 1 )
rpf.setParameterA( 2, 1, 0.75 )
print "    new value of a21 = ",rpf.getParameterA( 2, 1 )
print "default value of b21 = ",rpf.getParameterB( 2, 1 )
rpf.setParameterB( 2, 1, 7.4 )
print "    new value of b21 = ",rpf.getParameterB( 2, 1 )
print "default value of a33 = ",rpf.getParameterA( 3, 3 )
rpf.setParameterA( 3, 3, 0.1 )
print "    new value of a33 = ",rpf.getParameterA( 3, 3 )
print "default value of b31 = ",rpf.getParameterB( 3, 1 )
rpf.setParameterB( 3, 1, 6.35 )
print "    new value of b31 = ",rpf.getParameterB( 3, 1 )
anisoetch.setRPF(Silicon, rpf)
anisoetch.visualize()
if doc.IsOutputEnabled():
   Wafer.Save(doc.GetModel(),"Anisotropic Wet Etch",3)
Wafer.WriteOctree('1st_step_aniso.oct')
#============================================================
# Begin footer at end of process
```

```
if not doc.IsOutputEnabled():
   doc.SetOutputEnabled(True)
   Wafer.Save(doc.GetModel(),"Anisotropic Wet Etch")
doc.Save()
endTime = time()
doc.StartZsplat()
print "Build process completed."
print "Elapsed Time", int(endTime-startTime), "seconds."
#</div>
```

Python script for second etching step

```
#<div class="moz-text-flowed" style="font-family: -moz-fixed">
#! python
# -*- coding: utf-8 -*-
# Copyright (c) 2006, Coventor, Inc. All rights reserved.
#
# Autogenerated by Proc2Py on 1/23/2007, 9:14:27
# SEMulator3D-MEMulator 2006.500.1022.2
# This script was generated from the process file:
# AnisoEtch.vproc
# This python script can be modified by the user.
# However, if you regenerate this python script using the process to python writer
# your changes will be lost.
#============================================================
# import modules
from voxelModeler      import *
from time              import *
from etch3dx           import *
import math
startTime = time()
```

APPENDIX B (continued)

```
#============================================================
# Setup Masks
layoutFileName = "Model3.gds"
topCellName = "trench"
maskFileObj = MaskFile(layoutFileName, topCellName)
L0D0 = maskFileObj.GetLayer(0)
Aniso = maskFileObj.GetLayer(1)
substratemask = maskFileObj.GetLayer(2)
modelUnits = MICRONS
#============================================================
# Setup the required Modeler Objects
modelResolution = 4
doc = VoxelDocument("Model3_2nd_"+MEMulatorRoot.dateTime, modelResolution)
doc.SetProcessFilename("AnisoEtch.vproc")
doc.SetMaskFile("Model3.gds")
doc.SetModelUnits(modelUnits)
modelerObj = VoxelModeler(doc)
modelerObj.SetMaskUnits(maskFileObj.GetUnitsPerMicron())
modelerObj.SetBounds(GetMaskBounds(modelUnits))
lithographyResolution = 50
modelerObj.SetLithographyResolution(lithographyResolution)
#============================================================
# setup model output parameters
doc.SetOutputEnabled(True)
#============================================================
# Setup Materials
# Using Materials Database File:
C:\work\Etch3D\common\apps\SemulatorMaterialsDatabase.vmpd
Silicon = doc.AddMaterial("Silicon", (192,192,192), DIELECTRIC)
Air = doc.AddMaterial("Air", (), CONDUCTOR)
#============== Step : 0  ( Wafer Setup ) ==============#
```

```
print "Step 0 (Wafer Setup) : Create a new wafer (Wafer)"
waferBound = substratemask.GetBounds(modelUnits)
modelerObj.SetBounds(waferBound)
waferThickness = 250
# ==============================
Wafer = modelerObj.CreateEmptyWafer()
Wafer.ReadOctree('1st_step_aniso.oct')
#============== Step : 4  ( Anisotropic Wet Etch ) ==============#
print "Step 4 (Anisotropic Wet Etch) : Anisotropic etch on wafer (Wafer)"
temperature = 350
concentrationFactor = 0.5
waferType = Wafer100
angle,xax,yax,zax = getWaferRotation(waferType, 0)
anisoetch = getEtch3D(MonteCarlo)
anisoetch.setWafer(Wafer)
anisoetch.setWaferRotation(angle, xax, yax, zax)
anisoetch.setMask(cvar.kBottomSide, Aniso, False)
anisoetch.setEtchFrom(cvar.kTopSide, False)
anisoetch.setEtchFrom(cvar.kBottomSide, True)
anisoetch.setTemperature( temperature )
rpf = RPF_Cinterp(concentrationFactor)
# The following code shows how to modify rpf parameters
print "default value of a21 = ",rpf.getParameterA( 2, 1 )
rpf.setParameterA( 2, 1, 0.75 )
print "    new value of a21 = ",rpf.getParameterA( 2, 1 )
print "default value of b21 = ",rpf.getParameterB( 2, 1 )
rpf.setParameterB( 2, 1, 7.4 )
print "    new value of b21 = ",rpf.getParameterB( 2, 1 )
print "default value of a33 = ",rpf.getParameterA( 3, 3 )
rpf.setParameterA( 3, 3, 0.1 )
print "    new value of a33 = ",rpf.getParameterA( 3, 3 )
```

```
print "default value of b31 = ",rpf.getParameterB( 3, 1 )
rpf.setParameterB( 3, 1, 6.35 )
print "    new value of b31 = ",rpf.getParameterB( 3, 1 )
anisoetch.setRPF(Silicon, rpf)
anisoetch.visualize()
if doc.IsOutputEnabled():
   Wafer.Save(doc.GetModel(),"Anisotropic Wet Etch",4)
#============================================================
# Begin footer at end of process
if not doc.IsOutputEnabled():
   doc.SetOutputEnabled(True)
   Wafer.Save(doc.GetModel(),"Anisotropic Wet Etch")
doc.Save()
endTime = time()
doc.StartZsplat()
print "Build process completed."
print "Elapsed Time", int(endTime-startTime), "seconds."
#</div>
```

APPENDIX C

PHOTOLITHOGRAPHY PROCESSES

Negative Resist NR1-3000PY

(1) Clean using acetone/methanol/DI water and nitrogen dry
(2) Dispense photoresist NR1-3000PY (Futurrex Inc.) to cover 75% of the wafer
(3) Spin at 3000 rpm for 30 seconds
(4) Soft bake on hot plate at 155 ^{o}C for 60 seconds
(5) Expose using a EVG-620 mask aligner for 17 seconds
(6) Hot plate bake at 110 ^{o}C for 60 seconds
(7) Immersion develop in developer RD6 (Futurrex Inc.) for 27 seconds
(8) Measured photoresist thickness ~ 3.4 µm

Positive Resist AZ P4620

(1) Clean using acetone/methanol/DI water and nitrogen dry
(2) Dispense adhesion promoter HMDS and spun at 3500 rpm for 30 seconds
(3) Spin photoresist - AZ P4620 (Clariant Inc.) at 500 rpm for 10 seconds, then 2500 rpm for 60 seconds
(4) Soft bake on hot plate at 110^{o}C for 90 seconds
(5) Expose using EVG-620 mask aligner for 55 seconds
(6) Immersion develop with agitation in a 3 bath mixture of developer AZ 400K: DI Water (1:3), for 20 seconds each.
(7) Measured photoresist thickness ~ 9.6 µm

Positive Resist SC 1818

(1) Clean using acetone/methanol/DI water and nitrogen dry
(2) Dispense adhesion promoter HMDS and spun at 3000 rpm for 30 seconds
(3) Photoresist - SC 1818 (Shipley Inc.) spun at 3000 rpm for 30 seconds
(4) Soft bake in hot plate at 105 ^{o}C for 60 seconds
(5) Expose using EVG-620 mask aligner for 45 seconds
(6) Immersion develop in developer MF 319 (Shipley) for 70 seconds
(7) Hard bake in hot plate at 130 ˚C for 60 second

(8) Measured photoresist thickness ~ 2.44 µm

Negative Resist SU-8 50

(1) Pretreatment – solvent t cleaning and Oxygen plasma clean, followed by dehydration bake at 200 ˚C for 5 minutes
(2) Static dispense of SU-8 (Microchem), 500 rpm (100 rpm/Sec) for 10 seconds, then 2000 rpm (300 rpm/sec) for 30 seconds.
(3) Soft bake hot plate 65 ˚C for 6 minutes, then 95 ˚C for 20 minutes
(4) Expose EVG-620 mask aligner 55 seconds
(5) Post exposure bake hot plate 65 ˚C for 1 minutes, then 95 ˚C for 5 minutes
(6) Immersion develop in SU-8 developer for 7 minutes
(7) Rinse isopropyl alcohol (no water) and then nitrogen dry
(8) Hard bake hot plate 180 ˚C 10 minutes
(9) Thickness measured ~ 60 µm

PDMS Molding

(1) Mix 55g of 1:10 PDMS (Sylgard 184 – curing agent and polymer base)
(2) Pre-cure PDMS by pouring on Si master mold
(3) Degas in vacuum chamber
(4) Oven bake at 80 ˚C for 3-6 hours
(5) Peel PDMS from Si master

APPENDIX D

THROUGH WAFER NANOSTRUCTURES (INTERCONNECTS) IN POROUS SILICON

Introduction

The objective of this work was to demonstrate the ability to fabricate ultra-high aspect ratio nanostructures/nanowires (either single-segment Ni-Fe, Au or two-segment Ni-Fe/Au) with controlled diameter in porous silicon for potential bio-sensing applications. In this paper, we report on the fabrication of nanoporous silicon templates and subsequent electrodeposition and structural characterization of Ni-Fe, Au and Ni-Fe/Au segments. The ability to fabricate nanostructures in silicon templates with controlled and uniform nanometer-sized pores in large scale opens a new avenue for integration of nanostructures with Si based microelectronics.

The template synthesis of nanomaterials by electrodeposition is an elegant low-cost, high yield alternative to sophisticated methods such as molecular beam epitaxy, nanolithography and vapor-liquid-solid growth mechanisms. The key feature of the templating technique is ones' ability to control the size, length, shape and morphology of the material deposited by (a) controlling the template morphology and (b) controlling the synthesis parameters. In addition, electrodeposition provides the ability to introduce composition modulation or different functionalities (two-segment Ni-Fe/Au) along the wire length. Traditionally, the synthesis of nanostructures was done by deposition of desired material within monodispersed pores in templates such as alumina membranes (anodized aluminum films), nuclear track-etched polymer membranes and mesoporous silica.

However, the porous silicon template method reported herein has significant advantages over the traditional methods. The fabrication of porous silicon by electrochemical etching of silicon is a well-established technique. Until now, porous silicon was used either as a sacrificial material to fabricate free-standing structures and cavities or in photonic crystals and as sensors. We have instead used the ultra-high aspect ratio nanoscale pores created by electrochemical etching of silicon as a "nano-template" to create one-dimensional nanostructures, namely nanowires. The advantages of porous Si template are a) silicon is an economical, well-understood and rigid structural material, which yields to microfabrication. Unlike, porous alumina template which is fragile and unsuitable for device fabrication (because of the presence of a barrier layer,

that prevents direct physical and electrical contact between the nanowires and substrate). The nanowires fabricated in porous silicon are always physically and electrically addressable through the silicon substrate, b) currently, there are few methods to assemble and organize nanostructures on sensor surfaces. However, these techniques which include dielectrophoresis, polymer casting, epoxies, layer-by layer fluidic alignment or magnetic alignment involve tedious fabrication, transfer and alignment procedures externally on the sensor surface. In other methods, a two step process of first forming the porous alumina on silicon substrate and then depositing nanowire arrays were used. In contrast, porous silicon template based method will use a single process to directly integrate nanowires as functional in-situ structures in silicon electronics, optical, sensing or lab-on-chip (LOC) components, without contaminating the sensing surface, d) the templating and synthesis of nanowires can be localized at "regions of interest" using masking layers, thus enabling a rigid pathway for seamless integration with sensor arrays and CMOS microelectronic circuits on the same wafer, e) pore dimensions and morphology can be easily controlled by varying doping (n- or p-type) or applied current for electrochemical etching, f) length of the nanowire can be effectively controlled by varying the etching time. The silicon templating approach allows for synthesis of nanowires an order of magnitude longer (> 100 μm) than conventional templates: alumina, highly ordered pyrolytic graphite (HOPG) or polycarbonate (<10 μm).

To the best of our knowledge, there are only few available articles on electrodeposition of metallic nanostructures in porous silicon. Earlier work on electrodeposition or laser assisted deposition into porous silicon focused on improving the electrical conductivity and prevent degradation. In this work, we provide a detailed fabrication process and characterization of controlled ultra-high aspect ratio metallic nanostructures namely, single segment Ni-Fe or Au and two-segment Ni-Fe/Au directly templated in porous silicon.

Experimental details

. The nanoporous silicon template was prepared by electrochemical etching of the silicon substrate. Figure D.1 schematically illustrates the process flow for fabrication of nanoporous silicon and electrodeposition of single-segment nanostructures. The starting material for the template was chosen based on the target pore diameter. N-type 2" Si substrate (resistivity: 0.4-0.6

ohm-cm/doping density: 10^{16} cm^{-3}) was used for target pore diameter of 290 nm and P-type Si substrate (resistivity: 0.001-0.002 ohm-cm/doping density 10^{20} cm^{-3}) was used for target pore diameter of 40 nm. A 200 nm Al layer was deposited by e-beam evaporation on the backside of the template substrate, making it the working electrode (figure D.1a). Next this silicon wafer was mounted in a rig to ensure only the front side of the wafer was exposed to the etchant. The backside was then biased and the etchant, a mixture of 25% (v/v) HF/ethanol, was added to the rig. The wafer was electrochemically etched at a current density of 35 mA/cm^2, to obtain the nanopores (figure D.1b). Ethanol was added to the HF solution to 1) increase the wettability of porous silicon surface and 2) to remove hydrogen evolved during etching. During etching of p-type wafers, a potential of 5 V was applied and for n-type wafers, a potential of 15 V was applied with the same current density of 35 mA/cm^2 and HF concentration for both cases. The length of the nanopores was controlled by varying the etching time. This was followed by electrochemical deposition of the metal into the nanoporous silicon template. In case of Ni-Fe, a sulfate based electroplating bath of composition 200g/L $NiSO_4.6H_2O$, 8g/L $FeSO_4.6H_2O$, 5g/L $NiCl_2.6H_2O$, 25 g/L H_3BO_3, 3g/L Saccharin was used (figure D.1c). A Ni foil was used as anode to maintain constant metal ion composition and the electroplating was performed under current density of 3.5 mA/cm^2. Au was electrodeposited from a Transene 25E™ gold plating solution (Transene Inc.) at 4 mA/cm^2. A platinum mesh was used as the anode. For two-segmented (Ni-Fe/Au) nanostructures, electrodeposition was done sequentially, first Ni-Fe and then Au was electrodeposited, with thorough cleaning with DI water in between the two electroplating steps. The nanowires were about 250-300nm in diameter.

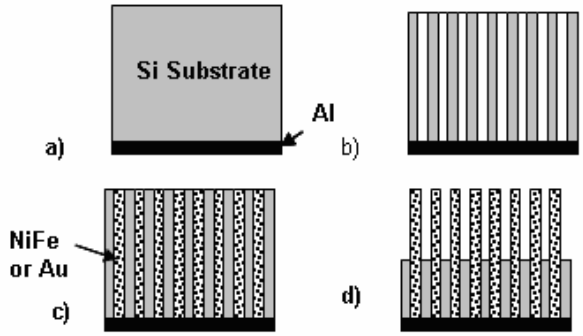

Figure D.1 Process flow for fabrication of nanowires. a) Starting Si substrate with Al working electrode, b) electrochemical Etching of Si, c) electroplating of Ni-Fe wires, d) partial nanowire release (10 μm, not to scale).

.

Results and discussion

Figure D.2 is an SEM micrograph of the n-type silicon substrate after etching for 100 minutes. The average pore diameter in this substrate was 290 nm with a pitch of 1 μm. The pores were 145 μm deep. Figure D.3 shows the SEM micrograph of 40 nm pores developed in p-type Si wafers, with a pitch of 0.6 μm. The porosity of the substrate was determined gravimetrically. Porosity is defined as the fraction, P of the total volume of the silicon sample V_s that is attributed to the pores V_{ps} $P = V_{ps} / V_s$ (D.1)

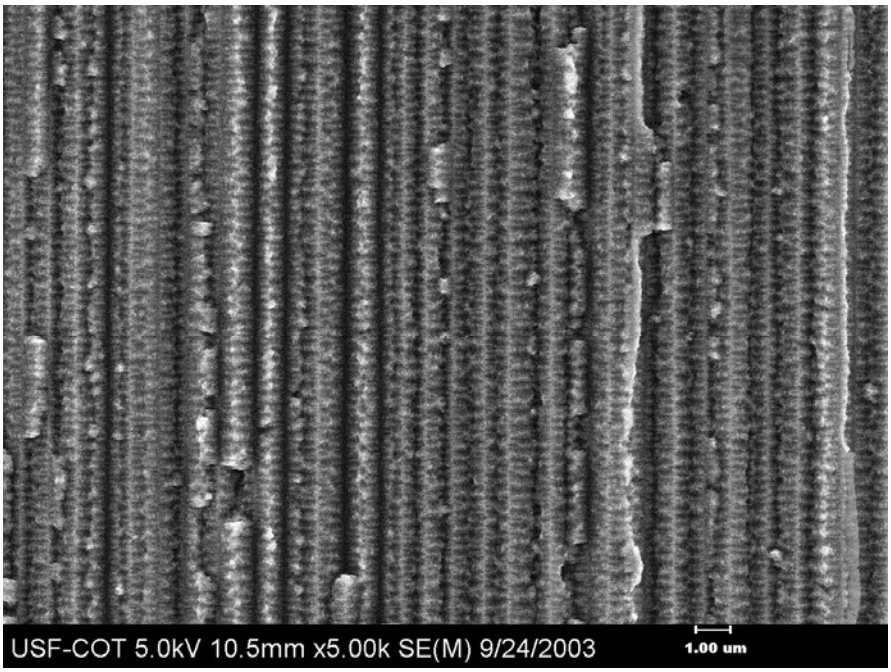

Figure D.2 SEM image of 290 nm diameter and 145 μm deep nanopores in n-type Si substrate. Resistivity: 0.4-0.6 ohm-cm electrochemically etched in 25% (v/v) HF/ethanol at a constant current density of 35 mA/cm^2.

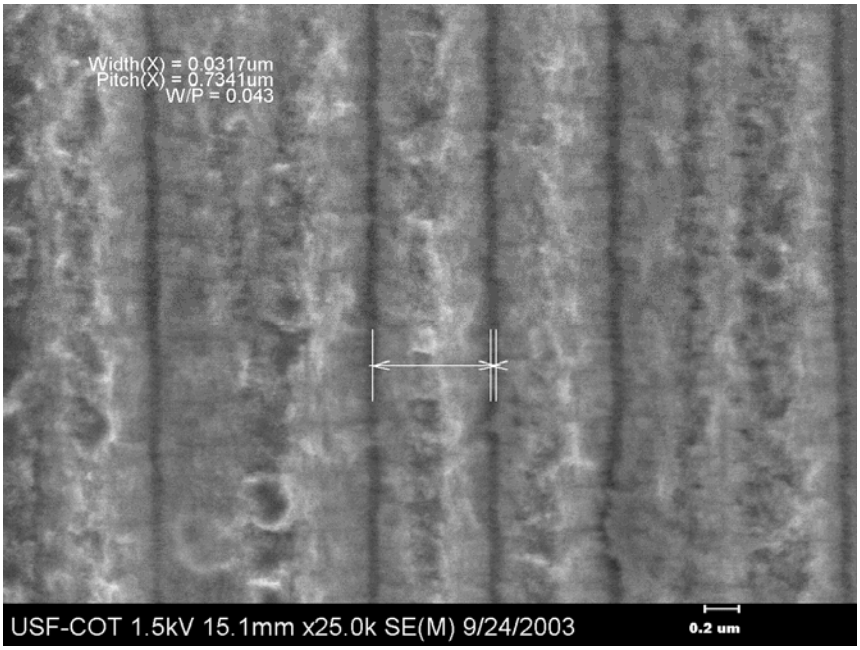

Figure D.3 SEM image of 40 nm diameter nanopores in p-type Si substrate. Resistivity: 0.001-0.002 ohm-cm) electrochemically etched in 25% (v/v) HF/ethanol at a constant current density of 35 mA/cm^2.

The porous silicon volume, V_{ps} can be calculated from the mass of etched silicon, Δm_e (determined by weighing the sample before and after etching) and silicon bulk density, ρ_s (2330 kg/m^3). While the volume of original silicon, V_s is given by the porous silicon layer thickness, L and the area, A exposed to the etching solution:

$$P = \Delta m_e / AL\rho_s \qquad \text{(D.2)}$$

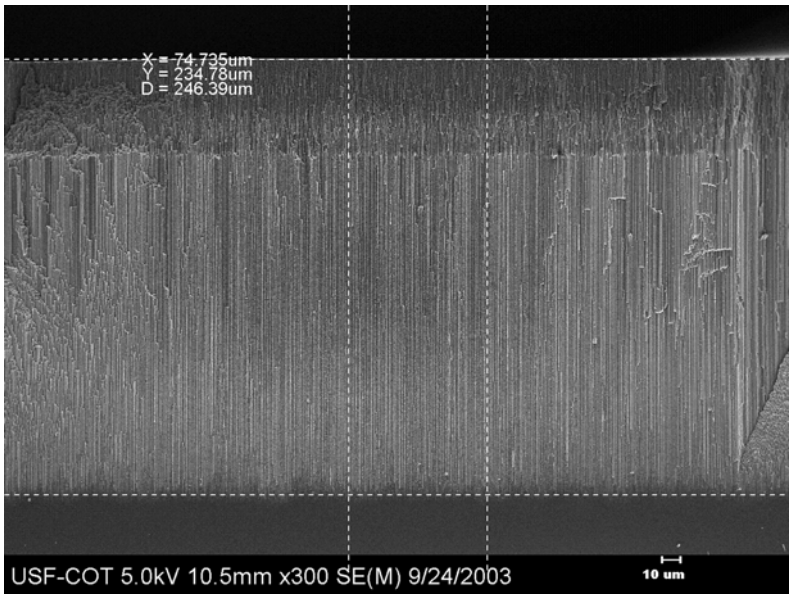

Figure D.4 SEM image of nanopores, 235 μm deep after 160 minutes of etching in 25% (v/v) HF/ethanol at a constant current density of 35 mA/cm^2.

Thus the porosity of n-type Si after 100 minutes of etching was calculated to be approximately 16 %. Further, the growth of pores was controlled by controlling the etching time. The pore growth rate, r is defined as the increase in pore length divided by the etch time. With constant etch current density and negligible diffusion gradient in the pores, the growth rate is given as:

$$r = l/t \tag{D.3}$$

Where l is the pore length and t is the total etching time. When the etching time was increased from 100 minutes to 160 minutes, the pore depth increased from 145 to 235 μm, suggesting an growth (etch) rate of 1.45 μm/min. Figure D.4 shows the SEM image of the 235 μm deep nanopores in n-type Si. The pore growth rate can also be controlled by changing the etching current (this changes the number of ions and hence the etch rate), substrate doping density, crystal orientation, HF concentration and temperature. Figure D.5 depicts the SEM image of single-segment Au nanowires. The other nanowires are explained in Chapter 6. Figure D.4 shows a cluster of Au nanowires released partially from the porous silicon template. The wires are multi-faceted with rough outer surface, replicating the structure of porous silicon pore walls.

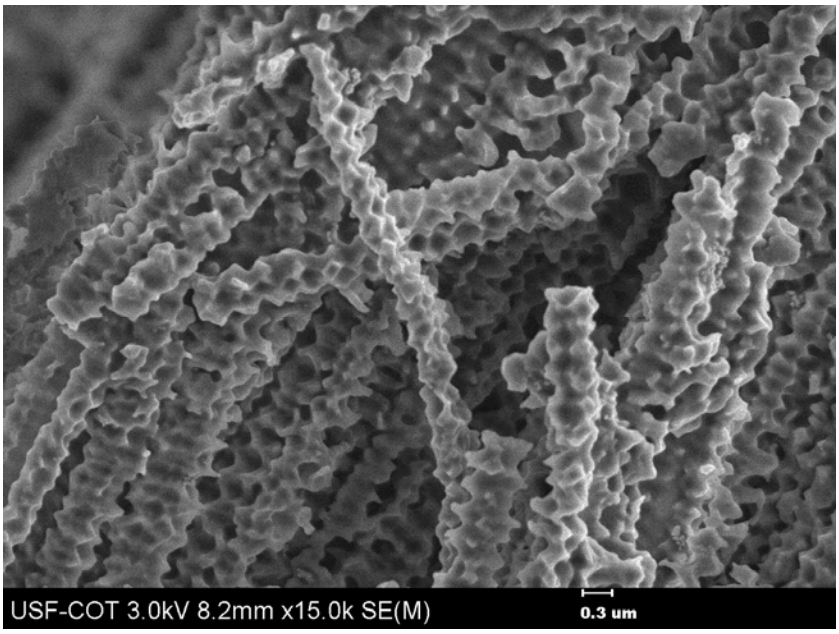

Figure D.5 SEM image showing cluster of 275±25 nm Au nanowires.

Summary

In this work, nanostructured silicon templates for growing nanowires/nanostructures by electrochemical etching technique were successfully synthesized. Long (up to 100 μm) Ni-Fe, Au and two-segmented Ni-Fe/Au nanostructures with diameter of 275±25 nm have been plated in these templates to demonstrate the feasibility of this approach. The ease in fabrication of the template and ability to control the diameter, length and porosity of the nanowires by tailoring the template are significant advantages of the Si template approach. This approach is also well-suited for integration of ordered nanostructures arrays as active functional components in silicon electronic and sensing devices.

APPENDIX E

MAGNETIC PROPERTIES OF NI-FE NANOWIRES: EFFECT OF TEMPLATE MATERIAL AND DEPOSITION CONDITIONS

Introduction

To date, most of the research work has focused on studying the magnetic properties by changing the electrodeposition parameters or template parameters. In this work, we present a comparative study of magnetic nanowires deposited in different templates. The magnetic properties of nanowire arrays are directly related to properties of the template such as pore dimensions, relative pore orientation, pore size distribution and pore surface roughness. Further, we also investigate the influence of applied magnetic field during electrodeposition of Ni-Fe nanowires on their crystallographic and magnetic properties. In addition to traditional templates such as porous alumina and polycarbonate, magnetic properties of nanowires deposited in porous silicon are also investigated. In a previous work, we have demonstrated the ability to control the porous silicon dimensions (pore diameter, 40-290 nm and length, up to 240 μm) and then electroplate metal ions into the pores. In order to investigate the magnetostatic coupling effect on the overall magnetic properties, nanowires with different wire lengths were prepared by controlling the electroplating time.

Experimental details

Magnetic nanowire arrays were prepared by electroplating Ni-Fe into the pores of Anopore® inorganic membrane (alumina), Nuclepore Polycarbonate track-etched membranes and porous silicon templates. Alumina and polycarbonate membranes were bought from Whatman Inc**.,** NJ, USA and were used after through cleaning in DI water and followed by drying. The porous silicon template was prepared in-house by electrochemical etching of silicon substrate. N-type 2" silicon substrate (resistivity: 0.4-0.6 ohm-cm) was electrochemically etched in a mixture of 1:1::49% HF:ethanol at a constant current density of 35 mA/cm^2. Ethanol was added to the HF solution to 1) increase the wettability of porous silicon surface and 2) to remove hydrogen evolved during etching. A film of aluminum (~ 1 μm) was evaporated on one side of all templates to serve as the working electrode. This was followed by electrochemical deposition of Ni-Fe into the templates from a sulfate based electroplating bath (200 g/L $NiSO_4.6H_2O$, 8 g/L $FeSO_4.6H_2O$,

5 g/L $NiCl_2.6H_2O$, 25 g/L H_3BO_3, 3 g/L Saccharin). As the stoichiometry of the Ni-Fe nanowires was significantly affected by plating temperature, pH, agitation conditions, current, and additives, all the parameters have been maintained constant, except the electroplating time. Ni foil was used as anode to maintain constant metal ion composition and the electroplating was performed under a current density of 3 mA/cm^2 at room temperature (20 ºC). The magnetic field applied during electroplating was perpendicular/parallel to the template plane.

The structure and morphology of the nanowires were analyzed under a Scanning Electron Microscope (SEM). While the com position and crystallographic structure of the electrodeposited Ni-Fe (after dissolving Al and silicon template) were investigated by Energy Dispersive Spectroscopy (EDS) and in an X'Pert PRO X-diffraction system (XRD) from Philips Analytical. An X-ray diffractometer with a monochromatized Cu Kα (λ = 15.4 nm) radiation in a Bragg-Brentano arrangement was used for this analysis. The Physical Property Measurement System (PPMS) from Quantum Design was used to measure the magnetic properties of the nanowires embedded within the templates.

Experimental results and discussion

Microscopy and Structural Characterization: Figure E.1(a-c) shows the SEM micrographs of porous silicon, alumina and polycarbonate templates respectively. The average pore diameter in porous silicon was 300±10 nm with an interpore distance of 800 nm after electrochemical etching for 100 minutes (figure E.1a). The pores were 145 μm in length with irregular walls and branched pores because of inherent defect regions in silicon. Figure E.1(b) and E.1(c) show the top surface of the alumina and polycarbonate templates of thicknesses 60 μm and 6 μm respectively. The pores are 200±10 nm in diameter with an interpore distance of about 250-300 nm in case of alumina and 250-600 nm in case of polycarbonate. Table E.1 summarizes the template/pore characteristics as measured with the SEM. It is evident from the table that the lattice parameter or inter-pore spacing of polycarbonate and porous silicon templates are much larger than that of alumina.

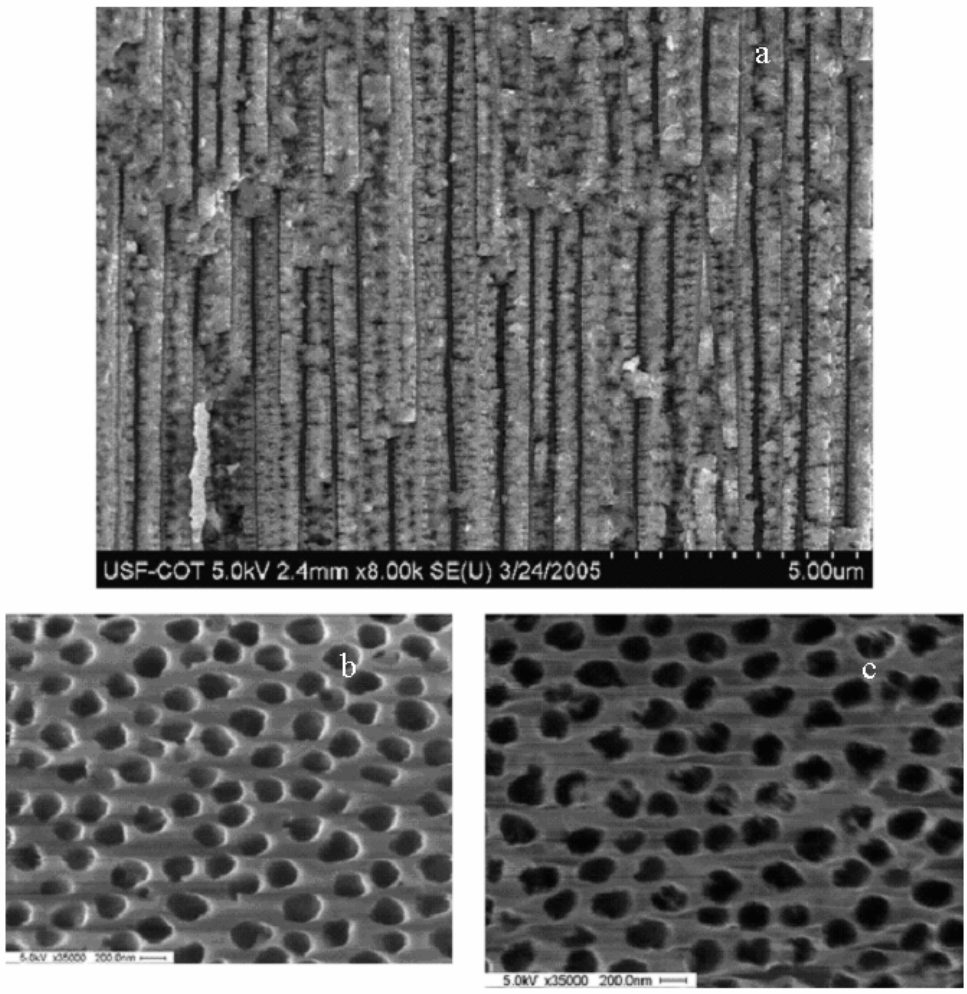

Figure E.1 a) SEM image of 280-300 nm diameter and 145 μm deep nanopores in n-type Si substrate b) SEM view of the starting alumina template c) SEM view of the polycarbonate template. The pores are 200 nm in diameter and 6 μm in depth. Alumina pores are 200 nm in diameter and 60 μm in depth.

Figures E.2(a) and E.2(b) show the SEM images of Ni-Fe nanowires (after removing the template) deposited in porous silicon and alumina templates respectively. Ni-Fe nanowires deposited in porous silicon were 275 ± 25 nm in diameter while Ni-Fe nanowires in alumina and polycarbonate were 180-200 nm in diameter. The length of the nanowire was initially calculated from the deposition charge and time and later verified using the SEM. The Ni-Fe nanowires' of varying lengths up to 5 μm were deposited in polycarbonate template to study length dependent

magnetic properties. The nanowires were seen to be textured and highly faceted with multiple grain boundaries. Further, analysis of the Ni-Fe nanowires deposited in porous silicon reveals irregular wire surface, wire breakage and branched growth of wires, which is probably due to the nature of porous silicon etching. While, nanowires deposited in alumina and polycarbonate had smooth and uniform surface morphology. However, nanowires deposited in such commercially available polycarbonate templates have an angle between the wire/pore axis and the normal to the plane typically between 0º and 34º. A quantitative Energy Dispersive Spectroscopy (EDS) spectrum was taken to determine the elemental composition of the Ni-Fe nanowires. A small amount of oxygen is seen in the spectrum, indicating oxygen absorption in the Ni-Fe from air.

Table E.1 Template parameters and characteristics.

Parameters	Porous silicon	Polycarbonate	Alumina
Pore size (nm)	290-310	190-210	190-210
Inter-pore distance (nm)	800-900	250-600	250-300
Pore density (pores/cm^2)	about 10^7	about 10^8	about 10^9

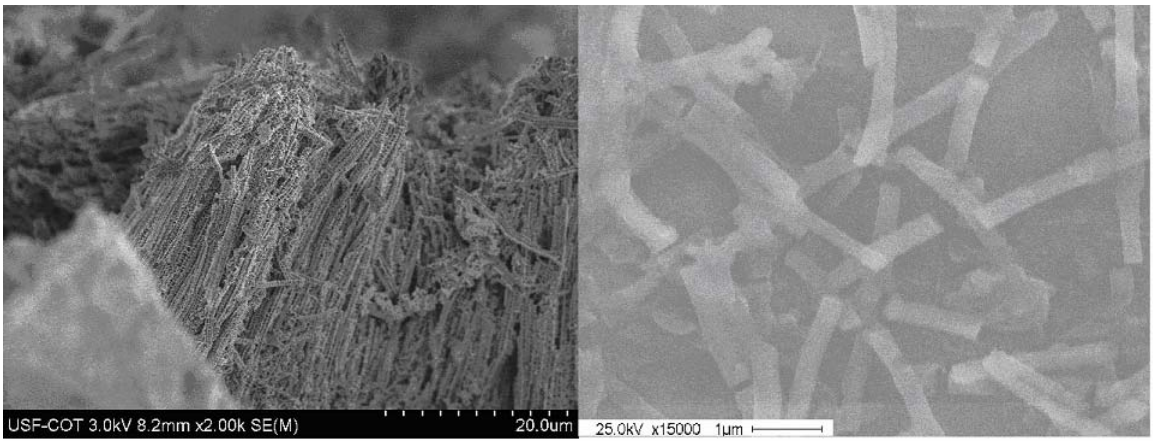

Figure E.2 SEM image of a cluster of 250-300 nm Ni-Fe nanowires (left), b) SEM view of nanowires released from alumina template (right). The wires are 200 nm in diameter, regular and uniform.

Figure E.3 shows the x-ray diffraction pattern the Ni-Fe nanowires (a) without magnetic field, b) with a magnetic field (about 320 Oe) applied perpendicular to the template plane during electrodeposition. Significant differences in crystalline structure are observed. The diffraction peak pattern further confirms the electrodeposition of Ni-Fe along with Ni. In absence of magnetic field, the pattern (figure E.3a) shows a strong peak for (111) $FeNi_3$ and (111) Ni along with other lesser peaks at (200), (211) for $FeNi_3$ and Ni. There is also evidence for formation of Ni-Si impurity phases from silicon template. A strong peak at (111) for Ni-Fe and Ni indicates grain orientation along the preferred (111) direction, but the other peaks suggest a polycrystalline nature for the Ni-Fe grains. When the nanowires are deposited with a perpendicular magnetic field (figure 3b, template dissolved) along with Ni-Fe (111), Ni-Fe (200) also becomes dominant. Hence, applied magnetic field has a strong influence on the textural and morphological changes in Ni-Fe. Importantly, the growth of (200) texture is enhanced with applied magnetic field. This may be due to: (1) induced convective solution flow near the template's vicinity, decreasing the thickness of the diffusion layer and therefore increasing the mass transport of active species, (2) in presence of magnetic field the Ni-Fe grains are forced to grow with c-axis along the orientation of applied magnetic field, inducing an enhanced (200) texturing. However, the applied field is not strong enough to totally force wire axis parallel to Ni-Fe c-axis.

Magnetic characterization*:* Next, we compare the magnetic properties of Ni-Fe nanowires deposited in different templates (porous silicon, alumina and polycarbonate) with/without applied magnetic field (about 320 Oe) during electrodeposition. The saturation magnetizations of Ni-Fe were measured to be about 1 T. Figure E.4 depicts typical magnetic hysteresis curves of Ni-Fe nanowires deposited without magnetic field, in a) porous silicon, b) alumina, c) polycarbonate templates. The hysteresis curves were measured with magnetic field either in-plane or out-of plane to the nanowires. As reported earlier by us in porous silicon and also evident from figure E.4, no/weak magnetic anisotropy is shown by these nanowires. For infinite long cylinders' strong shape anisotropy is expected with the magnetic easy axis aligning parallel to the long axis of the wires. Further, if the magnetocrystalline anisotropy is small compared to shape anisotropy, square hysteresis curve is expected, when magnetic field is applied in-plane with the wires. However, competition between the magnetocrystalline anisotropy, with preferred (111) direction and shape anisotropy (long magnetic cylinders), results in no net magnetic anisotropy. The

coercivity and squareness ratio (ratio of saturation magnetization to remnant magnetization) were in the range of 50-100 Oe and 0.1-0.18 respectively for all the measured samples. A similar weak anisotropy is shown by nanowires deposited with magnetic field (about 320 Oe) parallel to the template plane.

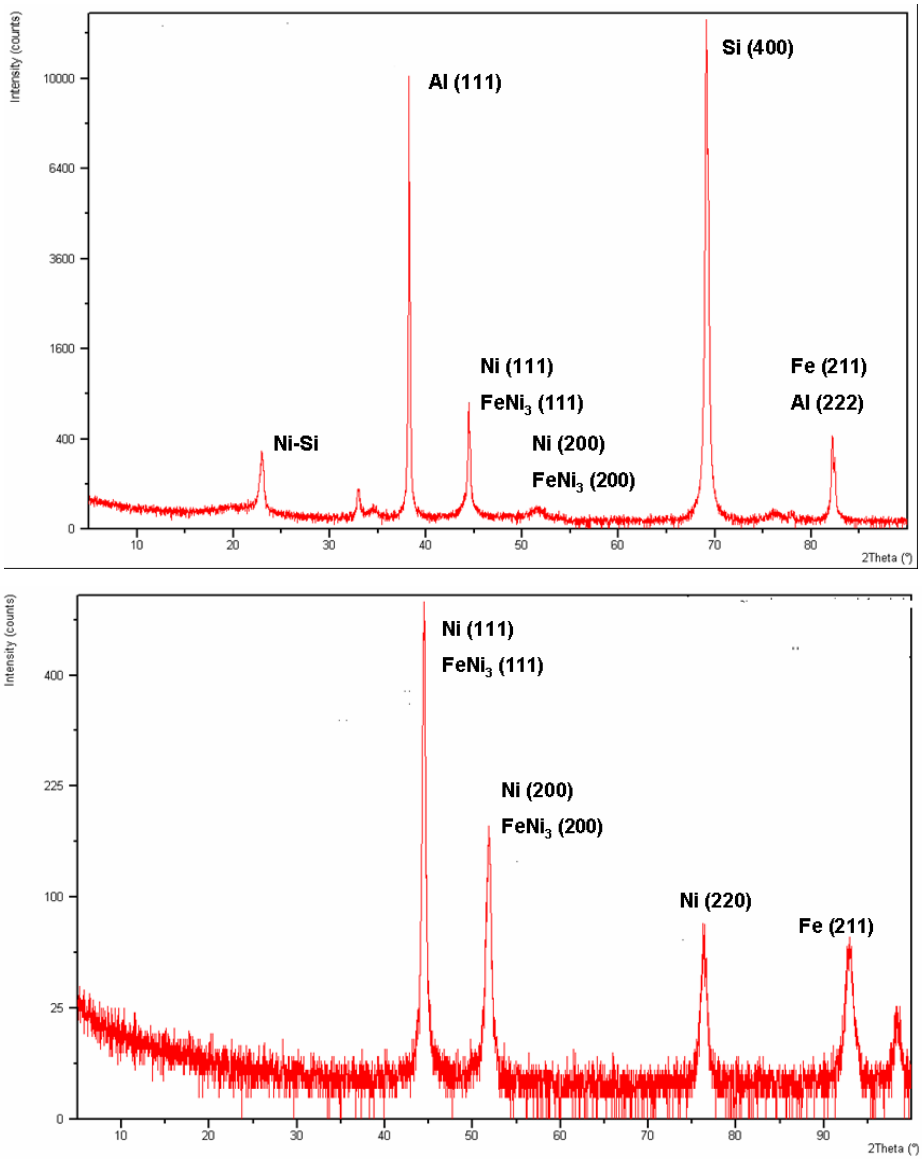

Figure E.3 X-ray diffraction pattern of Ni-Fe nanowires deposited in a) without magnetic field in porous silicon, b) with perpendicular magnetic field in polycarbonate template.

APPENDIX E (continued)

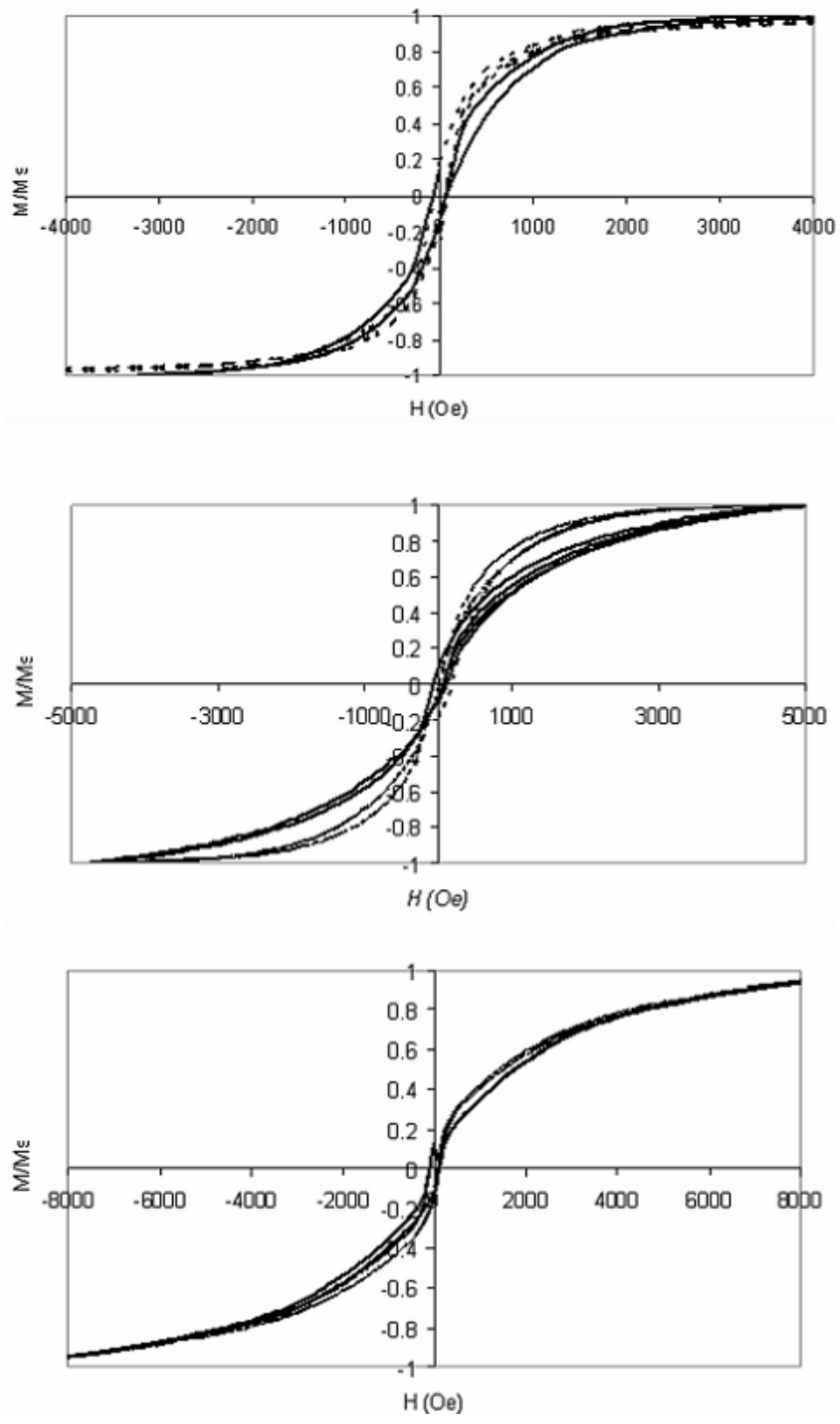

Figure E.4 Typical magnetic hysteresis curves of Ni-Fe nanowire arrays measured parallel and perpendicular to the template plane in a) porous silicon, b) alumina, c) polycarbonate in absence of magnetic field. H perpendicular (--), H parallel (-).

APPENDIX E (continued)

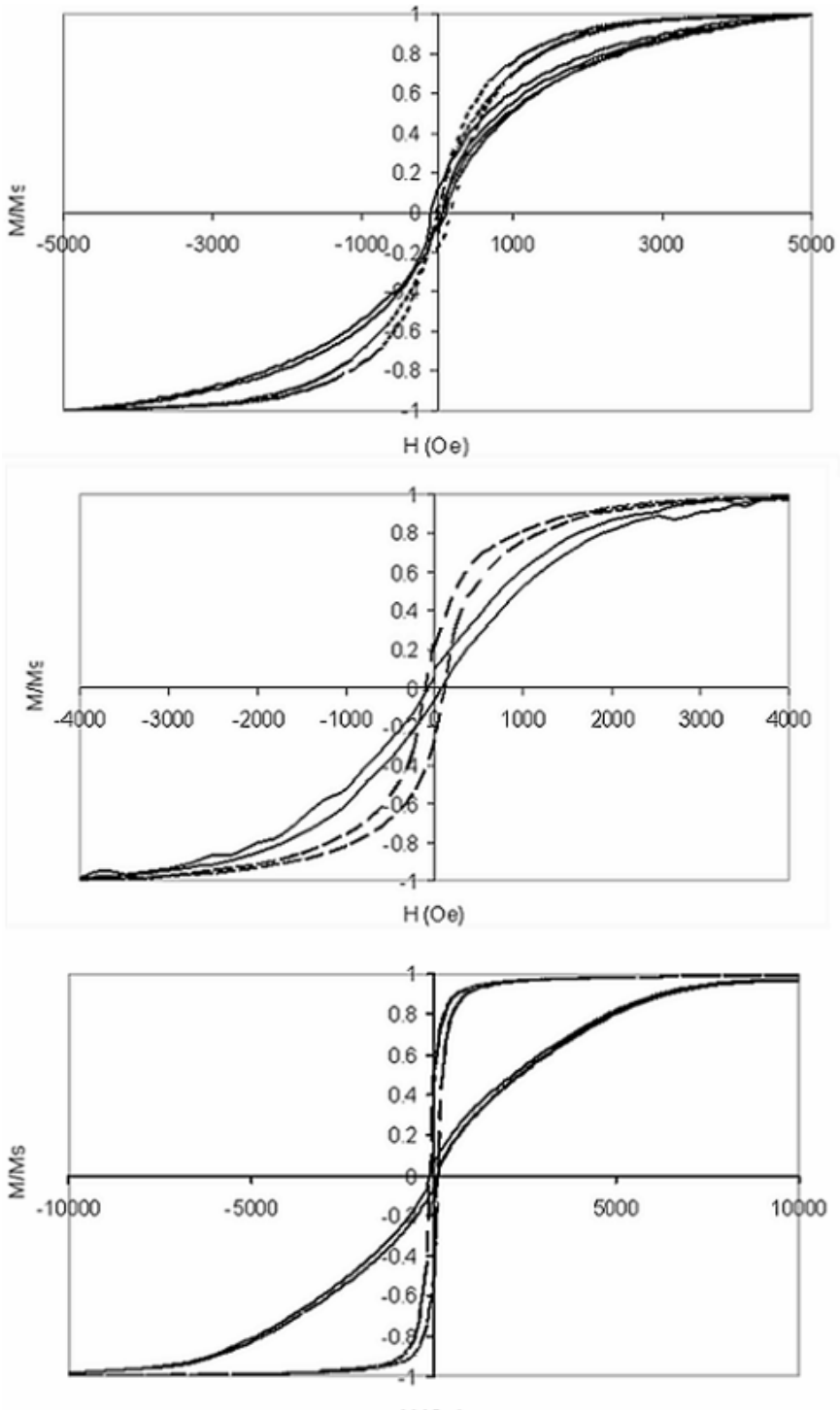

Figure E.5 Typical magnetic hysteresis curves of Ni-Fe nanowire arrays measured parallel and perpendicular to the template plane in a) porous silicon, b) alumina, c) polycarbonate in presence of perpendicular magnetic field. H perpendicular (--), H parallel (-).

A very different behavior is exhibited in Ni-Fe nanowires deposited with magnetic field (about 320 Oe) perpendicular to the template plane. Figure E.5 shows the typical magnetic hysteresis curves of Ni-Fe nanowires deposited in perpendicular magnetic field for a) porous silicon, b) alumina, c) polycarbonate templates. As shown in figure 5, all templates, in general exhibited perpendicular anisotropy with different squareness ratio and coercivity due inherent template characteristics. In porous silicon, template (figure E.5a), in-plane squareness ratio (0.2-0.22) and coercivity (100-130 Oe) were observed compared to very low values from out-of-plane and no magnetic field during deposition measurements. However, further enhancement is hindered by wire imperfections and surface roughness. In case of alumina template (figure E.5b), because of small magnetocrystalline anisotropy, the net magnetic anisotropy is mainly due to two terms: 1) anisotropy induced due to magnetic easy axis parallel to wire axis, 2) magnetostatic coupling between wires, which develops an easy axis perpendicular to wire axis. Because of higher pore density in alumina template (about 10^9 pores/cm^3) compared to polycarbonate/porous silicon (less than 10^8 pores/cm^3), the net contribution from dipole field (aligned perpendicular to wire) is to reduce effective anisotropy field given by:

$$H_k = \frac{2\pi M_s - 6.3 M_s r^2 L}{d^3} \tag{E.1}$$

M_s is the saturation magnetization, r is the wire diameter, L is the length and d is the interpore distance. The squareness ratio and coercivity in this case are, however, slightly improved to 0.25-0.28 and 200-220 Oe respectively from oriented growth of nanowires. Finally, in case of polycarbonate, (figure E.5c), a remarkable perpendicular anisotropy is exhibited. It can be seen that the maximum squareness ratio (0.58-0.60) and coercivity (400-425 Oe) are observed when the measuring magnetic field is in-plane with the nanowires. This suggests that application of perpendicular external magnetic field during electrodeposition in polycarbonate template results in highest perpendicular magnetic anisotropy. However, the slight shearing of the hysteresis curve is mainly due to the 34º (maximum) deviation between the pore axis and surface normal, along with the dipole interactions between the wires (interpore distance is 250-600 nm). Even though, the average interpore distance is much larger in polycarbonate compared to alumina, the wire interactions will occur for spacing less than 1.5 μm. This dipole wire interaction tends to align perpendicular to wire axis, resulting in decrease in squareness ratio.

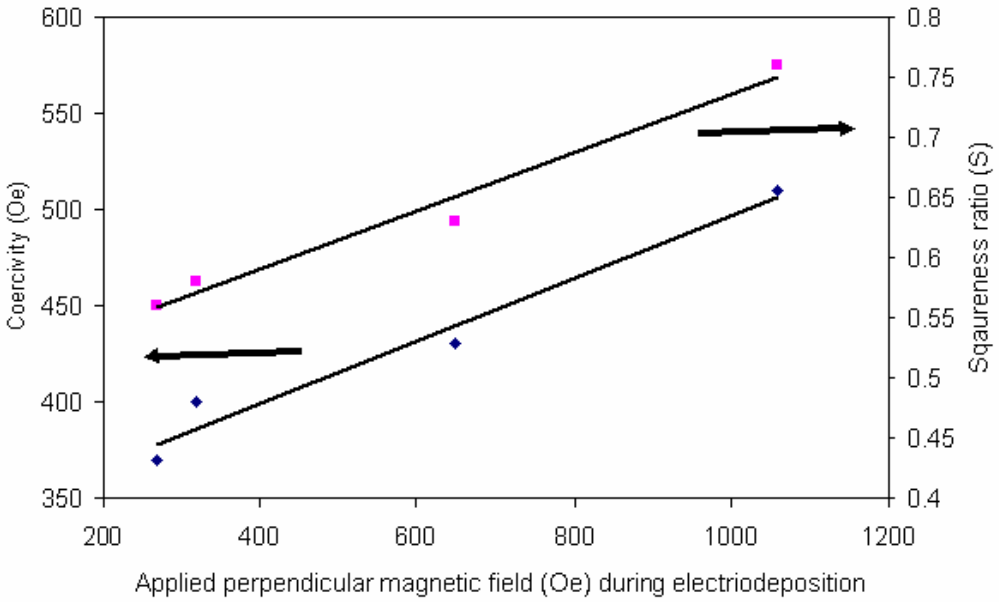

Figure E.6 Dependence of coercivity and squareness ratio on applied perpendicular magnetic field during Ni-Fe electrodeposition in polycarbonate template.

Next, the effect of varying the magnetic field perpendicular (270-1060 Oe) to the polycarbonate template during electrodeposition process was investigated. Figure E.6 shows the measured average coercivity and squareness ratio (M_r/M_s) as a function of perpendicular magnetic field during electrodeposition. With increase in applied magnetic field during electrodeposition both coerciviity and squareness ratio increases significantly. Squareness ratio of about 0.76 was observed for perpendicular magnetic field of 1060 Oe, indicating Ni-Fe growth with c-axis parallel to nanowire axis and hence enhanced perpendicular magnetic anisotropy. However this is still lower squareness ratio than the expected theoretical values because of the above stated reasons.

Lastly, the length effect was examined by depositing Ni-Fe nanowires of varying lengths (2-5 μm) in polycarbonate template in presence of magnetic field (320 Oe) during deposition. Figure E.7 shows the measured coercivity and squareness as a function of wire length. For magnetic field applied in-plane with the wire axis, as the wire length is increased, according to infinite long magnetic cylinders model, shape anisotropy should also increase. But our experiments show that both coercivity and squareness monotonically decreases, with increase in

wire length. This may be caused by length dependence on dipole interactions among wires as:

$$H_d = \frac{4.2 M_s r^2 L}{d^d} \tag{E.2}$$

M_s is the saturation magnetization, r is the wire diameter, L is the length and d is the interpore distance. In addition, as wire length increase, saturation magnetization also increases. Table E.2 summarizes the relevant magnetic characterization parameters for all template in presence and absence of external magnetic field during deposition

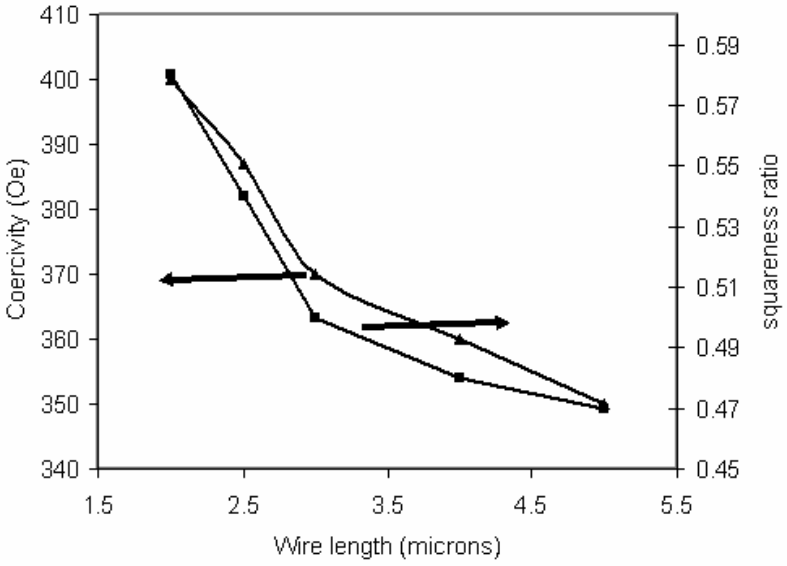

Figure E.7 Dependence of coercivity and squareness ratio on Ni-Fe wire length, deposited in polycarbonate template.

Summary

In summary, in this work, a systematic study was performed to study the structural and magnetic property of Ni-Fe nanowires as a function template material, applied magnetic field during deposition, wire length and field orientation during measurement. The applied magnetic field was shown to have strong influence on crystallographic and magnetic properties of Ni-Fe nanowires, in particular in the case of polycarbonate template, which showed highest coercivity

and squareness ratio. Application of magnetic field perpendicular to the template plane during deposition tends to force the Ni-Fe grains with c-axis along the orientation of applied field, thereby resulting in perpendicular shape anisotropy. Further, the influence of applied magnetic field strength and wire length on magnetic properties was also studied.

Table E.2 Magnetic characterization parameters for Ni-Fe nanowires in different template and magnetic field during deposition.

Template	Wire length (μm)	Magnetic field during deposition (Oe)	Coercivity (Oe)	Squareness ratio
Porous silicon	2 - 3	0	80-100	0.18
Alumina	2 – 2.3	0	60-80	0.15
Polycarbonate	2 – 2.2	0	50-65	0.12
Porous silicon	2 - 3	320	100-130	0.2-0.22
Alumina	2 – 2.3	320	200-220	0.25-0.28
Polycarbonate	2 – 2.2	320	400-425	0.58-0.60
Polycarbonate	2 - 2.2	270	379	0.52
Polycarbonate	2 - 2.2	650	460	0.63
Polycarbonate	2 - 2.2	1060	530	0.74
Polycarbonate	2.5-2.75	320	387	0.54
Polycarbonate	3 - 3.2	320	370	0.5
Polycarbonate	4 - 4.25	320	360	0.48
Polycarbonate	5 - 5.3	320	350	0.47

APPENDIX F

POROUS SILICON BASED MICRO DIRECT ETHANOL FUEL CELL

Overview

The development of micro power sources is critical for successful deployment of untethered, integrated MicroElectroMechanical Systems (MEMS), communication, computing, or implantable medical devices. Micromachined fuel cells are being actively pursued as viable on-board power sources for portable applications. This increasing interest in microfabrication of fuel cells stems from their potential advantages: simple construction, low temperature of operation, environmental friendliness, lack of moving parts, and competitive power and energy densities with batteries for portable power applications. Direct alcohol/air proton exchange membrane fuel cells (PEMFC) are of particular interest as they have the potential to be compact, do not require bulky external fuel-reforming system and have the ability to operate near room temperature. Additionally ethanol as a fuel possesses higher volumetric and gravimetric energy densities and, higher efficiency. It can be easily stored, handled and transported compared to other fuels. The key requirements in development of a fuel cell for man-wearable and implantable medical applications are: non-toxicity of fuel, orientation independence and self-activation/priming of the cell, without a need for an external active pump. The Direct Methanol Fuel Cell (DMFC), powered by electro-oxidation of methanol has been studied extensively. However, methanol cannot be used in medical applications as it is toxic, volatile and has a low boiling point. Additionally it cannot be transported on common-carriers (aircrafts, trains, buses). Ethanol is an attractive alternative fuel because it is a) non-toxic b) a rich source of hydrogen with large negative free energy and reaction kinetics, c) renewable, d) eco-friendly, and e) FAA approved chemical for on-board carriage (alcoholic beverages contain ethanol). These advantages can enable ethanol based fuel cells to power implantable medical devices such as micro-insulin pumps for controlled drug release, cerebrospinal shunt pump, pacemakers and for biotelemetry. To leverage this goal, an orientation independent, self priming, micro Direct Ethanol Fuel Cell (DEFC) with enhanced active electrode surface area, has been developed. The fuel cell is powered by ethanol at room temperature (23 ºC). The ability to use ethanol and operate at room temperature will enable bio-applications. The fuel stack uses novel porous silicon electrodes that are fabricated by wet etching through macroporous silicon technology. The pores developed in the porous silicon electrode act both as micro-capillaries/wicking structures and as built-in fuel

reservoir, thereby reducing the size of the fuel cell. The capillary action of the micro-pores of porous silicon electrode will pump the fuel towards the cell's reaction sites, irrespective of cell orientation. The capillary driving pressure across the meniscus of the porous electrode increases with decreasing pore diameter. The pore sizes dictate the pumping/priming pressure in the fuel cell. The porous silicon electrode thus eliminates the need for an active external fuel pump.

This concept of orientation independence and self-activation in fuel cells is different from conventional flow through fuel cell configurations where channels are micromachined in silicon substrate and an external pump is used for fuel supply. This work reports on the fabrication details and preliminary performance characteristics of such novel micro fuel cell using porous silicon electrodes, Nafion® 115 proton exchange membrane (PEM) and ethanol as the fuel.

Principle of operation

A fuel cell is an electrochemical device that converts chemical energy directly into electrical current. An electrochemical cell consists of a pair of electrodes (anode and cathode) and an electrolyte layer between the electrodes. At the anode, the fuel is oxidized, resulting in electrons that travel to the external load. At the cathode, the oxidant is reduced, resulting in consumption of electrons from the external load. The circuit is completed by the flow of ions from one electrode to the other through the electrolyte. The electrochemical reactions and the ions vary depending on the type of fuel cell.

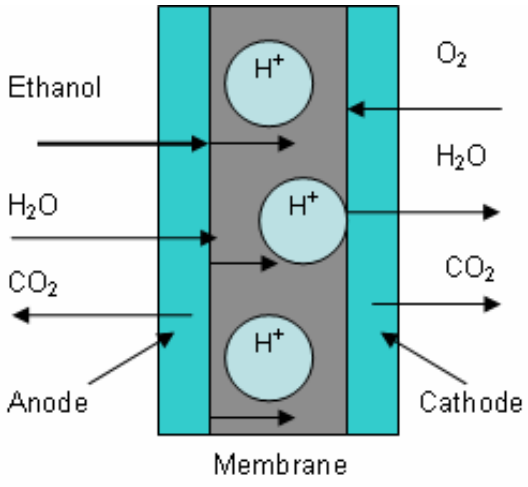

Figure F.1 Schematic illustration of a bipolar direct ethanol fuel cell (DEFC).

Figure F.1 schematically illustrates of the bipolar Direct Ethanol Fuel Cell (DEFC) structure. The bipolar DEFC structure consists of two (porous) electrodes, fuel micro-column (anode) and air micro-column (cathode) sandwiching an electrolyte (proton exchange membrane). The electrocatalyst, platinum is deposited on both the electrodes. In the case of a DEFC, ethanol/water mixture is supplied at the anode as fuel and the proton exchange membrane acts as the electrolyte. The following half cell reactions take place in presence of a platinum catalyst.

At the anode:

$$C_2H_5OH + 3H_2O \rightarrow 2CO_2 + 12H^+ + 12e^- \quad \text{(F.1)}$$

At the cathode:

$$3O_2 + 12e^- + 12\,H^+ \rightarrow 6H_2O \quad \text{(F.2)}$$

The overall reaction can be expressed as

$$C_2H_5OH + 3O_2 \rightarrow 2CO_2 + 6H_2O \quad \text{(F.3)}$$

At the anode, the fuel (ethanol/water mixture) is oxidized to carbon dioxide, hydrogen ions and electrons. The electrons produced at the anode flow through the external circuit to deliver power. The H^+ ions diffuse through the electrolyte (PEM) to the cathode and react with oxygen from environment using the electrons coming back from the external circuit, to form water.

Design and fabrication

The design of the porous silicon based micro fuel cell stack: Figure F.2a illustrates the cross-sectional view of the porous silicon based micro DEFC stack. This structure consists of a porous silicon anode (fuel micro-column) and a porous silicon cathode (air micro-column) sandwiching a Proton Exchange Membrane (PEM). The anode micro-columns serve as built-in fuel reservoir, while the cathode micro-columns are exposed to the atmosphere. Platinum is deposited on both the micro-columns to act both as an electrocatalyst and as a current collector. Nafion 115™ membrane acts as the PEM for the fuel cell.

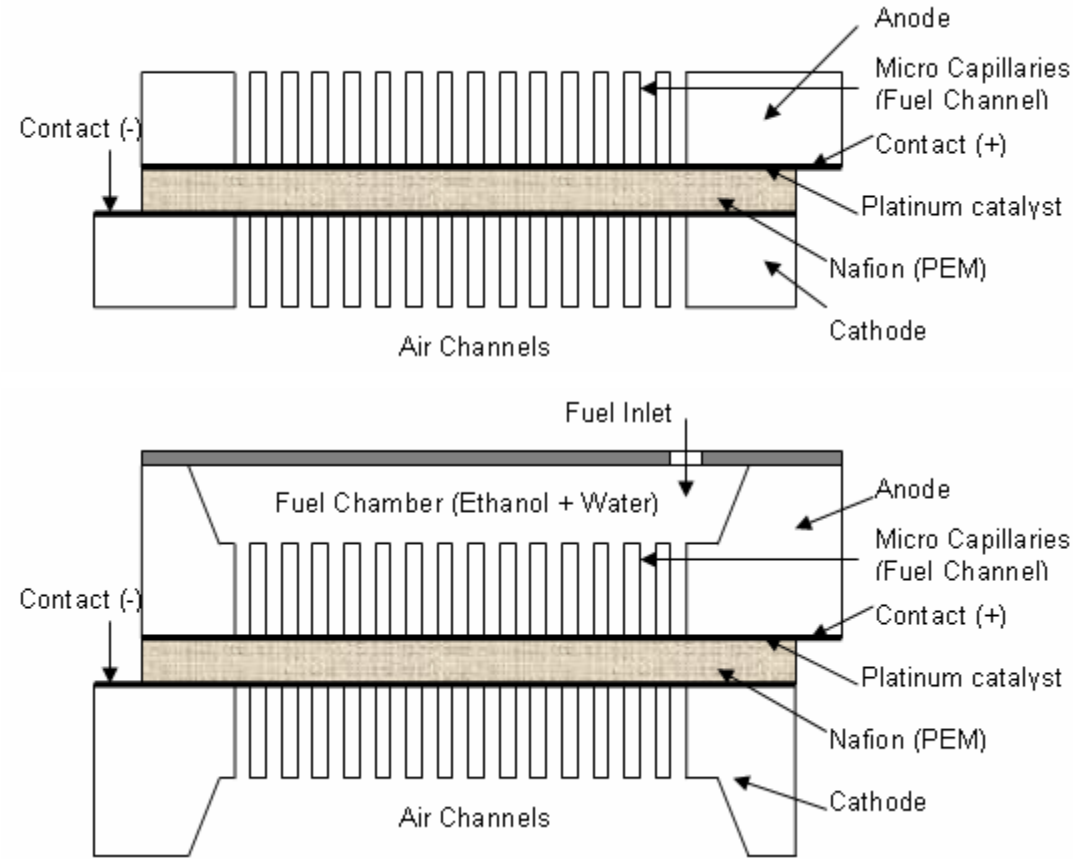

Figure F.2 a) Cross-sectional view of the porous silicon based micro DEFC stack, b) alternative design for the porous silicon based micro DEFC stack.

The porous silicon electrodes are fabricated using the Coherent Porous Silicon (CPS) technology. In the CPS etching technique, the (a) porosity and the (b) pore diameter of the electrodes can be carefully controlled. The control on porosity and capillary pressure (pore diameter) provides a control variable to minimize ethanol crossover. It has been demonstrated that for the given operating conditions fuel crossover can be reduced, when the fuel driving pressure is balanced across the electrodes. In this work, the cathode/anode driving pressures are balanced by controlling the pore diameter as the capillary pressure across the meniscus increases with decreasing pore diameter. Additionally, the capillary forces in the porous electrode result in fuel supply to the membrane at a stable pressure. The area of each electrode is 1 cm^2. As shown in figure F.2b, an alternate structure with 50 μm depth trench in the porous silicon substrate has also been designed for additional fuel storage. The fabrication process for making the porous silicon electrode is discussed hereunder.

Formation of porous silicon electrode: The porous silicon electrode was fabricated using the photo-electrochemical porous silicon etching technique. It was performed in a photon-assisted electrochemical etch rig, schematically illustrated in figure F.3. The wafer was anodically biased and the etching was done using 2% (v/v) HF solution and controlled current density. The backside of the wafer was exposed to light from a 250 W quartz-tungsten-halogen lamp. This light produces the electron-hole pairs that drive the silicon dissolution (etching) process. Figure F.4 illustrates the fabrication process flow for making porous silicon electrodes. The porous silicon fabrication started with a n-type, 250 μm DSP double side polished silicon wafer with resistivity of 25 Ω-cm. (F.4a, F.4b) The wafer was first oxidized to get an 300 nm thick oxide; the oxide on backside was then stripped. (F.4c) n+ diffusion from a solid source was then carried out to ensure an ohmic contact with the metal electrode. The resistivity of the doped region after diffusion was less than 0.1 ohm-cm. (F.4d) The anode metal (Al) was deposited on the backside of the wafer. (F.4e) The metal was patterned and etched to form the anode ring. (4f) The front side of the wafer was patterned with a mask for pore initiation by photolithography. The pattern, 10 μm squares at a pitch of 20 μm was transferred in the oxide. The oxide was etched in 10:1 Buffered Oxide Etch (BOE). (F.4g) Anisotropic etching of the pore initiation pits was carried out using KOH 25 wt%, resulting in inverted pyramids. These pyramidal etch pits concentrate the applied electric field and pore etching begins at these tip locations. (F.4h) Coherent Porous Silicon (CPS) etching was carried out to about 200 μm in the electrochemical etch setup. This resulted in circular pores perpendicular to the (100) silicon surface and directed towards the light, which is the source of holes were obtained. (F.4i) The Al electrode was then etched away. (F.4j) Finally, 50 μm Si was mechanically lapped from the backside of the wafer, using a Logitech PM5 lapping machine, to develop through-pores (Figure F.2a). Alternatively, a trench 50 μm in depth can be etched in the porous silicon substrate using TMAH at 90 ºC to develop through-pores (Figure F.2b). The pores were then converted into micro-capillaries capable of "wicking" the fuel through a light oxidation step. This technique results in well defined high aspect ratio circular columns (micro-capillaries) in Si substrate. Figure F.5a shows the SEM of the silicon substrate after the pore initiation lithography and etching. The square shape of the pores on the surface is because of pore initiation etching. The pore dimensions and pitch of the resultant circular pores can be tailored, to control the capillary pressure and fuel supply to the membrane. For this work, 10 μm diameter micro-capillaries with a pitch of 20 μm were designed and fabricated.

Figure F.5b shows the SEM cross-sectional view of the final through porous silicon substrate. The porous silicon substrate was then lightly oxidized. The hydrophilic nature of oxidized pore walls increases the angle of contact with the fuel, reducing the capillary pressure drop. This substrate is capable of constraining the fuel supply by 75% (capillary/silicon ratio).

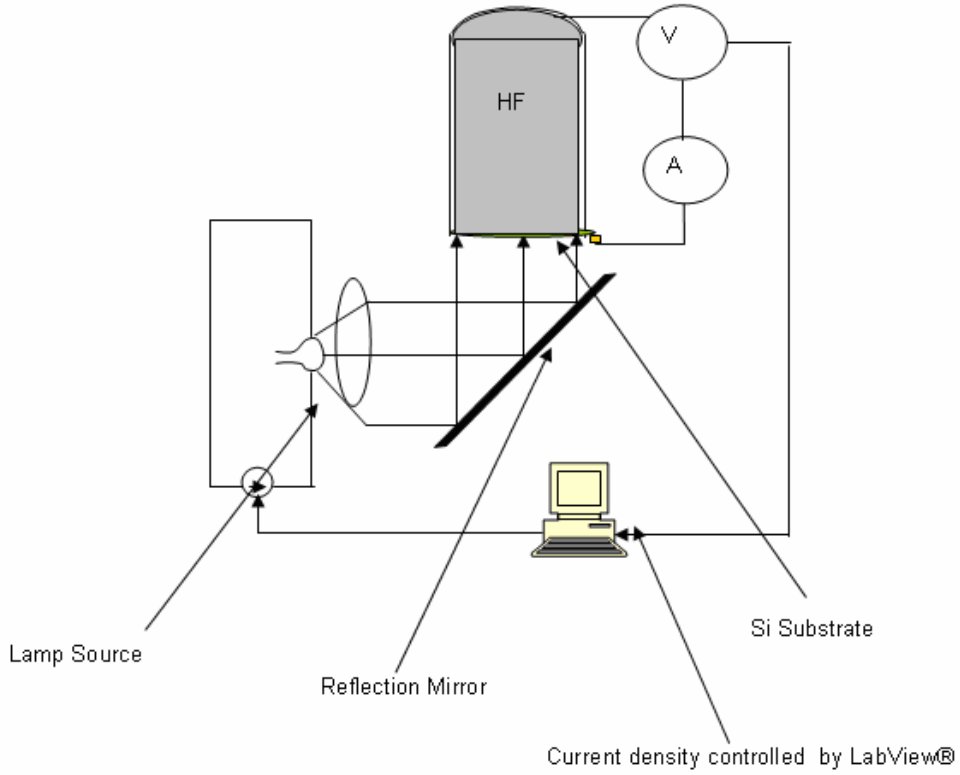

Figure F.3 Schematic of the setup for porous silicon etching.

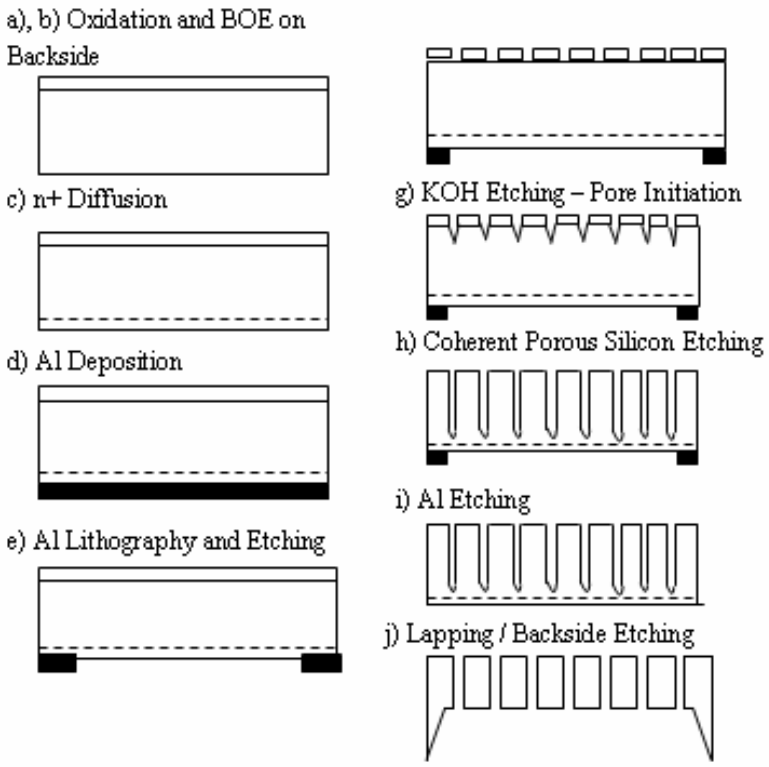

Figure F.4 Illustration of the fabrication process flow for making porous silicon.

Calculation of capillary effect in the micro-pores: It constitutes a two phase flow model. In two-phase flow in micro-channels, capillary force dominates the other two forces, gravitational and viscous, due to the small pore diameter. The capillary pressure is defined as the difference between the gas and liquid phase pressures at the curved meniscus interface. The classical two phase model, capillary force in a single micro-pore is given by the Young-Laplace equation:

$F_{upward} = T. (2\Pi r). \cos(\theta)$ (F.4)

T is the surface tension of the fuel, (approximately 36.375 mN/m at 23 ºC): derived from surface tension of ethanol and water, 22.75 mN/m and water 72.75 mN/m respectively), (2Πr) is the perimeter of the circular micro-column (10 μm in diameter), θ is the contact angle (at the solid/liquid interface, perfect wetting takes place and θ is 0). The corresponding pressure drop due to the upward capillary force is given by

$P = F_{upward} / \Pi r^2$ (F.5)

Every circular micro-pore thus acts a capillary and provides fuel at a higher pressure (14.55 KPa) to the membrane, without an active pump and irrespective of cell orientation. As a first scale approximation, the effect of CO_2 bubbles generated as a byproduct of the anodic reaction was not accounted for.

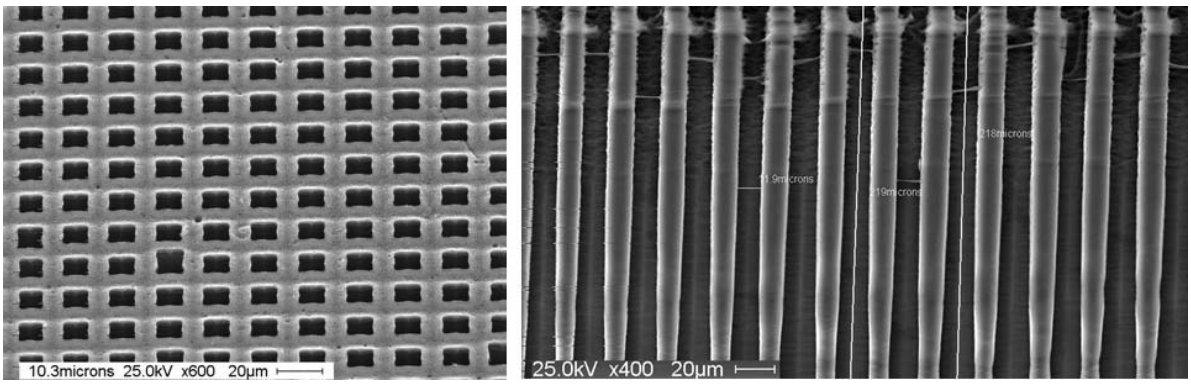

Figure F.5 SEM of the silicon substrate after the pore initiation lithography and etching (left), SEM cross-sectional view of the final through porous silicon substrate (right).

Metallization and assembly of the micro fuel cell: The substrate with micro-capillaries was than metallized on one side with a layer of Ti/Pt (80 nm/200 nm). The Pt layer acts both as an electrocatalyst for the reaction and as a current collector (electrode). The wafer was then diced to make the anode and cathode electrodes. A DuPont™ Nafion® 115 (thickness: 127 µm, weight: 250 g/m^2, conductivity: 0.083 S/cm) was used as the proton exchange membrane (PEM) for the cell. Prior to the assembly of the fuel cell stack, the membrane was pretreated in 1M H_2O_2 at 80 ºC for 1 hour, rinsed in DI water for 1 hour, and then immersed in 1M H_2SO_4 at 80 ºC for 1 hour. The metallized sides of the anode and cathode, the pretreated Nafion® 115 membrane were coated with Nafion® 5% solution. They were then, hot pressed at 160 ºC and 80 kg/cm^2 for 60 seconds to form the Membrane Electrode Assembly (MEA). The anode and cathode integrated with the PEM were connected to the external load circuit (potentiostat). Figure F.6 shows the SEM cross-sectional view the MEA fuel cell stack. The stack was sectioned by cleaving, as it tended to shatter during dicing. This may be due to the soft nature of Nafion membrane coupled with the vibrations in the dicing machine. The anode, cathode and the polymer electrolyte are

clearly visible in the figure F.6. Due to wafer cleaving across different planes, the pores in the SEM do not appear uniform and the polymer electrolyte appears torn.

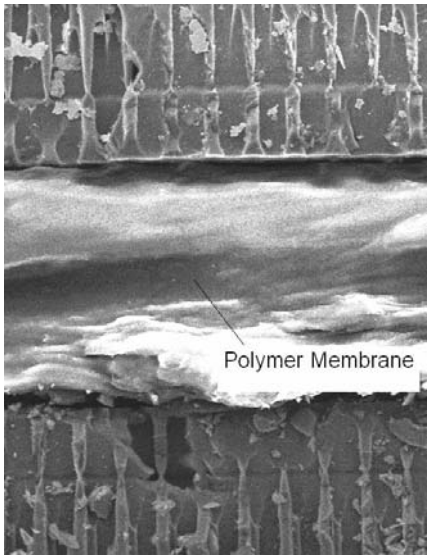

Figure F.6 SEM cross-sectional view of the membrane electrode assembly (MEA) in the fuel cell stack. The pores appear non-uniform and polymer membrane appears torn, because of wafer cleaving across different planes.

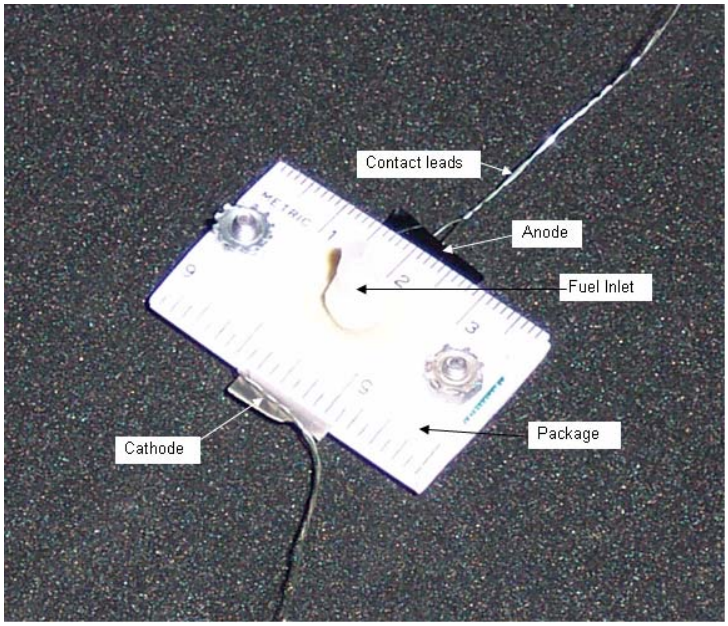

Figure F.7 Picture of the micro DEFC in a custom-built package. The image shows the inlet port for fuel and the contact leads from the anode and cathode electrodes.

Test results and discussion

The fuel cell was tested at room temperature in a custom-built package, as shown in figure F.7. A micro pipette was used to feed the fuel (5 µL of 8.5 M ethanol solution) to the anode side of the cell. As discussed above, the fuel was supplied at a pressure of about 14.55 KPa in each micro-capillary, independent of the orientation. On the cathode side of the fuel cell, oxygen was supplied from the environment. The anode and cathode were connected to an external varying load (potentiostat) to deliver electric power. The cell generated an open circuit voltage (OCV) of 260 mV at room temperature.

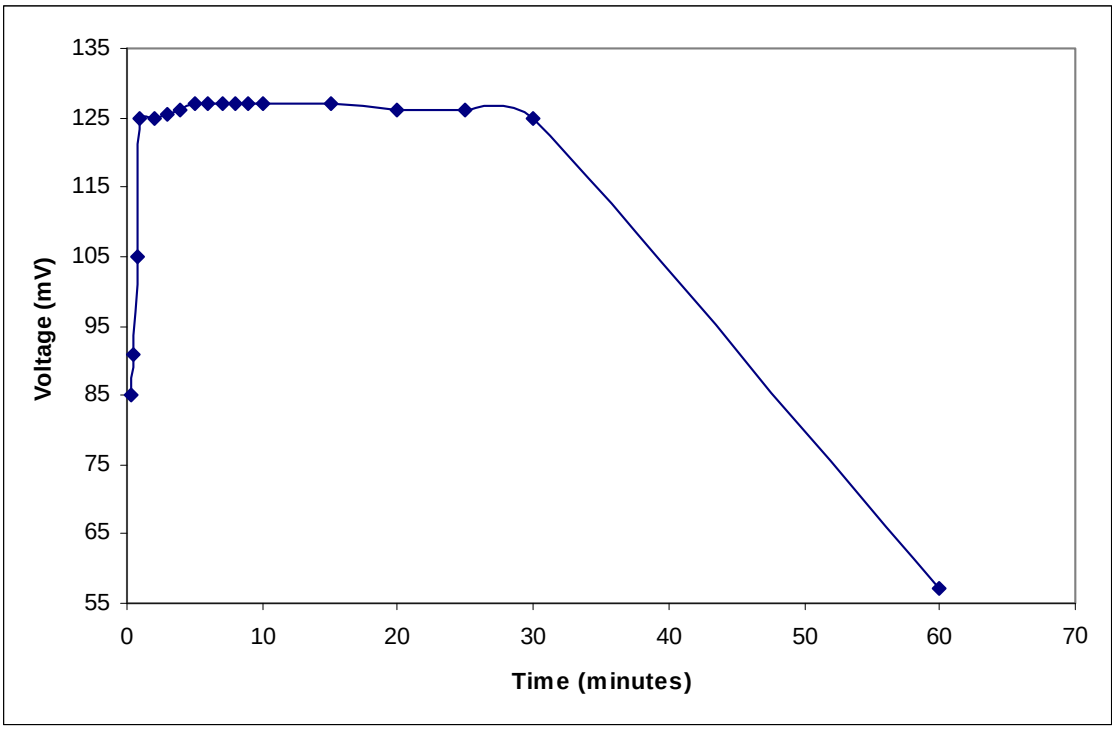

Figure F.8 Variation of cell voltage as a function of time for the micro DEFC. 10 µL of ethanol/water mixture (1:1) was used for this test.

Figure F.8 shows the variation of cell voltage as a function of time across a 10 Ω resistor. When a 10 Ω load was connected across the cell, the voltage generated was 127 mV. The decrease in voltage after certain time period was expected as the cell contains limited amount of fuel (5 µL) that depletes with time. For a fuel input of 5 µL of 8.5 M ethanol (theoretical capacity

equivalent: 27.5 mAH), the cell delivered 12.7 mAH. To establish the effect of orientation on cell performance, polarization curves (voltage versus current density) at different cell orientations were plotted. The polarization curves (Figure F.9) show the cell voltage as certain current is drawn from it. As more current is drawn from a cell, over-potentials reduce the effective voltage produced. The active cell area, the load on the cell, and the cell orientation determine this current. In general, polarization curves are unique to each cell and depend on the physical configuration of the cell. The porous silicon based micro DEFC has been characterized using this criterion.

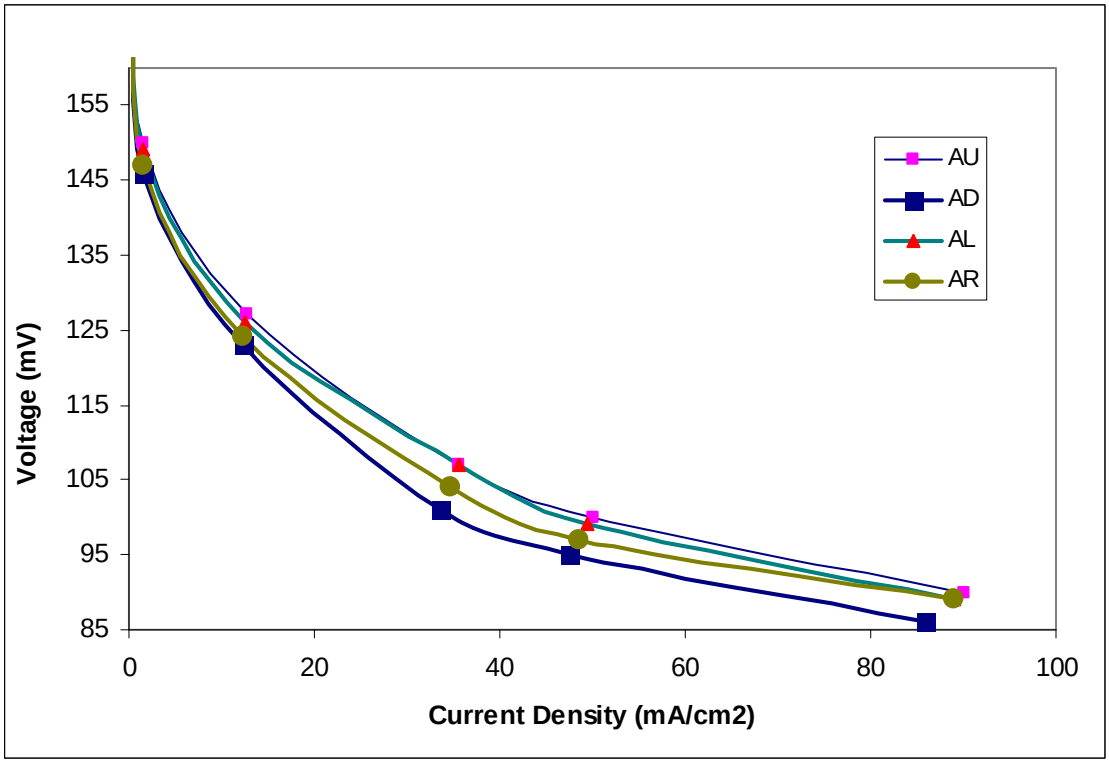

Figure F.9 Polarization curves at different cell orientations for the micro DEFC. The tests were performed with ethanol/water mixture (1:1) at room temperature. Cell orientations: anode facing up (AU), anode facing down (AD), anode on left (AL) and anode on right (AR).

Figure F.9 depicts the polarization curves for four different cell orientations and varying resistive loads measured at room temperature. The cell was tested in the following orientations: anode facing up (AU), anode facing down (AD), anode on left (AL) and anode on right (AR). The load across the cell was varied from 1 to 5000 Ω and measurements were recorded after the

voltage stabilized (15 minutes after startup). It is evident from the polarization curves that orientation had minimal effect on the cell voltage (< 5 mV change). This fuel cell produced a maximum power density of 8.1 mW/cm^2, which is comparable with larger ethanol-based fuel cells measured at room temperature (23 ºC). We believe that the increase in maximum power density and OCV compared to earlier results reported by us, are because of improved membrane and electrode bonding (pressure of 80 kg/cm^2 was used) and better assembly techniques. To better understand the reproducibility of the cell, voltage versus current density measurements were done repeatedly, as shown in figure F.10. The "anode up" orientation was maintained for these measurements. As in the previous instance, the load was varied from 1 to 5000 Ω and the measurements were recorded after the voltage stabilized (stable region in figure F.8). Five measurements were made at each load. Then statistical analysis was done with the standard deviation of the voltage values, which represent a 95% confidence in the data if the variability is normally distributed.

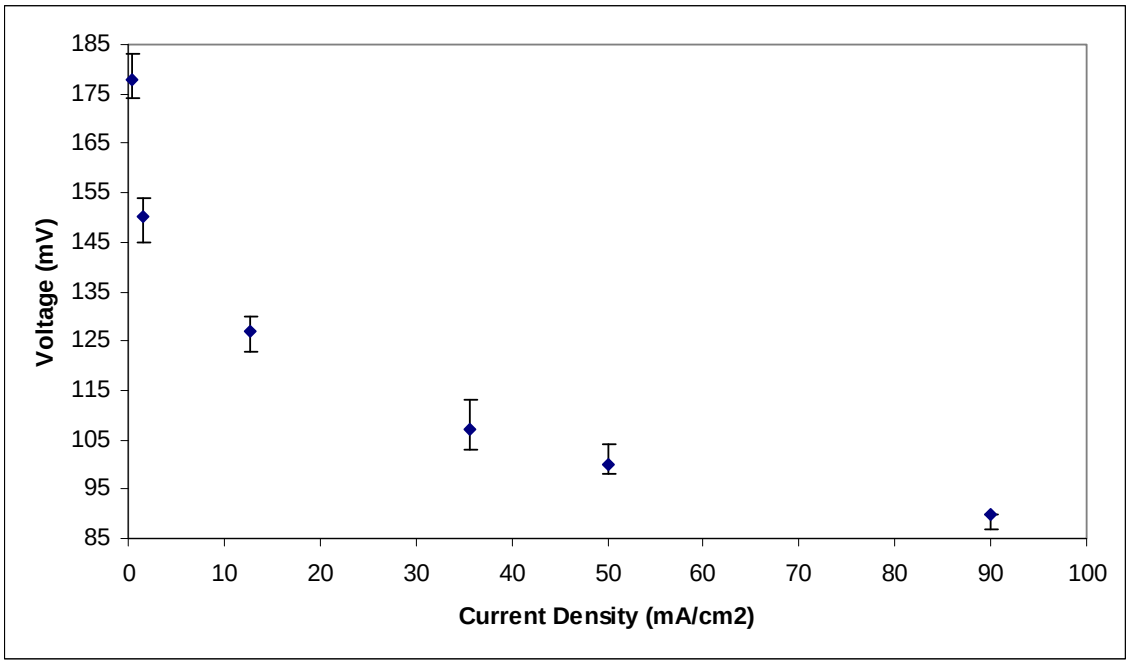

Figure F.10 Statistical analysis of voltage versus current density using voltage error bars. Load was varied from 1 to 5000 Ω and five measurements were made at each load.

It is evident that the open circuit voltage generated in this cell was significantly lower (0.26 V) than the theoretical Gibbs free energy value (1.1 V). This may be because of a) poor catalytic activity of pure platinum, b) poisoning of platinum electrodes from the intermediate reaction products such as carbon monoxide, which are result of dissociative chemisorption of ethanol, and c) ethanol crossover (even though reduced) from anode to cathode by means of diffusion and electro-osmotic drag, d) mass transport effects: build up of CO_2 gas bubbles at the porous silicon anode and e) recording data after the cell stabilizes, thus not accounting for the power generated in the early phase. To overcome these problems and to improve the voltage and power density, bimetallic platinum alloy based electrocatalysts (such as Pt-Ru, Pt-Sn or Pt-Mo) are under investigation.

ABOUT THE AUTHOR

Shyam Aravamudhan received the BE degree in Electrical and Electronics Engineering from University of Madras, India in 1999 and MS in Electrical Engineering from University of South Florida (USF), Tampa, FL in 2002. He is currently pursuing a PhD in Electrical Engineering at USF with specialization in MEMS and nanotechnology. As part of the Bio-MEMS and Microsystems Laboratory and Nanomaterials and Nanomanufacturing Research Center, his research includes development of MEMS and nano-based sensors for the marine environment, synthesis and characterization of nanostructures for magnetic, biological and through wafer interconnect applications and micromachined fuel cells.